Ecole Doctorale SIMPPÉ
Laboratoire LRGP

School of Chemical Engineering

Thèse

Présentée et soutenue publiquement pour l'obtention du titre de

DOCTEUR DE L'UNIVERSITE DE LORRAINE

Mention : Génie des Procédés

par **Zulfida Mohamad Hafis BIN MOHD SHAFIE**

Élaboration de membranes composites á fibres creuses á base de poly-4-méthyl-1-pentène et polydiméthylsiloxane comme couche intermédiaire revêtues d'une couche sélective de polyimide P84 pour la séparation de CO_2/N_2 et CO_2/CH_4

Date de soutenance : 1er décembre 2021

Membres du jury :

Directeurs de thèse :	**M. Abdul Latif BIN AHMAD**	**Professor, Universiti Sains Malaysia**
	Mme. Sabine RODE	**Professeur, Université de Lorraine**
Co-directrices de thèse :	**Mme. Siew Chun LOW**	**Associate Professor, Universiti Sains Malaysia**
	Mme. Bouchra BELAISSAOUI	**Maître de Conférences, Université de Lorraine**
Président de jury / rapporteur 1 :	**M. Jean-Christophe REMIGY**	**Professeur, Université Toulouse III – Paul Sabatier**
Rapporteur 2 :	**Mme. Nur Awanis BINTI HASHIM**	**Associate Professor, Universiti Malaya**

POLYDIMETHYLSILOXANE AND POLY(4-METHYL-1-PENTENE) AS GUTTER LAYER AND P84 POLYIMIDE COATED COMPOSITE HOLLOW FIBER MEMBRANES FOR CO_2/N_2 AND CO_2/CH_4 SEPARATION

by

ZULFIDA MOHAMAD HAFIS B MOHD SHAFIE

Thesis submitted in fulfilment of the
requirements for the Degree of
Doctor of Philosophy

December 2021

ACKNOWLEDGEMENT

Alhamdulillah the thesis is finally being done. I would like to thank all my lovely research supervisors; Prof. Ir. Dr. Abdul Latif Ahmad, Prof. Dr. Sabine Rode, Assoc. Prof. Dr. Low Siew Chun, and Assist. Prof. Dr. Bouchra Belaissaoui for their indebted guidance. Not to forgot, Dr. Denis Roizard for his research insight during my stay in France. Praise to the people of School of Chemical Engineering (SChE) Universiti Sains Malaysia and of Laboratoire Réactions et Génie des Procédés (LRGP) Université de Lorraine for their help throughout of my Ph.D. To Assoc. Prof. Dr. Hazwan Hussin and Prof. Dr. Afidah Abdul Rahim; the two person who make this dual-degree a possibility, to the people in USM-UL Center, to those in SIMPPÉ, to those in ENSIC, to those at the French Embassy, and to those in MTDC Laboratory; thank you very much for all your help throughout my journey. There are too many names to be listed, which without any of them, this thesis wouldn't be here. And the thesis won't feed me if it wasn't for the financial support by Prof. Latif, IPS USM under the Fellowship Scheme, and French Embassy in Malaysia under the French Government scholarship that allows me to spend my wonderful year in Nancy. I might not be the person I am today if not because of Prof JitKang who saw my potential during my undergraduate study and guide me to the world of academic research, which I never knew existed before. To my family especially my mum, you finally got a 'doctor'! Thanks for all the care you've given. And to my dearest wife Nur Dina, thank you for your continuous believe and moral support towards me. Good luck on your own Ph.D. journey! 2011-2021, a 10-years journey in USM has finally come to an end. This might be my victory, but it would not be a reality without the support of the people around me, with or without knowing. The thesis might end, but my gratitude goes on forever. Thank you, et merci beaucoup!

TABLE OF CONTENTS

LIST OF TABLES

LIST OF FIGURES

Page

LIST OF SYMBOLS

Symbol	Description	Unit
j	Permeate flux	cm^3 (STP).cm^{-2}.s^{-1}
P	Permeability	Barrer
p_0	Feed partial pressure	bar
p_ℓ	Permeate partial pressure	bar
ℓ	Thickness	µm
$\mathcal{P}$	Permeance	GPU
U_0	Dip coating speed	mm.s^{-1}
S	Stagnation point	-
δ	Boundary layer	-
h_0	Thickness of entrained fluid film / wet thickness	nm
η	Dynamic viscosity	cP or Pa.s
Bo	Bond number	-
ρ	Density	g.cm^{-3}
g	Gravitational acceleration	m.s^{-2}
e	Experimental constant	-
γ	Surface tension / surface energy	mJ.m^{-2} or mN.m^{-1}
b	Fiber radius	µm
D	Diffusivity / diffusion coefficient	cm^2.s^{-1}
α	Selectivity	-
d_p	Pore diameter	µm
R	Gas constant	$J \cdot K^{-1} \cdot mol^{-1}$
T	Temperature	K

M	Molecular mass	Da
K_n	Knudsen number	-
λ	Mean free path length	µm
Ψ	Restriction factor	-
τ	Normalized thickness	-
ε	Porosity	-
N_R	Restriction number	-
S	Solubility / gas sorption coefficient	$cm^3.cm^{-3}.cmHg^{-1}$
h, m	Gas pair constant	-
d_k	Kinetic diameter	pm
φ	Pressure ratio	-
Q	Permeate flow rate	$cm^3.s^{-1}$
A	Effective membrane area	cm^2
J	Gas molar flux	$gmol.cm^{-2}.s^{-1}$
r	Pore radius	µm
k	Boltzman constant	$J.K^{-1}$
p	Gas pressure	bar
R	Gas flow resistance	$GPU^{-1}.cm^{-2}$
V	Downstream volume	cm^3
β	Permeance efficiency	-
f	Penetration factor	-
c	Concentration	$mol.m^{-3}$
∇	Del operator	-
Ca	Capillary number	-

W	Weight / mass	g
h_f	Dry thickness	nm
κ^{-1}	Capillary length	µm
R_g	Gyration radius	nm
σ	Uniformity coefficient	-
T_g	Glass transition temperature	°C
ω	Selectivity efficiency	-
S	Spreading coefficient	$mJ.m^{-2}$ or $mN.m^{-1}$
θ_Y	Young's contact angle	°

Subscripts

i, j	Gas component / permeant of interest
LV	Liquid-vapor interface
SV	Solid-vapor interface
SL	Solid-liquid interface
1	Coating/selective layer, in composite form
2	Substrate skin layer, in composite form
3	Substrate bulk porous layer, in composite form
c	Coating/selective layer, free / peeled
s	Substrate layer, free / peeled
app	Apparent value
int	Intrinsic value

LIST OF ABBREVIATIONS

PSf	Polysulfone
CO_2	Carbon dioxide
CH_4	Methane
RO	Reverse osmosis
TR	Thermally rearranged
PIM	Polymers with intrinsic microporosity
ZIF	Zeolitic imidazolate framework
MMM	Mixed matrix membrane
GO	Graphene oxide
PDMS	Polydimethylsiloxane
PI	Polyimides
PMP	Poly(4-methyl-1-pentene)
N_2	Nitrogen
CFD	Computational fluid dynamics
PES	Polyethersulfone
LiCl	Lithium chloride
RiS	Resistance-in-series
TFC	Thin film composite
IP	Interfacial polymerization
TFN	Thin film nanocomposite
MPD	M-phenylenediamine
TMC	Trimesoyl chloride
MOF	Metal-organic framework
PIP	Piperazine
DGBAmE	Diethylene glycol bis(3-aminopropyl) ether
PMMA	Polymethyl methacrylate
MWCNT	Multi-walled carbon nanotube
MEDA	N-methyldiethanolamine
Pebax	Polyether block amide
PAA	Poly(amic acid)
LLD	Landau-Levich-Derjaguin

PA	Polyamide
DOX	Dioxane
O_2	Oxygen
N_2	Nitrogen
DMF	Dimethylformamide
PTMSP	Poly[(1-trimethylsilyl)-1-propyne]
COF	Covalent organic frameworks
PEO	Polyethylene oxide
PAI	Poly(amide imide)
H_2S	Hydrogen sulfide
SiO_2	Silica
CNT	Carbon nanotube
NMP	N-methyl-2-pyrrolidone
TEOS	Tetraethyl orthosilicate
DBD	Dibutyltin dilaurate
ZTC	Zeolite-templated carbon
FIB	Focused ion beam
BTDA	Benzophenone-3,3’,4,4’-tetracarboxylic dianhydride
SEM	Scanning electron microscope
GPU	Gas permeation unit
FTIR-ATR	Fourier transform infrared spectroscopy attenuated total reflectance
EDX	Energy-dispersive X-ray spectroscopy
HF	Hollow fiber
FE-SEM	Field emission scanning electron microscope
LLD	Landau-Levich-Derjaguin
vdW	Van der Waals
PVP	Polyvinylpyrrolidone
PEG	Polyethylene glycol
MW	Molecular weight
CTFE	Chlorotrifluoroethylene
DMAc	Dimethylacetamide
PVDF	Polyvinylidene fluoride

PPTA	Poly-p-phenylene terephthalamide
FIB	Focussed ion beam
SAXS	Small angle X-ray scattering
TEM	Transmission electron microscopy
HAADF-STEM	Hard angle dark-field scanning transmission electron microscopy
SDS	Polystyrene-b-polydimethylsiloxane-b-polystyrene
PTFE	Polytetrafluoroethylene
PAN	Polyacrylonitrile
PP	Polypropylene
O_2	Oxygen
UV	Ultraviolet

POLIDIMETILSILOKSANA DAN POLI(4-METIL-1-PENTENA) SEBAGAI LAPISAN PENYALUR DAN MEMBRAN GENTIAN BERONGGA BERSALUT POLIIMIDA P84 UNTUK PENELAPAN CO_2/N_2 DAN CO_2/CH_4

ABSTRAK

Kemungkinan untuk menggunakan poli(4-metil-1-pentena) (PMP) sebagai lapisan substrat-penyalur akan dikaji dan dibandingkan dengan polidimetilsiloksana (PDMS) yang selalu digunakan sebagai lapisan penyalur. PDMS akan disokong oleh poliethersulfona (PES) sebagai substrat yang telah diubah suai dengan lithium klorida (LiCl) untuk menghasilkan liang permukaan yang pelbagai. PMP merupakan polimer bersifat kaca yang mempunyai kebolehtelapan yang tinggi. Ini membolehkan PMP digunakan sebagai lapisan substrat dan penyalur bersama, yang dijangka boleh mengelakkan kerumitan yang dihasilkan oleh masalah penerobosan larutan dan resapan sisi pada antara-muka liang-tumpat dalam membran komposit. Hasil kajian mendapati bahawa komposit PES/PDMS yang dihasilkan berjaya memperolehi ketelapan setinggi 26.6 ± 2.6 GPU bagi N_2 dan 354.4 ± 27.9 GPU bagi CO_2. Namun begitu, nilai ini adalah lebih rendah dari yang ditawarkan oleh membran PMP asimetrik berkulit tumpat pada nilai 84.6 ± 6.2 GPU bagi N_2 dan 607.3 ± 31.3 GPU bagi CO_2. Masalah penerobosan larutan dan penyekatan geometri di antara-muka liang-tumpat PES/PDMS mengurangkan kecekapan penelapan membran tersebut serendah hanya 4% dari penelapan unggulnya, terutama bagi salutan yang nipis. Dengan menggunakan model rintangan-siri (RiS) yang diubah suai, satu korelasi telah digubal untuk meramal kecekapan membran komposit sebagai faktor ketelapan substrat sebelum disalut, ketelapan intrinsik lapisan penyalut, faktor geometri dan faktor penembusan. Keseragaman permukaan substrat, yang mana didapati merupakan pemalar kepada substrat yang digunakan juga didapati memainkan peranan penting

dalam mempengaruhi ketelapan membran komposit. Jika dibandingkan dengan PMP asimetrik dengan lapisan permukaan tumpat yang nipis, PMP mempunyai kelebihan jika dipilih sebagai lapisan substrat-penyalur bagi kajian ini kerana ia mempunyai rintangan keseluruhan yang lebih rendah berbanding dengan lapisan PES/PDMS dan tidak terjejas oleh masalah sekatan geometri dan penerobosan larutan. Oleh itu, membran asimetrik PMP telah dipilih sebagai lapisan substrat-penyalur bersama manakala gas N_2, CO_2, dan CH_4 telah dipilih sebagai model bahan telap untuk penghasilan membran komposit dengan poliimida P84 (P84 PI), polimer komersial yang terkenal untuk pengasingan gas dalam industri sebagai lapisan memilih. Pembuatan membran komposit berbilang lapisan biasanya terhad kepada kesesuaian pelarut untuk setiap lapisan yang mungkin merosakkan lapisan dibawahnya. Oleh kerana PMP tidak larut di dalam N-metil-2-pirolidona (NMP) yang digunakan untuk melarutkan P84 PI, gentian PMP didapati serasi untuk membentuk dwi-lapisan menerusi kaedah penyalutan celupan bersama P84 PI tanpa memerlukan apa-apa prarawatan untuk mengatasi masalah tenaga permukaan PMP yang rendah. Oleh itu, pelbagai kepekatan larutan P84 PI telah disediakan untuk menyalut-celup membran gentian berongga PMP berkulit tumpat pada kelajuan 5 mm/s. Membran ini telah diuji untuk diketahui prestasi kebolehtelapan gasnya. Hasil kajian mendapati kepemilihan ideal setinggi 42.36 ± 19.08 bagi CO_2/CH_4 dan 18.55 ± 6.06 bagi CO_2/N_2 telah dicapai dengan menyalutkan P84 PI berkepekatan 14% mengikut berat. Namun begitu, walaupun PMP mempunyai ketahanan yang tinggi terhadap pelarut NMP, P84 PI pada kepekatan rendah (2-10% mengikut berat) akan merosakkan lapisan permukaan kulit tumpat membran PMP yang nipis. Ini akan menjejaskan prestasi proses pemisahan membran komposit tersebut. Penelitian hasil kajian memberikan hipotesis bahawa proses pengeringan P84 PI berkepekatan rendah akan mengecutkan lapisan tersebut,

lalu mengoyak permukaan lapisan PMP dan mendedahkan struktur berliang di bawahnya. Oleh itu, kepekatan P84 PI sebanyak 14% mengikut berat telah dipilih sebagai kepekatan minimum polimer yang diperlukan untuk menghasilkan membran komposit P84 PI/PMP yang bebas dari sebarang kecacatan. Pada kepekatan ini, kelajuan menyalut-celup boleh dimanipulasi untuk mendapatkan lapisan memilih bebas kecacatan yang lebih nipis, sesuai untuk penghasilan membran komposit. Namun demikian, masalah nyahbasahan larutan penyalut masih berlaku, dan akan menjadi lebih teruk apabila ketebalan lapisan penyalut berkurang. Ini merendahkan prestasi kebolehtelapan gasnya di bawah nilai intrinsik P84 PI dan lebih kepada nilai intrinsik lapisan substrat-penyalur PMP.

POLYDIMETHYLSILOXANE AND POLY(4-METHYL-1-PENTENE) AS GUTTER LAYER AND P84 POLYIMIDE COATED COMPOSITE HOLLOW FIBER MEMBRANES FOR CO_2/N_2 AND CO_2/CH_4 SEPARATION

ABSTRACT

In this work, the possibility of using poly(4-methyl-1-pentene) (PMP) as substrate-gutter layer in composite membrane was compared with commonly used polydimethylsiloxane (PDMS) as gutter layer, supported on lithium chloride (LiCl) modified polyethersulfone (PES) porous substrate of varying surface pore architectures. High permeability, glassy nature of PMP allows it to be used as a co-substrate-gutter layer, which is expected to mitigate the complexity of solution intrusion and lateral diffusion at dense-porous interface in composite membranes. Results showed that the fabricated composite PES/PDMS was able to obtain permeance as high as 26.6 ± 2.6 GPU for N_2 and 354.4 ± 27.9 GPU for CO_2 at about 1 μm coating thickness. Nevertheless, these values are lower than asymmetric dense skin PMP membrane at 84.6 ± 6.2 GPU for N_2 and 607.3 ± 31.3 GPU for CO_2. Solution intrusion and geometric restriction at the PES/PDMS dense-porous interface reduces its permeance efficiency to as low as 4% of its supposedly ideal permeance at low coating thickness. Using modified resistances-in-series (RiS) model, a correlation was developed to predict the composite membrane's efficiency as a factor of the pre-coat substrate's permeance, coating layer's intrinsic permeance, geometric factor, and penetration factor. It was elucidated that substrate surface uniformity also significantly affects the resulting composite membrane permeance, which was found to be a constant of the substrate used regardless of the coating layer thickness. In comparison, asymmetric PMP with thin dense surface layer was noted to be advantageous as the substrate-gutter layer for the current work as it possesses a lower overall resistance as

compared to the PES/PDMS layers and was not affected by geometric restriction and solution intrusion. Hence, asymmetric PMP membrane was chosen as a co-substrate-gutter layer while N_2, CO_2 and CH_4 gases were chosen as the model permeants for further composite membrane fabrication with P84 polyimide (PI), a commercial polymer notable for gas separation in industry, as selective layer. Fabrication of multi-layered composite membranes are usually limited by the suitability of the solvent for each layer's fabrication, which might damage the underlying layers. As PMP is non-soluble in N-methyl-pyrrolidone (NMP) that is used for dissolving P84 PI, it was found that PMP fiber is compatible to form a bilayer through dip coating with P84 PI, without the need for pre-treatment to overcome the low surface energy of PMP. Hence, P84 PI of various concentration was dip coated at 5 mm/s onto PMP-based dense skin hollow fiber membrane and tested for gas permeation performance. Results showed that ideal selectivity as high as 42.36 ± 19.08 for CO_2/CH_4 and 18.55 ± 6.06 for CO_2/N_2 was achieved at 14 wt.% P84 PI coating. Nevertheless, despite of PMP's resistibility to NMP, introduction of P84 PI at low concentration (2-10 wt.%) damages the thin, dense skin layer of the PMP's membrane surface which jeopardize the composite's separation performance. It is hypothesised that P84 PI's shrinkage during drying period tore the underlying dense PMP layer, exposing the porous structure underneath. Hence, there exist a minimum P84 PI polymer concentration in which defect free P84 PI/PMP composite membranes can be made, which is at about 14 wt.%. At this concentration, dip coating speed can be manipulated to obtain a thinner selective layer suitable for composite membrane fabrication, although dewetting of the coating solution still occurred and magnified as the coating thickness is reduced, reducing the gas selectivity below the intrinsic values of P84 PI and more towards the intrinsic values noted by the PMP substrate-gutter layer.

ÉLABORATION DE MEMBRANES COMPOSITES Á FIBRES CREUSES Á BASE DE POLY-4-MÉTHYL-1-PENTÈNE ET POLYDIMÉTHYLSILOXANE COMME COUCHE INTERMÉDIAIRE REVÊTUES D'UNE COUCHE SÉLECTIVE DE POLYIMIDE P84 POUR LA SÉPARATION DE CO_2/N_2 ET CO_2/CH_4

RÉSUMÉ

La structuration de membranes composites est inévitable pour la prochaine étape de développement de membranes à matrices mixtes (MMM), car l'utilisation de membranes asymétriques couramment non composites signifierait que la majorité des additifs seraient gaspillées dans le support poreux. Dans cette thèse, la possibilité d'utiliser du poly-4-méthyl-1-pentène (PMP) comme substrat et comme couche intermédiaire dans une membrane composite a été comparée au polydiméthylsiloxane (PDMS), qui est couramment utilisé comme couche intermédiaire. Il est supporté sur un support poreux en polyéthersulfone (PES), modifié avec du chlorure de lithium (LiCl) pour obtenir des architectures variables de surface de pores. La membrane composite à base de PDMS/PES a montré une perméance de 26,6 ± 2,6 GPU pour le N_2 et de 354,4 ± 27,9 GPU pour le CO_2 avec une épaisseur de revêtement minimale d'environ 1 µm. Cependant, cette valeur est inférieure à celle obtenue avec la membrane dense asymétrique à base de PMP ; 84,6 ± 6,2 GPU pour le N_2 et 607,3 ± 31,3 GPU pour le CO_2. Bien que le PDMS ait une perméabilité intrinsèque bien supérieure à celle du PMP, la membrane composite à base de PDMS/PES souffre d'un problème d'intrusion de solution et de restriction géométrique à son interface dense – poreux, ce qui réduit sa perméance à 4% de sa perméance supposée idéale, à faible épaisseur de revêtement. Il est en outre élucidé que l'uniformité de la surface du support poreux affecte également de manière significative la perméance de la membrane résultante. En comparaison, la membrane à base de PMP asymétrique avec une fine couche dense s'est avérée avantageuse en tant que support et couche intermédiaire, car elle permet d'atténuer le problème d'interface noté précédemment pour les membranes composites tout en étant très perméable, minimisant ainsi la résistance au transfert. Les gaz $N_2/CO_2/CH_4$ ont été choisis comme gaz perméants modèles pour la fabrication ultérieure de membranes composites à base de polyimide P84 (P84 PI) comme couche sélective. Cependant, la faible énergie de surface du PMP

limite sa compatibilité pour former une membrane composite. Il a été montré qu'il est possible de déposer par immersion le P84 PI sur une membrane PMP à couche dense, sans qu'il y ait besoin de prétraitement. Du P84 PI a été déposé par immersion à 5 mm/s sur une membrane de PMP à fibre creuse et à peau dense. Différentes concentrations de la solution de dépôt ont été étudiées. Les membranes composites ainsi fabriquées ont été testées pour vérifier leur performance de perméation des gaz. Les résultats ont montré une sélectivité idéale aussi élevée que 42,36 ± 19,08 pour le CO_2/CH_4 et 18,55 ± 6,06 pour le CO_2/N_2. Ces valeurs ont été atteintes pour des solutions de dépôt à 14 % en masse de P84 PI. Toutefois, malgré la résistance du PMP au solvant agressif N-méthyl-2-pyrrolidone (NMP), utilisé pour la solvatation du P84 PI, l'utilisation du P84 PI à faible concentration (2 - 10 % en masse) endommage la couche dense du PMP. Ceci compromet les performances de séparation de la membrane composite. Il est supposé que le rétrécissement du P84 PI lors du séchage a déchiré la couche de PMP sous-jacente. Ainsi, il existe une concentration minimale de polymère P84 PI pour laquelle une couche sélective sans défaut peut être réalisée (qui est d'environ 14 % en masse). À cette concentration, la vitesse de revêtement par immersion peut être contrôlée pour obtenir une couche sélective sans défaut et mince,adaptée à la fabrication de membranes composites. Ceci, bien que le démouillage de la solution de revêtement se produise encore et s'amplifie à mesure que l'épaisseur du revêtement est réduite.

CHAPTER ONE

INTRODUCTION

1.1 Surpassing the Upper Bound: Is It the Only Concern?

Membrane gas separation has seen its light with its first successful use in 1979 using polysulfone (PSf) hollow fibers by Jay M.S. Henis and Mary K. Tripodi from Monsanto Company (now part of Air Products and Chemicals Inc.) (Galizia *et al.*, 2017, Henis and Tripodi, 1980). Today, industrial membrane gas separation has been dominated primarily by polymeric membranes due to the high cost of inorganic membranes and instability of liquid membranes (Baker, 2004). After 42 years with current market sales at $1.0-1.5 billion/year in 2017, this is expected to further increased year by year particularly in the developing processes such as in carbon dioxide / methane (CO_2/CH_4) separation (Galizia *et al.*, 2017, Baker and Low, 2014).

Unlike other separation methods, membrane gas separation requires no phase changes and regeneration of absorbent, which makes it more energy efficient and less complicated to operate than other technologies. Nevertheless, even though separation has been observed as early as 1831, membrane gas separation only finds its way into commercialization in the 1980s due to the low fluxes recorded far below any economical and practical interest. This remained to be the case until the development of asymmetric membranes for reverse osmosis (RO) in 1961 which spurred the interest for the same concept in gas separation (Baker, 2002). With time, further developments in the domain have seen membranes with better performance since its initial run off.

However, the work in Robeson (1991) have suggested the trade-off between selectivity and permeability in polymeric membranes, which is defined by the solution-diffusion mechanism. This trade-off, later revised in Robeson (2008), shows

minimal increment in the upper bound line for all major gas separation process, with almost no new conventional polymeric materials existing above the line. This line, initially empirical, was proven to be a fundamental limitation through first principle calculation in Freeman (1999). Since then, it has become the benchmark for fellow researchers to justify the potential of new membrane materials and for researchers to surpass the line.

Indeed, the upper bound line pose to be a hurdle that not able to be surpassed by the conventional polymers defined by the solution-diffusion mechanism. There are several proposed solutions to bypass this elusive line, but by far two of the most common strategy is based on (i) developing or improvising new polymeric materials such as thermally rearranged (TR) polymers and polymers with intrinsic microporosity (PIM) which maximize the kinetic or diffusion coefficient of gas transport through ingenious polymer structural design (Robeson, 2008, Bernardo *et al.*, 2009, Lee *et al.*, 2020), and (ii) incorporating inorganic materials (fillers) such as zeolitic imidazolate framework (ZIF) or fixed-site carrier with certain functionality into the polymer matrix to enhance the performance of existing polymers through a secondary pathway or transport mechanism noted by these fillers (Galizia *et al.*, 2017, Li *et al.*, 2015, Ding, 2019). These two strategies were found to be very promising and have countlessly proven to surpass the line. Nevertheless, the solutions are not without its own problem. For example, PIM membranes are subjected to significant physical aging and plasticization (Baker and Low, 2014), while most TR polymers are insoluble in most organic solvents which limits its processability (Galizia *et al.*, 2017).

Incorporation of fillers, coined as mixed matrix membrane (MMM) are the more common approach found in literature, owing to the already established performances of inorganic and facilitated transport membranes. The dispersion of

molecular sieves or materials with specific chemical/coordinative functionality can improve the membrane's permeance through better gas diffusivity or through facilitated diffusion (Galizia *et al.*, 2017, Ding, 2019). However, there are still no commercial mixed matrix gas separation membranes to date, and only one known commercial MMM for water based RO application, in the form of thin film composite membrane (NanoH_2O, 2017). This leads to a question; despite of better performance, why MMM did not get a commercial breakthrough in industry?

Baker and Low (2014) have suggested the following barriers retarding membrane gas separation research from venturing outside of the laboratory:

(i) Single gas performance does not predict the performance in industry

(ii) Performance of thin membranes are different from its thick films

(iii) There are other limitations that should be considered such as pressure ratio limit from the process point-of-view

(iv) Useful membranes need to be thin and can be made into large area

(v) Long term stability is important before optimization

(vi) Good membrane processing can tolerate high-cost membrane materials

Point (ii), (iv), and especially (vi), which are defined by materials and fabrication methodology will be the main interest of this thesis. Indeed, economic evaluation of membrane technology against other major players has been the benchmark for commercialization since the early days. Zeolite and carbon membranes, despite of its advantages, did not find widespread use due to its scale-up difficulty and high fabrication cost (Baker and Low, 2014). Similarly, high cost of some of the fillers may inhibit the widespread use of this technology. For example, it is estimated that a membrane should cost around \$50/m^2 for it to be economically attractive, but fillers

such as graphene oxide (GO) and ZIF-8 can cost around $168/g and $54/g respectively (SigmaAldrich, 2021a, SigmaAldrich, 2021b). For 1 kg of polymeric membrane material, about 20 m^2 of asymmetric membrane can be made (Baker and Low, 2014). Hence, blending 1 wt.% of ZIF-8 into 1 kg of polymer would already cost around $540 more, or about half of the upper cost limit (at $1000 per 20 m^2).

The use of asymmetric membrane, first pioneered in Loeb and Sourirajan (1963) for RO was a revolutionary idea during that time. Despite being developed almost 60 years ago, it is still the design of choice for many commercial polymeric membranes due to its simpler manufacturing method. As a very thin dense skin layer can be made to maximize permeance, the design gave membranes a significant economic advantage, which spurred the birth of membrane gas separation (Galizia *et al.*, 2017). Nevertheless, for MMM, the incorporation of these expensive fillers means it will be wasted in the bulk of the substrate, not on the dense surface. On the other hand, majority of laboratory scale research conducted for MMM uses thick dense polymer (between 100-200 μm) for their studies (Rahman *et al.*, 2013, Sun *et al.*, 2020) which is not economical for commercialization due to its low permeance value. Typical industrially viable membrane should have selective layer thickness between 0.1-1.0 μm or even less (Galizia *et al.*, 2017, Baker, 2004), meaning it needs some sort of supporting structure to be mechanically competent. Dense membrane fabrication also cannot be translated into hollow fibers which are the more beneficial configuration for gas separation due to its higher productivity per unit volume, or better packing density (Moch, 2004). An anisotropic design, either through composite fabrication or Loeb-Sourirajan's asymmetric structure would hence be necessary for this purpose. Based on the discussions above, perhaps composite membrane is a better design for filler integration to make it more cost effective (Baker and Low, 2014, Chuah *et al.*,

2018, Dai *et al.*, 2016, Baker, 2002). Nevertheless, transferring the achievement of MMM in dense films to hollow fiber composite membranes would be a challenge (Yampolskii, 2012). Understanding the limitation of multi-layered composite membranes would be important so that the performance of potential thin selective layer, whether with or without filler integration, is not being degraded by incompetent membrane design.

On the other hand, despite of thousands of variations of polymeric membrane work found in literature, 90% of the current membranes in the market is still consist of fewer than 10 base polymeric materials used since 1990 (Galizia *et al.*, 2017, Baker and Low, 2014). In fact, a lot of literature can be found surpassing or having comparable performance in the upper bound graph as compared to the current membrane materials, (Comesaña-Gándara *et al.*, 2019, Galizia *et al.*, 2017, Lin and Yavari, 2015) yet none has entered the market. While the upper bound can be a great screening tool for new membranes, real world application can give these materials a major drawback due to natural phenomenon such as gas-membrane interactions in mixed gas permeation, plasticization, and physical aging. The upper bound lines are useful indeed for gauging a new membrane material in ideal conditions but are far from the end of the study. A working membrane should be able to withstand the real-world condition and with a bench life of at least 3-5 years to be worth investing (Baker and Low, 2014).

Process limitation such as temperature and pressure of the feed gas also needs to be considered, which can vary considerably. For example, membranes for CO_2 capture from flue gas needs to be robust to high temperature which is achievable only for some number of polymers such as polybenzimidazole (Kenarsari *et al.*, 2013). On the other hand, biogas upgrading process can be operated at a much milder

condition at room temperature and less than 10 bar (Vrbová and Ciahotný, 2017). Hence, realistic conditions need to be considered when new membranes are evaluated (Galizia *et al.*, 2017).

In the end, the upper bound line, despite being a powerful benchmark for new research in the domain, remains to be a crude way for gauging its actual reliability. As new membranes continue to be piled up in the literature, lack of consideration beyond the comparison with the upper bound line inhibits any potential contenders to be meaningful. Lesson learned from the research works in the past 40 years has given us some important guideline for a better output in industrial gas separation membrane research. Nevertheless, more work still needs to be done before a reliable and economical membrane surpassing the upper bound line can be found. MMM research particularly possess an interesting gap where most reported membrane configuration and geometry in literature is thick flat sheets. In this regard, before promising fillers performance can be tested in real world condition, a suitable multi-layered composite membrane structure made from materials of known reliability would need to be fabricated.

1.2 Problem Statements

Despite of the augmented performance of MMM in literature, it is yet to be economically viable to compete with the current commercial membrane gas separation. Other than the possible filler-polymer incompatibility and defects, the high cost of specialized fillers may inhibits the potential of these new membranes for commercialization (Galizia *et al.*, 2017, Bernardo *et al.*, 2009). Simple solution to this problem is by dispersing the fillers only on the thin selective layer of the membrane where its functionality can be maximised, which can be achieved through multi-layered composite membranes. This membrane design should be able to support

expensive material costing in the selective layer; as much as $25 000 to $50 000/kg of the selective layer's material while still being economically viable (Baker and Low, 2014). At the same time, the selective layer, where flow resistance would be the highest, can be made as thin as possible to maximise the membrane's permeate flux. As such, sure enough that for any MMM with expensive fillers to be cost-competitive, multi-layered composite design would be the most attractive route (Pixton and Paul, 2018). However, better understanding on the limitation of the multi-layered composite membranes would be needed so that the performance of the thin selective layer is not being degraded by incompetent membrane design.

Looking at the timeline of membrane fabrication history for gas separation (Koros and Pinnau, 2008), it is without a doubt that fabrication of multi-layered composite membrane is more complex despite of its looks. Firstly, there are two interfacial problems that would need to be elucidated:

(i) Lateral diffusion at the composite layer's interface for thin selective layer. As the selective layer thickness approaches the porous substrate's surface pore size, gas flow across the selective layers start to deviate from ideality which reduces its permeance (Ghadimi *et al.*, 2018, Wijmans and Hao, 2015, Kattula *et al.*, 2015, Hao *et al.*, 2020).

(ii) Impregnation of selective layer solution into the porous substrate, which increases the gas flow resistance due to increased flow length in the low permeability dense layer regime (Henis and Tripodi, 1981, Salih *et al.*, 2014, Pixton and Paul, 2018, Cay-Durgun *et al.*, 2020).

These problems can be minimized by proper control of surface pores of the support substrate, introduction of a gutter layer in between the selective and substrate layer, or

both. Fabrication of porous substrates have numerous routes, but the most common is through phase inversion process to yield an asymmetric structure with highly microporous surface architecture (Baker, 2002). On the other hand, polydimethylsiloxane (PDMS) has mainly been used as the gutter layer due to its high permeability, low selectivity characteristics (Dai *et al.*, 2016). Hence, good fabrication design is needed to make a good composite structure, with the end target is to ensure majority of the resistance being on the thin selective layer. Tackling all these problems require deep understanding on the chemistry behind membrane formation for both porous and dense structures, on top of the flow dynamics across the complete composite and the science of thin coating formation. For the current work, interest is given primarily on the lateral diffusion. Although, the effect of intrusion by coating layer should not be totally neglected.

These problems can also be solved by fabricating a dense skin asymmetric membrane, as a co-substrate and gutter structure. The use of a single continuous material would avoid both lateral diffusion and any solution impregnation into the porous substructure. On top of that, formation of dense gutter layer can also help to form a thinner selective layer (Salih *et al.*, 2014). However, a lot of materials used for asymmetric membrane fabrication lacks the high permeability suited as a gutter layer and are prone to dissolution by the selective coating solvent, such as PSf and polyimides (PI). On the other hand, rubbery polymers with high permeability lacks the necessary mechanical strength to be asymmetric and self-supporting, making materials such as PDMS unsuited for this purpose. Poly(4-methyl-1-pentene) (PMP) on the other hand, suit this description. PMP, a relatively high free volume glassy polymer, has not been used as a gutter layer in literature, despite of its moderately high permeability of about 9.87 and 128 Barrer for nitrogen (N_2) and CO_2 respectively (Yasuda and

Rosengren, 1970). Although the value is below the permeability of PDMS, PMP is advantageous as its high permeability yet glassy structure should allow it to be used as both support and gutter layer. Hence, the possibility of PMP to be used as co-substrate-gutter layer and its performance will need to be elucidated and compared with microporous substrate supported PDMS composite structure.

Another significant problem normally encountered in multi-layered composite fabrication is various design and compatibility limitation such as suitability of solvent used for selective layer with the underlying support (Pixton and Paul, 2018) and water-swollen hydrogel formation in the pores of the substrates during coating using interfacial polymerization technique (Baker, 2004). There are no specific solutions to these problems as it depends between chosen layers, but possible problem sources would be due to coating wettability, methodology, and compatibility. For example, PMP is known to have a low surface energy (Slepička *et al.*, 2012) which may limit its wettability with other polymer solution for composite formation. On the other hand, organic solvents used for selective layer's dissolution may swelled the dense PDMS, and worse, penetrated into the underlying substrates, which might be vulnerable to the said solvents (Lee *et al.*, 2003a). Other than the problems noted for multi-layered composite membrane above, it is important to note that the membranes still need to adhere to the limitations of asymmetric membrane structure. Selective layers need to be as thin as possible while being free of defects to avoid loss of selectivity (Yampolskii, 2012). To minimize the impact of porous-dense interfacial problems noted previously and to minimize coating thickness, this problem would be studied on the dense-dense selective-gutter layer.

To ensure the reliability of the formed multi-layered composite membrane, suitable selective layer with known industrial reliability will be chosen such as P84 PI

and coated on the chosen substrate-gutter structure. Gas performance testing will be made for CO_2/N_2 and CO_2/CH_4 ideal gases as some of the most common industrial gases available such as in biogas upgrading, natural gas separation, and flue gas carbon capture (Ding, 2019). The performance of the complete multi-layered composite membranes would need to be compared to its dense, self-standing performance to ensure negligible negative impact from either defect formation or interfacial based resistance (lateral diffusion and solution intrusion at the porous-dense interface).

1.3 Research Objectives

As discussed in earlier sections, this thesis work aims to fill in the research gap noted between the plethora of MMM research in literature and cost-effective membrane design where these expensive materials can be concentrated on. This is done by fabricating multi-layered composite membrane and elucidating the flow dynamics across it. To realise this, three objectives are to be achieved:

i) To elucidate the influence of substrate-gutter design (composite vs asymmetric) on the lateral diffusion and solution intrusion across the layered composite membrane using experimental, theoretical modelling and computational fluid dynamics (CFD) simulation.

ii) To elucidate the layer-layer compatibility between the gutter (PMP) and P84 PI selective layer.

iii) To quantify the permeation performance of the multi-layered composite membrane with P84 PI as selective layer made through dip-coating and compared to its dense membrane counterpart.

1.4 Scope of Research

In the current work, multi-layered composite membrane fabrication will be studied as a whole, from the substrate design to the selective layer coating methodology. Nevertheless, it would not venture into actual MMM integration and will be left for future works due to its own complexity. It is however important to consider on the future direction of the current work for eventual integration. For example, dispersion of graphene oxide has been noted to be very good in NMP (Paredes *et al.*, 2008) and hence should be a suitable candidate for dispersion in various known polymers used in membrane gas separation for subsequent studies.

Polyethersulfone (PES) was chosen as the substrate material due to its high mechanical strength and familiarity for membrane fabrication. Lithium chloride (LiCl) was used to modify the pore structure of the polymer, to obtain substrates of different surface pore architectures. On the other hand, PDMS will be used as the gutter layer and initial 'selective layer' for the first two parts of the study. The choice of PDMS is without a doubt, necessary, as it is the material of choice for gutter fabrication and defects coating. This part of the study will be made in flat sheet configuration. In this way, the substrates can be modified freely and important parameters for substrate fabrication can be noted.

On the other hand, a commercial membrane made of PMP will be used as co-substrate-gutter layer, supplied by 3M Deutschland GmbH under the tradename Oxyplus ®. The dense skin asymmetric hollow fiber membrane is commercialized for blood oxygenation. As this is a commercial membrane which may be made of proprietary additive formulation instead of purely neat PMP, a dense flat sheet PMP will also be casted for direct comparison.

The flow dynamics across the substrate-gutter layer will also be studied theoretically through resistances-in-series (RiS) model and simulated using CFD. Purpose of this study is to see how asymmetric structure can be beneficial in mitigating the lateral diffusion and solution intrusion effect caused by porous-dense composite structure interface. The modelling will be limited by the experimental permeation data, as PDMS can have a significantly higher intrinsic permeability as compared to PMP and PES being far less permeable. The configuration of the membrane, whether flat sheet or hollow fiber will not be important as the flow dynamics at the membrane surface level will be a factor of material properties and pore structures, not the configurations. Hence, we can see the limits of PMP as a co-substrate-gutter layer and the important parameters need to be controlled for PDMS and its PES substrates.

Finally, a selective layer will be coated on top of the chosen substrate-gutter layer. Scope of this research will be limited to choosing selective layer from conventional polymers used in gas separation, as these polymers have been tested and verified to be viable for gas separation application in industry. Important notes will be the suitability and compatibility of this polymer with the gutter layer, whether it is PDMS or PMP. Some preliminary study will be conducted, and coating through dip-coating process will be made.

For all cases, starting from the porous substrates' fabrication, N_2 and CO_2 single gas will be used as feed for permeation studies. These two gases are commonly used and are available for industrial application, hence will be suited for early studies, where the membrane's characteristics are yet to be known. Near the end of the study, as selective layer coating interactions and performances become clearer, CH_4 will be introduced as an additional feed to better elucidate the complete membrane's permeability characteristics. The work will not venture into the MMM regime but will

be discussed in the literature review section as an extension to the selective layer's further studies.

1.5 Significance of Current Work

Various MMM work aiming to surpass the upper bound line can be found in literature yet majorly lacks consideration beyond the laboratory scale testing. It is possible that one of them might be the revolutionary idea for real world application. But before this to be found, a suitable multi-layered composite membrane needs to be fabricated. Highly porous substrate with good surface pore architecture needs to be designed, which requires deep understanding in the science of membrane formation. The interactions with the subsequent layer will also be important and need to be understood.

Use of PMP as co-substrate-gutter layer has not been found in literature. While previous work uses a separate substrate and gutter materials, the use of common material for both purposes would help to mitigate problems in lateral diffusion and solution intrusion, on top of minimizing fabrication cost and complexity. The study of flow dynamics across this structure, as compared to the separate substrate-gutter design would open new idea or perhaps new materials for this purpose. The use of PMP's composite structure with other polymers would also be a new item in the inventory of composite membrane materials available as very few PMP laminated membrane can be found in literature.

While no fillers will be incorporated into the selective layer in this work, the success of this work will better elucidate the best design for composite membranes, the flow dynamics across composite membranes, and creating a new layered polymer composite. This will become the base for subsequent study in MMM.

1.6 Organization of Thesis

This thesis is organized into five main chapters. In Chapter One, introduction of this work is made, with focus on the history of gas separation membrane up to the findings of polymeric membrane upper bound line which explains the stagnation of industrial membrane progress. Some possible solutions to the upper bound problem and how solely surpassing the line is a bad strategy for useful research is discussed. The introduction is followed by the problem statement of the current work, highlighting on the challenges and its possible solutions, as related to the objectives of this work. The research gap and main objective is noted; to develop a multi-layered composite membrane and elucidating the flow dynamics across it. This would be fulfilled through three sub-objectives. Research scope and organization of this thesis is then discussed.

In Chapter Two, some history on composite membrane research and various selective layer fabrication methodology available are reviewed. Interests are given primarily on the dip coating due to its simplicity and mature theoretical background and on interfacial polymerization which is the most common method used for composite RO membrane. Other non-conventional methods are briefly discussed. Short review on the substrate requirement and hollow fiber configuration are made. This is followed by the current and future challenges in multi-layered composite membrane and the problems associated with filler incorporation for MMM fabrication, as an extension or future requirements of the current work. The role of this research in filling up the gap in knowledge is elucidated.

In Chapter Three, the methodology for the overall research is discussed in detail alongside with the equations used for calculations. The chapter outline starts with the materials and chemicals used for the experiment. It is followed by overall

experimental work plan, membrane preparation procedure, and testing procedure. Characterization techniques used and their parameters are discussed in detail.

In Chapter Four, the results and discussions are presented through five subchapters. In the first sub chapter, interest is given on fabricating PES porous substrate through phase inversion technique. LiCl was used to modify the PES surface and bulk pore structures. The resulting substrates are then coated with PDMS of different thickness in the next subchapter to elucidate the influence of substrate design on the composite performance. For the third subchapter, focus is given to the commercial PMP hollow fiber membrane performance and its stability for use as co-substrate gutter. All these data are then compiled and used to model the flow dynamics, permeance, and resistance across the membrane in the fourth subchapter. The work continues with compatibility studies of the selective layer with the substrate-gutter and ended with actual coating and performance elucidation of the complete composites in the fifth subchapter.

Lastly in Chapter Five, the findings of the current work are summarized and related with the research objectives. Significant findings are highlighted, and recommendations are given for future work on the composite membranes.

CHAPTER TWO

LITERATURE REVIEW

2.1 History and Motivation for Composite Membrane in Gas Separation

The idea behind the fabrication of membranes with thin selective layer can be traced back to the success of Loeb and Sourirajan (1963) from UCLA in fabricating asymmetric polymeric membranes. The membrane, which consist of a thin surface layer and a thick, porous sublayer made up of the same polymer were made through phase inversion; a common methodology in membrane research nowadays but was a breakthrough during that period. Nevertheless, the use of this methodology is with one significant limitation; inability to separate the materials between the supporting layer and its selective layer. While not being a significant problem in lab scale, commercial potential of the membranes would highly depend on the material cost and its mechanical viability, particularly when utilizing the expensive high-performance material.

Using the same concept, approach to separate the layers were made to better control the properties of the membrane by laminating together separate specialized layers to create what is called as composite membrane. Eventually, thin film composite (TFC); first developed by Peter S. Francis from North Star Research and Development Institute for reverse osmosis (RO) membranes were born and became the new contender to the original Loeb-Sourirajan's asymmetric polymeric membranes (Cadotte and Petersen, 1981, Francis *et al.,* 1966). The idea was then adapted for gas separation membrane by Henis and Tripodi (1981) from Monsanto Company (now part of Air Products and Chemicals Inc.) to first made composite membrane economically feasible for industrial application. Nevertheless, this

composite membrane is more of a pinhole plug rather than a true multilayer composite; the separation performance is still being governed by the relatively dense substrate skin layer rather than the coating itself. In this literature, interest will be given mainly towards the multilayer membrane, with some extension towards nanoparticle incorporation.

In its infancy, TFC was introduced through composite laminate technique to create thin selective layer, between 20 to 5000 nm in thickness, for RO application using cellulose acetate (Cadotte and Petersen, 1981). Over time, various other methodologies were founded aimed to create an even thinner surface layer, with interfacial polymerization (IP) remain as one of the most associated thin film fabrication methodologies. Notwithstanding the limitation of the thin film material itself, the utilization of thin film nanocomposite (TFN) in membrane separation processes were proposed by Jeong *et al.* (2007). The success of TFN has ever since became the research attention for water-based membrane separation since 2012 (Lau *et al.*, 2015).

Being the derivative of anisotropic membrane, application of thin film methodology can be found extensively in the literature for dense membrane application such as desalination, nanofiltration, forward osmosis, and gas separation. In either TFC or TFN, the utilization of composite skin structures enable the researchers to significantly have better control on the separating layer, making an ultrathin surface coating to be practically achievable on top of reducing the capital cost of the membrane (Kattula *et al.*, 2015). Despite of its water based application origin, TFC/TFN for gas separation has now diverts itself with its own potential and problem, particularly due to its better process ability and lower capital cost as compared to the ceramic membrane counterpart (Wong *et al.*, 2016). It is however noted that the

utilization of TFC/TFN for gas separation is still inferior as compared to the water-based application.

As in the anisotropic membranes, the molecular separation and permeation performance of the membrane is highly regarded towards the dense selective layer while the mechanical viability of the membrane is regarded towards the porous support. Nevertheless, composite membranes such as TFC have the added benefit for better control of the membrane layers to its specific functions (Ghadimi *et al.*, 2018), on top of allowing the use of more expensive materials (usually in the separating layer) in a thin, localized structures instead of being used for the whole membrane. Through the utilization of thin layered membrane, higher permeance value can be achieved for highly selective polymer layer, which are normally grounded by its intrinsic physical limitation (reduction in diffusion coefficient with tighter molecular spacing) as explained in the well-known Robeson upper bound limits (Robeson, 2008, Robeson, 1991). The increase in permeance are fundamental as noted in the volume flux equation for gas separation in dense membranes as (Baker, 2004):

$$j_i = \frac{P_i\,(p_{io} - p_{i\ell})}{\ell} \tag{2.1}$$

Where j is the permeate flux, P is the membrane's permeability; a measure of the membrane's ability to permeate gas, p_o and p_ℓ are the partial pressure of the gas component i on either side of the membrane, and ℓ is the membrane thickness. The ratio of P and ℓ is called the membrane permeance, $\mathcal{P}$. Hence, reduction in membrane thickness would ideally increase the permeance and the permeate flux, reducing the areas needed to achieve a specific downstream capacity target of separation unit. For example, to achieve downstream permeate gas flowrate of 10 with $(p_{io} - p_{i\ell})$ = 1, the reduction in selective layer thickness with P_i = 10 from 1 to 0.1 would increase the

permeate flux and decrease the required membrane area by ten-fold without affecting the selectivity of the membrane. Note that in composite design, this equation would only govern the thin, dense selective layer. Hence, the increased overall thickness needed for mechanical stability which are mainly contributed by the porous substrate would not contribute to the reduction in gas flux.

Despite of countless reported literature on non-composite dense membrane in flat sheet configuration, its application is highly limited in industry. Baker and Low (2014) has pointed out several lessons on the current gap and strategy to bridge the research between lab scale and industrial usage. Particularly, the membrane material needs to be capable to be formed into thin membranes and packaged into large area membrane modules. So, anisotropic hollow fiber membranes would be suited for this purpose. However, for a nanocomposite membrane to be cost viable, the usually expensive nano fillers need to be concentrated only on the thin selective layer, which is not possible in anisotropic single material membrane design. Hence translating the work into hollow fiber poses several significant challenges. Fabricating a thin, dense membrane in hollow fiber form is impossible to be viable due to manufacturing and mechanical limitations. TFC membrane design can however bypass this limitation by separating the functions of these layers.

Meanwhile, alternative membrane materials (inorganic membranes) have been developed from metals, ceramics, or pyrolyzed carbon. Even though the features of some inorganic materials are well above the polymer trade-off curve, it is difficult to replicate large-scale modules with thousands of square meters of membrane area due to the high capital expenses. For instance, zeolite and carbon membranes, despite of its advantages, is extremely expensive with the costs of the membrane modules currently in excess of US\$3000/m^2 (Baker and Low, 2014). Additionally, the

brittleness and low surface to volume ratio of inorganic membranes present difficulties in optimising their uses in the gas separation industry (Goh *et al.*, 2011). To overcome this problem, many significant studies as well as research reports have pointed out on the possibilities of mixed matrix membrane (MMM) for gas separation processes, which combines the cost and flexibility of polymeric membranes with the performance of inorganic membranes, have been published in recent years. The dispersion of inorganic fillers in a polymer matrix is as depicted in Figure 2.1.

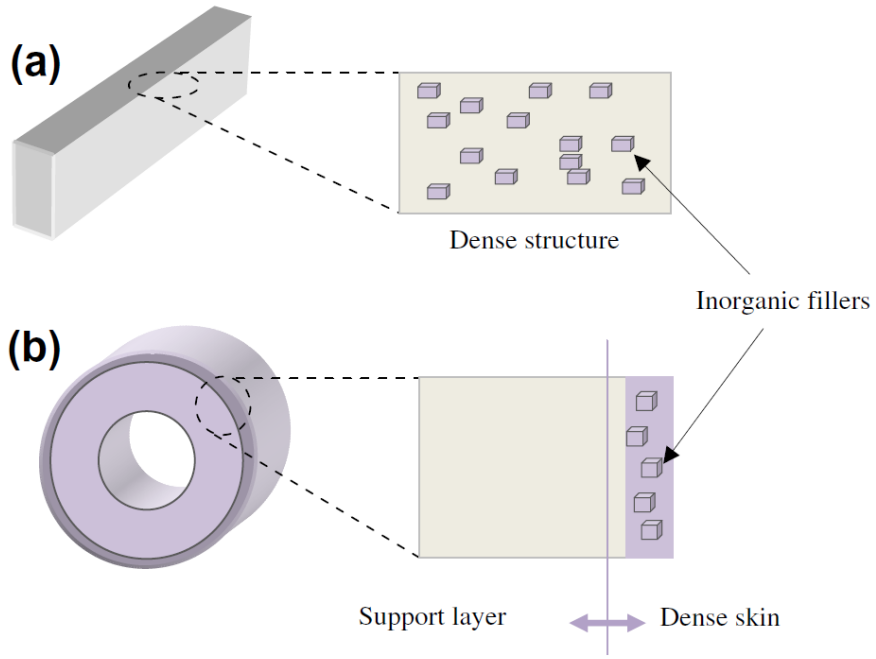

Figure 2.1: Mixed matrix membranes in configuration. (a) isotropic flat dense mixed matrix membrane, (b) asymmetric hollow fiber dense skin mixed matrix membrane (Goh *et al.*, 2011)

Nevertheless, for a thick, dense membrane structure usually noted in literature, the incorporation of these expensive fillers means it will be wasted in the bulk of the substrate instead of the dense surface. Majority of laboratory scale research conducted for MMM employs thick dense polymer between 100-200 µm for their studies due to their simplicity (Rahman *et al.*, 2013, Sun *et al.*, 2020), although not being economically viable for commercialization due to its low permeance value. Typical industrially viable membrane should have selective layer thickness between

0.1-1.0 μm or even less (Galizia *et al.*, 2017, Baker, 2004), indicating that it requires some sort of supporting structure to be mechanically competent. Dense membrane fabrication also cannot be translated into hollow fibers which are the more beneficial configuration for gas separation due to its higher productivity per unit volume, or better packing density (Moch, 2004). An anisotropic design, either through composite fabrication or Loeb-Sourirajan's asymmetric structure would hence be necessary for this purpose. Based on the discussions above, perhaps composite membrane is a better design for filler integration to make it more cost effective (Baker and Low, 2014). Nevertheless, transferring the achievement of MMM in dense films to hollow fiber composite membranes would be a challenge (Yampolskii, 2012).

2.2 Composite Membrane Design

Fabrication of TFC/TFN in principle would consist of a thin selective layer, thicker, porous support layer, and nano additive (for TFN). The discrete fabrication methodology of the selective layer and the support layer is beneficial in optimizing the layers to its full potential, based on its intended application (Wong *et al.*, 2015). It is also beneficial as an engineering solution for some of the high potential polymers to be used as selective layer, since it may not be suited to be fabricated in asymmetric membrane morphology due to its intrinsic weak mechanical properties (Salih *et al.*, 2014), on top of substantially reducing the cost of the expensive specialized polymers (Tsai *et al.*, 1995). Formation of the composite membranes can be made by both ex-situ; e.g. by casting the selective thin layer separately and then laminate it to the porous support, or in-situ; e.g. by coating the support in a polymer solution, followed by subsequent drying to solidify the solution (Cadotte and Petersen, 1981). Composite membranes generally aim to improve gas transport properties with negligible resistance on the porous support layer (Pinnau and Koros, 1991, Wijmans

and Hao, 2015). Hence, three parameters would need to be optimized to theoretically maximize the separation performance: (i) high gas selectivity and (ii) high permeance of the surface selective layer, and (iii) low gas transport resistivity for the support substrate layer. Membrane should exhibit high selectivity to have the required product purity, while having high permeance to reduce the capital cost by increased membrane area (Kattula *et al.*, 2015).

On the other hand, the introduction of nano additives into the TFC have received a tremendous attention by the research community. The non-exhausting list of combination between the layers and the additives open various alteration to the already high potential TFC. The typical morphology of TFC and TFN is represented in Figure 2.2, while Table 2.1 summarizes fabricated TFC/TFN found in literature in recent years.

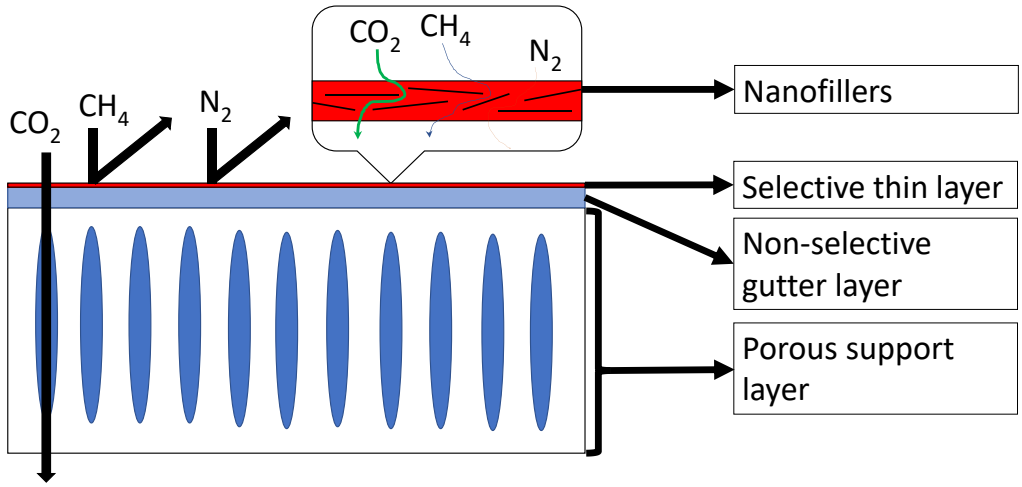

Figure 2.2: Thin film nanocomposite membrane design

Table 2.1: Fabricated TFC/TFN found in literature

Selective Layer	Method	Application	Reference
Polyamide (MPD – TMC, with MOF UiO-66)	Interfacial polymerization	Forward osmosis	(Ma *et al.*, 2017)
Polyamide (MPD – TMC)	Interfacial polymerization	Forward osmosis and reverse osmosis	(Tiraferri *et al.*, 2011)
Polyamide (MPD – TMC, functionalized with GO)	Interfacial polymerization	Antibacterial – reverse osmosis	(Perreault *et al.*, 2014)
Polyamide (MPD – TMC, with zeolite A nanoparticles)	Interfacial polymerization	Reverse osmosis	(Jeong *et al.*, 2007)
Polyamide (PIP – TMC, with SAPO-34)	Interfacial polymerization	Nanofiltration	(Liu *et al.*, 2015)
Polyamide (DGBAmE – TMC, with PMMA grafted MWCNTs)	Interfacial polymerization	Gas separation (CO_2/N_2, CO_2/CH_4)	(Wong *et al.*, 2015)
Polyamide (MEDA-TMC)	Interfacial polymerization	Gas separation (CO_2/N_2)	(Yuan *et al.*, 2012)
Polyetheramine (diamine-TMC)	Interfacial polymerization	Gas separation (CO_2/N_2, CO_2/CH_4)	(Salih *et al.*, 2014)
Teflon AF1600, Hyflon AD80, and Hyflon AD40	Coating (machine casted)	Gas separation (CO_2/N_2)	(Zhu *et al.*, 2016a)
Polyimide (Matrimid 5218)	Coating (pour-over)	Gas separation (O_2/N_2)	(Wessling *et al.*, 2001)
Pebax MH1657	Coating (pour-over)	Gas separation (CO_2/CH_4)	(Ahmadpour *et al.*, 2014)
Pebax MH1657/PEG	Dip coating	Gas separation (CO_2/H_2, CO_2/N_2, CO_2/CH_4)	(Car *et al.*, 2008)
Polyimide (PAA – triethylamine)	Dip coating	Gas separation (CO_2/N_2)	(Yanagishita *et al.*, 2001)
GO	Dip coating	Gas separation (H_2/CO_2, H_2/N_2)	(Zeynali *et al.*, 2018)
Pebax MH1657	Spray coating	Gas separation (CO_2/N_2)	(Jiang *et al.*, 2021)

MPD = m-phenylenediamine; TMC = trimesoyl chloride; MOF = metal-organic framework; GO = graphene oxide; DGBAmE = diethylene glycol bis(3-aminopropyl) ether; PMMA = polymethyl methacrylate; MWCNTs = multi-walled carbon nanotubes; PIP = piperazine; MEDA = N-methyldiethanolamine; Pebax = polyether block amide; PEG = polyethylene glycol; PAA = poly(amic acid)

2.3 Coating Methodologies

The thin film is the heart of the composite membrane; being the site for molecular separation to take place. Typical thickness for the selective layer to be considered as thin film is below 100 nm (Zhu *et al.*, 2016a, Kattula *et al.*, 2015), although higher thickness at about 1 μm has also been reported. Here the review will take consideration of all thin film methodologies regardless of the reported end thickness and consider it as a TFC, if the selective layer is far thinner than the bulk of the membrane. In all methodologies, the layers can be independently optimized according to the application needs (Jeong *et al.*, 2007). With negligible support layer mass transfer resistance, the performance of TFC/TFN membrane can be characterized by Equation (2.1) as noted previously. From this equation, increasing the membrane's flux can be achieved through three pathways; (i) increase in the driving force (partial pressure) (ii) improvement of the selective layer's gas permeability, and (iii) lowering the selective layer's thickness. Option (i) however is limited to real world practicality especially by the increase in capital cost with increased feed pressure and more of a process-controlled parameter, making option (ii) and (iii) as the methodology of choice for membrane research. The permeance of the selective layer can thus be increased with thinner selective layer, or with better selective layer's permeability (Kattula *et al.*, 2015). The prior option is a matter of proper methodology to fabricate the membrane and will be the focus of this subsection. In fact, the need to reduce the thickness of the separating layer was the motivation for TFC fabrication. Several methodologies have been proposed for TFC fabrication ever since its earliest convention, summarized in Table 2.2.

Table 2.2: Comparison of thin film selective layer fabrication method

Method	Advantages	Disadvantages	References
Composite laminate	• Cheap and simple methodology • Can be use with many polymers	• Poor adhesion between the selective film and the support layer (in wet condition) • Ex situ fabrication • Hollow fiber configuration may not be possible	(Cadotte and Petersen, 1981, Kiesow *et al.*, 2013)
Polymer solution coating (dip/spin coating, pour over, etc.)	• Simple and matured methodology • In situ fabrication • Better adhesion between layers	• Limited solvent resistance of support layer • Defects are easy to be formed • Film thickness increased with substrate porosity	(Tsai *et al.*, 1995, Zhang *et al.*, 2021)
Reactive monomer coating (in situ polymerization)	• Better adhesion between layers • In situ fabrication • Very thin film can be formed (down to 40 nm) with defect free surface	• Limited solvent resistance of support layer • Limited to several polymers with reactive monomers • May require additional stimuli to start the polymerization process • Polymerization may take some time to occur	(Liu and Martin, 1991)
Plasma deposition	• In situ fabrication	• Complex fabrication methodology • Relatively more expensive	(Park *et al.*, 2016)
Interfacial polymerization	• Layer thickness is self-limiting; ultrathin film is possible • In situ fabrication • Minimized defect formation • Tunable functional groups • Easy to scale up	• Limited to several polymers • Reaction controlled, prone to side reaction • Utilization of more chemicals	(Yuan *et al.*, 2012)

2.3.1 Composite Laminate

Composite laminate is the earliest methodology developed for membrane thin film fabrication, which utilize float casting to fabricate the selective layer and ex-situ lamination of the substrate layer with the thin film, creating the composite membrane. Float casting, first prepared in Francis *et al.* (1966) for RO membrane, was conducted generally by dissolving the polymer in organic solvent to create a concentrated polymer solution. The solution is then poured onto the water surface, spontaneously dispersing it into solid thin film on the surface. The thin film was then merged with the support layer ex situ. This methodology was found to be applicable for a lot of polymers. On the other hand, solution casted thin film has also been utilized whereby the polymer solution is casted on a smooth glass plate under predetermined thickness, dried to remove the solvent, and immersed in water bath to separate the thin film from the glass. The design of composite lamination in water bath (float casting) is given in Figure 2.3.

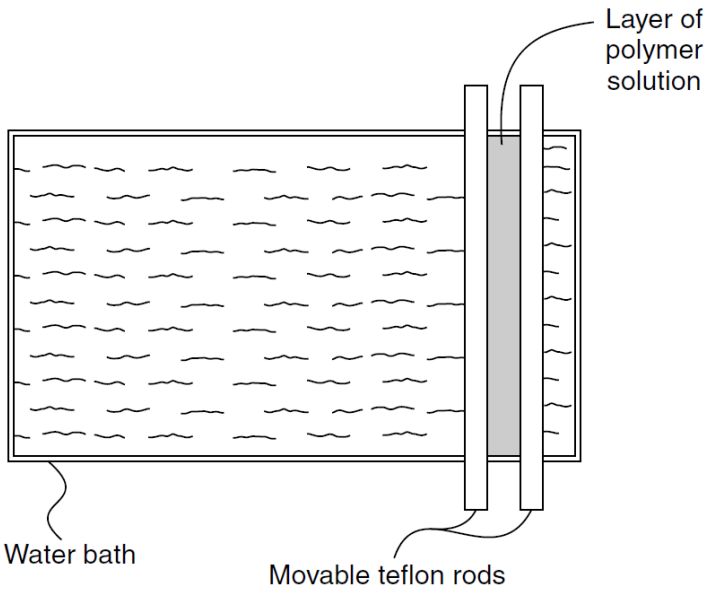

Figure 2.3: Schematic of the apparatus developed by Ward III *et al.* (1976) for float casting composite laminate fabrication method

Despite of its simplicity, ultrathin composite membrane would be hard to be made through this method as breakage of the thin film and defects formation become more imminent, on top of the low adhesion strength between the layers (Francis *et al.*, 1966). Lack of significant advantages over other in situ methodologies and low adhesion between the layers have so far niche the float casting methodology only for free standing thin dense film rather than in composite configuration through composite laminate (Kiesow *et al.*, 2013), albeit that the adhesion was noted to be better when the composites were dried. Nevertheless, the use of float casting can still be beneficial especially for the independent study on the thin film properties. On the other hand, several works have noted the potential of float casted polymers by dispersing monomer-particle solution blend to create a thin monolayer on the water surface, which eventually polymerized by photopolymerization (Figure 2.4). This creates a bi-continuous low permeability polymer-particle alternate structures, enabling unique permeant pathways only through the highly selective porous particle structures with no regards on the polymer matrix permeability or through polymeric micro-sieves upon removal of the embedded particles (Yan *et al.*, 2012, Kiesow *et al.*, 2013). The methodology has been tested to both single layer fabrication and in composite laminate with micro-molded substrate layer. It was noted that the photopolymerized monomer formed a layer of about 1800 nm in thickness. Although, this thickness may be due to the need to compensate the larger zeolite particle size used in these studies, not its lower thickness limit. It should be noted however that the ultrathin film formation is only possible due to the particle assisted wetting phenomenon (Kiesow *et al.*, 2013); which isn't possible without the inclusion of nanosized particles. Hence, spreading or wetting of the coating solution would be important for composite laminate method to be viable.

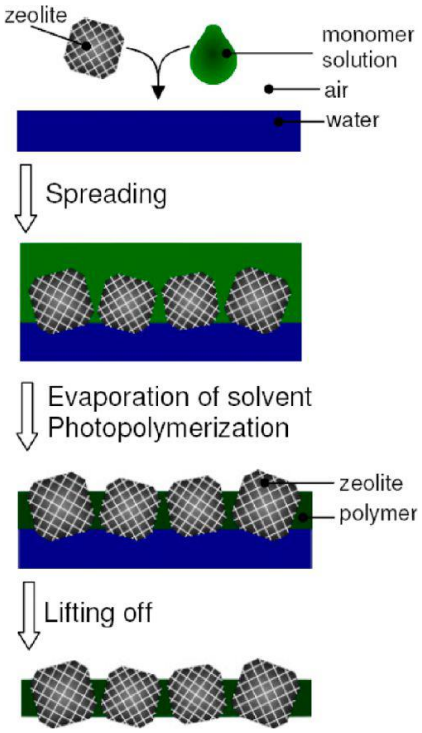

Figure 2.4: Preparation of bi-continuous composite monolayer with embedded zeolite through float casting – photopolymerization technique (Kiesow *et al.*, 2013)

2.3.2 Dip Coating

Another fabrication methodology, dip coating is one of the most common methodology for composite membrane fabrication generally due to its simplicity, maturity, and effectiveness. It can be defined as the deposition of liquid phase coating solutions onto the surface of any substrate (Ceratti *et al.*, 2015). The process of dip coating implies several stages: immersion, start-up, deposition, drainage, and evaporation, as illustrated in Figure 2.5. The process begins with the immersion of the substrate in the coating solution at a constant speed where it remained inside for a defined time (typically 30s), therefore ensuring proper contact between the substrate and the solution. A coherent liquid film is then entrained on withdrawal of the substrate from the coating solution. Excess of the coating solution was then drained from the surface which then consolidates by evaporation of the sedimentary wet coating, forming a layer on the substrate. The first three stages (a-c) are necessarily sequential

whereas the last two stages (d-e) are concomitant. However, immersion and start-up (a-b) and drainage and evaporation (d-e) can occur concurrently depending on the properties of the substrate and the coating solution. For instance, the immersion and start-up stage occur concurrently in the usage of non-reacting solution while the drainage and evaporation occur in the usage of highly evaporative solution. The continuous dip coating process is depicted as shown in (f) where the stages were carried out sequentially after each other.

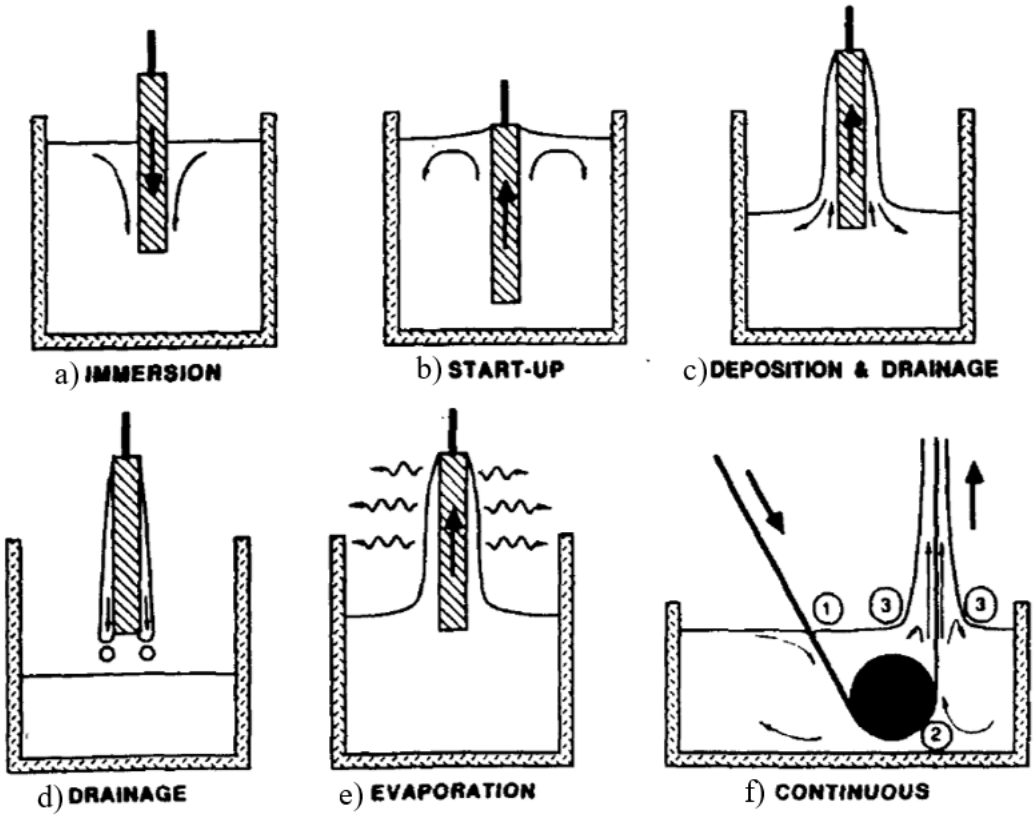

Figure 2.5: Stage of dip coating process (Scriven, 1988)

In dip coating, the substrate is withdrawn vertically from the solution reservoir at a constant speed, U_0 which entrains the liquid due to viscous force between the substrate surface and the coating solution. On the other hand, the solution is also being retained in the coating solution reservoir due to capillary and gravitational forces. These opposite forces create a solution boundary layer that branches into two

at the equilibrium stagnation point S, somewhere above the liquid surface. The process is as shown in Figure 2.6.

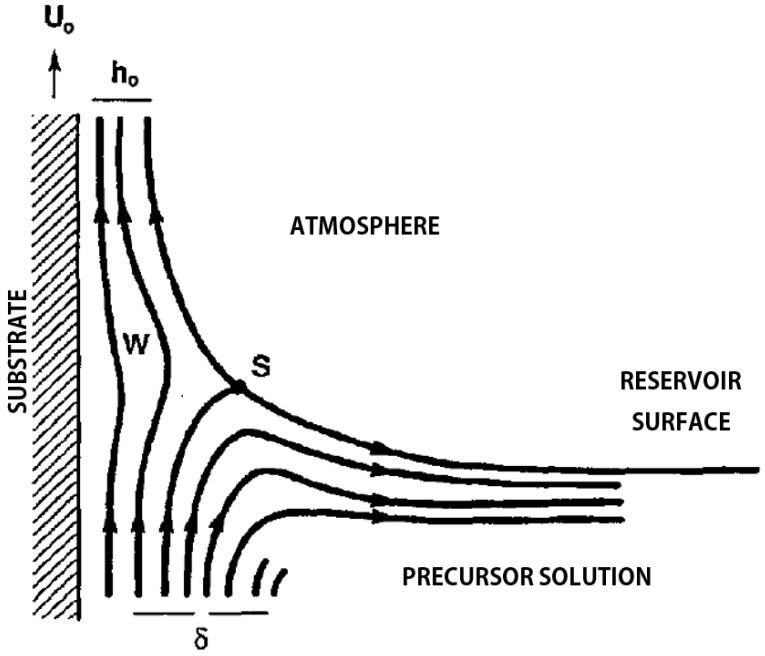

Figure 2.6: Illustration of the coating solution flow patterns during the deposition regime of dip-coating process. U_0 is the withdrawal speed, S is the stagnation point, δ is the boundary layer, and h_0 is the thickness of the entrained fluid film on the substrate (Brinker, 2013)

As evaporation and draining of the coating layer took place, the film position and shape of the film profile will remain relatively steady with the reservoir surface as the substrate continues to move upward at a constant U_0. Near to the coating's solidification, the entrained film takes on an approximate wedge-like shape and terminates in a well-defined drying line, as illustrated in Figure 2.7. Non-volatile species such as polymer that formed the as-deposited layer can then be further cured to form a solid coating.

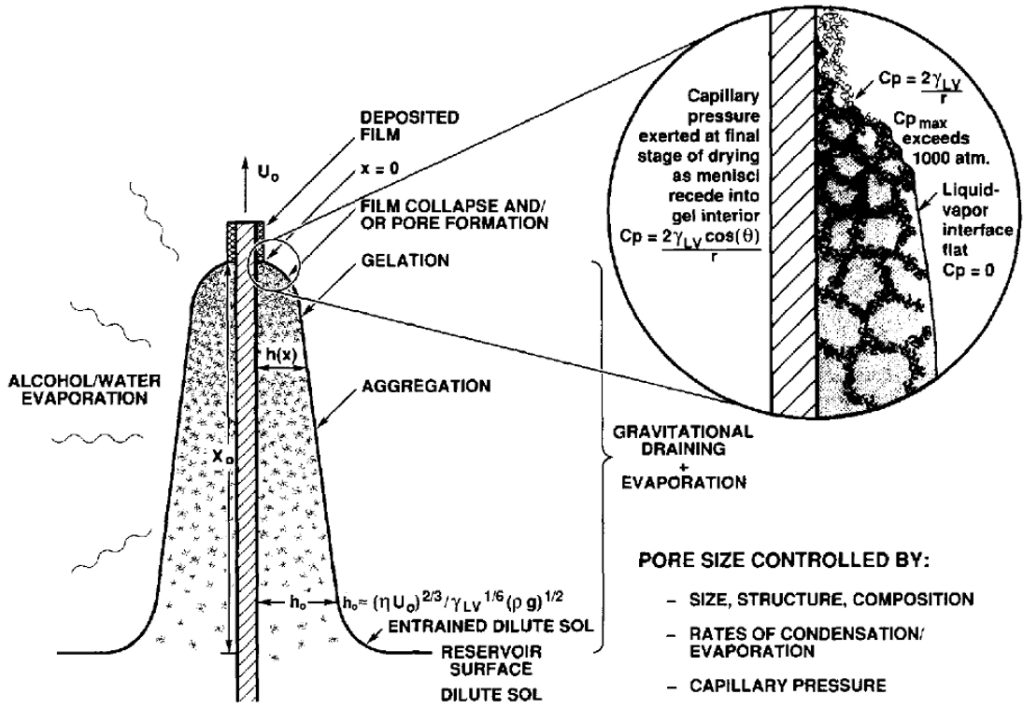

Figure 2.7: Schematic diagram of the drying and draining regime during dip-coating process (Brinker, 2013)

As noted earlier, the formed wet film thickness and position of the stream line are governed by competition between various forces; the most prominent of which are between viscous drag and capillary and gravitational force (Scriven, 1988). Despite that, there is usually a specific operating range for each coating system that allows the formation of smooth and uniform coatings. Withdrawal speeds typically range from l to 15 mm/s, albeit this is still dependent on the solvent and precursor system used (J. Puetz and Aegerter, 2004). Lower withdrawal speed is difficult to manage as a smooth withdrawal is needed for a good coating uniformity, while withdrawal speeds of more than 15 mm/s frequently resulting in wet film running and curtaining. In practice, to keep the deposition time low, it is still preferable to work at medium concentrations but with fast withdrawal speeds.

For plate coating, when the liquid viscosity, η and substrate speed, U_o are high enough to hold the curvature of the meniscus down, the deposited wet film

thickness h_0 can be known when the viscous drag and gravity force are in balance. This is given by Landau and Levich (1988) where:

$$h_0 = e\left(\frac{\eta U_o}{\rho g}\right)^{\frac{1}{2}} \tag{2.2}$$

where ρ is the liquid density, g is the acceleration of gravity, and e is experimental constant. On the other hand, when liquid viscosity and substrate speed are not high enough (typically in the range of ~1-10 mm/s), the force competition becomes three sided with the additional effect by capillary forces. The equation governing the resulting h_0 now becomes:

$$h_0 = e\frac{(\eta U_o)^{\frac{2}{3}}}{\gamma_{LV}^{\frac{1}{6}}\rho g^{\frac{1}{2}}} \tag{2.3}$$

where γ_{LV} is the surface tension of the liquid-vapor interface. It is reported that the exponent in the withdrawal speed is determined by the chemical characteristics of the coating solution, with values ranging from 0.5 to 0.7 (J. Puetz and Aegerter, 2004), while h_0 is limited to coating speed above 1 mm/s (Grosso *et al.*, 2015). In the case where cylindrical fibers were used, h_0 can be approximated by the Derjaguin model (Tsai *et al.*, 1995, Zhang *et al.*, 2021):

$$h_0 = 1.34b\left(\frac{\eta U_o}{\gamma_{LV}}\right)^{\frac{2}{3}} \tag{2.4}$$

Where b is the fiber radius. This is then known as Landau-Levich-Derjaguin (LLD) theory, in reference to their contributions. It was noted that thickness of the coating increased with fiber porosity due to the capillary action of the solvent increasing the solution viscosity near the fiber wall, significantly overestimate the model (Tsai *et al.*, 1995). This effect, however, can be minimized by pre-wetting the fibers with the coating solvent, reducing the end coating thickness of the fiber. On the other hand, the

equation also suggests that at a fixed coating condition, h_0 is proportional to b. Hence, thinner h_0 will be achieved when the fibers are small (Zhang *et al.*, 2021). This would be an advantage for membrane gas separation which benefits from high surface area to volume ratio of small diameter fibers. Nevertheless, while this methodology seems to be identical to the ex-situ composite laminate, dip coating is however limited by the solvent resistance of the substrate layers. The coating solution must also be dilute enough, which tend to migrate upon drying; producing defects on the surface (Cadotte and Petersen, 1981).

Theory behind dip coating has been mostly well developed. For thin film development on a fiber, gravitational force is usually negligible compared to the capillary forces (Lasseuguette *et al.*, 2013). This can be predicted by calculating Bond number, Bo:

$$Bo = \frac{\rho g b^2}{\gamma_{LV}} \tag{2.5}$$

Where ρ is the solution's density, g is the gravitational constant, b is the fiber's radius, and γ_{LV} is the solution's surface tension. Gravitational influence can be neglected when Bo is less than unity.

2.3.3 Interfacial Polymerization

One of the most promising methodology for selective layer formation has been noted to utilize interfacial polymerization (IP) technique. First pioneered by P.W. Morgan and S.L. Kwolek for RO membrane, the formation of thin film through this method requires in-situ polycondensation reaction between monomers in aqueous and organic phase, interacting in-situ on the support layer surfaces. Despite of its fundamental complexity relative to the dip coating methodology, IP exhibit a major advantage due to its self-limiting reaction whereby the formed film restricts the

subsequent monomers reactions, creating a very thin skin layer in the order of 0.1 to 1.0 µm with minimal defects (Wong *et al.*, 2016, Wong *et al.*, 2015). Low cost, ultrathin selective layer can hence be fabricated in-situ. On the other hand, the penetration of the film into the porous structures of the substrate layer enhanced the adhesion between the two layers, minimizing interface defects that may resulting in the degradation of membrane's performance. As the formed polymers are usually insoluble in organic liquids, this method provide significant advantages for the selective layers (Francis *et al.*, 1966).

IP thin film layers are formed primarily by Schotten-Baumann reaction of which requires the irreversible reaction between bi/polyfunctional acid chloride monomers (organic phase) and bi/polyfunctional monomers containing active hydrogen groups such as –OH, –NH, and –SH (aqueous phase) (Ghosh *et al.*, 2008, Wittbecker and Morgan, 1959), forming polyesters, polyamides, thiol based polymers, or any other derivatives, depending on the type of monomers. The reaction can be generally represented as (Morgan, 2002):

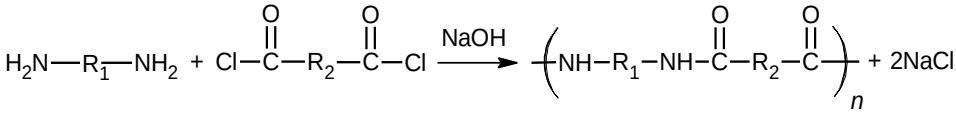

(2.6)

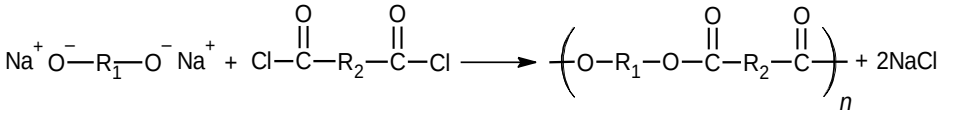

(2.7)

Where the first reaction is between the organic group with the amino group in the water-based monomer to produce amide group while the second reaction is between the organic group with the ester group in the water-based monomer. In both cases, addition of inorganic base compound, e.g., NaOH, Na_2CO_3 etc. is necessary as acid receptor to absorb the acidic proton formed or activate the diol groups. Without the inclusion of the base compound, the reaction will halt due to the protonation of the

amine reactant, or inactivation of the diol groups, depending on the reactants. The acid receptor is usually added to the water phase, and extracts the by-product acid from the polymerization zone (Morgan, 2002). Note that the polymerization requires at least two functional groups on each monomer for polycondensation to be formed.

Polymer formation take place at or near to the liquid interface between the two monomer solutions, with reaction and end-product properties differing between the polymers formed (Morgan, 2002). Liquid-vapor reactions have also been noted particularly for polyureas and polyoxamides formation, albeit no work on membrane application has been noted so far. In membrane fabrication, polycondensation of the polymers need to be conducted without stirring to create a dense thin film on the inter-surface of the solution. As the reaction can be conducted at room temperature and pressure, its utilization and scale up is feasible. Notwithstanding the main reactions in (2.6) and (2.7), these reactions however are limited by the hydrolysis side reaction of the acid chloride group with water and the base compound (Salih *et al.*, 2014):

$$\begin{aligned} -COCl + H_2O &\longrightarrow -COOH + HCl \\ Na_2CO_3 + HCl &\longrightarrow NaCl + NaHCO_3 \\ 2(-COOH) + Na_2CO_3 &\longrightarrow 2(-COONa) + H_2O + CO_2 \end{aligned} \qquad (2.8)$$

The introduction of interface layer has been claimed to suppress the hydrolysis of the organic phase. Salih *et al.* (2014) noted that the introduction of PDMS interlayer on the support substrate prior to the IP process yield no Na element detected, which originates from the base compound used; Na_2CO_3. This claim however can be disputed due to the very low atomic weight percent by the EDS study on top of the high solubility of all Na compounds used in the study should dissolved the components during the washing period. It was also noted that an interlayer situated between the

support and the selective layer was able to suppress the selective layer's thickness down to 100 nm, far lower than other thin film fabrication methodology.

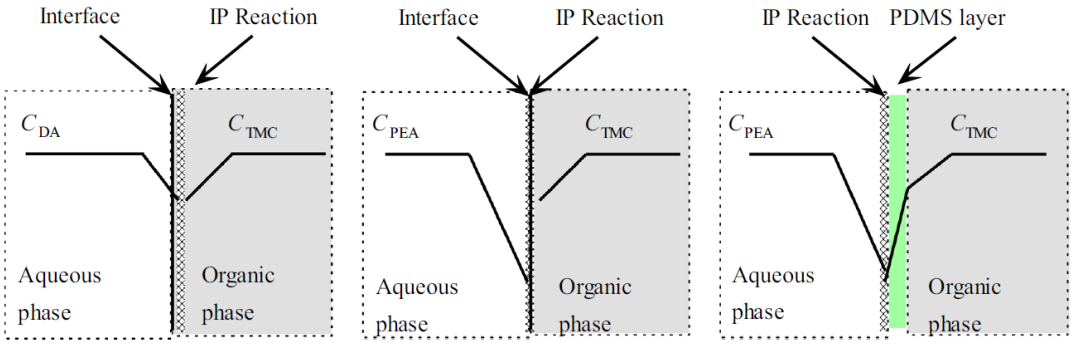

Figure 2.8: Monomer concentration of (a) molecular diamine on substrate without interlayer, (b) polyetheramine on substrate without PDMS interlayer, and (c) polyetheramine on substrate with PDMS interlayer (Salih *et al.*, 2014)

Polymerization predominantly occurs in the organic phase due to the low solubility of most acid chlorides in water, making the use of excess amine over acid chloride to be the common practice (Ghosh *et al.*, 2008). Choice of monomers for IP is important particularly in limiting the thickness of the selective layer and creating a defect free membrane through minimizing the secondary reaction (Salih *et al.*, 2014). MPD and TMC are the commonly used monomers for polyamide (PA) thin film fabrication (Wong *et al.*, 2016). The organic phase can be dissolved in a polar organic solvents like hexane, naptha, cyclohexane, Freon halocarbons, or isoparafin (Ghosh *et al.*, 2008). Summary of the IP monomers used in literature for thin film fabrication is summarized in Table 2.3.

Table 2.3: Interfacial polymerisation choice of chemicals used in literature

Selective Layer	Aqueous Phase	Organic Phase	Reference
Polyamide	MPD	TMC/Isopar-G	(Tiraferri *et al.*, 2011, Perreault *et al.*, 2014, Ghosh *et al.*, 2008)
Polyamide	MPD	TMC/hexane	(Jeong *et al.*, 2007, Ma *et al.*, 2017)
Polyamide	DGBAmE	TMC/hexane	(Wong *et al.*, 2015)
Polyamide	PIP	TMC/DOX/hexane	(Liu *et al.*, 2015)
Polyetheramide	Diamine	TMC	(Salih *et al.*, 2014)
Poly(MEDA–TMC)	MEDA	TMC	(Yuan *et al.*, 2012)
Polyamide	DNMDAm + DGBAmE	TMC	(Li *et al.*, 2012)
Polyamide	TETA	TMC	(Jiao *et al.*, 2021)
Poly(PIP-amide)	PIP	TMC	(Misdan *et al.*, 2014)

MPD = 1,3-phenylenediamine; TMC = 1,3,5-benzenetricarbonyl trichloride; DGBAmE = diethylene glycol bis(3-aminopropyl) ether; PIP = piperazine; DOX = dioxane; MEDA = N-methyldiethanolamine; DNMDAm = 3,3 ′ -diamino-N-methyldipropylamine; TETA = triethylenetetramine

IP methodology is affected by several parameters such as the molecular structures, monomer concentration, organic solvent, additives, reaction time, and preparation conditions (Wong *et al.*, 2016). Choice of organic solvent particularly is one of the main parameter needs to be controlled as it will affect several other polymerization factors (Wittbecker and Morgan, 1959). Relative diffusivity, $D_{relative}$ of aqueous monomers in the organic solvents are negatively related to the solvent's viscosity by (Yuan *et al.*, 2012):

$$D_{relative} = \frac{\eta_{water}}{\eta_{solvent}} \tag{2.9}$$

Where η represents the dynamic viscosity. The work by Yuan *et al.* (2012) suggested that higher solubility and lower diffusivity of the aqueous monomer chosen in organic solvent would produce thicker, less crosslinked, and more crystalline skin layer. Hence, the choice of organic solvent to maintain low aqueous monomer solubility and high diffusivity would be vital in characterizing the performance of the selective layer

(better permeance, selectivity, and plasticization resistance). On the other hand, concentration of organic phase determines the skin thickness while concentration of aqueous phase determines the crosslinking extent (Yuan *et al.*, 2012). High performance membrane can hence be made by decreasing organic phase concentration and increasing aqueous phase concentration. The strength of the films is also an emerging factor to be considered. The strongest films are derived from aliphatic and aliphatic-aromatic polyamides, and some polyurethanes (Morgan, 2002).

Despite of the success of thin film preparation particularly through IP, the thin layer can only be fabricated ever so thin before eventually reached its limit. Other than the mechanical limitation of the thin film, the permeance would also eventually decrease as the thickness became comparable to the surface pore size of the porous substrate (Pinnau and Koros, 1991, Zhu *et al.*, 2016a, Kattula *et al.*, 2015). Without the proper optimization of its support layer, these limitations would significantly reduce the separation efficiency, due to lateral diffusion effect which caused geometric restriction near the dense-porous interface. Detailed discussion will be made in separate section. On the other hand, despite of its extensive research for RO membrane, the same success could not be generally translated for gas separation membrane (Yuan *et al.*, 2012). Notwithstanding of the similar methodology used for IP in both water and gas based membrane separation processes, it was noted that the typical amine monomers used in water based membrane is unsuited for gas separation purposes as introduction of bulky groups in diamine moieties increases permeability at the expense of selectivity (Wong *et al.*, 2015, Sridhar *et al.*, 2007). IP also created highly crosslinked layer on the surface, but less crosslinked, more permeable hydrogel layer in pores of the substrate layer. The hydrogel formation, while being water swollen and offers little resistance in RO application, became rigid glass in dry conditions, creating

a low permeability, high resistivity region in the substrate pores (Morgan, 2011, Baker, 2004). This hinders the potential of IP to be used in gas separation. However, the use of gutter layer may be able to help alleviating this problem.

2.3.4 Methodology Limitations for Hollow Fiber Configuration

Hollow fiber is the preferred configuration for membrane gas separation process (Koros and Zhang, 2017, Pinnau and Koros, 1991). While dense skin asymmetric hollow fibers can be spun, the lack of precise control on the thin surface layer resulting in unavoidable surface defects which will affect the permeation performance, making its industrial practicality highly limited and normally needs to be coated with a secondary high permeability polymer (Henis and Tripodi, 1981). Despite of the possible use of dense thin film membrane in flat sheet configuration, translating the work into hollow fiber configuration poses several significant challenges, particularly in maintaining the membrane's self-supporting requirement. Thin dense membrane in hollow fiber form is impossible to be viable due to manufacturing and mechanical limitations.

A thin film composite membrane would need to be developed for nanofillers incorporation to be utilised in hollow fiber configuration. Multilayer hollow fibers fabricated through multibore spinneret have been reported but is expected to have high thickness for membrane fabrication. Composite laminate on the other hand, would be practically impossible to be made for hollow fiber. Meanwhile, dip coating methodology is one of the easiest method to fabricate supported thin film in hollow fiber configuration (Tsai *et al.*, 1995). Equation (2.4) also suggested that thin fiber dip coating would be advantages due to the possibility of finer coating thickness. Besides that, one of the ways to incorporate the thin film nanocomposite onto the hollow fiber substrate is through interfacial polymerization. Recent work has

suggested the possibility to benefit from IP for hollow fiber configuration by circulating the organic and aqueous solution in the lumen and the outer surface respectively while maintaining a good pressure control so the reactions can occur on the inner surface (Yang *et al.*, 2021). Nevertheless, the unwanted formation of hydrogel in the porous structure of the substrates is still a problem need to be elucidated before IP can be confidently utilized in gas separation.

2.4 Porous-Dense Interface

2.4.1 Influence of Porous Substrate Layer

Notwithstanding the importance of substrate layer as the backbone of thin film composite membrane, this unsung hero is commonly ignored by the research community. It is understandable that the lack of contribution of porous substrate layer on the gas separation performance of composite membrane makes the research unattractive, but its importance and influence on the selective layer's real-world performance cannot be denied.

In principal, substrate layer of TFC/TFN is a 150-200 µm thick porous structure with minimum tortuosity and just the right pore size to minimize the mass transport resistance, yet high in mechanical strength to support the thin film and withstand compression under high differential pressure (Kattula *et al.*, 2015). Hence, ideal substrate layer would be made up of pores small enough to maximize the compression strength, but large enough to avoid significant resistance to the permeating gas (Zhu *et al.*, 2016a). Typical substrate layers were found to be low in porosity between 0.01 to 0.1 to improve the mechanical properties, and surface pore size less than 100 nm to provide smooth surface for the selective layer deposition (Kattula *et al.*, 2015). Common methodology for substrate layer fabrication is by phase

inversion, albeit other methodologies such as track-etch (Zhu *et al.*, 2016a) have also been utilized in literature.

Resistance across the composite membrane has been proposed as a series of transport resistance (reciprocal of pressure normalized gas permeability), analogous to the electrical resistance, first by Henis and Tripodi (1981). The gas transport resistance can be correlated with the gas selectivity, α by (Pinnau and Koros, 1991):

$$\alpha_{i,j} = \frac{\frac{\ell_1}{P_{j,1}} + \frac{\ell_2}{P_{j,2}}}{\frac{\ell_1}{P_{i,1}} + \frac{\ell_2}{P_{i,2}}} \tag{2.10}$$

Where ℓ is the thickness of the layer, P is the permeability, subscript 1, 2 is the skin layer and its substrate respectively, and subscript i, j is the gas pair of interest. Figure 2.9 represents the visualized resistance model for the composite membrane.

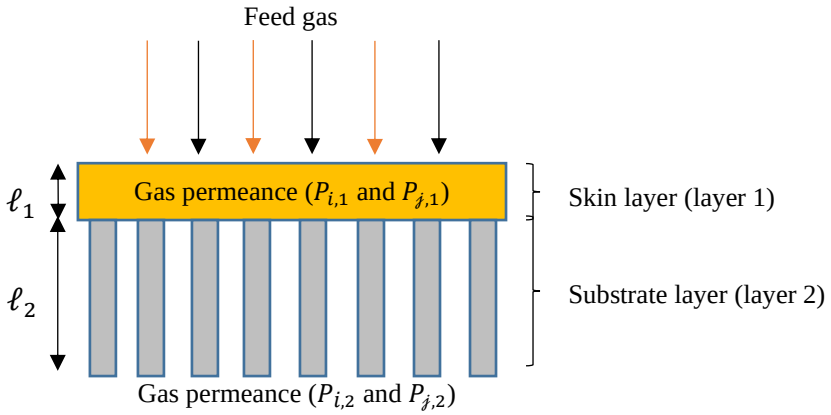

Figure 2.9: Visual representation of the transport resistance in composite membrane

From the equation, plot of gas selectivity versus the ratio of substrate-selective skin layer resistance can be made to show the influence of resistance on the gas selectivity. By assuming the substrate to exhibit Knudsen selectivity of 0.935 and hypothetical selective layer intrinsic O_2/N_2 selectivity of 2, 4, 6, and 8, membrane selectivity was initially skin layer dependent; limited by the intrinsic selectivity of the selective skin layer. Nevertheless, with increasing layer resistance ratio (e.g.,

increasing the substrate layer resistance), the selectivity would eventually be substrate dependent, as represented by Figure 2.10.

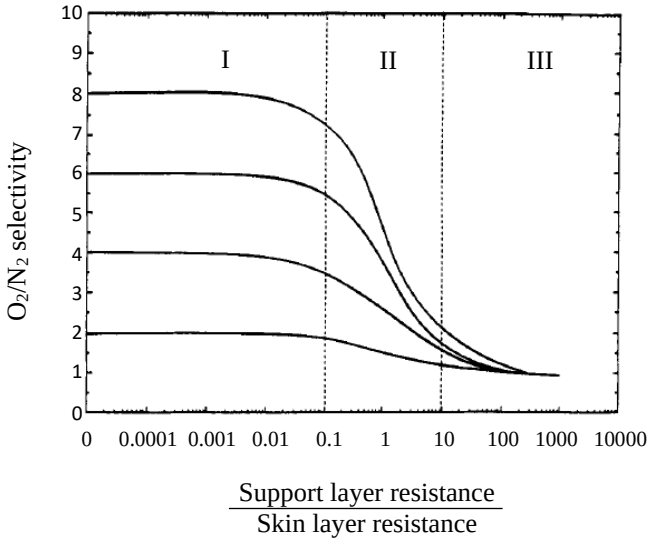

Figure 2.10: Influence of substructure resistance to skin layer resistance ratio on O_2/N_2 selectivity of different intrinsic selectivity. Area I = selectivity determined by skin layer, area II = selectivity is influenced by substructure, area III = selectivity is determined by substructure (Pinnau and Koros, 1991)

Generalizing from this result, the rule of thumb for any composite membrane is to limit the substrate structure's resistance to skin layer resistance to be less than 10:

$$\frac{(\frac{\ell}{\overline{P}})_{i,2}}{(\frac{\ell}{\overline{P}})_{i,1}} < 10 \qquad (2.11)$$

Intuitively, as the layer's resistance are also dependent on its thickness, introduction of thinner selective layer would decrease the denominator of equation (2.11). Permselectivity of the membrane would hence decrease relatively due to (i) overall impact by the transport resistance in the substrate layer and (ii) restriction of concentration profile of penetrant in the selective layer (Pinnau and Koros, 1991, Zhu *et al.*, 2016a). This would hence make the permselectivity of composite membranes to be lower than the intrinsic selectivity of the selective layer, limiting its effectiveness.

Lowering the gas transport resistance for the substrate layer can be achieved through decreasing its thickness or increasing its permeability. For gas separation in porous structure, permeability of a hypothetical gas molecule i is governed by the Knudsen diffusivity, D_i:

$$D_i = \frac{d_p}{3}\sqrt{\frac{8RT}{\pi M_i}} \tag{2.12}$$

Where d_p is the diameter of the porous substrate, R is the gas constant, T is the temperature, and M is the molecular mass of the gas. The rule of thumb for gas separation in porous substrate layer can be determined using Knudsen number, K_n given by:

$$K_n = \frac{\lambda_i}{d_p} \tag{2.13}$$

Where λ is the gas mean free path length. For $K_n < 1$ convective flows will dominate the gas transport without any separation outcome. On the other hand, for $K_n \geq 1$, Knudsen diffusivity became apparent, and separation occurs based on the differences of the gas molecular weight.

Several studies were found on improving the performance of substrate layers. Tiraferri *et al.* (2011) have studied the effect of PSf-dimethylformamide (DMF) concentration on the surface pore size and the width of the fingerlike pore structures of the porous substrate layers formed through phase inversion. Their finding indicates a decrease in both surface pore size and fingerlike pore width with increasing polymer concentration. On the other hand, Zhu *et al.* (2016a) aim to verify experimentally the theoretical model proposed on the transport resistance with 85% reduction in gas permeance upon the introduction of substrate layer as compared to a free standing thin film. It was found that gas permeance would increase with increasing porosity (at

constant pore size) and with decreasing pore size (at constant porosity) due to geometric restriction or lateral diffusion.

Mechanical strength of the substrate layer has also been studied by Tiraferri *et al.* (2011). Under the pressure of 27.6 bar, the percentage of substrate compaction was found to be decreasing with increasing polymer concentration but shows an upward parabola trend with solvent concentration. Other than the fabrication methodology, due to the porous structures of the substrate layer, it can be important for it to be post-treated to minimize pore collapse. High surface tension of water increased the tendency of the pore to be pressurized upon the evaporation of surface water and the subsequent capillary action of in-pore water, creating a partial vacuum inside the pore structures. This increases the possibility for the membrane pore structures to collapse during drying period. Several methodologies were noted such as those proposed by Wong *et al.* (2015) which utilizing ethanol-hexane. Similar methodology was used by Jawad *et al.* (2015), albeit it was incorporated during the phase inversion period as an alternative to vacuum drying. Nevertheless, this methodology could be utilized during the post-processing for the same purposes.

In summary, substrate layer should have pore size identical to an ultrafiltration membrane. While the resistance effect by the substrate layer should be easily elevated by controlling the membrane pore size formation, larger pore size would also affecting the membrane's mechanical strength. On the other hand, substrate layer's surface pore size and distribution (thin film-substrate interface) can become a major concern due to the limited diffusion pathways of the gas molecules across the composite layers. This will next be discussed.

2.4.2 Lateral Diffusion / Geometric Restriction

From molecular point of view, the discontinuity between the slow permeating dense and the fast-permeating porous part of the composite creates a funnelling effect for the permeating gas near these interfaces. This pore restriction poses two problems; (i) increase in molecule's diffusion path length, which makes the actual diffusion length to be much higher than the selective layer's thickness, and (ii) increase in the velocity of molecules near the pore opening due to restricted flow by Venturi effect. These two effects generate concentration gradient of diffusing molecules at the pore opening, which increases the top layer diffusion resistance higher than its intrinsic resistance (Wijmans and Hao, 2015). It has been suggested that the effect will become prominent as the selective layer thickness approaching the pore size of the support layer (Zhu *et al.*, 2016a). The problem is visualized as in Figure 2.11.

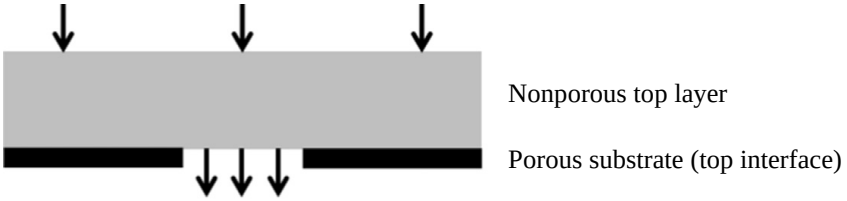

Figure 2.11: Diffusion of molecules across composite dense selective layer through the porous substrate. Diffusion is restricted at the choke point of the substrate's surface; the pore opening (Wijmans and Hao, 2015)

While this has been suggested to have minimal effect on the gas selectivity, permeance on the other hand are highly affected; suggesting that the problem is not dependent on the gas permeated. This reduction in permeance can be represented by the restriction factor, Ψ given by (Zhu *et al.*, 2016a, Wijmans and Hao, 2015):

$$\Psi = \frac{(\frac{P}{\ell})_{effective}}{(\frac{P}{\ell})_{intrinsic}} \tag{2.14}$$

Where P is the permeability coefficient and ℓ is the thickness of the selective layer. To further elucidate the problem, Wijmans and Hao (2015) has studied the effect of

this phenomenon through three dimensional CFD simulation, which suggested reduced effect on the permeance for highly porous substrate. The permeance efficiency was also affected by the thickness of the selective film which decreases when it gets thinner. The thickness, pore size, and porosity were noted to be correlated to the restriction factor by:

$$\lim_{\tau \to \infty} \Psi = 1 \ \ and \ \ \lim_{\tau \to 0} \Psi = \ \varepsilon \tag{2.15}$$

Where ε is the porosity of the substrate and τ is the normalized thickness given by film thickness ℓ over pore radius of the substrate. This pose a major limitation for TFC/TFN with ultrathin selective layer, whereby with the decrease in film thickness, film – substrate interface became a major concern; the effective gas permeation is limited by the porosity of the substrate. To determine the impact of substrate's pore morphology, porosity, and selective layer's thickness on the membrane's flux performance, Wijmans and Hao (2015) has proposed a semi-empirical equation based on the restriction factor correlation represented by:

$$\Psi = \frac{\varepsilon + 1.6\, N_R^{1.1}}{1 + 1.6\, N_R^{1.1}} \ ; \ N_R = \frac{\varepsilon . \tau}{1 - \varepsilon} \tag{2.16}$$

Where N_R is Restriction Number; a dimensionless number between zero (complete pore restriction) and infinity (no pore restriction).

This problem has also been experimentally studied by Zhu *et al.* (2016a) by altering the surface pore size and porosity of the substrate layer and compared with CFD 3D model. It was shown that substrates with smaller pores and high in porosity is advantageous in mitigating the interface restriction, on top of uniform pore dispersion throughout the membrane surfaces. These results are in line with the correlation proposed by Wijmans and Hao (2015) in equation (2.16), and CFD results predicted by Kattula *et al.* (2015). Nevertheless, simply reducing the pore size would

increase the overall resistance of the substrate layer, limiting the gas transport. On the other hand, increase in porosity may limit the functionality of the substrate layer as the mechanical backbone under high pressure, suggesting the reason for the lack of commercial TFC/TFN with porosity above 10%. In fact, it was shown by Kattula *et al.* (2015) that the membrane's permeance efficiency decreased to as low as 10% at τ of 10 for 1% porosity model with uniform pore dispersion of two times the diameter between the radius of adjacent surface pores, and only reached 50% efficiency at τ of 5 for 10% porosity model under the same pore dispersion condition. By default, although reducing the skin thickness can increase the permeance, the efficiency however would always be compromised.

Another way to elevate this problem is through the introduction of gutter layer at the dense-porous interface; an additional dense layer on top of the substrate made up of high permeability, low selectivity material such as poly[(1-trimethylsilyl)-1-propyne] (PTMSP) and polydimethylsiloxane (PDMS) (Kattula *et al.*, 2015, Salih *et al.*, 2014). Several 3D CFD model has been developed and was noted to significantly improve the permeance with minimal effect on the selectivity (Wijmans and Hao, 2015, Kattula *et al.*, 2015). The introduction of gutter layer (yellow layer) channels the permeate from the dense selective layer (green layer) into the surface pores reducing the geometric restriction imposed by the porous substructures (grey layer), as illustrated in Figure 2.12. This can be seen from the curvature of arrow flow perpendicular to the membrane's surface. For flow on top of the dense part of the substrate, significant deviation from a straight pathway can be seen for thin coating layer. Meanwhile, by introducing gutter layer, gas flow starts to be less curved and thus the impact of lateral diffusion can be elevated. Introduction of gutter layer was able to increase the permeance efficiency up to three-fold from 21% to 64% for

normalized gutter thickness (gutter thickness over pore radius ratio) of 1 at 10% porosity, signifying its effectiveness in mitigating the geometric restriction of ultrathin selective layer (Kattula *et al.*, 2015).

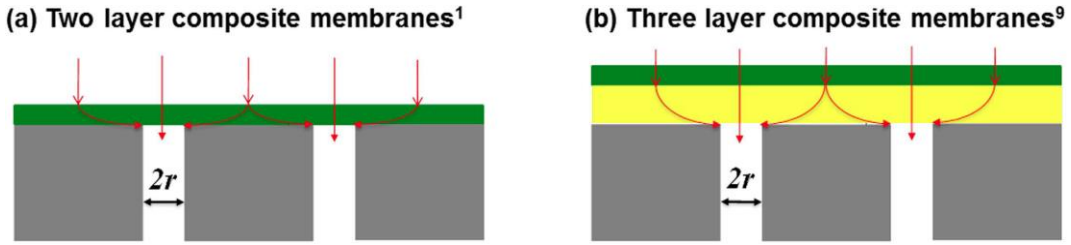

Figure 2.12: Channelling of permeate to the porous substructures for (a) conventional two layers TFC versus (b) three layers TFC (Kattula *et al.*, 2015)

Nevertheless, increase of the gutter layer thickness was noted to have competing effect between helping to channel the gas transport between the dense selective layer to the porous substrate layer, and increasing the resistance of the composite membrane. Kattula *et al.* (2015) suggested gutter layer thickness to be 1 to 2 times the radius of the pore (equivalent to τ between 1 and 2) for maximum permeance with negligible selectivity decrease while Wijmans and Hao (2015) suggested τ between 1 and 10, although it was also noted that the effect of τ on the permeance is not very critical; precise tailoring of the gutter layer would hence be unnecessary. It is also important to note that the introduction of additional layers would still introduce additional resistance, on top of the increased cost and possible incompatibility at both sides of the gutter layer interface. It is also possible to elevate the problem by using high permeability materials as the substrate layer to help channelling the permeating gas through the solid part of the substrate. Although, this would be limited by the number of materials available that possess the correct properties, as it needs to be highly permeable yet glassy enough to be self-supporting. Several reported works on using gutter layer is presented in Table 2.4.

Table 2.4: Current material used as gutter layer in literature

Material	Permeability	Selectivity	Reference
PDMS	CO_2 = 1 900 GPU at 170 nm	CO_2/N_2 = 9.1	(Halim *et al.*, 2014)
PTMSP	CO_2 = 4 448 GPU at 490 nm	CO_2/N_2 = 3.9	(Peter and Peinemann, 2009)
Covalent organic frameworks (COFs)	CO_2 = 25 000 GPU at 55 nm	CO_2/N_2 = 1.3	(Ying *et al.*, 2021)
Chitosan	CO_2 = 5 733 GPU at <10 nm	CO_2/N_2 = 1.0	(Kouketsu *et al.*, 2007)
Teflon AF2400	CO_2 = 31 500 GPU at 75 nm	CO_2/N_2 = 3.3	(Yoo *et al.*, 2018a)
ZnTCPP MOF nanosheet	CO_2 = 18 600 GPU at 25 nm	CO_2/N_2 = 0.98	(Liu *et al.*, 2018)

2.4.3 Solution Intrusion / Solution Impregnation

Solution intrusion is a physical phenomenon due to the formation or adhesion of low permeable coating layer polymers in the pore of the substrate, which increases the flow distance of penetrating gases across the less permeable layer, increasing the membrane resistance in the substrate region. Impregnation of coating solution are normally due to capillary pressure, p_c at the surface pores, which is given by the Young-Laplace equation:

$$p_c = \frac{2\gamma_\ell cos\theta}{r_c} \tag{2.17}$$

Where γ_ℓ is the surface tension of the liquid, θ is the contact angle of the liquid with the capillary's surface, and r_c is the radius of the pore. From the equation, lower pore size or lower contact angle would increase the capillary pressure that propel the penetration of the coating solution into the pores. Lower contact angle is however important for a good coating of the substrate as wetting of substrate's surface by the coating solution is required to allow thinner coatings to be formed.

The influence of solution intrusion is normally represented by the depth of penetration, which assumes a complete intrusion into the substrate pore up to a certain distance. This depth can be predicted using a correlation proposed by Chung (1997), although the equation, which was developed based on the resistances-in-series model did not consider the effect of lateral diffusion. On the other hand, recent studies have confirmed that pore could be only partially coating the side walls, which reduces the pore size instead of filling the surface pores (Li *et al.*, 2019). The two penetrating processes proposed in literature is represented as in Figure 2.13. Pore wall coating, being still porous, could in turn redirect any additional resistance by the solution intrusion towards the lateral diffusion instead.

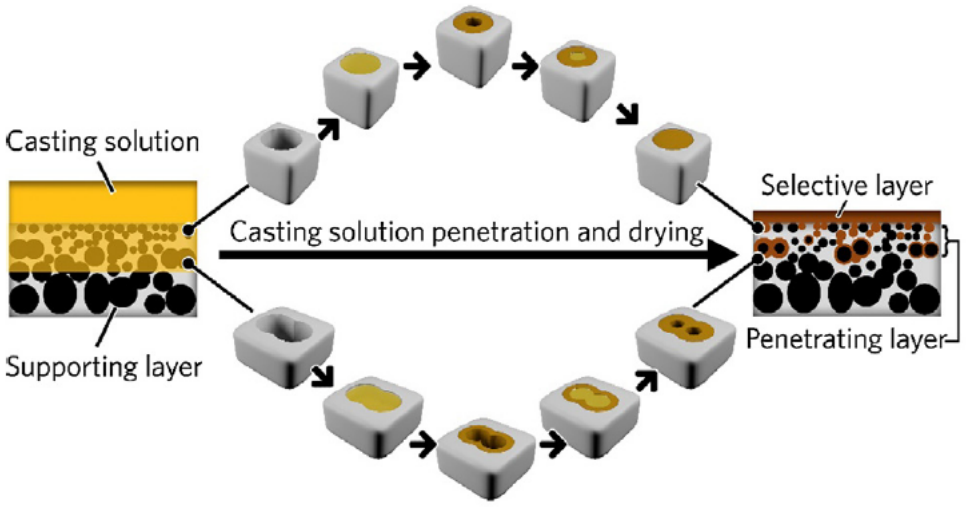

Figure 2.13: Schematic illustration of the penetrating process (Li *et al.*, 2019)

Solution penetration is relatively undesirable as it can significantly increase the flow resistance in the substrate layer. This is indeed the case as noted by Hao *et al.* (2020), where they find out penetration of 1 nm adds resistance equivalent to the resistance of 160 nm top layer in their CFD analysis. On the other hand, Li *et al.* (2019) suggested that effect of solution penetration on the gas transport resistance is stronger at the early stage of penetration, meaning even a small penetration would have

significantly large effect on increasing the resistance. This is shown by Chung (1997) to be in between 10-100 nm where normalized permeance drop from 0.9 down to 0.4, although this might differ based on the composites studied.

There have been several attempts to quantitatively measure the penetration depth or degree in recent literature. Qin *et al.* (2015) reported the use of Focused Ion Beam (FIB) nanomachining to expose the cross-sectional layer of polymeric-inorganic multi-layer composite structures and then visually analysed using SEM and TEM. While the method proves to be reliable, cutting a full polymeric composite layer might be difficult as compared to the more rigid inorganic substrate. On the other hand, Li *et al.* (2019) suggested the use of small angle X-Ray scattering (SAXS) to measure the variations of nano-pore size distribution in polymeric membranes. This method, while looks promising, is limited by the lack of consideration for pores that were fully filled.

The effect of solution intrusion can be reduced by pre-wetting the substrate with non-solvent of the coating materials. As the liquid already fills up the pore structure, coating solutions cannot penetrate the substrate easily. This simple method has proven to be effective to minimize solution intrusion but are unable to completely remove its effect (Jin *et al.*, 2017, Li *et al.*, 2019, Cay-Durgun *et al.*, 2020). Reduction of pore penetration also means lower attachment point for coating layer, which will affect the layer-layer adhesion. Another passive method is by having an asymmetric design in the surface pores, with increasingly larger pore size in downward direction. This would be beneficial to limit any further penetration deep into the substrate. This physical limit has been noted by Hapgood *et al.* (2002), where macro-void formation in granular packing would limit the flow of the fluid.

2.5 Choice of Materials

Selective layer's permeability is one of the macro parameters that governs the flux performance of the membrane. Under the solution-diffusion mechanism, permeability is defined by the product of the diffusivity or diffusion coefficient, D and solubility or gas sorption coefficient, S of the penetrants in the selective layer's polymer:

$$P = DS \tag{2.18}$$

Diffusivity can be defined as the mobility of the individual molecules in the membrane material, a kinetic property of the polymer; while solubility is the number of molecules dissolved in the membrane material, a thermodynamic property of a polymer (Cong *et al.*, 2007, C&EN, 1980, Baker, 2008). The transport properties of the permeant across the thin film is thus influenced by the permeant's size, shape, and polarity (Car *et al.*, 2008). Hence, selective layer's choice of material would theoretically be the most important parameter for gas separation membrane as it would define the resulting flux and separation performance of the composite membrane. Nevertheless, real composite membranes also require good material choices for the substrate and possibly gutter layer, as both played an important role in optimizing the performance of the fabricated membranes, as discussed previously.

Diffusion and sorption of gas molecules across solid polymers are a complex interaction which depends on a lot of factors. Hence, determination of these properties independently for all available polymers are practically difficult to achieve, particularly due to the vague nature of polymer's structure (C&EN, 1980). Several theories have been developed in explaining the phenomena, although no simple equation can be devoted to predicting the coefficients over different polymers with certain accuracy. As the mechanism is based on the gas diffusivity, permeation across

the polymeric membrane is usually increases with temperature. The effect of pressure on the other hand will be based on the gas-polymer interaction itself, depending on the nature of both (Park and Lee, 2008). Nevertheless, at a fixed condition, permeability of a polymer can be known easily using a simple bubble flowmeter. The permeability of CO_2, N_2, and CH_4 gas molecules in a polymer of choice is represented by Table 2.5.

Table 2.5: Gas permeability of common polymer used in gas separation (Abetz *et al.*, 2006)

Polymer	**Permeability at 30 °C (Barrer)**			**Ideal selectivity**	
	N_2	**CO_2**	**CH_4**	**CO_2/N_2**	**CO_2/CH_4**
Polyimide (Matrimid)	0.32	10.7	0.25	33.4	42.8
Cellulose acetate	0.21	6.3	0.21	30.0	30.0
Polysulfone	0.25	5.6	0.25	22.4	22.4
Polyetherimide	0.047	1.32	0.035	28.1	37.7
Polycarbonate, brominated	0.18	4.23	0.13	23.5	32.5
Polyphenyleneoxide	3.81	75.8	11	19.9	6.9
Polymethylpentene	6.7	84.6	14.9	12.6	5.7
Polydimethylsiloxane	250	2 700	800	10.8	3.4
Ethyl cellulose	3.2	26.5	19	8.3	1.4

Based on Equation (2.18), polymers can thus be sub-divided into two classes: glassy and rubbery polymer. Glassy polymers are usually much more selective for smaller molecules as the diffusion coefficient of these polymers are more dependent on molecular size of the permeant than its rubbery counterpart (Car *et al.*, 2008, Chung *et al.*, 2007). This is because larger molecules can interact with more of the segments of glassy polymer's rigid polymer chains, limiting its mobility (Baker, 2008). In the application of biogas upgrading for example, the three main gas components; CH_4, N_2, and CO_2 have a relatively appreciable difference in its kinetic diameter (3.80, 3.64, and 3.30 Å for CH_4, N_2, and CO_2 respectively), ensuring a higher CO_2 selectivity under diffusion coefficient effect alone. On the other hand, rubbery

polymers are much more effective in separating gases based on the solubility (Park *et al.*, 2017). Solubility is influenced by the condensability of the permeant, in which the coefficient increases with increasing condensability (Baker, 2008). As a rule of thumb, larger molecules are usually more condensable than smaller one. This suggests that diffusivity and solubility coefficients are affected reciprocal to each other, as noted in Figure 2.14.

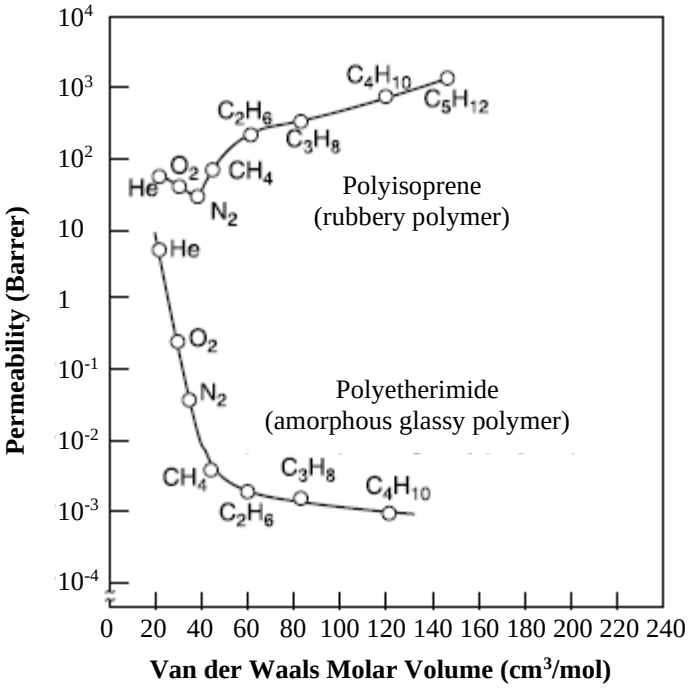

Figure 2.14: Permeability as a function of molar volume for a rubbery and a glassy polymer (Baker, 2008)

Based on this information, the choice of polymer type will thus depend on the application of the membrane itself. Despite of the high permeability of rubbery polymers, selectivity is highly limited for small gas molecule permeation. Hence for CO_2/N_2 or CO_2/CH_4 application, better separation would be made when utilizing glassy polymer-based membrane. Most glassy polymers also have relatively high process ability making it attractive for membrane fabrication (Henis and Tripodi, 1981), although gas permeability in glassy polymers can be influenced by the preparation methodology such as solvent and temperature (Zhu *et al.*, 2016a). Glassy

polymer is however, affected by plasticization phenomenon which rubberize the polymer; making its selectivity deteriorates. Real world application can also be limited by other factors such as the intrinsic limitation as imposed by the Roberson's upper bound, on top of the physical and chemical properties of the polymers such as inverse relation between the diffusivity/solubility coefficients, process ability, crystallinity (Yuan *et al.*, 2012, Salih *et al.*, 2014), plasticization, and mechanical strength (Salih *et al.*, 2014) of the polymer.

Here some of the most interesting polymer used in gas separation is mentioned. Typical glassy polymers used are polysulfone, cellulose acetate, and polyimides (Chung *et al.*, 2007). This is expected by the higher selectivity of the gas which ensures a higher intrinsic limitation of the gas flux performance across the membrane, on top of other engineering factors including process ability, mechanical strength, and long-term stability. In recent years, the use of copolymer such as Pebax, a commercial poly(ether block amide) has been considered by researchers due to its unique mix of both polyamide; a glassy polymer and polyether; a rubbery polymer (Ahmadpour *et al.*, 2014). This improves the free volumes of a supposedly rigid structures of pristine glassy membrane. Polyethylene oxide (PEO) is also an interesting polymer due to its high affinity of CO_2. However, preparation of neat PEO membrane is not practical due to its high crystallinity limiting the gas molecular transport and weak mechanical properties limiting its real world application (Salih *et al.*, 2014).

For IP based TFC, majority of the selective layer's choice of material has been noted to utilized polyamide, using polyamines and polyacyl halides as monomers due to polyamide's high mechanical strength, thermal stability, chemical resistivity (Wong *et al.*, 2016). Its high CO_2 transport permeability makes it an interesting material for CO_2 based separation. However, the limitation of hydrogel formation in

IP as discussed previously should be considered. It has also been reported that polymers with high gas permeability should have (i) at least one rigid divalent subunit with no colinear bond extensions, (ii) at least one bond should be unable to rotate around 360 °C for sterical reasons, and (iii) 50% or more of the main chain atoms are aromatic (Abetz *et al.*, 2006). Poly(amide imide) (PAI) were noted to have this characteristics. It was also found that PAI can resist plasticization due to the strong intermolecular interactions. Nevertheless, the amide bond was noted to prevent high diffusion coefficients despite of its good selectivity (Abetz *et al.*, 2006). Specially designed polymers, such as modified fluorinated polyimides and some of the 6FDA-based polyimides were sometimes too expensive, not attractive enough as compared to the commercial polymers, or unreliable in field condition due to plasticization and physical aging. The selectivity of the material used, despite of having exceptional ideal selectivity for the binary gas pair of interest, may also drop significantly under real gas mixtures as high solubility gas can cause excessive swelling to the material, increasing the permeability of the slower gas (Abetz *et al.*, 2006).

Creative solutions to these limitations have been proposed such as using co-polymers and crosslinked structures, but no definitive application has been seen yet for bulk of the polymers developed for gas separation in literature. In the end, the lack of information is probably one of the reasons why despite of thousands of variations of polymeric membrane work found in literature, 90% of the current membranes in the market is still consist of fewer than 10 base polymeric materials used since 1990 (Galizia *et al.*, 2017, Baker and Low, 2014). It is possible that the breakthrough polymer is already among us, just not yet being noticed.

Interest will thus be given towards polyimide (PI), being the largest group of polymers utilized in CO_2 membrane gas separation. It is hard to generalize the

properties of PI as it can be significantly different from one another. Nevertheless, a lot of PI were found to be close to the Roberson's upper limit, with promising results in CO_2/N_2 and CO_2/CH_4 separation in literature (Favvas *et al.*, 2017, Robeson, 2008). 6FDA-based PI for example, can possess extremely high CO_2 permeability. Hence, despite of its high cost, the use in composite configuration may benefit its usage. It has also recently reported that 6FDA-DAM PI membrane was able to benefit from plasticization effects in which the H_2S/CH_4 selectivity was maintained at around 31 even at high permeation pressure (Liu *et al.*, 2020). Commercial benzophenone-3,3',4,4'-tetracarboxylic dianhydride (BTDA)-based PI such as Matrimid on the other hand, has seen significant interest in gas separation as it has been shown to have a good balance of selectivity and permeability, on top of being feasible for scaling up, although it is shown to be susceptible to plasticization (Sridhar *et al.*, 2007, Castro-Muñoz *et al.*, 2017). In 2016, PI membrane made out of BTDA-TDI/MDI, commercially named as P84 was patented by Evonik Fibres GmbH, signifying its potential (Visser *et al.*, 2016). The chemical structure of this polymer is given as in Figure 2.15.

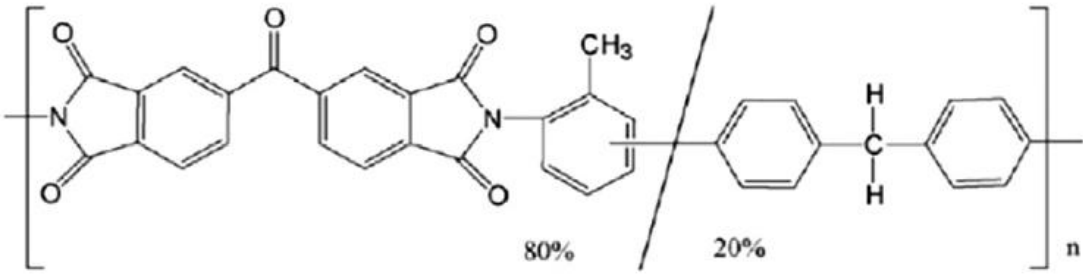

Figure 2.15: Chemical structure of P84 polyimide (Favvas *et al.*, 2017)

P84 PI is interesting due to the reported acceptable selectivity drop for CO_2/CH_4 separation in binary gas mixtures (Sridhar *et al.*, 2007). Research on this polymer has also been increasing due to their favourable physico-mechanical and chemical properties. Although, BTDA-based commercial PI polymer is usually low in

permeability as compared to their 6FDA-based counterpart (Chen *et al.*, 2015). Nevertheless, this opens the possibility for improvements through MMM. Literature found on dense and asymmetric P84 PI is given as in Table 2.6.

Table 2.6: Dense/asymmetric P84 PI membrane for gas separation

Configuration	**Thickness (skin)**	**Permeability (Barrer)**	**Selectivity**	**Reference**
Flat sheet (dense)	-	N_2 = 0.05 CO_2 = 1.37 CH_4 = 0.028	CO_2/N_2 = 27.4 CO_2/CH_4 = 48.9 N_2/CH_4 = 1.78	(Hosseini and Chung, 2009)
Flat sheet (dense)	50 μm	CO_2 = 1.2 CH_4 = 0.02	CO_2/CH_4 = 50	(Tin *et al.*, 2004)
Flat sheet (dense, annealed at 200 °C)	309 μm	N_2 = 0.13 CO_2 = 1.82	CO_2/N_2 = 14.3	(Shen and Lua, 2010)
Flat sheet (dense)	-	CO_2 = 14.4 CH_4 = 0.43	CO_2/CH_4 = 33.4	(Sridhar *et al.*, 2007)
Flat sheet (dense)	20 μm	N_2 = 0.025* CO_2 = 0.99	CO_2/N_2 = 40.2	(Barsema, 2003)
Hollow fiber (asymmetric)	56 nm	N_2 = 0.032* CO_2 = 1.29*	CO_2/N_2 = 40.4	(Etxeberria-Benavides *et al.*, 2019)
Flat sheet (dense)	20 μm	N_2 = 0.035* CO_2 = 1.28	CO_2/N_2 = 36.6	(Etxeberria-Benavides *et al.*, 2019)
Flat sheet (dense)	20 μm	CO_2 = 2.66 CH_4 = 0.049	CO_2/CH_4 = 54.1	(Guo *et al.*, 2018)
Flat sheet (dense)	-	N_2 = 0.044 CO_2 = 0.89	CO_2/N_2 = 20.2	(Shen and Lua, 2012)
Flat sheet (dense)	85 μm	N_2 = 0.09 CO_2 = 1.12	CO_2/N_2 = 12.4	(Lua and Shen, 2013b)
Flat sheet (asymmetric)	500 nm	N_2 = 0.07* CO_2 = 0.9*	CO_2/N_2 = 20	(Lua and Shen, 2013a)
Flat sheet (dense)	-	CO_2 = 0.72 CH_4 = 0.016*	CO_2/CH_4 = 44	(Sheng *et al.*, 2020a)
Hollow fiber (asymmetric)	-	-	CO_2/N_2 = 13.6 CO_2/CH_4 = 12.5	(Sheng *et al.*, 2020b)

Table 2.6: Continued

Configuration	Thickness (skin)	Permeability (Barrer)	Selectivity	Reference
Hollow fiber (asymmetric, annealed at 180 °C)	-	-	CO_2/N_2 = 9.5 CO_2/CH_4 = 8.1	(Sheng *et al.*, 2020b)
Flat sheet (dense)	-	N_2 = 0.048 CO_2 = 0.56 CH_4 = 0.022	CO_2/N_2 = 11.6 CO_2/CH_4 = 25.3 N_2/CH_4 = 2.2	(Hosseini *et al.*, 2014)
Flat sheet (dense)	30 μm	CO_2 = 2.25 CH_4 = 0.04	CO_2/CH_4 = 56	(Pulyalina *et al.*, 2018)
Flat sheet (dense)	-	CO_2 = 1.4 CH_4 = 0.03*	CO_2/CH_4 = 47	(Escorihuela *et al.*, 2018b)
Hollow fiber (asymmetric)	0.5 μm	N_2 = 0.47* CO_2 = 4.9* CH_4 = 0.55*	CO_2/N_2 = 10.43 CO_2/CH_4 = 8.82	(Favvas *et al.*, 2013)
Flat sheet (dense)	40 to 60 μm	N_2 = 0.37 CO_2 = 5.7 CH_4 = 0.87	CO_2/N_2 = 15.7 CO_2/CH_4 = 6.6	(Karkhanechi *et al.*, 2012)
Flat sheet (dense)	-	CO_2 = 0.63 CH_4 = 0.12	CO_2/CH_4 = 5	(Bakhtiari *et al.*, 2011)
Hollow fiber (asymmetric, PDMS coated)	0.85 μm	N_2 = 0.22 CO_2 = 4.68 CH_4 = 0.21	CO_2/N_2 = 20.93 CO_2/CH_4 = 21.89	(Gunawan *et al.*, 2021)
Hollow fiber (asymmetric, annealed at 300 °C)	91 nm	CO_2 = 3.77* CH_4 = 0.059*	CO_2/CH_4 = 63.9	(Visser *et al.*, 2016)
Hollow fiber (asymmetric, annealed at 310 °C)	91 nm	CO_2 = 2.64* CH_4 = 0.03*	CO_2/CH_4 = 87.8	(Visser *et al.*, 2016)

Permeability marked with * were manually calculated by multiplying the permeance with the layer thickness

Other than the literature reported permeability and selectivity results, it is also important to note that the degree of crystallinity and processing methodology of the polymer could also affecting the performance of the membrane. For example, PMP, being a semi-crystalline polymer, has piqued the interest of researchers due to its peculiar crystal properties, which is less dense than its amorphous counterpart (Lopez and Wilkes, 1992). Consequently, the loose packing of the PMP's crystalline region also contributes to higher permeability of the polymer, which may leads to reduced PMP selectivity (Markova *et al.*, 2020a). Meanwhile, degree of crystallinity can be changed depending on how thermal treatment is done (Fu *et al.*, 2016). Increased degree of crystallinity would have lower permeability and increased selectivity, which can ranged between 20 Barrer for degree of crystallinity of 1 and 110 Barrer for degree of crystallinity of 0, for CO_2 permeation at 35 °C (Yoshimizu *et al.*, 1998, Puleo *et al.*, 1988). This has also been reported by Fu *et al.* (2016) for O_2 permeability where the permeability increased a bit with increased crystallinity. Crystalline structure of PMP, ranging from type I to type V can also change depending on how the PMP is processed (Lopez and Wilkes, 1992, Tanigami *et al.*, 1985, Fu *et al.*, 2016, Mohr and Paul, 1990), which may also affects the resulting permeability. Some of the results found in literature on the effect of polymer's crystallinity on its performance is given as in Table 2.7.

Table 2.7: Comparison of crystallinity degree, permeability, and selectivity of PMP in literature

Degree of crystallinity	Permeability (Barrer)			Selectivity			Reference
	N_2	CO_2	CH_4	CO_2/N_2	N_2/CH_4	CO_2/CH_4	
-	9.87	128	-	12.97	-	-	(Yasuda and Rosengren, 1970)
-	7.4	99.1	-	13.39	-	-	(Makhloufi *et al.*, 2013)
-	-	129.1	16.1	-	-	8.02	(Nematollahi *et al.*, 2015)
-	6.7	84.6	14.9	12.63	0.45	5.68	(Nunes and Peinemann, 2006)
0.51	9.26	107.5	19.8	11.61	0.47	5.43	(Puleo *et al.*, 1988)
0.20	5.02	67.9	10.5	13.53	0.48	6.47	(Puleo *et al.*, 1988)
0.76	5.93	73.8	13.0	12.45	0.46	5.68	(Puleo *et al.*, 1988)
0.61	6.7	84.6	14.9	12.63	0.45	5.68	(Mohr and Paul, 1990)
0.51	6.5	83.0	13.1	12.77	0.50	6.34	(Mohr and Paul, 1990)
-	5.36	-	12.1	-	0.44	-	(Roux and Paul, 1992)
0.69	7.6	84.0	12.7	11.05	0.60	6.61	(Markova *et al.*, 2020b)

2.6 Current and Future Challenges

2.6.1 Upper Bound Line

Tradeoff between gas permeability and selectivity is an ongoing problem for polymeric membranes especially for gas separation. High permeable membranes tend to exhibit low selectivity, and vice versa for low permeable membranes. Statistical data on the gas permeation properties of various materials exhibit an upper bound, given by (Park *et al.*, 2017, Robeson, 1991):

$$\alpha_{i,j} = h_{i,j} P_i^{-m_{i,j}} \quad (2.19)$$

Where subscripts i and j refers to the gas pair of interest and h and m are the parameters depending on the gas pair. Under several hypotheses (Park *et al.*, 2017), it was then noted that m depends on the ratio of gas molecule diameters, $(d_{k,j}/d_{k,i})^2 - 1$, where ($d_{k,j}$ and $d_{k,i}$ are the kinetic diameters of the larger and smaller gases respectively, while the parameter h depends on the gas solubility m, and an adjustable constant related to the average distance between polymer chains and chain stiffness.

Even though the upper bound idea was originally used primarily to homogeneous polymer membranes, comparing permeability and selectivity data on upper bound plot is still a common technique to evaluate membrane material performance. The latest major trend in the upper bound, revisited in 2008 noted only minimal shifts in this limitation as compared to the original studies in 1991 despite of the abundance of work conducted on membrane gas separation. Various approaches to exceed the upper bound have been explored, including surface modification, facilitated transport, phase separated polymer blends, and mixed-matrix membranes (MMMs). Thermally rearranged polymer has recently found its way in surpassing the upper bound for CO_2/CH_4 gas pair as its unique molecular structures increases the free volume of the glassy polymers allowing enhances permeability of gas molecules without sacrificing the selectivity (Ghalei *et al.*, 2017, Park *et al.*, 2017). In addition, with the aids of powerful molecular dynamic simulation, ideal candidates with refined diffusion coefficient can be identified and prepared for gas separation application.

2.6.2 Performance versus Reliability

For some application such as in biogas upgrading, high selectivity is more important than permeability for practical industry applications (Ding, 2019). Figure

2.16 illustrates how selectivity would be advantages for process with high feed CO_2 content, and how the impact in industrial applications is affected by permeability and selectivity of a membrane. Pressure ratio, φ, which limits the permeate CO_2 concentration to a certain limit, is given by the equation (Baker, 2004):

$$\varphi = \frac{p_{0,i}}{p_{\ell,i}} \tag{2.20}$$

Where p_0 is the feed partial pressure and p_ℓ is the permeate partial pressure of gas i. Despite of what the ideal selectivity proposes, actual separation achieved would never exceed φ in the separation of mixed gas. Hence, in addition to pure gas performance, mixed gas and effects of pollutants must be evaluated to assess the full potential of polymeric membranes for practical applications. A promising novel membrane material should also have much higher membrane selectivity than the currently available commercial membranes, preferably with a relatively similar or better permeability. Finally, the novel material's ability to be produced into a membrane module on a big scale must be assessed.

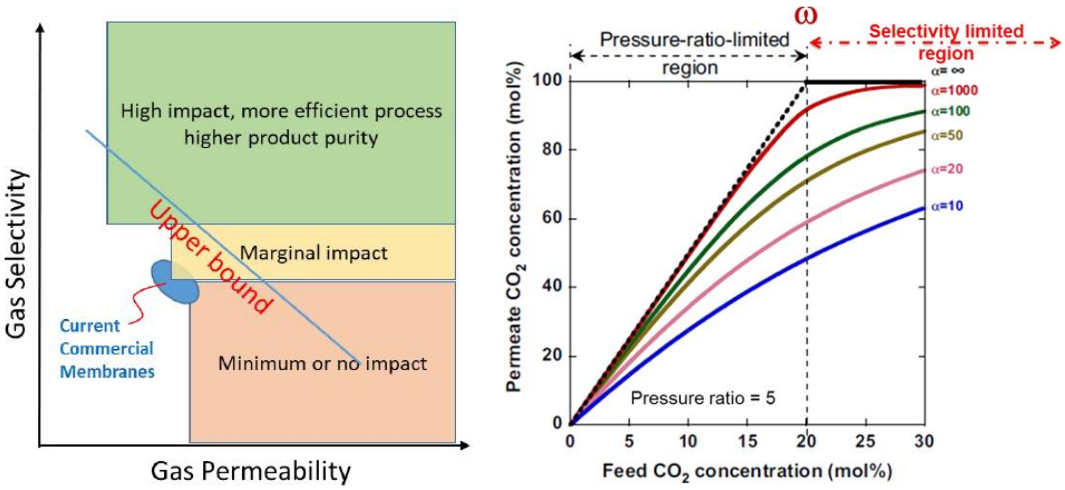

Figure 2.16: [Left] Impact of membrane performance for industrial applications. [Right] Effect of membrane selectivity on the membrane performance (Ding, 2019)

Plasticization is another common phenomenon in gas separation, caused by highly sorbing gases such as CO_2 and by condensable gases such as propane and

propylene in glassy polymers (Wessling *et al.*, 2001). The effect can be observed from (i) increase in gas permeability with feed pressure, (ii) reduction in permselectivity coefficients, and (iii) suppression of glass transition temperature (Kapantaidakis *et al.*, 2003). It was also noted that permeability would also increase in time beyond the plasticization pressure (Wessling *et al.*, 2001). Despite of positive nature in (i), this would in turn also increases the retentate permeability and hence reducing the selectivity of the membrane, making it unreliable and undesirable for long term application. Plasticization normally occurred when it reached the required pressure (hence the plasticization pressure), as the plasticization phenomena overcome the initial decrease in permeability as shown in Figure 2.17. Nevertheless, this problem is particularly important for thin film as it has been noted to be accelerated without minimum known plasticization pressure (Wessling *et al.*, 2001). Several method has been reported to suppressed plasticization such as through (i) blending with less plasticizable polymer, (ii) chemical crosslinking, and (iii) thermal treatment (Kapantaidakis *et al.*, 2003), but continuous effort has been made by the research community to minimize the effect.

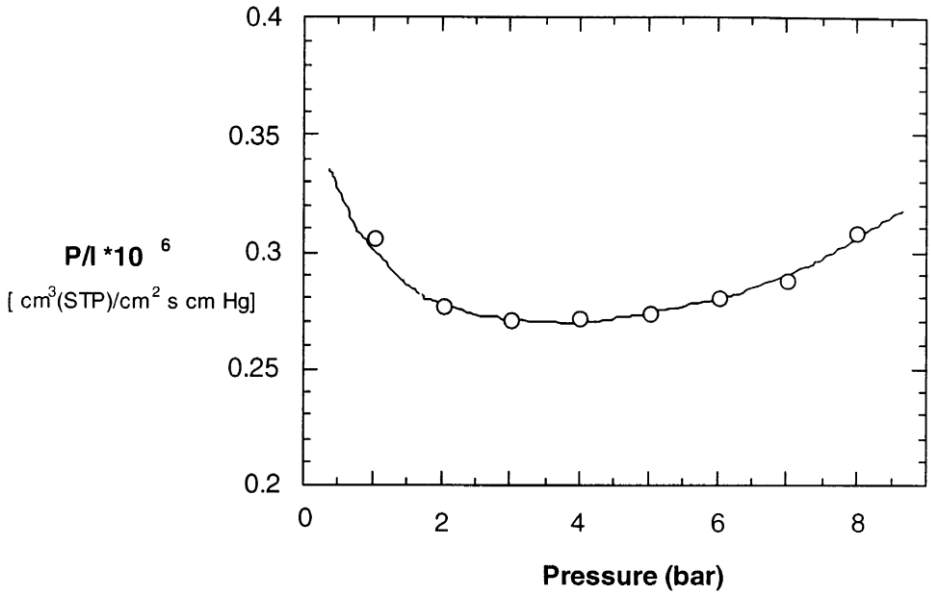

Figure 2.17: Effect of pressure on the permeance of polyimide membrane (Wessling *et al.*, 2001)

2.6.3 Defects on Thin Film

While the choice of material, especially for the selective layer would ideally determine the upper limit performance of the membrane, real world cases would usually be lower than that particularly due to defect formation. In asymmetric membrane, reducing the skin layer thickness has been noted to cause an increase in its defects, which eventually decrease the selectivity (Pinnau and Koros, 1991). The thin structure of selective layer has also been noted to exhibit defects on dry commercial RO membranes when tested for gas permeation (Louie *et al.*, 2008). In fact, it is known that gas separation membrane exhibits tighter minimum defects requirement as it is much more sensitive than RO membrane (Baker, 2004). These defects limit the efficiency of gas separation due to the availability of Knudsen diffusion pathways through the defects.

It has been proposed that subsequent coating on the thin film could plug in the defects and hence forcing the feed gas to permeate through the dense film structures (Louie *et al.*, 2008). In their work, Pebax was used to coat the formed polyamide

surface, resulting in improved gas selectivity at the cost of lower gas permeability. This method was firstly used by Henis and Tripodi (1981), which spurs the commercialization of gas separation membranes in the 1980s. Hence, it is expected for similar method to be applied on TFC membrane. On the other hand, introduction of interface gutter layer such as PDMS could also suppress defects (Salih *et al.*, 2014) on top of acting as the adhesive and preventing the penetration of aqueous or organic solution into the porous support layer (Yuan *et al.*, 2012). This methodology is thought to be more appreciable for composite structure as it reduces the number of layers needed that might reduce the composite's eventual permeability, on top of creating a better base for thin film formation. Nevertheless, this also means any selective layer defects would not be covered.

2.6.4 Nanofillers Incorporation

With the extend of nanotechnology, nano additives or nanofillers have become an interest in membrane technology to further enhance the performance of the membrane. Intrinsic polymer properties, even for highly permeable polymers rarely allows for any significant improvement in pristine membranes, as reported by Roberson's upper limit (Ghalei *et al.*, 2017). This pushes the researchers to create another blend of membranes coined as mixed matrix membrane (MMM); polymeric membrane with interblending of fillers aimed to enhance the properties of the composites. With fillers occupying up to 50% of the membrane's total weight, utilization of some expensive fillers would be detrimental to the membrane's attractivity as fillers incorporated beyond the thin dense layer would only increases the overall cost with minimal to no benefits to the separation results of the fabricated asymmetric membrane (Wong *et al.*, 2016). Hence, thin film nanocomposite (TFN) was born; where the nano additives are added selectively to the layer of interest

(normally the selective layer); reducing the cost of material through separate fabrication of the layers. Several examples of MMM found in literature is given as in Table 2.8.

Table 2.8: MMM for membrane gas separation

Selective Layer	Thickness (selective layer)	Nano Additive	Permeability (Barrer)	Selectivity	Reference
P84 PI	20 μm	ZIF-8	CO_2 = 11.02 CH_4 = 0.12	CO_2/CH_4 = 92.03	(Guo *et al.*, 2018)
P84 PI	-	Silica, SiO_2	N_2 = 0.047 CO_2 = 0.92	CO_2/N_2 = 19.57	(Shen and Lua, 2012)
P84 PI	85 μm	Silica, SiO_2	N_2 = 0.03 CO_2 = 0.86	CO_2/N_2 = 28.67	(Lua and Shen, 2013b)
P84 PI	-	$Ni_3(HCOO)_6$ crystals	CO_2 = 1.3 CH_4 = 0.019*	CO_2/CH_4 = 67	(Sheng *et al.*, 2020a)
P84 PI	30 μm	Nano-diamonds	CO_2 = 1.61 CH_4 = 0.022	CO_2/CH_4 = 75	(Pulyalina *et al.*, 2018)
P84 PI	-	BCZY	CO_2 = 1 CH_4 = 0.015*	CO_2/CH_4 = 64.6	(Escorihuela *et al.*, 2018b)
P84 PI	-	Zeolite 13X	N_2 = 0.23 CO_2 = 11.22 CH_4 = 0.45	CO_2/N_2 = 49.8 CO_2/CH_4 = 25.1	(Karkhanechi *et al.*, 2012)
P84 PI (PDMS coated)	2.24 μm	ZTC	N_2 = 0.64 CO_2 = 19.57 CH_4 = 0.55	CO_2/N_2 = 30.68 CO_2/CH_4 = 35.54	(Gunawan *et al.*, 2021)
P84 PI	40-80 μm	CNT	CO_2 = 1.08 CH_4 = 0.1	CO_2/CH_4 = 11	(Bakhtiari *et al.*, 2011)

Permeability marked with * were manually calculated by multiplying the permeance with the layer thickness

Addition of nano additives can be advantages through four pathways; (i) improving compaction resistance, (ii) increase selectivity through impermeable inorganic filler, (iii) improve selectivity through permeable inorganic filler, and (iv) facilitated transport through reactive fillers (Abetz *et al.*, 2006). For TFN aimed for surface layer nano additives, the first advantage may not be vital due to the dense

nature of the thin film, which would be able to accommodate the high pressure with minimal compaction. Although, nano additives may also be added to the substrate layer which is more prone to the compaction problem. On the other hand, addition of impermeable or permeable nano additives such as zeolites, metal organic frameworks (MOFs), inorganic and organic frameworks, and covalent organic frameworks can improve membrane's selectivity by disrupting the polymer chain packing and chemical properties, increase the free volume of the polymer matrix, and/or induce a more tortuous path for gas transport across the dense layer (Abetz *et al.*, 2006, Wong *et al.*, 2016). On the other hand, permeable fillers are also advantageous in improving the selectivity by creating an alternative route for small molecules to pass through the porous filler structures while restricting the movement of larger molecules (Abetz *et al.*, 2006). The addition of carrier nano additives that can react reversibly with the gas of interest could also improve the performance of the membrane (Abetz *et al.*, 2006). Apart from the blending of nano additive in TFN configuration, it is also possible to instead functionalize it on the selective layer's surface, as noted by Perreault *et al.* (2014). The use of float casting to create a bi-continuous thin film structure has also been noted previously in Section 2.3.1, which is noted to require the inclusion of nanosized particles to induce particle assisted wetting.

2.6.5 Particle Agglomeration and Incompatibility

Like other nano additive modification in membrane technology, agglomeration of the additives remains as a major concern for TFN. The lack of dispersion of the nano additives have been linked to the reduction in active surface area of functional additives and formation of defect holes in the thin film structures (Lau *et al.*, 2015). The lack of compatibility between the film matrix and the nano additives also caused significant negative traits such as leaching during the IP process

(Lau *et al.*, 2015, Ma *et al.*, 2017). The dissociation of the fillers is expected to deteriorate the performance of the membrane significantly with time, especially for gas application due to the formation of voids left from the leaching. Nano additives should be dispersible in the monomer solution; aqueous or organic. Nevertheless, it has also been noted that excessive removal of aqueous phase during IP process caused high amount of additive leaching. Dispersing in organic solutions nevertheless have been less attractive due to its higher difficulties (Lau *et al.*, 2015).

2.6.6 Alignment of Additive Structures

Due to the small thickness of the selective layer, incorporation of nano additives in TFN would require special care. Non-isotropic or non iso-geometric additives may induce different effects on the membrane performance when oriented differently. For example, Wong *et al.* (2015) has noted that the use of MWCNT in their work would cause protruding additives over the polyamide thin film, which have a thickness of around 0.15 µm. Nevertheless, this protruding fillers may or may not benefit the performance of the membrane, depending on the additives functionality (Kiesow *et al.*, 2013). In order to mitigate this issue, the use of sublayer such as PDMS coating before the IP has been suggested, on top of physically reducing the size of the additives below the thin film thickness (Wong *et al.*, 2015). Nevertheless, this is more of a problem or limit posed by the nanofillers itself rather than the problem of the membrane. Reducing the defect formation in the selective layer should be the main priority beforehand.

2.7 Research Gap

Despite of the composite design advantages, there are several potential difficulties or limitations that need to be considered for a good multi-layered composite membrane fabrication:

(i) Lateral diffusion at the composite layer's interface for thin selective layer. As the selective layer thickness approaches the porous substrate's surface pore size, gas flow across the selective layers start to deviate from ideality which reduces its permeance (Ghadimi *et al.*, 2018, Wijmans and Hao, 2015, Kattula *et al.*, 2015, Hao *et al.*, 2020).

(ii) Impregnation of selective layer solution into the porous substrate, which increases the gas flow resistance due to increased flow length in the low permeability dense layer regime (Henis and Tripodi, 1981, Salih *et al.*, 2014, Pixton and Paul, 2018, Cay-Durgun *et al.*, 2020).

(iii) Fabrication design and limitation such as suitability of solvent used for selective layer with the underlying support (Pixton and Paul, 2018) and coating limitation such as water-swollen hydrogel formation in the pores of the substrates during coating using interfacial polymerization technique (Baker, 2004).

These problems can be solved or minimized by proper control of the substrate surface pore, introduction of a gutter layer in between the selective and substrate layer, or both. Introduction of dense gutter layer could also help to fabricate a thinner surface selective layer as noted in several literature (Shen and Lua, 2010, Salih *et al.*, 2014). Meanwhile, the use of a single co-substrate-gutter structure may also help to elevate this problem. Improvement and better understanding on the interfacial layer-layer properties of the composite membranes are vital prior to any in-depth MMM studies, so that maximum benefit can be gained from the MMM.

CHAPTER THREE

METHODOLOGY

3.1 Materials and Chemicals

All the materials and chemicals used in this work are listed as follows in Table 3.1.

Table 3.1: List of materials and chemicals

Materials/Chemicals	Grade	Supplier	Purpose
Polyethersulfone (PES)	Ultrason E6020P	BASF	Base porous substrate polymer
N-methyl-2-pyrrolidone (NMP)	EMPLURA	Merck	Solvent for PES and P84 polyimide (PI)
Lithium chloride (LiCl)	ACS Reag., Ph Eur.	Merck	PES additive
Poly(dimethylsiloxane) (PDMS)	Hydroxy terminated, viscosity 2550-3570 cSt	Sigma	Dense gutter layer polymer
N-heptane	Anhydrous, 99%	Sigma	PDMS solvent
Tetraethyl orthosilicate (TEOS)	Reagent grade, 98%	Sigma	PDMS crosslinker
Dibutyltin dilaurate (DBD)	95%	Sigma	PDMS crosslinking catalyst
Oxyplus capillary membrane	PMP 90/200	3M Membrana	Commercial anisotropic dense skin membrane
P84 polyimide (PI)	Granular, solution grade	HP Polymer GmbH	Selective layer polymer

3.2 Overall Research Flow

The work was divided into four parts: (1) PES/PDMS composite membrane fabrication and performance, (2) commercial PMP anisotropic dense skin membrane & dense PMP membrane performance, (3) resistances-in-series (RiS) and CFD modelling near gutter-substrate membrane interface, and (4) dip coating of thin P84 PI selective layer and composite membrane performance. The overall research flowchart is summarized in Figure 3.1.

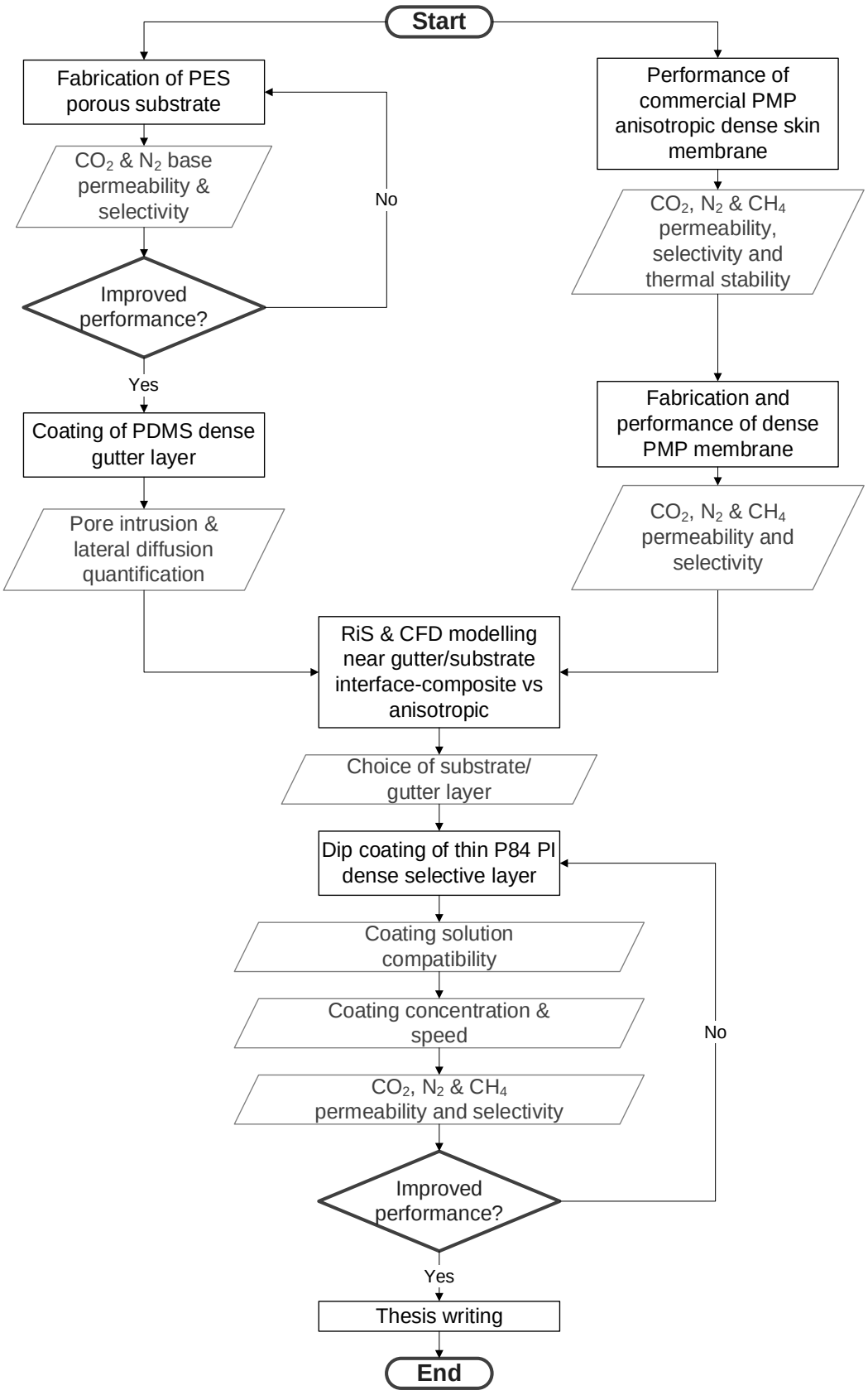

Figure 3.1: Overall research methodology flowchart

3.3 Part I – PES/PDMS Composite Membrane Fabrication and Performance

3.3.1 Preliminary Studies – PES/NMP Ratio

To study the effect of LiCl on the PES pore structure, NMP and PES's mass will be made constant throughout the subsequent study. Hence, a suitable PES/NMP ratio need to be defined. Several membranes of different PES/NMP ratio were prepared by adjusting the PES content between 4 to 12g to yield PES/NMP ratio of 0.10, 0.14, 0.19, 0.24 and 0.29, with similar concentration of LiCl at 2 wt.%. As LiCl forms complex structure with NMP (El-Kafrawy, 1982, Lee *et al.,* 2002)**,** NMP and LiCl's mass were locked at 42g and 1g respectively for all samples**.** Method of dope solution and membrane preparation is similar as in the subsequent subchapter 3.3.3. Surface and cross-sectional SEM was conducted at x1000 magnification, while image analysis of the membrane's surface was conducted using ImageJ to yield the surface pore distribution. Corresponding characterization methodology will be discussed in subchapter 3.7.

3.3.2 Preliminary Studies – Dope Solution Characteristics

3.3.2 (a) Rheological Properties

Sample of dope solutions were prepared as in the subchapter 3.3.3, following the composition in Table 3.2. Rheological properties of the dope solutions were characterized according to the steps to be discussed in subchapter 3.7.

3.3.2 (b) Cloud Point Titration

Sample of dope solutions were prepared as in the subchapter 3.3.3, following the composition in Table 3.2. Assuming a well-mixed and with similar mass of dope solutions (10g), water as nonsolvent was added in small volume increment and mixed until the solution turns cloudy. The experiment was conducted at a fixed

temperature (30°C) and repeated at least thrice. Composition of the mixture at its cloud point was calculated for all dope solutions and plotted into a ternary diagram.

3.3.3 PES Substrate Layer Fabrication

PES flakes were dried in vacuum oven under the temperature of 110 °C for about 5h. LiCl was premixed with NMP using magnetic stirrer for 1 h at 60°C, 300 RPM. All solutions were then mixed with PES flakes that have been dried earlier for 18 h at 60°C, 400 RPM. Once fully mixed, the dope solutions were placed in ultrasonicator bath for degassing purpose, for another 1 h. The composition of the dope solution is summarized in Table 3.2. PES/NMP mass ratios were maintained at 0.19 for all samples based on the results of the preliminary study in 3.3.1.

Table 3.2: Composition of PES substrate layers

Samples	**Compositions (wt. %)**		
	PES	**NMP**	**LiCl**
Pristine	16	84	0
LiCl_1%	16	83	1
LiCl_2%	16	82	2
LiCl_3%	16	81	3
LiCl_4%	15	81	4

Porous substrate layers were then fabricated using the synthesised dope solutions. Flat sheet membranes were casted through dry-wet phase inversion method, with filtered water as non-solvent. Coagulation bath temperature was maintained at room temperature, and casted with blades of 200 µm thickness. Dry phase was maintained for 45 s before the samples were being immersed in the coagulation bath for 24 h. Casting was performed at about 20 °C and relative humidity of about 60-70%. The prepared samples were then dried at room temperature for at least 5 days.

3.3.4 PDMS Dense Coating Fabrication

To test the performance of the substrate layers in composite form, thin film of PDMS layer was fabricated on top of the substrates. The PDMS solution was prepared using the formulation adapted from Salih *et al.* (2014). PDMS, DBD and TEOS were mixed in the ratio of 3:1:1 by weight in heptane, with PDMS concentration of 3 wt.%. The mixed solution was sonicated for a few minutes in an ultrasonicator bath before being used. Prior to coating, the substrate of interest was sandwiched between a custom-made holder (Figure 3.2), thoroughly cleaned using deionized water, and dried in an oven at 70 °C overnight. The prepared mould was then left to cool to room temperature. Prepared PDMS solution was then poured onto the assembled substrate based on the designated mass as noted in Table 3.3. It is then left to be dried in room temperature for 3 h. Afterwards, the samples were further dried overnight in an oven at 70 °C to fully cured the coating and remove any traces of solvent left. The composite membranes were then cut out from the mould and ready to be tested.

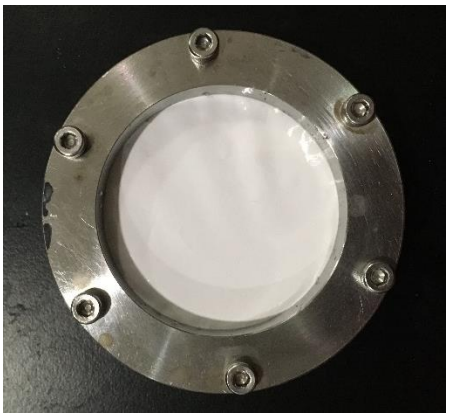

Figure 3.2: Custom holder with the assembled PES substrate layer for PDMS coating

Table 3.3: Prepared PDMS composite samples on the PES substrate and their labels

PES substrate	Mass of PDMS coating solution (g)			
	4.0	**2.0**	**1.0**	**0.5**
Pristine	P(4.0)	P(2.0)	P(1.0)	P(0.5)
LiCl_1%	×	×	×	×
LiCl_2%	L2(4.0)	L2(2.0)	L2(1.0)	L2(0.5)
LiCl_3%	×	×	×	×
LiCl_4%	L4(4.0)	L4(2.0)	L4(1.0)	L4(0.5)

For the separated layers of the PES/PDMS composite membrane, the layers of 4.0g composites were carefully removed under water (deionized) and dried in oven overnight at 70° C. Free PDMS layer was transferred onto a filter paper for analysis and performance testing. Meanwhile, for the long shelf-time study, the composites were simply stored in a closed petri dishes at room temperature with no further treatment. All samples were let to cool down slowly to room temperature (when heated) before further manipulation.

3.3.5 Performance Testing

Gas flow permeation performance of all samples were tested in dead-end mode using the setup in Figure 3.3 (retentate line was closed). Pieces of the substrate samples were cut in circle with effective diameter of 1.6 cm and fitted into a suitable module with underneath porous metal support. N_2 and CO_2 single gas was used as the model gas and introduced across the samples with feed pressure between 1 and 6 bar gauge, 1 bar increment. Permeated gas was released to atmospheric pressure. The pressure was being stabilized for a certain amount of time before the permeate flow rate was registered using bubble soap flowmeter. Time taken for the bubble to travel by 50 ml was noted. The experiment was conducted at room temperature (T ~ 25 °C) and repeated at least thrice. The gas permeance, $\mathcal{P}_i$ (in GPU) was calculated using the equation:

$$\mathcal{P}_i = \frac{12443.42\ Q_i}{A.\Delta p_i} \tag{3.1}$$

Where Q is permeate flow rate [cm^3(RTP)/s], A is the effective membrane area [cm^2], Δp is the transmembrane pressure [bar], and subscript i is the gas of interest (N_2 or CO_2). Similar methodology was repeated for the composite membranes and its derivatives but with effective diameter of 3.9 cm, feed pressure between 1 and 4 bar gauge with 1 bar increment, and bubble flowmeter travel volume of 1 ml (for N_2) and 10 ml (for CO_2). The setup was purged with the gas of interest for several minutes prior to stabilization period started. The ideal selectivity, α for CO_2/N_2 gas pair tested can then be calculated by:

$$\alpha_{CO_2/N_2} = \frac{\mathcal{P}_{CO_2}}{\mathcal{P}_{N_2}} \tag{3.2}$$

Where $\mathcal{P}_{CO_2}$ and $\mathcal{P}_{N_2}$ is the gas permeance of CO_2 and N_2 respectively. The performance tests were conducted on at least 3 different samples to obtain an average.

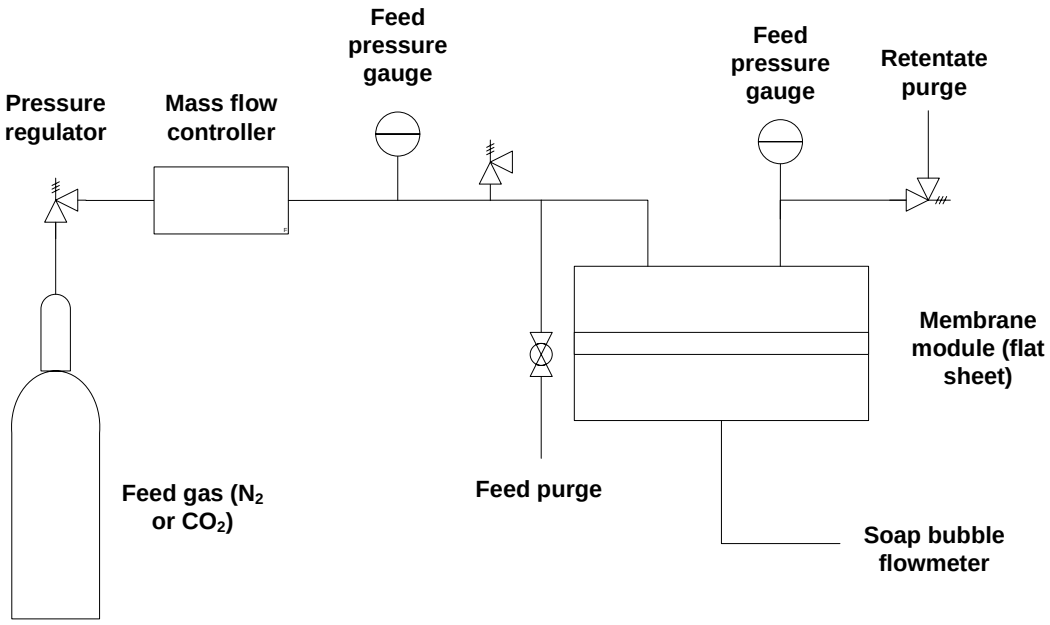

Figure 3.3: Membrane gas permeation test rig configuration (soap bubble flowmeter)

3.3.6 Pore Flow Models

For membrane gas separation through microporous membrane, assuming in its simplest form (across cylindrical capillaries), the gas molar flux, J (gmol/cm^2.s) is governed mainly through these two equations (Baker, 2004):

(i) For Knudsen flow (pore size $\lesssim$ mean free path of the gas of interest):

$$J = \frac{4r\varepsilon}{3}.\left(\frac{2RT}{\pi M}\right)^{\frac{1}{2}}.\frac{p_0 - p_\ell}{\ell.RT} \tag{3.3}$$

Where r is the pore radius, ε is the membrane's porosity, M is the molecular weight of the gas, ℓ is the pore's length, R is gas constant, T is permeation temperature, and p_0 and p_ℓ is the absolute pressures of the gas at the beginning and at the end of the pore ($z = 0$ and $z = \ell$, respectively). For asymmetric membranes, this characteristic is defined to be on the skin layer, hence r = surface pore size, ε = surface porosity, and ℓ = skin thickness. Also, for N_2, $M = 28.0134$ g/mol. On the other hand, mean free path, λ is given by:

$$\lambda = \frac{kT}{\sqrt{2}\pi d_k^2 p} \tag{3.4}$$

Where k is Boltzman constant at 1.380649 x 10^{-23} J/K, T is gas temperature, d_k is particle's kinetic diameter, and p is the gas pressure. For N_2, d_k will be at 364 pm.

(ii) For Poiseuille flow (pore size $\gg$ mean free path of the gas of interest):

$$J = \frac{r^2\varepsilon}{8\eta}.\frac{[p_0 - p_\ell][p_0 + p_\ell]}{\ell.RT} \tag{3.5}$$

Where η is the gas viscosity. For N_2, the value will be at 17.82 x 10^{-6} Pa.s at 25 °C.

Other flow mechanisms such as molecular sieving (applicable for membranes with pore size < 1 nm which is not possible for polymeric membranes), surface diffusion (noticeable when pore diameter is below 10 nm), and capillary condensation will not be considered. This should be at least true for non-condensing gas such as N_2 and for polymeric microfiltration/ultrafiltration membranes used as porous substrates. Effect of pore tortuosity is also neglected.

3.3.7 Layer and Composite Resistance

For the current work, there are several permeance, $\mathcal{P}$ values measured, and each of these permeances can be used to calculate the resistance of the layers. The gas flow resistance, R for gas i is given by:

$$R_i = \frac{\ell}{P_i A} = \frac{1}{\mathcal{P}_i A} \tag{3.6}$$

Where P is the intrinsic/effective permeability, ℓ is the thickness, A is the area, and $\mathcal{P}$ is the intrinsic/effective permeance, or P/ℓ. These layers and its relationships are:

(i) Complete PES/PDMS composite membrane: R_T is the measured resistance across the composite of area A_1. Using Equation (3.6):

$$R_{T,i} = \frac{1}{\mathcal{P}_{T,i} A_1} \tag{3.7}$$

Where $\mathcal{P}_{T,i}$ is the effective permeance of the composite. R_T is related to the other resistances by:

$$R_{T,i} = R_{1,i} + R_{2,i} + R_{3,i} \tag{3.8}$$

Where the subscript 1, 2 and 3 represents the layers of the composite membrane. Layer 1 refers to the dense coating layer, layer 2 is the substrate's skin layer with solution penetration from layer 1, and layer 3 is the highly porous/macropore region of the substrate. Resistance of the

substrate layer is assumed to be concentrated only on the porous skin, hence $R_3 = 0$. At the same time, solution penetration will not go to the macropores, thus penetration is less than ℓ_2. The relationship is visualized as represented in Figure 3.4:

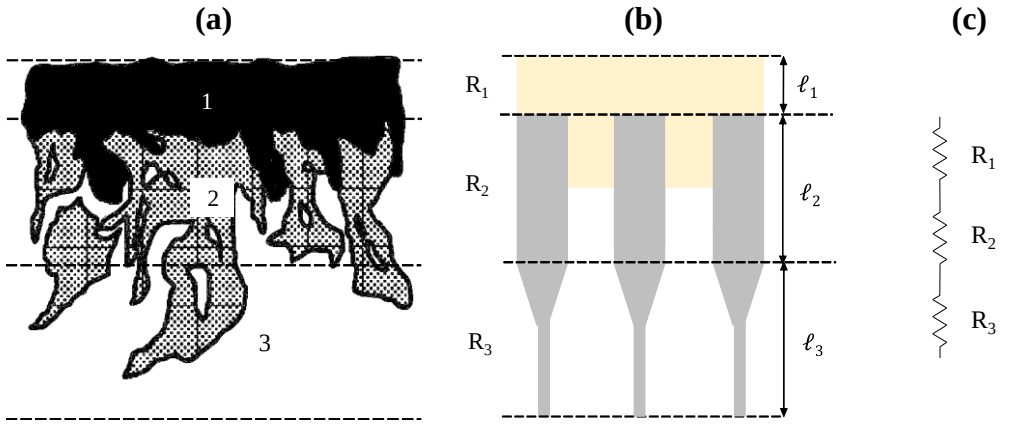

Figure 3.4: Resistances-in-series model visualization. (a) Actual composite membrane structure, figures modified from He *et al.* (1996), (b) Simplified model structure of composite membrane, (c) Resistance contribution and its relationship

From Equation (3.8), the ideal resistance of the composite membranes would be governed only by the sum of the individual layer's resistance, which is predictable as the influence of solution intrusion has already been included in the measured R_2. Any deviation or addition of resistance is caused by geometric restrictions or lateral diffusion near dense-porous interface.

(ii) Free, separated dense PDMS surface layer: dense, free-standing surface coating layer or layer 1 with area A_1 would give the ideal coating resistance, R_c and its intrinsic permeability, P_c. These are related through Equation (3.6):

$$R_{c,i} = \frac{\ell_1}{P_{c,i}A_1} = \frac{1}{\mathcal{P}_{c,i}A_1} \tag{3.9}$$

Ideally, $R_c = R_1$, as $P_c = P_1$. R_c would be the lowest resistance possible for the defect-less dense layer 1 with thickness ℓ_1 and area A_1 (intrinsic resistance of the coating layer).

(iii) Free, separated PES substrate layer: total resistance in layer 2, R_2 can be measured. This includes any solution intrusion from layer 1, if any. Using Equation (3.6):

$$R_{2,i} = \frac{\ell_2}{P_{2,i}A_1} = \frac{1}{\mathcal{P}_{2,i}A_1} \tag{3.10}$$

Where P_2 and $\mathcal{P}_2$ is the effective permeability and permeance of the whole layer 2, respectively.

(iv) Precoated PES substrate layer: permeance of the precoated PES substrate would represent the original, unclogged, and unpenetrated substrate. This would be the ideal and minimum substrate resistance, R_s. Using Equation (3.6):

$$R_{s,i} = \frac{\ell_2}{P_{s,i}A_1} = \frac{1}{\mathcal{P}_{s,i}A_1} \tag{3.11}$$

Where P_s and $\mathcal{P}_s$ is the effective permeability and permeance of the precoated substrate, respectively. Ideally, $R_2 = R_s$, achieved when no solution penetration occurred. Any discrepancy in the resistance value of R_2 and R_s would be originated from the solution intrusion of the porous substrate.

3.3.8 Sample Characterization

For the PES substrate, the samples were characterized for both surface (x3K magnification) and cross section (x1K magnification) using SEM, bulk thickness using micrometer thickness gauge, skin thickness, surface pore structures, and surface

pore distribution using image analysis, and bulk porosity using water displacement method. As for the PES/PDMS composites and its derivations, the samples were characterized for surface (x3K, x10K, x15K, and x50K magnification) and for cross section (x1K, x1.2K, x3K, and x5K magnification) using SEM, post-dried surface pore structures and coating thickness using image analysis, PES-PDMS functional group analysis using FTIR-ATR, and PES/PDMS coating-substrate interface using EDX with image analysis using ImageJ at x15K magnification. All characterization methodologies will be explained in detail in subchapter 3.7.

3.4 Part II – Dense PMP Fabrication and Asymmetric Dense Skin PMP Membrane Performance

3.4.1 Fabrication of Dense Flat Sheet PMP Membrane

Dense PMP membrane was made by dissolving 2 wt.% of PMP pellets into cyclohexane at 60 °C overnight in a closed container. Mixed solution is then sonicated at the same temperature for 30 minutes. The solution was then carefully flattened onto an 8.7 cm diameter glass petri dish using a micropipette on a weighing scale to obtain 2g or 3g of PMP solution in each petri dish. The sample was then transferred into an oven to be dried at 70 °C for 1 day. Dried samples were then peeled from the petri dish in distilled water and transferred onto a filter paper before being dried again in the oven for another day.

Similar solution mixing and fabrication steps were taken for glass casted samples, expect that 3 wt.% solution was used. Flat sheet membranes were casted as in subchapter 3.3.3, using blades of 500 µm thickness. Dry phase inversion was employed, with 1 h drying in normal oven, and additional 1 day drying in vacuum. Dried samples were then peeled from the glass as noted before.

3.4.2 Module Preparation of Asymmetric PMP Hollow Fiber Membrane

Ten fibers of about 14 cm in length was bundled and prepared into a module. The fibers were cleaned with ethanol and distilled water, potted together using Araldite® two-parts epoxy, and sealed on one end while attached into a Swagelok® connector on the other, as in Figure 3.5. Other than cleaning the fibers from any preservatives on the membrane surface, the fibers were used without prior modification or treatment.

Figure 3.5: Prepared fiber bundles

3.4.3 Performance Testing

Flat sheet dense samples were tested following the method explained previously in subchapter 3.3.5 with effective diameter of 3.9 cm, tested at room temperature, and feed pressure at 5 bar gauge using N_2, CO_2, and CH_4 gases. However, permeation flow rate was measured using constant volume method for permeate pressure up to 0.1 bar at room temperature (25 °C). The gas permeance, $\mathcal{P}_i$ (in GPU) was calculated using the equation:

$$\mathcal{P}_i = \frac{3594078.86 \left(\frac{dp}{dt}\right)_i V}{TA.\Delta p_i} \tag{3.12}$$

Where $\frac{dp}{dt}$ is permeate's rate of pressure increase [bar/s], V is downstream volume at 4 cm^3, T is permeation temperature [K], A is the effective membrane area [cm^2], Δp is the transmembrane pressure [bar], and subscript i is the gas of interest (N_2, CO_2, or CH_4). The performance tests were conducted on at least 2 different samples to obtain

an average. Linear normalized pressure over time was validated, as presented in Appendix A. The modified setup is given in Figure 3.6.

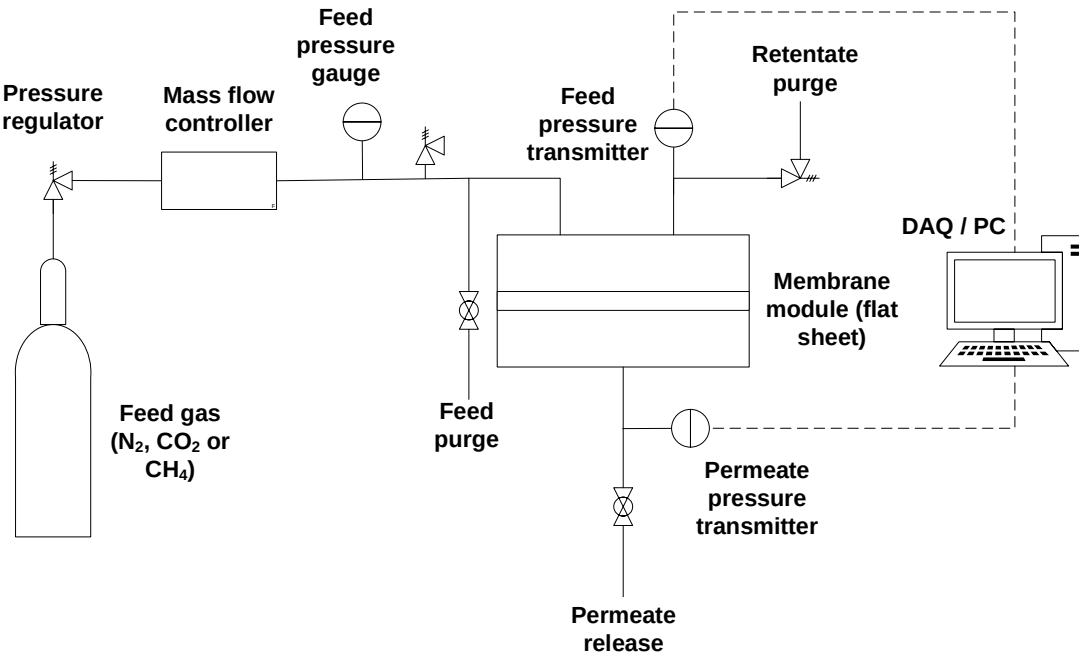

Figure 3.6: Membrane gas permeation test rig configuration (constant volume method)

For the hollow fiber (HF) performance testing, the prepared membrane module was fitted into a pilot unit (Figure 3.7) and tested with feed pressure of 1 to 5 bar gauge while the permeate at atmospheric pressure. A digital flowmeter was used to determine the flowrate of the permeating gas. The testing was conducted at 35 °C in dead end mode while the average last 10 data was taken as the final permeate flow rate when the permeate flow rate is stable for at least 1 hour. N_2, CO_2, and CH_4 gas was used for this test, and the final value was averaged between the pressure difference and 8 test samples. The gas permeance, $\mathcal{P}_i$ (in GPU) was calculated using the equation:

$$\mathcal{P}_i = \frac{222.2\ Q_i}{A.\Delta p_i} \tag{3.13}$$

Where Q is permeate flow rate [cm^3(STP)/min], A is the effective membrane area [cm^2], Δp is the transmembrane pressure [bar], and subscript i is the gas of interest (N_2, CO_2, or CH_4).

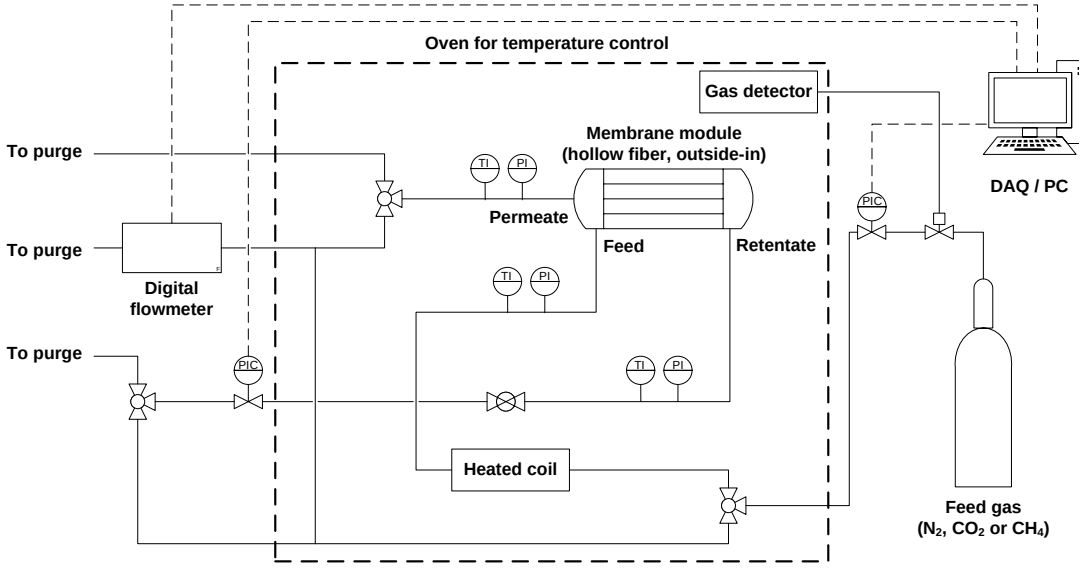

Figure 3.7: Membrane gas permeation test rig configuration (pilot unit with digital flowmeter and automated pressure control)

For the temperature stability test, membrane modules were tested at an increasing testing temperature of 25, 30, and 35 °C using N_2 gas. It is then cooled off naturally for 1 day in the setup without any gas pressure, before being repeated at the same increasing testing temperature. Similar testing methodology was used as mentioned before. The final value was averaged between 3 test samples. Meanwhile, resistance of the samples followed the method explained previously using Equation (3.7), using the permeation data of 35 °C samples.

3.4.4 Sample Characterization

The samples were characterized for surface (x3K magnification) and for cross section (x600, x2K, and x15K magnification) using FE-SEM. The dimensions of the samples were also verified using the micrographs. The functional groups of the

samples were analysed using FTIR-ATR. All characterization methodologies will be explained in detail in subchapter 3.7.

3.5 Part III – Resistances-in-Series and CFD Model Near Dense-Porous Membrane Interface

3.5.1 Permeance Efficiency and Ideal Permeance

Resistance-in-series (RiS) model visualised in Figure 3.4 relates the composite resistance with its component substrate and coating resistance through Equation (3.8). To recall:

$$R_{T,i} = R_{1,i} + R_{2,i} + R_{3,i} \tag{3.8}$$

Where 1 and 2 refers to the layers of the composite. In an ideal condition (no solution intrusion and lateral diffusion), $R_1 = R_c$ and $R_2 = R_s$. With $R_3 = 0$, the ideal total composite resistance, R_T^{ideal} is given by:

$$R_{T,i}^{ideal} = R_{c,i} + R_{s,i} \tag{3.14}$$

Using the definition of Equation (3.6) and substituting Equation (3.9) and (3.11) gives:

$$R_{T,i}^{ideal} = \frac{1}{\mathcal{P}_{T,i}^{ideal} A_1} = \frac{\ell_1}{P_{c,i} A_1} + \frac{1}{\mathcal{P}_{s,i} A_1} \tag{3.15}$$

Where ℓ_1 is the thickness of the coating layer, P_c is the intrinsic permeability of the coating layer, and $\mathcal{P}_s$ is the permeance of the substrate. $\mathcal{P}_{T,i}^{ideal}$ is thus equals to:

$$\mathcal{P}_{T,i}^{ideal} = \left(\frac{\ell_1}{P_{c,i}} + \frac{1}{\mathcal{P}_{s,i}} \right)^{-1} \tag{3.16}$$

Actual or effective permeance of the composite, $\mathcal{P}_T$ will be lower than the ideal value because of lateral diffusion and solution intrusion. The reduction in permeance is thus expressed by permeance efficiency, β which includes both effects. β can thus be determined by:

$$\beta = \frac{\mathcal{P}_{T,i}}{\mathcal{P}_{T,i}^{ideal}} \tag{3.17}$$

3.5.2 Contribution of Lateral Diffusion and Solution Intrusion

As noted in Section 3.3.7, differences in the value of the resistance of free PDMS layer (R_c) and from R_1 (calculated from total composite resistance minus the free/peeled PES substrate resistance, $R_T - R_2$) would be caused by geometric restriction or lateral diffusion near dense-porous interface. Hence, restriction factor, Ψ is introduced. R_c measurement has also been noted previously in Section 3.3.7. When $\Psi = 1$ (no lateral diffusion), $R_1 = R_c$ and when lateral diffusion effects occurred, $\Psi < 1$ and $R_1 > R_c$. By the definition of resistance in Equation (3.6):

$$R_{1,i} = \frac{\ell_1}{P_{1,i}A_1} = \frac{1}{\mathcal{P}_{1,i}A_1} \tag{3.18}$$

As $R_1 = R_c$ when no lateral diffusion occurred, $P_1 = P_c$. Similarly, as R_1 increase because of lateral diffusion, P_c is modified by $0 \leq \Psi \leq 1$ to obtain the equivalent P_1, where $P_c > P_1$. Hence, $P_1 = \Psi P_c$. Equation (3.18) is now modified into:

$$R_{1,i} = \frac{\ell_1}{\Psi P_{c,i}A_1} = \frac{1}{\Psi \mathcal{P}_{c,i}A_1}, 0 \leq \Psi \leq 1 \tag{3.19}$$

Where ΨP_c is the effective or apparent permeability of R_1 and would be lower or equal to P_c. Ψ can also be defined as:

$$\Psi = \frac{R_{c,i}}{R_{1,i}} = \frac{R_{c,i}}{R_{T,i} - R_{2,i}}, R_{1,i} \geq R_{c,i} \tag{3.20}$$

For R_2, the actual resistance value could be measured directly from the free/peeled PES substrate layer by Equation (3.10) in Section 3.3.7. When the resistance is higher than the resistance of a precoated PES substrate (R_s) as defined by Equation (3.11), any discrepancy in the resistance value of R_2 and R_s would be originated from the solution intrusion of the porous substrate. In a similar fashion as above, penetration

factor, f is thus introduced, where $f = 1$ **(**no solution penetration) at $R_2 = R_s$ and $f < 1$, $R_2 > R_s$ when penetration occurred. Using the definition of R_2 in Equation (3.10):

$$R_{2,i} = \frac{\ell_2}{P_{2,i}A_1} = \frac{1}{\mathcal{P}_{2,i}A_1} \tag{3.10}$$

When R_2 increase because of solution intrusion, P_s is modified by $0 \leq f \leq 1$ to obtain the equivalent P_2, where $P_s > P_2$. Hence, $P_2 = fP_s$. Equation (3.10) is now modified into:

$$R_{2,i} = \frac{\ell_2}{fP_{s,i}A_1} = \frac{1}{f\mathcal{P}_{s,i}A_1}, 0 \leq f \leq 1 \tag{3.21}$$

Where fP_s is the effective or apparent permeability of R_2, which is lower or equal to P_s. f can also be defined as:

$$f = \frac{R_{s,i}}{R_{2,i}}, R_{2,i} \geq R_{s,i} \tag{3.22}$$

Consequently, the total resistance of the composite (R_T) can be presented in terms of P_c and P_s. From Equation (3.8), and by substituting Equation (3.19) and (3.21):

$$\begin{aligned} R_{T,i} &= \frac{1}{\mathcal{P}_{T,i}A_1} \\ &= R_{1,i} + R_{2,i} \\ &= \frac{\ell_1}{\Psi P_{c,i}A_1} + \frac{\ell_2}{fP_{s,i}A_1} \\ &= \frac{1}{\Psi\mathcal{P}_{c,i}A_1} + \frac{1}{f\mathcal{P}_{s,i}A_1} \end{aligned} \tag{3.23}$$

Definition of R_T in Equation (3.17) is given as $\mathcal{P}_{T,i} = \beta\mathcal{P}_{T,i}^{ideal}$. Hence:

$$R_{T,i} = \frac{1}{\beta\mathcal{P}_{T,i}^{ideal}A_1} = \frac{1}{\Psi\mathcal{P}_{c,i}A_1} + \frac{1}{f\mathcal{P}_{s,i}A_1}, 0 \leq \beta \leq 1 \tag{3.24}$$

β is a factor of both Ψ and f, which can be solved by comparing with R_T^{ideal} in Equation (3.15). β can thus be solved as:

$$\beta = \frac{(\Psi f)(\mathcal{P}_s + \mathcal{P}_c)}{f\mathcal{P}_s + \Psi\mathcal{P}_c}, 0 \leq \beta \leq 1 \tag{3.25}$$

3.5.3 2D-CFD Across Composite Layers

Two-dimensional computational fluid dynamics (CFD) was conducted to study the gas flow pattern across the composite layers. Method for simulation was modified from the work of Kattula *et al.* (2015). Basically, transport across the layers were assumed to be only diffusive with the driving force represented by concentration. In a single non reacting permeant and steady state condition, the diffusion is thus governed by Fick's law and transport equation:

$$J_i = -D_i \nabla c_i \quad (3.26)$$

$$\nabla . J_i = 0 \quad (3.27)$$

Where J is the flux, D is diffusion coefficient, and c is concentration. Subscript i would represent the permeant of interest, and ∇ is del operator in 2D. This should be accepted as gas separation across dense structure is governed by solution-diffusion model, which in its rudimentary form is a Fick's diffusion (Baker, 2004). The design of the model and its key dimension is given as in Figure 3.8.

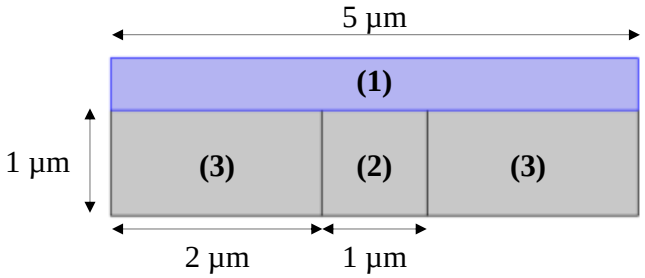

Figure 3.8: Schematics illustrating the geometry and the region separation of the 2D model

Simulation was conducted using the commercial COMSOL Multiphysics software. For this simulation, the feed concentration is taken at 10 mol/m^3, diffusion coefficient of the solid area is taken at 34 x 10^{-6} cm^2/s (diffusion coefficient of N_2 in PDMS (Merkel *et al.*, 1999)) while the porous part is taken at 0.212 cm^2/s (self-diffusion coefficient of N_2 (Winn, 1950)), both at a constant value throughout the select regions. The permeate concentration is at 1 mol/m^3, while the sides are taken as

in symmetry. Two variations in thickness of area 1 were made at 0.5 or 1.0 μm, while the penetration depth (area 2) is taken as 0 or 0.5 μm from the bottom line of coating layer. Other dimensions were fixed as in Figure 3.8. Diffusion coefficient of region 1 is always the value of PDMS while diffusion coefficient of region 3 is always following the value of N_2. Meanwhile, diffusion coefficient of region 2 is taken either to follow the value of PDMS, or to be impermeable. In this study, the interest is mainly in the flow pattern of the permeating flux across materials with different diffusivity, coating thickness, and penetration depth. Hence, this model should be sufficient to represent any permeating non-reacting solutes across the composite (or asymmetric) layers.

3.6 Part IV – Dip Coating of Thin P84 PI Selective Layer and Performance

3.6.1 Fabrication of P84 PI Dense Flat Sheet Membrane

P84 PI flakes were dried in vacuum oven under the temperature of 110 °C for about 5h. Then, 10 wt.% of P84 PI was dissolved in NMP for 18h at 60°C, 400 RPM. Once fully mixed, the solution was placed in ultrasonicator bath for degassing purpose, for another 1h. P84 PI dense membrane was simply made by pouring and flattening 0.5g of the solution in glass petri dish of 8.7 cm in diameter. The petri dish was then placed in a pre-heated oven at 60 °C and left to dry for 1 day.

3.6.2 Permeation Measurement Using Time Lag Equipment

Due to the low permeance of thick P84 PI layer, time lag equipment was employed to measure the permeance and selectivity of CO_2, N_2 and CH_4 gas across the dense P84 PI flat sheet membrane. Fabricated P84 PI flat sheet membrane was cut into a circle of 1.2 cm in diameter and placed into the module. A feed tank was then filled with about 4 bars of the gas of interest, and permeation test was conducted at 35 °C.

The feed pressure and permeate pressure increase was measured until a steady-state condition is achieved. The resulting permeability was calculated based on the following equation.

$$P_i = \frac{35940788645 \left(\frac{dp}{dt}\right)_i V\ell}{TA.\Delta p_i} \tag{3.28}$$

Where $\frac{dp}{dt}$ is permeate's rate of pressure increase [cmHg/s], V is downstream volume at 88.37 cm^3, T is permeation temperature [K], A is the effective membrane area [cm^2], Δp is the transmembrane pressure [cmHg], and subscript i is the gas of interest (N_2, CO_2, or CH_4). The setup is given in Figure 3.9. The test was repeated 5 times for each gas.

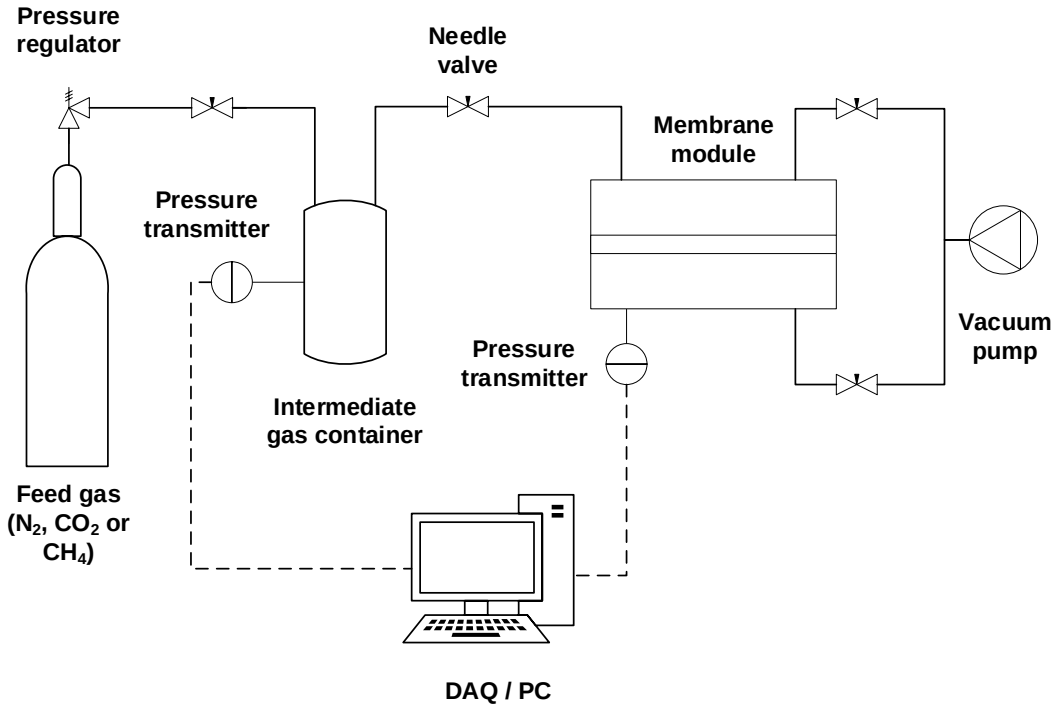

Figure 3.9: Membrane gas permeation time lag test rig

3.6.3 Permeation Measurement Using Steady State Equipment

For the effect of NMP solvent soaking and drying temperature across the PMP hollow fiber membrane, preparation method follows as discussed in 3.4.2. The

prepared hollow fibers were then directly dried in oven at 60 °C for 18h or immersed in NMP for 3h or 3 days before being dried in oven at 60 °C for 18h. It is then tested following the method discussed in 3.4.3 using the setup in Figure 3.7. The experiments were repeated twice.

For the permeation across composite PMP/P84 PI hollow fiber membrane, module preparation is as discussed in 3.4.2, while testing method follows as discussed in 3.4.3, using the setup in Figure 3.6. The flat sheet module was changed with hollow fiber module in this case. Permeation was conducted at 5 bars or 8 bars, at room temperature. The performance tests were conducted on different samples at least five times for the effect of polymer coating concentration, and at least twice for effect of coating speed, to obtain an average. Before module preparation, the PMP fibers were coated with P84 PI using the methodology to be discussed next.

3.6.4 Coating of P84 PI on Dense Skin PMP Asymmetric Hollow Fiber

P84 PI coating solution was mixed following the method in 3.6.1, but at various other concentrations (2, 6, 10 and 14 wt.%). PMP hollow fiber was firstly assembled on a custom holder and cleaned thoroughly with ethanol and deionized water to remove any contaminants. The coating was made though dip coating, at a speed of 1, 3, or 5 mm/s. Dipping was made once, with holding time of 30s in the prepared solution. The environment temperature during the coating was fixed at 60 °C, 20% humidity in a closed, controlled custom-made chamber. The equipment used for the dip coating is as presented in Figure 3.10. Coated fibers were left in the chamber for at least 1h before being transferred into an oven to be further dried at 60 °C for 17h. It is then transferred into a vacuum oven for another 1 day before it is ready to be potted into module as in Section 3.4.2.

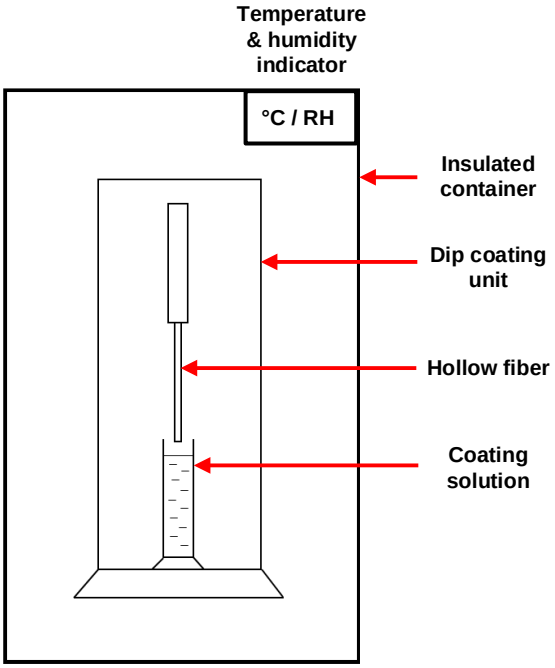

Figure 3.10: Dip coating equipment with custom made temperature-controlled chamber

3.6.5 Theoretical Thickness by Dip Coating Method

For Newtonian fluid, the wet coating thickness, h_0 is given by the Landau-Levich-Derjaguin (LLD) equation as:

$$h_0 = 1.34bCa^{2/3} \tag{3.29}$$

$$Ca = \frac{\eta U_0}{\gamma_{LV}} \tag{3.30}$$

Where b is the fiber outer radius measured at 190 µm, and Ca is the capillary number, η is liquid viscosity, U_0 is coating velocity set at 5 mm/s, and γ_{LV} is the liquid surface tension. η changed with increasing P84 PI concentration, given by the equation:

$$\eta = 1.3085e^{34.789\left(\frac{W_{polymer}}{W_{solution}}\right)} \tag{3.31}$$

Where $\frac{W_{polymer}}{W_{solution}}$ is the weight fraction of the polymer. The equation is made through best fitting of literature viscosity data as in Appendix B. Dry coating thickness, h_f is thus assumed to be:

$$h_f = h_0 \left(\frac{w_{polymer}}{w_{solution}}\right) \frac{\rho_{solution}}{\rho_{polymer}} \tag{3.32}$$

Where ρ is density of the solution or polymer.

LLD law is limited to several conditions, especially in the context of this experiment, as follows:

(i) Influence of gravity is negligible over the capillary force (Lasseuguette *et al.*, 2013). This is calculated using Bond number, Bo as:

$$Bo = \frac{\rho g b^2}{\gamma_{LV}} \tag{3.33}$$

Where ρ is the solution's density and g is the gravitational acceleration at 9.81 ms^{-2}. LLD law holds true when $Bo < 1$. This is also equals to the condition when total thickness ($b + h_0$) is much lower than the capillary length, κ^{-1} at:

$$\kappa^{-1} = (\gamma_{LV}/\rho g)^{1/2} \tag{3.34}$$

(ii) Ca < 0.64 (Quéré, 1999). Equation (3.29) is limited by the condition as $b \ll h_0$, at $Ca \ll 1$. Equation (3.29) diverged at Ca < 0.64 to White and Tallmadge correction equation:

$$h_0 = \frac{1.34 b Ca^{2/3}}{1 - 1.34 Ca^{2/3}} \tag{3.35}$$

(iii) There exist a critical minimum thickness threshold for partial wetting coating, due to the increased action of van der Waals (vdW) force between the atoms at the liquid-solid and liquid-gas interfaces in nano thin film approximately below 100 nm (Alizadeh Pahlavan *et al.*, 2018, Fondecave and Wyart, 1997, Quéré, 1999).

3.6.6 Sample Characterization

The samples were characterized for surface (x1K and x3K magnification) and for cross section (x300, x1K, and x5K magnification) using SEM. The thickness of the coating was also measured using the micrographs. The functional groups of the samples were analysed using FTIR-ATR. All characterization methodologies will be explained in detail in subchapter 3.7.

3.7 Characterization Methodology

Depending on the requirement stated in the previous subchapter, various characterizations have been conducted on the membrane layers by following these methodologies.

3.7.1 Rheology of Dope Solutions

Rheological properties of dope solutions were characterized using rheometer (Brookfield DV-III Ultra) at room temperature. The spindle speed was maintained at 15 RPM and let to stabilize for several minutes before the values were taken. The torque % was maintained between 20 to 90 % to avoid errors. The testing was repeated at least thrice.

3.7.2 Cross Sectional and Surface Morphologies

Surface image and cross-sectional image for the samples were observed under scanning electron microscope, SEM (Hitachi TM 3000 Tabletop) or FE-SEM (FEI Quanta 450 FEG). Samples were coated with thin layer of gold/palladium using sputter coater (Quorum SC7620) for 90s (less than 3K magnification) or 15s (more than 3K magnification). As for the cross-sectional morphology, clean cut of the samples was obtained by immersing the samples in liquid nitrogen for a few minutes and gently being fractured.

3.7.3 Surface Pore Image Analysis

Surface pores were characterized using the SEM micrograph images of the fabricated substrates. The images were analysed using ImageJ software by applying bandpass filter of between 3-100 pixels and suppressed horizontal stripes to obtain much clearer and sharper images. Next, the micrograph's threshold was set automatically using 'Yen' method for better consistency. The number of pores and the area of 'black' pores on the cleaned micrographs were then calculated. Size distribution of the pores were calculated by assuming each 'black spot' as a surface pore opening, finding its equivalent diameters, and then segregated into groups according to their diameter size in the increment of 0.1 µm. The process was repeated at least thrice on different images of the samples and the average statistics were taken.

3.7.4 Bulk and Surface Porosity

The bulk porosity, ε_b of the samples were determined through its dry-wet weight. The samples were immersed in deionized water for 24 h. Then, the weight of the wet samples was measured after wiping off excess water on the outer surfaces using filter paper. Afterwards, the wet samples were dried in an oven for another 24 h before it was weighted again. The bulk porosity can hence be calculated using the following equation:

$$\varepsilon_b\ (\%) = \frac{\left[\frac{W_w - W_d}{\rho_w}\right]}{\left[\frac{W_w - W_d}{\rho_w}\right] + \frac{W_d}{\rho_p}} x\ 100\ \% \tag{3.36}$$

Where ε_b is the membrane bulk porosity, W_w is the wet membrane weight (g), W_d is the dry membrane weight (g), ρ_w is the water density (1.00 g/cm^3), and ρ_p is the polymer density (1.37 g/cm^3).

On the other hand, surface porosity, ε_s was calculated based on the data gathered from the SEM micrograph image analysis. The surface porosity is given by:

$$\varepsilon_s\ (\%) = \frac{A_p}{A_t} x\ 100\ \% \tag{3.37}$$

Where A_p is the total area of the surface pores from the SEM image and A_t is the substrate's total surface projected area, which is equivalent to 60 µm x 45 µm for all cases. An average value of 3 samples were taken for both bulk and surface porosity.

3.7.5 Surface Functional Groups

Chemical bonding or functional groups present on the samples were determined using Fourier transform infrared spectroscopy attenuated total reflection, FTIR-ATR (Thermo Scientific Nicolet Nexus 670). All samples were scanned over the wavenumber range of 650 to 4000 cm^{-1} (resolution: 4 cm^{-1}) using OMNI diamond accessory. An average spectrum of 32 scans were recorded per sample characterized. 3 areas were characterized for every sample to ensure consistent results.

3.7.6 Elemental Distribution

The distribution of elements across the samples were determined using EDX (INCA, Oxford Instruments) through elemental mapping. Mapping images were superimposed using ImageJ by merging colour channels.

CHAPTER FOUR

RESULTS AND DISCUSSIONS

4.1 LiCl Modified PES Porous Membrane – Base Substrate Formation

Formation of composite layered membrane requires supporting substrate to provide the necessary mechanical strength to the overall structure. This layer should be highly porous and low in gas flow resistance with relatively good mechanical viability at high feed pressure. Hence, asymmetric porous membrane made through phase inversion should be a suitable method to fabricate the needed polymeric base substrates (Lee *et al.*, 2003b). While usually being neglected, the characteristics of the substrate can be very important as it can influence the overall membrane performance (Baker, 2004, Koros and Pinnau, 2018). Hence, for this subchapter, asymmetric PES porous substrate was fabricated in-house through dry-wet phase inversion method, with LiCl as pore former. Emphasis is given on the surface pore architecture, as the entry point of gases across the substrate and where the selective or gutter layer attached to, the importance of which has been described in Chapter Two.

4.1.1 Preliminary Study – Choice of PES/NMP Ratio

To study the effect of LiCl on the PES pore structure, PES/NMP's mass ratio had to be kept constant throughout the study. Hence, firstly a suitable PES/NMP ratio had to be defined. Figure 4.1 represents the surface and cross-sectional micrographs and the surface pore size distribution of the substrate layer made with different PES/NMP ratio between 0.10-0.29, with constant amount of LiCl at 2 wt.%. Overall results suggested that high PES/NMP ratio creates a denser surface with a more uniform finger-like void protruding vertically across the substrate. Surface micrograph at 3000x magnification for PES/NMP ratio of 0.29 showed very dispersed

and minimal distribution of surface pores. Substrates with dense surface layer would be advantageous in minimizing coating solution penetration and coating thickness during composite fabrication (Koros and Pinnau, 2018, Salih *et al.*, 2014) but would unnecessarily increase the gas flow resistance across the substrate, affecting the separation and decreasing the permeating flux (Baker, 2004**).** Hence, unless the substrate material is suitable to use as gutter layer, substrates with dense surface are not advantageous for composite formation. This also indicates the PES/NMP ratio of 0.29 is not suitable to be used as the substrate layer in this work despite of its more structured cross-sectional void. On the other hand, low PES/NMP ratio increased the surface porosity at the cost of possibly weaker mechanical strength. This is suggested from the surface micrograph for PES/NMP ratio of 0.10, which showed the sample "burn" during SEM analysis (after being focussed only for a few seconds), as compared to the other samples. While this burn does not prove a weak mechanical strength on its own, this effect suggested that the PES/NMP ratio produced a very thin polymer network that would surely be detrimental to the mechanical strength of the substrate.

Similarly, quantitative surface pore distribution analysis was only possible for PES/NMP ratio of 0.14, 0.19 and 0.24, with decreasing number of surface pores (from 2 082 ± 30 down to 663 ± 14) and slight increase in mean pore size (from 0.61 ± 0.01 µm to 0.88 ± 0.02 µm) with increasing PES/NMP ratio. The trade-off between surface pore architecture and the bulk pore design would be an important aspect for optimizing the substrate for industrial application, which would affect the resulting composite membrane performance and its mechanical strength. Nevertheless, 0.19 was chosen as the suitable ratio for further study, which should possess moderately high surface pores and mechanical strength.

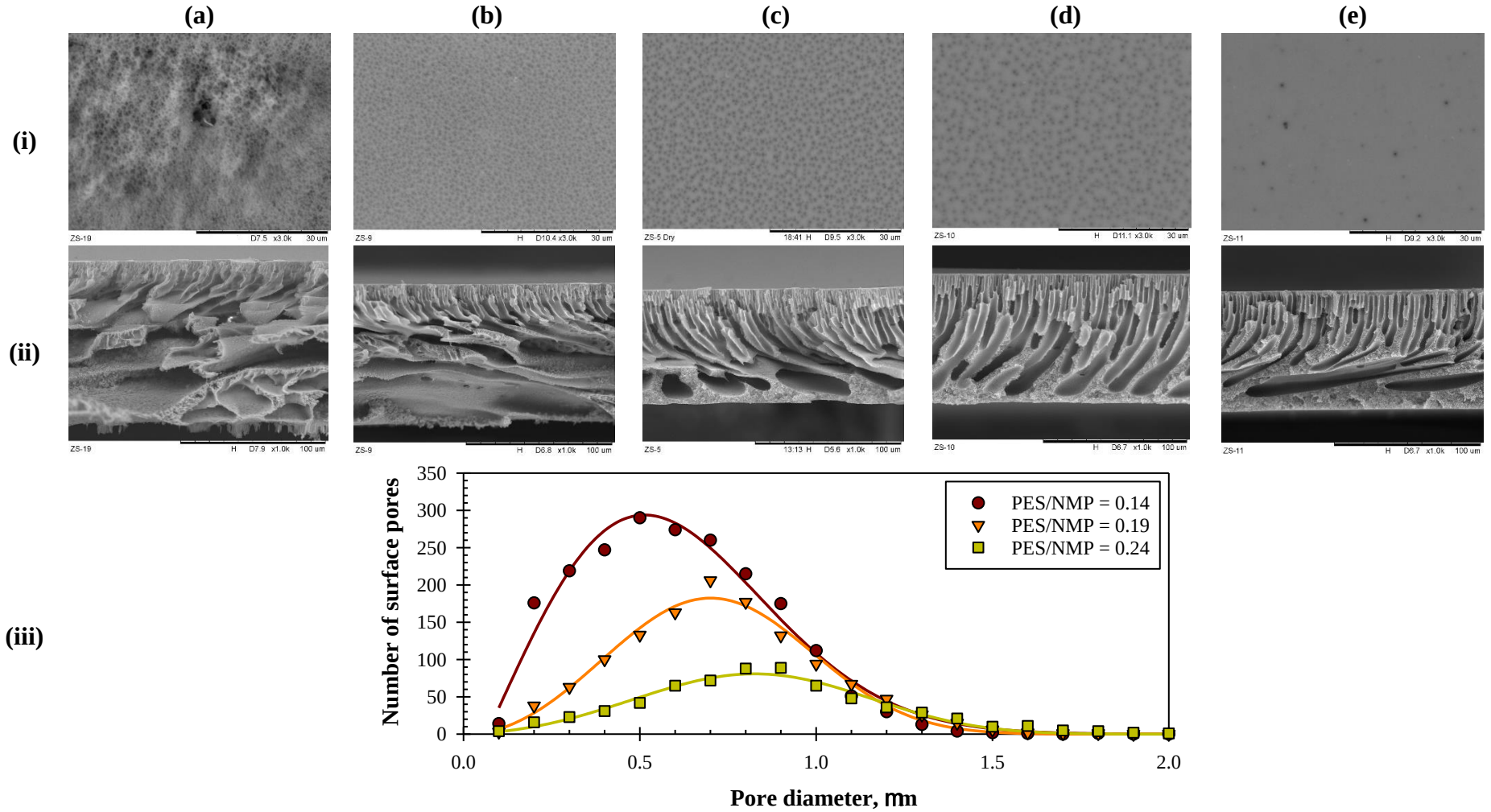

Figure 4.1: Micrograph of (i) surface at x3K magnification and (ii) cross-section at x1K magnification of the substrate layer made with different PES/NMP ratio. (a) 0.10, (b) 0.14, (c) 0.19, (d) 0.24, (e) 0.29. (iii) Surface pore size distribution of the substrate samples

4.1.2 Dope Solution Characteristics

The dope solution viscosity and cloud point of polymer-solvent-nonsolvent mixture can give an insight to the resulting substrate's morphology. In fact, understanding on the phase separation kinetics and polymer precipitation process have been known for many years as the key to produce a well-controlled membrane free of macro-voids (Henis, 2018). Hence rheological, and thermodynamic characterization of the dope polymer solutions were made. Figure 4.2 represents the evolution of dope solution's viscosity at 25 ℃ with increasing LiCl concentration. Introduction of LiCl exponentially increased the solution's viscosity by a factor of 1.4 for every 1 wt.% increase, up to 2 819 ± 63 cP for 4 wt.% LiCl solution as compared to pristine PES solution at 689 ± 8 cP. Significant increase of viscosity in LiCl containing dope solution has been known to be caused by the formation of LiCl complex with the polar, aprotic solvent such as NMP due to their strong ion-dipole interactions (El-Kafrawy, 1982, Lee *et al.*, 2002). This increment in viscosity can decrease the solvent-nonsolvent kinetics, causing slower rate of demixing during coagulation period. Possible consequences include the suppression of macro-void formation and tendency towards sponge like morphologies, due to the slower propagation of the polymer-poor nucleus to form macro-void and finger-like structures (Guillen *et al.*, 2011, Mohsenpour *et al.*, 2016). In comparison, viscosity increase by 0-4 wt.% LiCl (689 cP to 2 819 cP) is much more prominent as compared to pore formers such as PEG (MW 0.4 kDa, 0-15 wt.%, from 500 cP to 970 cP), but not as much as PVP (MW 1 300 kDa, 0-10 wt.%, from 500 cP to 12 750 cP). Nevertheless, the high viscosity increase by PVP is only seen for high MW polymer (Sadrzadeh and Bhattacharjee, 2013). Skin layer was also noted to be thicken with increasing viscosity.

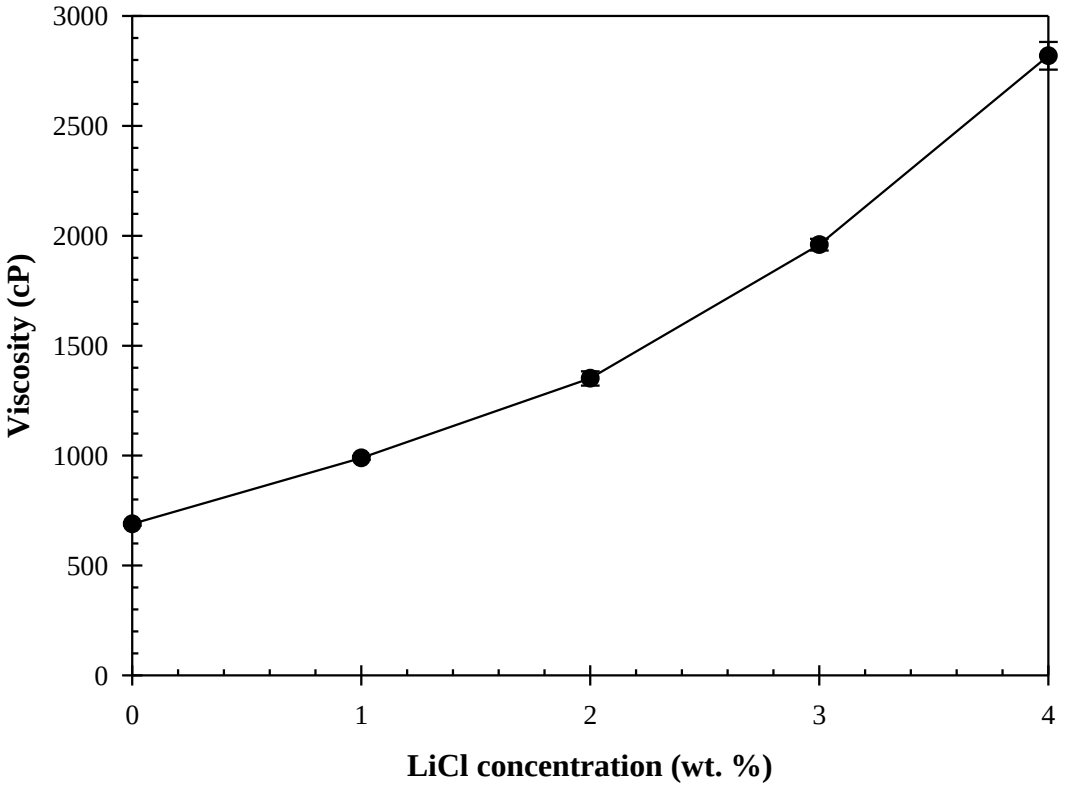

Figure 4.2: Effect on dope solution's viscosity at 25 ℃ with increasing LiCl concentration

On the other hand, Figure 4.3 represents the ternary diagram of the PES-NMP/LiCl-water system and the impact of increasing LiCl concentration on the solution's stability point, made through cloud point titration of the polymer-solvent-nonsolvent system. As water as non-solvent is slowly added into the homogeneous casting solution consist of fixed PES/NMP ratio and weight and variable LiCl concentration, the amount of water needed before the solution demixed (becomes cloudy) can be determined. To simplify the quaternary solution system into a ternary diagram, LiCl and NMP is represented together as they are premixed during solution preparation. In this way, NMP-LiCl becomes a pseudo-solvent of the pseudo-ternary system. Inclusion of LiCl into the dope solution shifted the solution's stability point (point on binodal line) towards the PES-NMP/LiCl axis. For every 1 wt.% LiCl, the stability point moved to the left axis by 5 to 10%. Hence, with increasing LiCl

concentration, lower volume of nonsolvent will be needed for polymer precipitation, and the instability region of the system widens. This phenomenon is common for many pore forming additives in literature (Sadrzadeh and Bhattacharjee, 2013, Kim and Lee, 1998, Mohsenpour *et al.*, 2016, Shi *et al.*, 2008), but the degree of its effect differs between ternary systems.

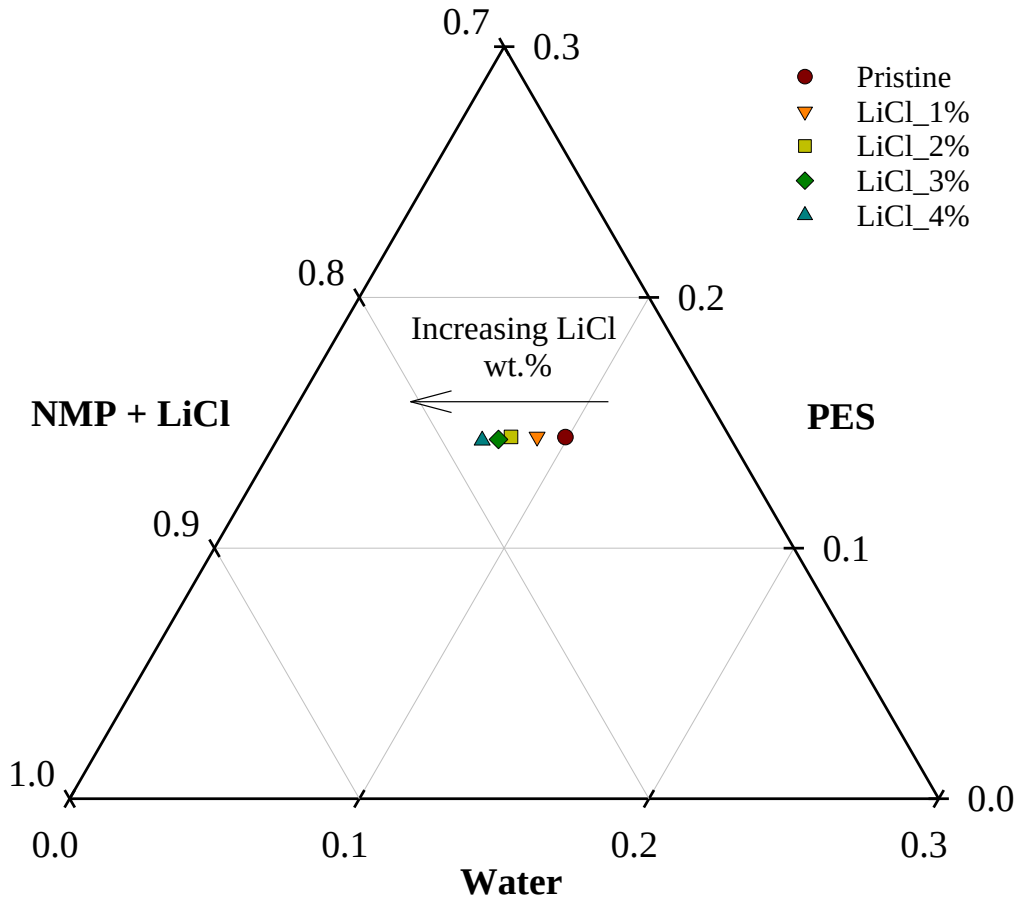

Figure 4.3: Effect on the solution's stability point with increasing LiCl concentration

In comparison, LiCl showed comparable shift of solution's stability point from the pristine solution (between 9.96% for 1 wt.% up to 28.41% for 4 wt.% LiCl), as compared to other pore formers in literature such as PEG at 10.89-49.68% (MW 0.4 kDa, 5-15 wt.%) and high MW PVP at 25.74-38.34% (MW 1 300 kDa, 5-10 wt.%) for the same PES/NMP/water system (Sadrzadeh and Bhattacharjee, 2013), although the miscibility gap (percentage of water at stability point for a fixed solvent/polymer percentage) for pristine dope solution differs a bit at 0.1111 (compared to this work at

0.0991). As solvent-nonsolvent exchange occurred during membrane coagulation process, composition of the solution changes. Nucleation of polymer-rich and polymer-poor region occurred throughout the solution as the composition moves into the instability region, creating the polymer matrix and the needed porosity. Nevertheless, polymer-poor phase can propagate deeper into the membrane thickness if the demixing kinetics are not properly controlled, creating finger like voids or worse, large macro-void (Young and Chen, 1995, Guillen *et al.*, 2013) which can affect the resulting substrates mechanical strength. This is the opposite of the effect seen by the increase of kinetic hindering noted previously.

It is important to note that the resulting effect of thermodynamics and solvent exchange kinetics are not independent but intertwine between the parameters. Competing effect of these parameters create a trade-off in which thermodynamic instability would enhance demixing while reducing the solvent-nonsolvent kinetics renders the demixing rate to slow down (Lee *et al.*, 2003b). Consequently, the resulting membrane morphology can be highly different depending on the tug-of-war between these two parameters. For this study, the main interest is on the control of surface pore architecture for composite membrane fabrication rather than optimizing the substrate's structure. LiCl have been shown to possess a comparable thermodynamic instability effect as high MW PVP but with lower resulting viscosity, at similar concentration. High MW (1 300 kDa) PVP was noted to form better sponge-like structure at 10 wt% but also significantly increased skin layer thickness presumably due to the increased viscosity (Sadrzadeh and Bhattacharjee, 2013). Hence, the use of PES/NMP/LiCl for this work would be interesting due to the lack of literature and as lower viscosity at the same concentration compared to high MW PVP may have a better skin/surface architecture due to lower solvent-nonsolvent exchange kinetics (Guillen *et al.*, 2013).

4.1.3 Surface and Bulk Structure Analysis

Figure 4.4 represents the surface and cross-sectional micrograph of the substrate samples at x3000 and x1000 magnification respectively, with inserts of the analysed surface pore structures superimposed on the surface micrograph. Significant differences can be seen between the samples with increasing concentration of LiCl. Surface pore size seems to be increased with increasing LiCl concentration, but at the same time significant reduction in surface pore density can be noted visually. Nevertheless, the cross-sectional micrograph suggested a reduction in macro-void size with LiCl content, with longer finger-like pore structure extruding from the surface. This suggested better mechanical strength of the substrate, but at the probable cost of higher substrate's gas flow resistance (Guillen *et al.*, 2011). Similar trend could be seen in the literature for LiCl incorporated PVDF hollow fiber membranes where the morphology transformed from finger-like to sponge-like with the increase of LiCl content (Mansourizadeh and Ismail, 2010), although the use of different base polymer may have different interactions between the mixture's components. Similarly, the work by Zheng *et al.* (2016) on PVDF/CTFE/PEG/LiCl/DMAc membranes have noted the increase in surface pore interconnectivity and cross-sectional void size reduction with increasing LiCl content. This is however arguable for comparison as the presence of PEG may contribute to the differences in the trend. Another work by Lee *et al.* (2002) for poly(amic acid)/LiCl/NMP membrane also reported the evolution of the samples' cross-section micrograph from finger-like to sponge-like with the increase in LiCl concentration. In all these literatures, LiCl content is within 0-5 wt.%, but using different base polymer. Nevertheless, finger-like void and macro-void was unable to be completely removed in this work.

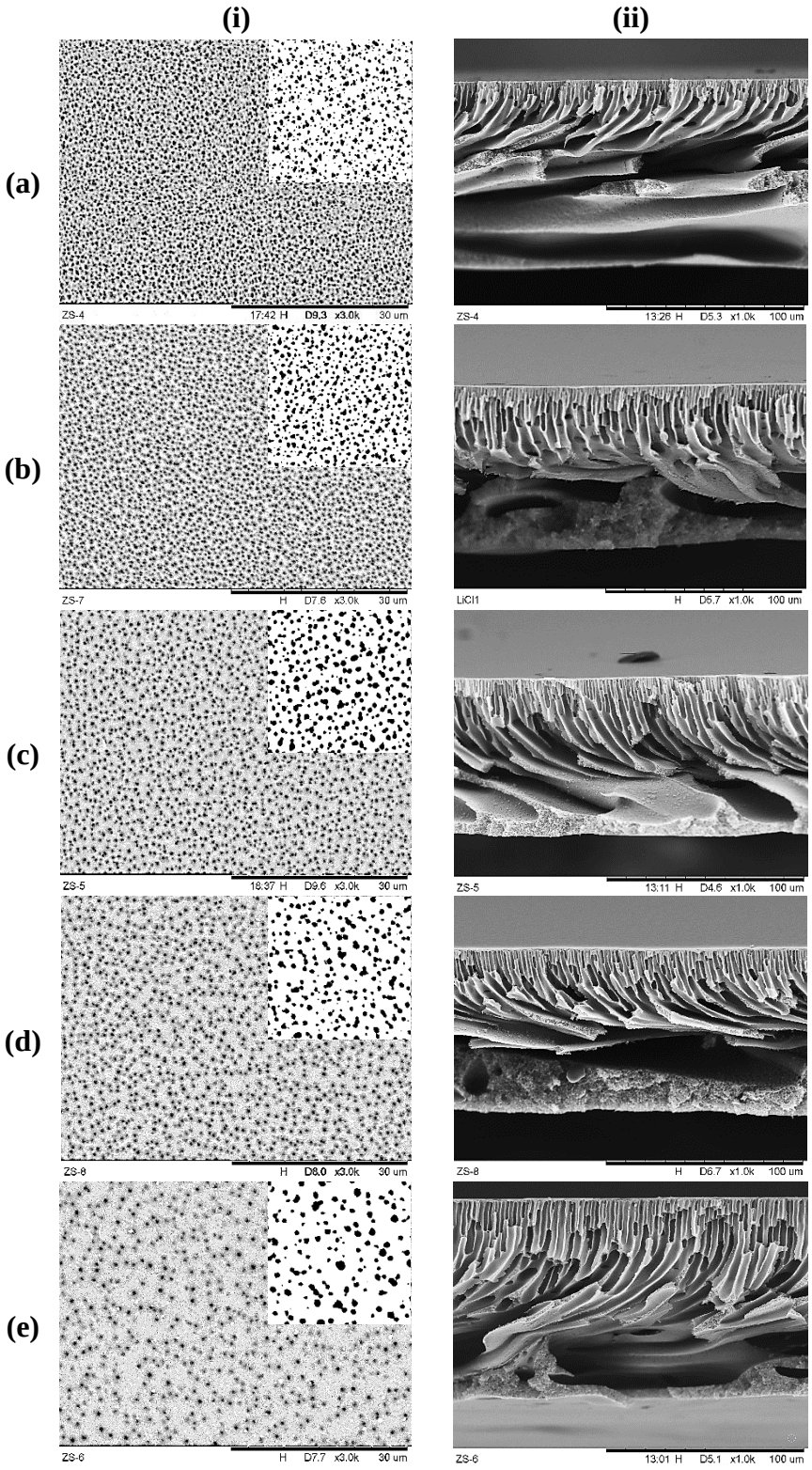

Figure 4.4: Substrate layer surface and cross-sectional micrograph for all samples. (i) surface at x3K magnification and inserts of analysed micrographs at similar magnification, (ii) cross section at x1K magnification. (a) Pristine, (b) LiCl_1%, (c) LiCl_2%, (d) LiCl_3%, (e) LiCl_4%

Based on these observations, the visual morphology for the cross section corresponds well with the hypothesis proposed earlier by the characteristics of the dope solution. Increase in viscosity by higher LiCl wt. % creates a thicker and denser skin, slowing down the precipitation of underneath layer (Mansourizadeh and Ismail, 2010). Nevertheless, there has been a lack of literature data on the surface pore distribution and architecture by the influence of pore formers, which is important in the context of this thesis. The kinetic hindrance and pore forming properties of LiCl would then have a competing effect between surface pore size/porosity improvements and denser skin structure. Its influence on the surface pore sizes and surface pore density will be discussed later in Table 4.2.

SEM micrograph presented above suggest a minimal difference on the bulk substrate thickness, but increased skin layer thickness with increasing LiCl content. Table 4.1 represents the measured substrate thickness using a micrometer screw gauge at over 5 different points and the skin layer thickness measured from the SEM micrograph at x5000 magnification. Thickness variation was noted to range between 78-100 µm between lower and upper limit (22 µm differences). Final membrane thickness is to be determined by the influence of kinetics and thermodynamics during phase inversion. Lower thickness are to be expected when kinetic effects outweigh the thermodynamic instability of the system (Zhou *et al.*, 2010). In this condition, diffusion of nonsolvent into the coagulating membranes would be minimize, resulting in lower final thickness when LiCl content increases. This is indeed the case for this work where high kinetic resistance LiCl samples exhibit lower thickness, except for LiCl_1%. Nevertheless, with minimal impact of bulk thickness in few micrometer ranges for porous structures, these fluctuations in overall thickness should not significantly influence the resulting gas permeance as compared

to the other parameters of the fabricated substrates. Interestingly, skin thickness was noted to increase exponentially with LiCl concentration at a similar rate to the viscosity increase, which is by a factor of 1.4 for every 1 wt.% increase.

Table 4.1: Substrate layer bulk and skin thickness with increasing LiCl concentration

Substrate samples	Bulk thickness (μm)	Skin thickness (μm)
Pristine	90 ± 2	0.21 ± 0.02
LiCl_1%	98 ± 2	0.28 ± 0.02
LiCl_2%	82 ± 4	0.45 ± 0.02
LiCl_3%	86 ± 1	0.63 ± 0.05
LiCl_4%	89 ± 7	1.02 ± 0.07

Quantitative analysis on the mean surface pore diameter, surface pore density, bulk porosity, and surface porosity is presented in Table 4.2. Mean surface pore diameter was noted to increase in LiCl incorporated samples with an increase of 98 % for the 4 wt.% sample as compared to the pristine membrane. The quantitative values are in line with the visuals from Figure 4.4, while validation of the image processing technique used is presented in Appendix C, suggesting good measurement. Nevertheless, this is contrary to literature where mean pore size was noted to decrease and far smaller than the one in this work with increasing LiCl content (Mansourizadeh and Ismail, 2010, Idris *et al.*, 2010, Ahmed *et al.*, 2010), although in all cases the mean pore size was determined from solute transport data and gas permeation test. These two methodologies from the literature represent the bulk mean pore size along the thickness, which can be influenced by the gas flow chokepoint inside the substrate, if any. While this chokepoint will affect the substrate's gas permeation performance, it will not be contributing to the pore intrusion and lateral diffusion unless it is located at the surface. On the other hand, bulk porosity was noted to be increased by 1.99 % for 4 wt.% LiCl sample as compared to the pristine membrane. Again, the results are in contrary to the reported literature for PVDF-LiCl sample where the bulk porosity

was noted to be lower than the pristine membrane (Mansourizadeh and Ismail, 2010). Nevertheless, it is possible for the bulk porosity to increase upon increasing LiCl concentration despite the reduction in micro-void size due to the formation of fine spongy pores (Lee *et al.*, 2002), which might be the case for this work. The use of PVDF which are interacting with the LiCl might also contribute to the different influence. Interestingly, surface pore density was consistently reduced with higher LiCl concentration due to larger surface pores and increased pore distance, as qualitatively noted from the SEM micrograph.

Table 4.2: Average surface pore diameter, surface pore density, bulk porosity, and surface porosity of the substrate samples

Substrate samples	**Mean surface pore diameter (nm)**	**Surface pore density (x1000 mm^{-2})**	**Bulk porosity (%)**	**Surface porosity (%)**
Pristine	456 ± 1	972 ± 4	78.6 ± 0.2	15.9 ± 0.1
LiCl_1%	550 ± 10	815 ± 7	78.9 ± 0.2	19.4 ± 0.6
LiCl_2%	733 ± 14	472 ± 13	79.6 ± 0.2	19.9 ± 0.2
LiCl_3%	742 ± 23	363 ± 15	79.6 ± 0.1	15.6 ± 0.3
LiCl_4%	901 ± 13	200 ± 6	80.6 ± 0.4	12.8 ± 0.1

With changes in bulk porosity at 0.3-1.0 % for every 1 wt. % increase in LiCl concentration, similar changes in surface porosity are noted to be much higher at 0.5-4.3 %. This is due to the sample's anisotropic design, with significant changes noted from pristine to 2 wt.% LiCl at 4 % increase for surface porosity but only 1 wt.% increase in bulk porosity. Meanwhile, the increase of surface porosity is maximum at 2 wt.% and starts to decrease beyond 3 wt.% LiCl. Thermodynamic instability is known to influence more on increasing bulk porosity while demixing kinetics would influence more on surface pore size and macro-void density. This is also supported by the work of Sadrzadeh and Bhattacharjee (2013) where bulk porosity increased significantly as thermodynamic influence increases. As LiCl-NMP solution is prone to high viscosity increase with increasing LiCl concentration, it is suggested that the

pore forming ability of LiCl (due to thermodynamic instability) starts to be overwhelmed by its kinetic hindrance (due to higher viscosity) at around 2-3 wt. % LiCl. This trend is also in line with the literature for PVDF/NMP/LiCl dope solution (Mansourizadeh and Ismail, 2010).

To further elucidate the surface characteristics of the substrate, surface pore size distribution was plotted. Figure 4.5 represents the surface pore size distribution for the substrate samples. The distribution fits well into Weibull distribution with R^2 between 0.94-0.99, as noted by the fitted line's graph. Mode of the distribution is noted to be in between 0.3-0.9 µm with 90 % of the distribution is below the pore diameter of 0.8 µm (for pristine) and 1.2 µm (for LiCl_4%), placing the substrates pore at the interface between ultrafiltration and microfiltration regime (Baker, 2004).

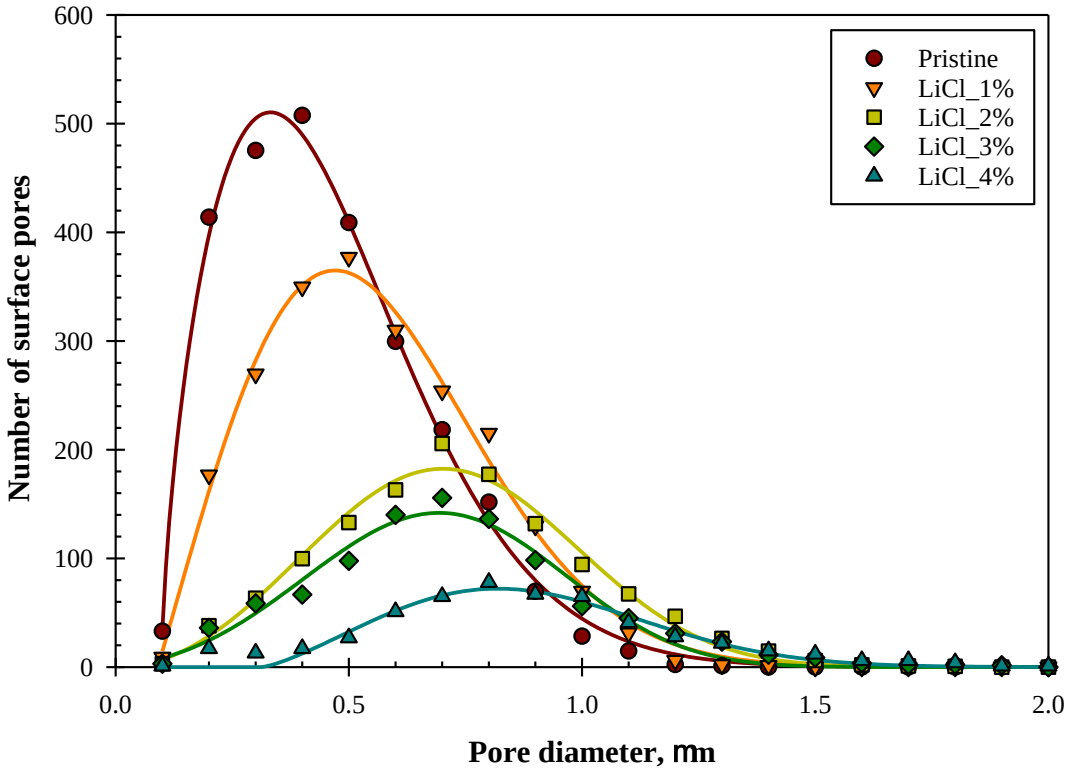

Figure 4.5: Number of surface pores and pore size distribution of the membrane substrates over the substrate's surface projected area (60 µm x 45 µm)

While the mode value of the distribution (surface pore diameter) significantly increased with LiCl concentration, it came with reduced frequency (lower number of surface pores). The frequency of the modal pore diameter was decreasing rapidly from 508 for pristine samples down to only 78 for LiCl_4% over the same surface area. This finding supports the hypothesis earlier where increased pore size came at the cost of reduced pore density, which could be important for the design of composite thin film membrane. On the other hand, pore distribution tends to become symmetrical at higher LiCl content, which suggested that the skewed distribution at lower LiCl concentration might be due to limited and poor pore detection by the image analysis software for pores below 0.1 µm.

The use of NMP as solvent has been suggested to create the highest number of surface pores among the common solvents for PES polymer (Ghadimi *et al.*, 2018). This shows that the decrease in surface pore counts to be contributed only by the pore formers. It was also noted from literature that permeance efficiency decreased with higher PES concentration due to reduced surface pore count and increase in average pore size, a characteristic like in this work. As increased PES concentration will also affect its viscosity, it is hypothesized that pore formers will also produce the same results, especially for highly viscous solutions. Nevertheless, the use of pore formers also affects the thermodynamics of the phase inversion so the use of other pore formers may show significantly different results.

Careful judgement needs to be done in interpreting the results in this subchapter. SEM micrographs requires metal coating to increase conductivity and are subjected to electron beam which may alter the surface pore structures (Khulbe *et al.*, 2008). On the other hand, as SEM in this work was conducted at 15kV, it would be high enough to be able to penetrate beyond the immediate substrate surface and

registered pores located few nanometers underneath it (Zhou *et al.*, 2007). Hence this will exaggerate the surface pore size. Should the choke point really be at the apparent surface and be as small as in literature, this would mean that there is a steep change with pore depth between immediate surface pores and the underlying pores. This information can be important as continuously increasing pore circumference into the depth of the substrate can give an important insight towards the coating solution's penetration, which can be beneficial (or not) towards the composite formation. Image analysis using SEM also holds significant uncertainty because of the need to select the image threshold for image analysis (Hao *et al.*, 2020). Nevertheless, similar protocol used for all samples would permit direct comparison between the substrate samples.

4.1.4 Gas Flow Permeation

Figure 4.6 represents the N_2 gas flux for pristine and LiCl modified samples with increasing pressure. All data points were taken after a pressure holding time of at least 5 minutes. The substrates were able to withstand up to a maximum of 6 bars of pressure without bursting, except for pristine membrane due to its high gas flux. Nevertheless, subsequent test on an alternative set-up verifies that all substrates were able to withstand up to 10 bars of transmembrane pressure even for the pristine sample (Appendix D), although the pressure holding time for this equipment was less than 1 minute. Almost linear increment in gas flux over 6 bar transmembrane pressure suggested that no significant compaction nor pore collapse occurred during testing period.

Despite of the increase in surface pore size and surface porosity at 1 and 2 wt.% LiCl as noted in the previous section, surprisingly the gas flux was reduced. Reduction was noted from the slope of the linear fitting to be decreasing in exponential where the flux ratio between the samples to be 0.64, 0.50, 0.34, and 0.66 for

pristine/LiCl_1%, LiCl_1%/LiCl_2%, LiCl_2%/LiCl_3%, and LiCl_3%/LiCl_4% respectively. This trend suggested that increased LiCl concentration up to 2 wt. % reduced the substrate's gas flux at a diminishing rate before the reduction rate starts to increase again. It is unclear whether this trend has to do with the increase in surface porosity, but it might partially explain the phenomena.

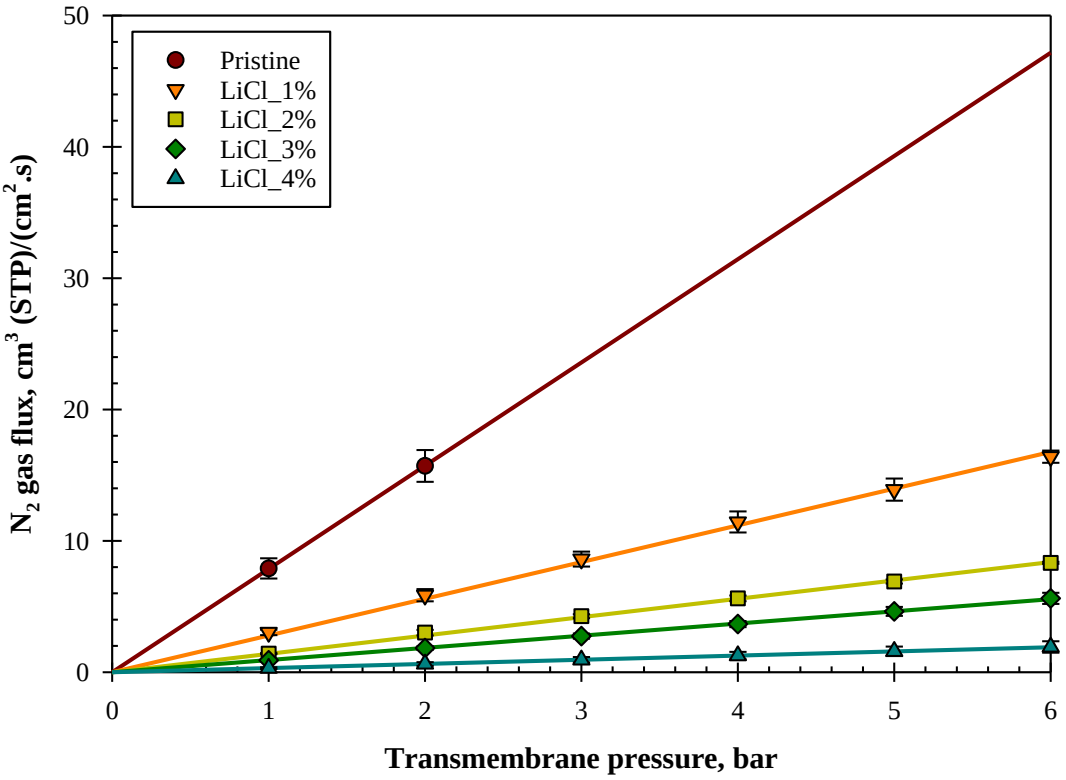

Figure 4.6: Membrane substrate layer's N_2 gas flux over different transmembrane pressures

So far, literature data has suggested otherwise. In contrast, highest gas permeance was noted when high LiCl content was incorporated for sample of PAA based membrane, due to the formation of fine porous sponge-like structure by LiCl (Lee *et al.*, 2002). Nevertheless, the extend of macro-void reduction is far less in this work as compared to the mentioned work, where the macro-void was able to be removed completely at 5 wt.% of LiCl. Interestingly the incorporation of LiCl in PPTA/PVDF was also shown to possess the same pore evolution trend (long finger-

like pores with increased porosity and pore diameter) as in this work, but with increased water flux and declined PEG rejection (Li *et al.*, 2014). Increase in water flux was also noted in several other literatures (Idris *et al.*, 2010, Ahmed *et al.*, 2010). It is highly likely that the use of LiCl creates a more hydrophilic structures which would help to channel the water feed. In this case, it would help the membrane in water-based application, but not as in gas separation. Due to this reason, it is hard to quantify and compare the results with literature. The best comparison found so far is by the work of Mansourizadeh and Ismail (2010) where the N_2 permeance was decreased with LiCl content. However, mean pore size was noted to also decrease in this case, although it was calculated using the gas permeation test.

As mentioned previously, sensitivity of the substrate's gas flow resistance was expected to be minimal. In the range of ± 22 μm from the pristine membrane thickness, negligible thickness effect can be concluded from flux reduction this high. Insignificant differences in bulk porosity also suggested that it should not be the reason for this flux reduction. One explanation is the skewed pore size distribution at lower LiCl concentration as mentioned in the previous section. Sub 0.1 μm surface pores might significantly be abundant for pristine sample, which would contribute to the substrate's flux results. Should this be true, it would reduce the value of average surface pore size and increase the surface porosity presented in Table 4.2 especially for pristine substrate. Another possible explanation is the formation of chokepoint in the substrate as mentioned earlier. However, literature has so far suggested that the skin layer is the one responsible for separation performance (Shih *et al.*, 1990, Baker, 2004), which means the smallest pores should be located on the surface and already be measured through SEM. An exception would be if the samples exhibit significantly different immediate pore sizes. Some literatures have also noted that pore collapse

could contribute to the decline in permeability as the collapsed porous structures became dense polymer film (Pinnau and Freeman, 1999, Khare *et al.*, 2007, Gao and Chung, 2019). In this work particularly, the substrates were air-dried directly after the end of coagulation process, which increases the possibility for pore collapse. Notwithstanding the concern, no sign of pore collapse can be seen for all samples based on the SEM micrograph in Figure 4.4, while the gas flux for pristine membrane was already higher than the others even at low pressure difference, suggesting that pore collapse is minimal, occurred only at a higher pressure, or not happening at all in the period of this experiment.

Before further conclusion is made, the permeance of the substrate layer was calculated. Performance of the substrate layer can sometimes significantly impact the overall composite performance. Hence the influence of the layer on the gas permeation performance should be elucidated. Figure 4.7 represents the CO_2/N_2 permeance of the substrates and their ideal selectivity. Indeed, similar trend was noted for CO_2 where the gas flux (hence the permeance) decreased with LiCl content. However, this confirmed that the substrate is governed mainly by the Knudsen regime, with average selectivity of around 0.8 for CO_2/N_2, which is in line with Knudsen flow selectivity for the gas pairs. All permeances were in two standard deviations from the sample average. Large permeance range can be noted for all samples (100 000 GPU difference between pristine and LiCl_4% substrate for N_2). The decrease in permeance between the different samples from pristine to 4 wt.% LiCl might be due to the increasing thickness of the skin (Table 4.1) and decreasing surface porosity (Table 4.2) which is related to the porosity of the skin.

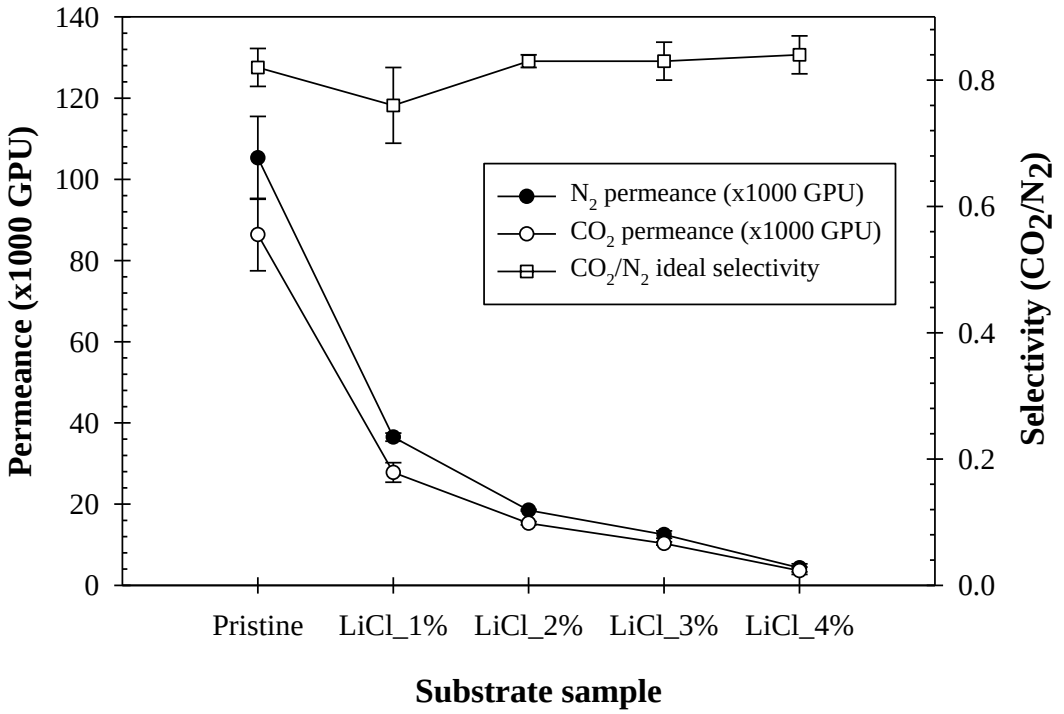

All permeance and selectivity was taken at 6 bars transmembrane pressure value except for pristine due to equipment limitation (1 bar)

Figure 4.7: CO_2/N_2 permeances and the ideal selectivity of the substrate samples

Substrate samples of at least 2 900 GPU in this work should possess permeance high enough to be use as substrate layer. Literature has recommended that substrate to be at least 5-10 times more permeable than the selective layer to ensure minimal flow resistance by the substrate (Kattula *et al.*, 2015, Baker, 2004). Hence, maximum selective layer intrinsic permeance suitable for fabrication of composite membrane with this substrate should be around 290 GPU which is achievable for a lot of known materials. Any resistance contribution by the substrate layer can also be said to be originated by Knudsen flow, which will be further discussed next.

4.1.5 Performance Comparison with Pore Flow Models

Table 4.3 represents the comparison between the permeance of experimental results with Knudsen and Poiseuille flow, calculated using the pore dimensions and skin thickness measured from the SEM micrographs. To recall, for Knudsen flow:

$$J = \frac{4r\varepsilon}{3}.\left(\frac{2RT}{\pi M}\right)^{\frac{1}{2}}.\frac{p_0 - p_\ell}{\ell.RT} \tag{3.3}$$

Where r is the pore radius, ε is the membrane's porosity, M is the molecular weight of the gas, ℓ is the pore's length, R is gas constant, T is permeation temperature, and p_0 and p_ℓ is the absolute pressures of the gas at the beginning and at the end of the pore ($z = 0$ and $z = \ell$, respectively). For asymmetric membranes, this characteristic is defined to be on the skin layer, hence r = surface pore size, ε = surface porosity, and ℓ = skin thickness. Also, for N_2, $M = 28.0134$ g/mol. Meanwhile, for Poiseuille flow:

$$J = \frac{r^2\varepsilon}{8\eta}.\frac{[p_0 - p_\ell][p_0 + p_\ell]}{\ell.RT} \tag{3.5}$$

Where η is the viscosity of the gas. For N_2, the value will be at 17.82 x 10^{-6} Pa.s at 25 °C.

Table 4.3: Comparison of N_2 permeance between experimental and calculated Poiseuille/Knudsen flow

Substrate samples	Average pore radius (r) / mean free path (λ)	Experimental permeance (x1 000 GPU)	Poiseuille permeance (x1 000 GPU)	Knudsen permeance (x1 000 GPU)
Pristine	2.7	105.3	265 492.6	65.5
LiCl_1%	19.4	36.5	354 342.7	72.6
LiCl_2%	25.8	18.5	404 355.9	62.1
LiCl_3%	26.1	12.5	231 599.7	35.1
LiCl_4%	31.7	4.3	170 698.8	21.3

All the theoretical values are higher than the one registered by the experiments, except for Knudsen permeance of pristine sample. As experimental

results already shown that the gas selectivity follows Knudsen diffusion, gas permeation is highly unlikely to be mainly governed by Poiseuille flow, which is comparable to the results presented here where the calculated permeance are highly exaggerated for all cases. On top of that, extrapolation of the experimental permeance value down to zero pressure suggested the apparent permeance and the average permeance of the substrates did not change much between 1-6 bar with standard error around 2% from the average, confirming the negligible contribution of Poiseuille flow for all samples (Wang *et al.*, 1990).

Nevertheless, the theoretical values proposed by the Knudsen equation is still exaggerated for LiCl incorporated samples and below the experimental value for the pristine sample. While permeance value differences for pristine membrane can be explained by Poiseuille flow contribution, this cannot be the case for the other samples. Knudsen diffusion occurs when the mean free path (λ) of the molecule is larger than average pore radius (r), or at $r/\lambda < 1$. For nitrogen gas, the mean free path at 25 °C was noted to be around 85.1 nm at 1 bar which is between 2.7-5.3x, and around 14.2 nm at 6 bar which is between 16.1-31.8x the measured surface pore diameter of the substrates in this work. These values are indeed too high for Knudsen diffusion to take place primarily. In fact, some contribution of Poiseuille's flow are to be expected for membranes with pores of 0.1 µm or larger (Baker, 2004). Consequently, as the theoretical Knudsen permeance was higher than the experimental values, this suggested that the pore size from the SEM micrograph did not represent the average of the substrates.

In both models, there are three geometrical parameters of the sample that can be modified: (i) pore radius, (ii) porosity, and (iii) thickness. As the experimental

permeances were confirmed to exhibit Knudsen selectivity, these values were back calculated using Equation (3.3) to obtain the corresponding parameters. The results are presented in Table 4.4. As expected, the resulting surface pore radius calculated from the equation was decreasing with increasing LiCl content. This behaviour is much more consistent with most literature as noted in Section 4.1.3 (Mansourizadeh and Ismail, 2010, Idris *et al.*, 2010, Ahmed *et al.*, 2010). Nevertheless, surface porosity was also noted to be significantly downgraded for all cases except for pristine membrane, where it was increased. Similar observation was noted for the resulting skin thickness.

Table 4.4: Back calculated substrate's surface pore radius, surface porosity, and skin thickness using Knudsen flow equation

Substrate samples	**Surface pore radius (nm)**	**Surface porosity (%)**	**Skin thickness (μm)**
Pristine	371.0	25.9	0.1
LiCl_1%	138.3	9.7	0.6
LiCl_2%	109.1	5.9	1.5
LiCl_3%	131.9	5.6	1.8
LiCl_4%	90.8	2.6	5.1

While it is hard to measure the skin thickness accurately, the values from these calculations are far higher than the one measured from the SEM in Table 4.1, up to 4 μm difference for LiCl_4% sample. Hence, the thickness increase from the calculation is highly unlikely. It is possible that the chokepoint of the pore in the skin layer is not near the immediate surface and the skin pores are not uniform along the thickness, causing surface porosity to not represent the bulk porosity of the skin layer. Discrepancies between pore sizes noted from image analysis and permeation data has also been noted in the work by Hao *et al.* (2020) and AlMarzooqi *et al.* (2015). This complication is noted especially for non-ideal pore structures with non-uniform pore size along the membrane thickness and erratic pore distribution, which is common in

phase inversion membrane as in this work. Hence, discrepancy between the actual experimental value and the model value in this work is also highly likely to be caused by differences in surface pore size and to a certain extent, the surface porosity. This suggested that the surface pore sizes measured using the SEM micrographs may not represents the true nature of the average surface pore structures which are much smaller, as predicted in Table 4.4. It is known that gas permeation results across porous membranes are dictated by the average pore design (i.e., size, porosity, distributions, and density) across the thickness (Alkan and Groves, 1978), while the pore design in the skin layer dictates the permeation result of asymmetric membranes (Wang *et al.*, 1990), hence the possible source of discrepancy. Using the calculated average pore radius from the model, this put the substrate's pore in a true ultrafiltration regime (Baker, 2004). It is also important to note that tortuosity of the pores was not considered in the current work, which may be severe and become the source of deviation between the experimental and model results.

4.2 PES/PDMS Composite – Impact of Pore Intrusion and Lateral Diffusion

In the previous subchapter, LiCl was proven to be able to variate the surface pore architecture of PES substrate. While the bulk pore structure was full of large macro void and finger-like structure, the substrate was able to maintain its mechanical integrity up to 6 bars. Nevertheless, despite the high permeance of all substrate samples, performance of the composite structure is affected by the interaction between the coating solution and the pores on the substrate surface (Chung, 1997, Wijmans and Hao, 2015). Hence, in this subchapter, study is focused on elucidating the performance of PDMS coated PES substrates. PDMS of various thickness will be coated on three different PES substrates with different surface pore structures: pristine,

LiCl_2% and LiCl_4%. Emphasis will be made on the effect of coating solution penetration and lateral diffusion.

4.2.1 PES Substrate's Stability in Drying Condition

The substrates in Section 4.1 were previously dried in room temperature for several days. Nevertheless, coating of PDMS using the method by Salih *et al.* (2014) needs to be dried at an elevated temperature, which may affect the pore structure and permeance of substrate. Hence, the SEM surface micrograph of pre-oven and post-oven substrates were compared, as represented in Figure 4.8. Minimal differences were noted for the pristine substrate, but significant reduction of the number of surface pores were observed for the case of LiCl_2% and LiCl_4%. Literature have suggested that thermal annealing would shrink the membrane pore sizes and therefore reduces the membrane's porosity (Li *et al.*, 2004, Kusworo *et al.*, 2017, Gholami *et al.*, 2003). However, the literatures did not mention the reduction in surface pore density. It is possible that some of the surface pores collapse during the drying process in this work, as noted in the work of Park *et al.* (1999) and Subrahmanyan (2003) on polysulfone membrane. This collapse, which are the most prominent on the top skin layer of asymmetric membrane could contribute to the apparent reduction in surface pore density.

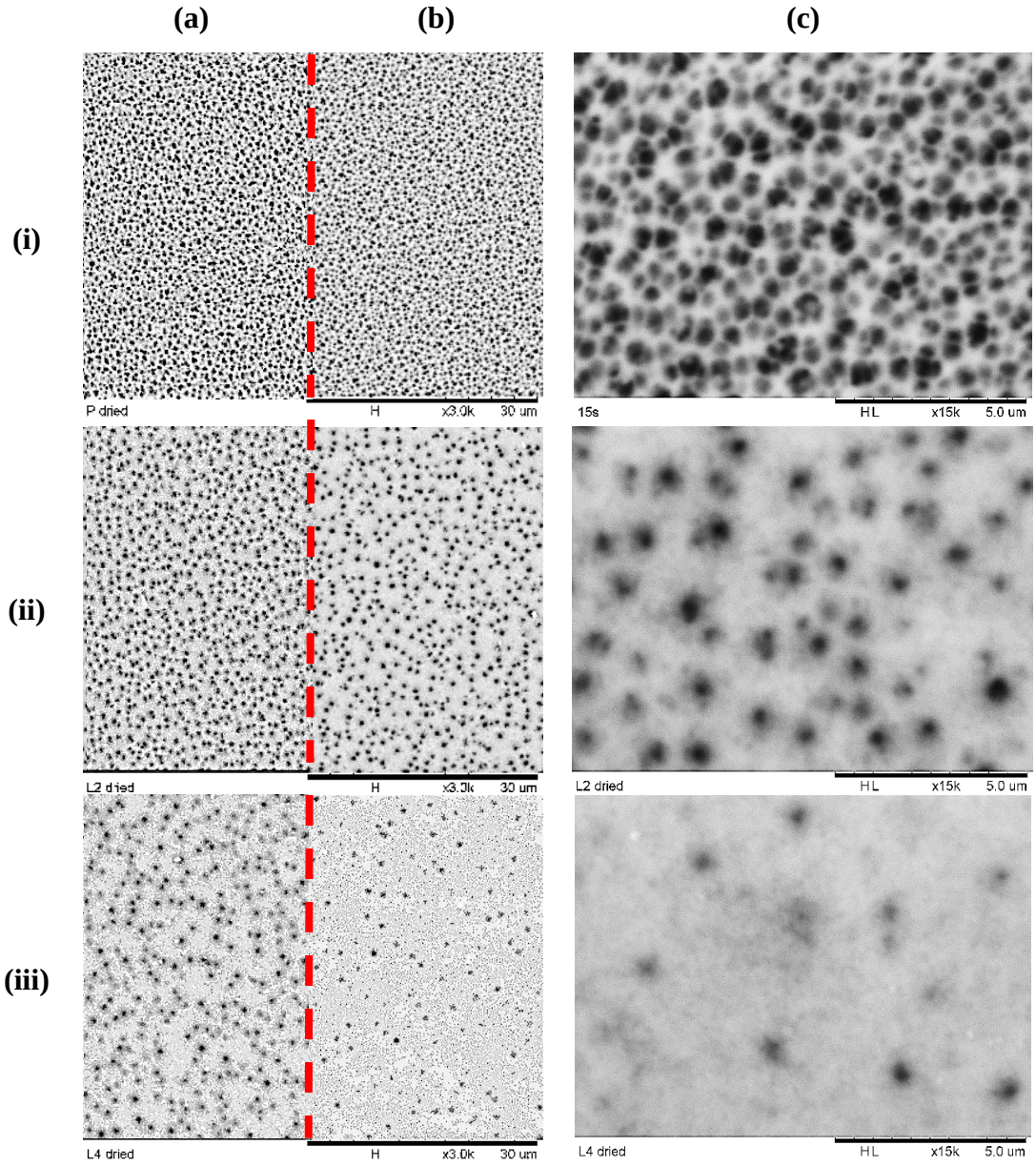

Figure 4.8: Comparison of surface SEM micrograph of (a) pre-oven substrates at x3K magnification, (b) oven dried substrates (70 °C) at x3K magnification, and (c) oven dried substrates (70 °C) at x15K magnification. (i) Pristine, (ii) LiCl_2%, (iii) LiCl_4%

N_2 permeance of pre-oven and post-oven substrates for pristine, LiCl_2% and LiCl_4% were also compared, as shown in Figure 4.9. As expected, all samples have registered a reduced permeance after the oven drying. Pristine substrate only recorded 11.7-12.3% flux reduction, but a much significant reduction was observed for LiCl_2% and LiCl_4% substrates, which were 42.8-47.7% and 43.4-44.1% respectively. Nevertheless, all substrate samples still registered permeance value of

above 2 344 ± 18 GPU, which is much higher than the PDMS base permeance at 3.75 ± 0.12 GPU (for PDMS thickness of 49.73 ± 0.56 µm).

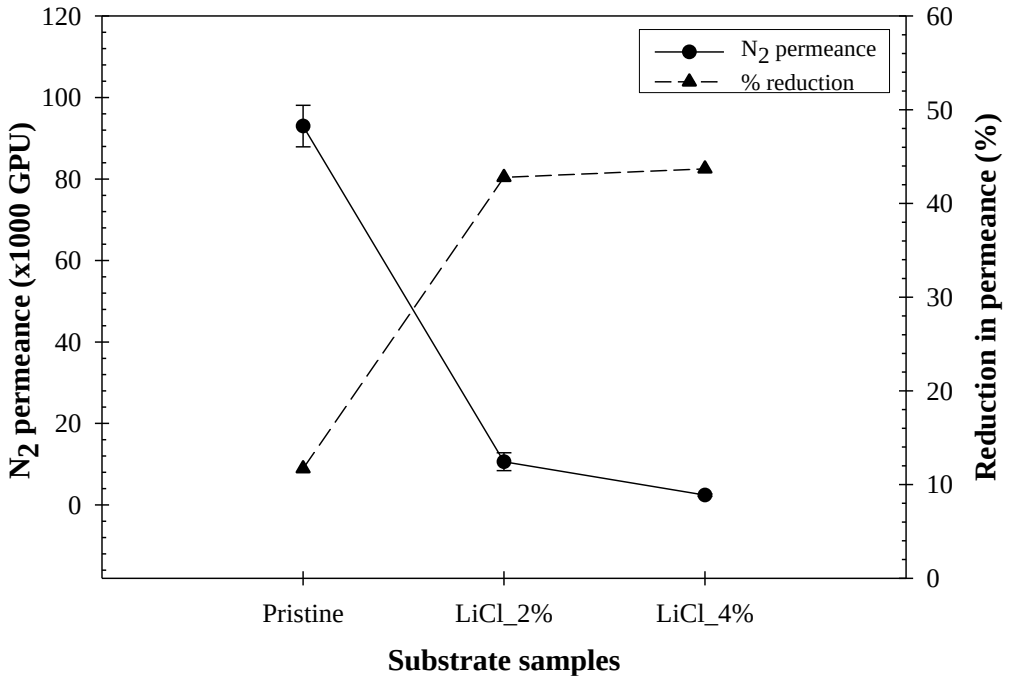

Figure 4.9: N_2 permeances for post-oven substrates and its reduction percentage compared to the pre-oven values (70 °C)

4.2.2 PDMS Coating Validation

As various mass of PDMS solutions were poured onto over the same substrate area, different thickness of PDMS layer can be formed. To visualize this PDMS layer, SEM cross sectional micrographs were taken at x1200 magnification for all composite samples, as represented in Figure 4.10. PDMS layers from 0.5g, 1.0g, 2.0g, and 4.0g solution in n-heptane were successfully fabricated on top of pristine, LiCl_2%, and LiCl_4% substrates, represented by the red hue to aid visually. The bulk pore structure of the substrates remained intact with no sign of collapse, while the resulting PDMS layers formed ranged from a very thick structure to almost non-visible at this magnification.

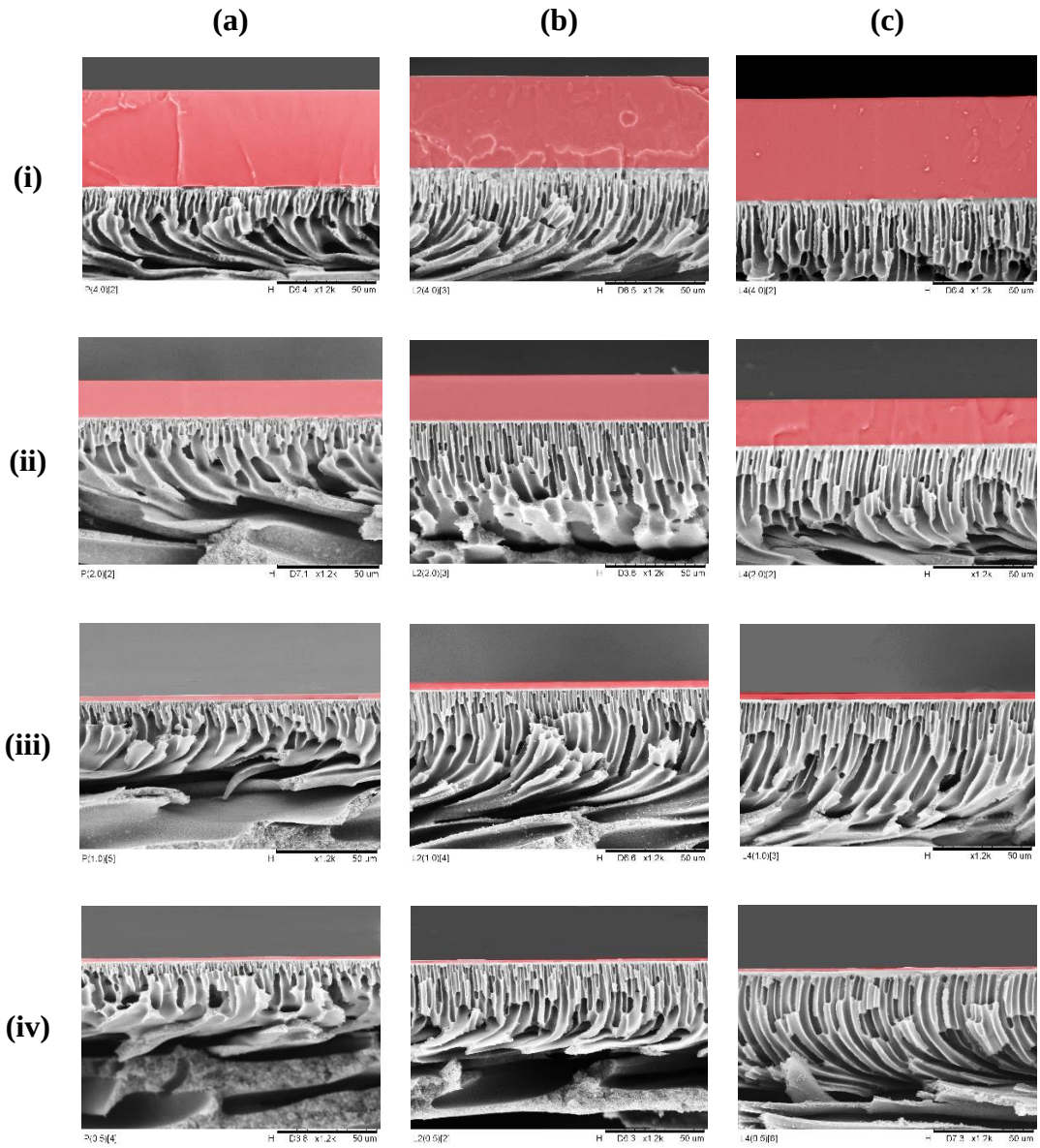

Figure 4.10: PES-PDMS interface cross-sectional micrograph at x1.2K magnification, focussing on the PDMS layers (highlighted in red). PDMS solution coating (i) 4.0g, (ii) 2.0g, (iii) 1.0g, (iv) 0.5g. Substrate sample (a) Pristine, (b) LiCl_2%, (c) LiCl_4%

From these micrographs, it seems that visually, PDMS layer did not penetrate the bulk of the porous substrates and remained only on the top layer. This is supported by the almost similar thickness of the fabricated PDMS layer regardless of the substrate used. Nevertheless, it is possible that some of the PDMS coating solution penetrated to the depth of the skin layer up to the maximum values presented previously in Table 4.1 (the highest at 1.02 ± 0.07 µm for LiCl_4% substrate). On the

other hand, there were no visible cracks, pores, or pinhole of the PDMS layers, suggesting that the resulting PDMS layer is dense.

To quantify the PDMS thickness, the micrographs of the dense layer were measured using image analysis and were illustrated in Figure 4.11. Higher magnifications were used for all samples for a better measurement and improved resolution. As mentioned earlier, different substrate used did not significantly changes the thickness of PDMS coating, which confirmed that PDMS solution intrusion is, if happened, were limited to the skin of the substrates. This is reasonable, considering that the maximum skin layer thickness is at about 1 μm for LiCl_4% substrate, which is under the error range for most of the samples. It is also important to note that this method is very localized to certain part of the composite membranes. While at least 6 different sample batches were used and 6 different measurements were taken per sample batch, the standard error remains to be between 4.0% and 20.1%. Minor localize variation in thickness of the samples limits the degree of certainty of this measurement to conclude the possible pore intrusion into the membrane. On the other hand, almost linear increase in thickness was seen with increasing weight of PDMS coating solution.

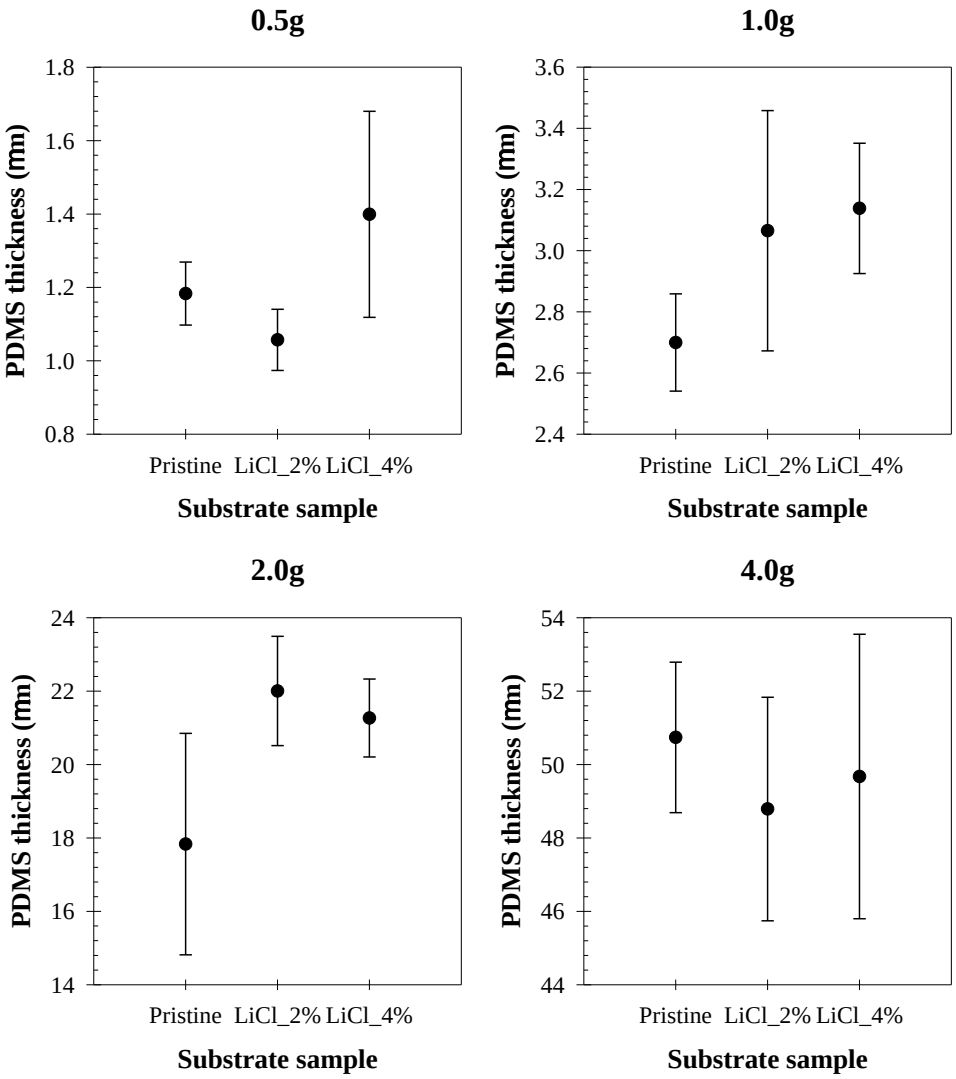

Figure 4.11: Measured thickness of PDMS layer on different substrate samples, based on the poured mass of the PDMS solution

The reported thickness here ranges from half of the substrate thickness at 50.74 ± 2.05 µm for 4.0g PDMS solution coating, to about 1.06 ± 0.08 µm at 0.5g PDMS solution coating. On the other hand, similar works on PDMS interlayer coating have suggested a thinner PDMS coating at 550 nm (Salih *et al.*, 2014) and 490 nm (Hu *et al.*, 2017). Nevertheless, preliminary study made on pristine PES substrate (Appendix E) could not fabricate thinner PDMS coating at mass below 0.5g without the loss of CO_2/N_2 selectivity, suggesting either incomplete covering by PDMS or breaking of the resulting dense layer. This is probably due to the larger surface pores in this work. The lower limit of the formed PDMS layers need to be made as thin as

possible to minimize gas flow resistance. Nevertheless, as any pinhole defects on the PDMS may contribute to the solution penetration for the subsequent selective layer, the loss of selectivity suggesting that thinner PDMS layers were not reliable enough to be considered in this case.

To further validate the formation of PDMS layers, FTIR was used to analyse the top (PDMS coated) surface of membrane and compared to the spectrum of PES flakes, as represented in Figure 4.12. All composite samples exhibit similar spectra as compared to hydroxy terminated PDMS, as noted in SpectraBase (2020) with distinguishing peaks at around 2940 cm^{-1} from C-H stretching vibrations of methyl group ($-CH_3$) (Salih *et al.*, 2014, Merck, 2021a) and Si-O-Si stretching multicomponent peaks between 900-1200 cm^{-1} (Hu *et al.*, 2017, Johnson *et al.*, 2013) which is not available on the PES flake spectrum. $Si-CH_3$ stretching, and CH_3 deformation vibration peak can also be observed at around 780 cm^{-1} and 1260 cm^{-1} respectively (Hu *et al.*, 2017, Johnson *et al.*, 2013). However, small characteristic peaks of PES were noted for all the composite samples at around 1440 and 1560 cm^{-1}, representing the C=C stretching from the aromatic benzene ring (Merck, 2021a, Verma *et al.*, 2019). On the other hand, SO_2 stretching vibration could also be found at around 1140 cm^{-1} while peak at 1240 cm^{-1} represents the C-O-C linkage (Han *et al.*, 2010, Verma *et al.*, 2019). These PES peaks were probably visible due to the transparent nature of PDMS and the thin PDMS layers formed by 0.5g PDMS solution. Nevertheless, this confirms the formation of PDMS layers on the PES substrate and can hence also be extended as validation for the thicker composite samples.

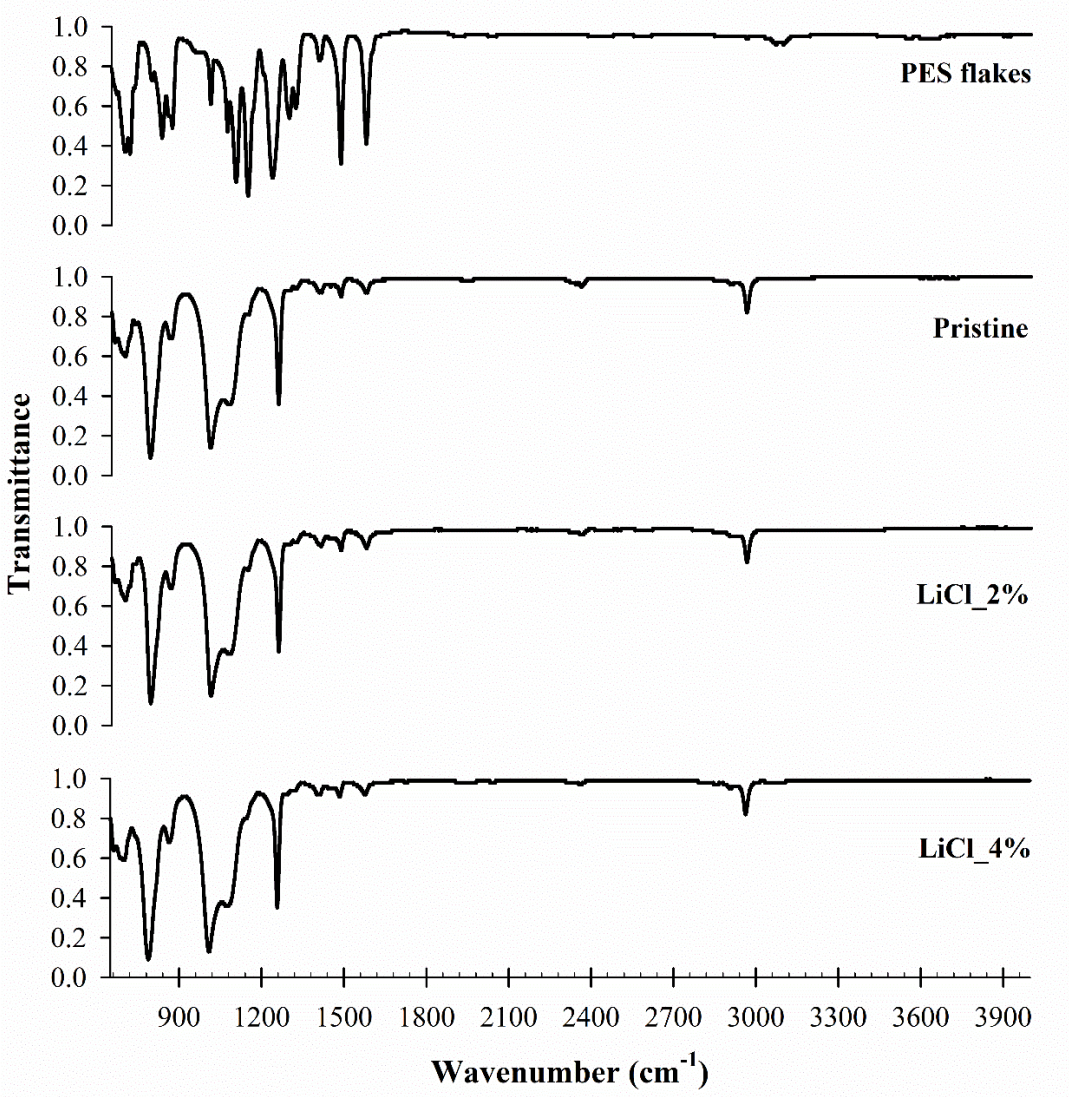

Figure 4.12: FTIR spectrum of the PES flakes and PDMS coating layer for 0.5g PDMS solution on various PES-based substrates (Pristine, LiCl_2%, and LiCl_4%)

4.2.3 PES-PDMS Interface Analysis

By analyzing the atomic composition near the layer's interface, dispersion of Si atom (from PDMS) can be quantified. Hence, EDX mapping of Si and S (from PES) near the 4g PDMS layer's interface at x15K magnification is presented in Figure 4.13, together with its corresponding SEM micrographs. Si was noted to be concentrated on the surface layer and S to be concentrated on the substrate, which corresponds well when compared with the SEM micrographs. Nevertheless, no distinguishable Si-S overlapping can be found for all the cases, suggesting that solution

penetration is either very minimal, at most in the order of 1-2 µm, supporting the previous observation on the PDMS thickness. It is however important to note that the green Si were also sparsely dispersed in the substrate layer for all samples, which may suggest that some PDMS were able to penetrate deep into the pores. However, the dispersion was not localized in the void area, therefore, it may be due to noise during the mapping procedure.

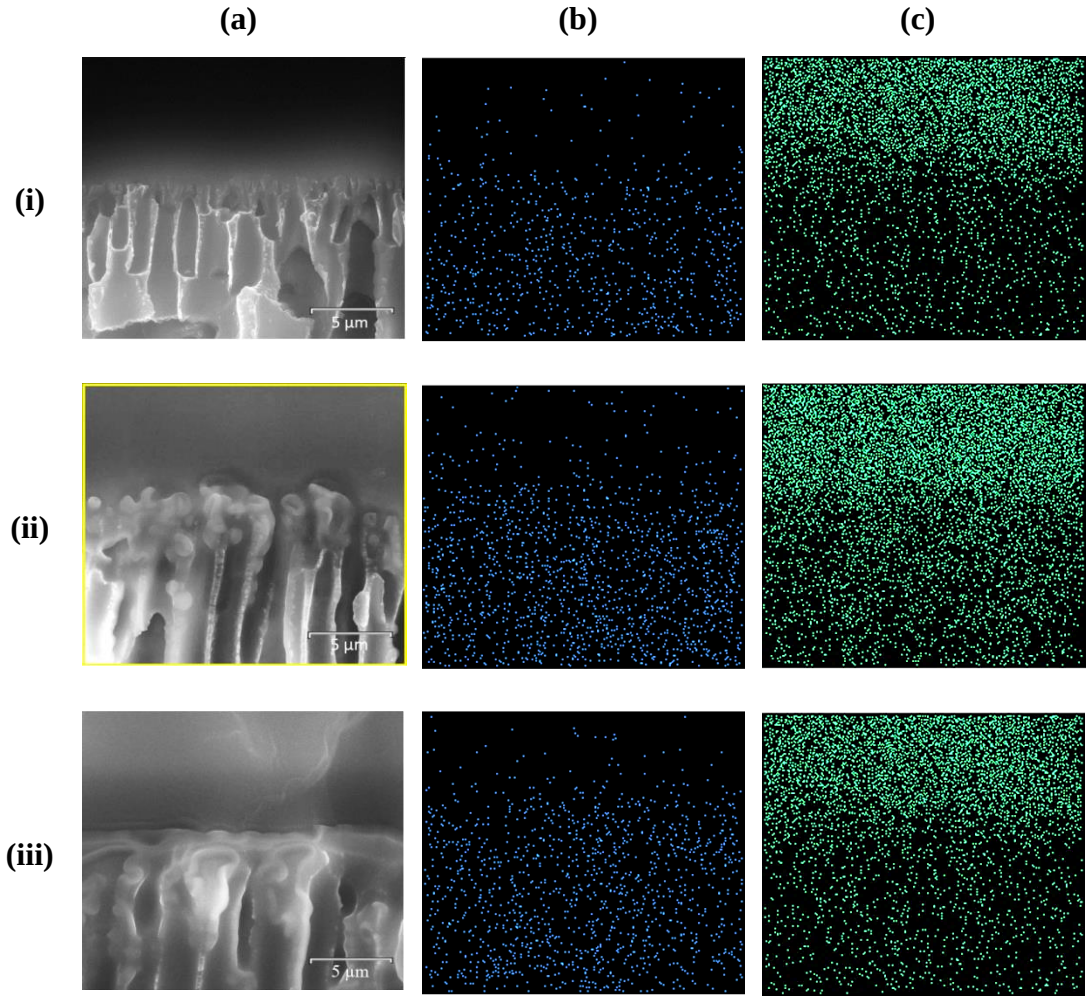

Figure 4.13: (a) SEM cross sectional micrograph near the layer's interface, (b) elemental mapping distribution of S (from PES, in blue), and (c) Si (from PDMS, in green) near the composite interface at x15K magnification for PDMS solution coating of 4g. Substrate sample (i) Pristine, (ii) LiCl_2%, (iii) LiCl_4%

Several attempts have been made in literature to visualize the penetration degree of composite membranes experimentally. Qin *et al.* (2015) for example, uses both SEM and EDX as in this work on PDMS coated PES/Boehmite and PES/α-Al_2O_3 dual layer as substrates. The use of focused ion beam (FIB) nanomachining technique was able to cut the cross section of the membrane precisely for both SEM and TEM purposes, with clear penetration of Si from PDMS into the sublayer. However, the use of interlayer α-Al_2O_3 particles may induce high PDMS penetration and hence better contrast on the penetration signal compared to the underlying PES substrate. Another work uses a more indirect technique such as small angle X-ray scattering (SAXS) by measuring the relative reduction in the pore's gyration radius, R_g, before and after coating of PSf/PDMS composites. Penetration degrees were hence defined as relative reduction of R_g, and noted to be increased with increasing casting thickness, although the R_g reduction was noted only up to 10 nm maximum, with penetration degree of 0.17 (Li *et al.*, 2019). Meanwhile, hard angle dark-field scanning transmission electron microscopy (HAADF-STEM) was also used to quantify the penetration of polystyrene-b-polydimethylsiloxane-b-polystyrene (SDS) triblock copolymers in PTFE at around 1.0-2.2 µm for selective layer thickness of 125 µm in the work of Shin *et al.* (2017).

Penetration of liquid into porous substrates are governed mainly by capillary force (Hapgood *et al.*, 2002, Rosenholm, 2015), while gravitational influence is expected to be minimal as the hydrostatic pressure exerted by coating solution would be negligible (Ding and Harris, 2017). Rough estimate suggested that capillary pressure exerted would at least be around 0.81 bar for cylindrical pore of 500 nm, which is the upper limit of the pore radius as measured in Table 4.2 (details of calculation is summarized in Appendix F). Meanwhile, at thicker PDMS coating

(pouring 4.0g PDMS solution coating to produce about 0.25 cm of thickness), hydrostatic pressure would be negligible at only around 0.00017 bar, which is in line with the claim above. Considering that PDMS solution was poured in excess (4.0g) to cover the whole substrate in this work, the resulting capillary forces would surely cause the solution to penetrate the pores. Nevertheless, the results in Figure 4.13 suggested otherwise.

For polymeric solution such as in the case of PDMS in n-heptane, penetration of the solvent would follow the mechanism as discussed before. However, the ability of polymer molecules to penetrate the pores might be different. At minimum solute interaction and no external forces, the penetration of the dispersed polymeric materials would be governed mainly by the size exclusion of the polymer relative to the substrate's pore (Day *et al.*, 1978). Low molecular mass compounds would penetrate the pores together with the solvent, but higher ones will be mostly retained (Rukhlya *et al.*, 2011). However, for PDMS used in this work, it has approximated molecular weight of 33.2-37.8 kDa (equivalent to PDMS hydrodynamic diameter of 1.76-1.84 nm). This would still be small enough for significant PDMS polymer to penetrate the substrates (detailed calculations shown in Appendix G).

One hypothesis to explain the lack of deep solution intrusion into the pore is due to the asymmetric substrate design with increasingly larger pore size in downward direction. This would be beneficial to limit any further penetration beyond the nano porous skin layer. This physical limit has been noted by Hapgood *et al.* (2002), where macro-void formation in granular packing would limit the flow of the fluid. Evaporation of the solvent (n-heptane) and crosslinking of PDMS also increases the viscosity of the solution up to a point it solidified completely (tested to be around 15-20 minutes), which also helps to limit the propagation of any further penetration

over time. Consequently, PDMS solution could not penetrate deep into the substrate despite of the high PES wettability by n-heptane. This hypothesis is also aligned with the work of Shin *et al.* (2017) and Jin *et al.* (2017).

Penetration of PDMS into the substrates were also evaluated from the surface point-of-view. The substrates were carefully detached from the PDMS layer and analyzed, as presented in Figure 4.14. Significant differences can be noted for pristine substrate samples, which exhibit a lot of white dispersion on the surface, presumably adhered PDMS. However, only minor differences could be seen for LiCl_2% and LiCl_4% substrates, with similar surface pore distribution. This however, suggested that PDMS was penetrating the substrate, at least for the pristine.

It is unclear why only pristine substrates exhibit significant PDMS adhesion while no sign of PDMS was noted for the LiCl_2% and LiCl_4% substrates. It is possible that lower surface porosity exhibited by these substrates (previously reported in Table 4.2) did not provide enough anchoring point for the PDMS to hold on to when being peeled. As a result, no PDMS traces can be visually found for these two lower porosity substrates. This, however, did not confirmed that PDMS did not penetrate the pores, as low penetration depth may cause the penetrated PDMS to be peeled together. On the other hand, Li *et al.* (2019) have suggested that penetrated polymers did not formed a solid structure in the void across the whole penetration region, but instead sticks to the wall of the pores, hence reducing its gyration radius. Regardless of the penetration morphology and despite that solution penetration could contribute to better adhesion between the layers, it would also degrades the composite membrane performance as it significantly increases the gas flow resistance with increasing depth of the penetration thickness (Shin *et al.*, 2017). A study by Hao *et al.* (2020) suggested that for low porosity (0.6%) track-etch support, penetration of 1 nm

would create additional resistance equivalent to 160 nm of the selective layer. Hence, it is logical to avoid any form of penetration into the substrate layer.

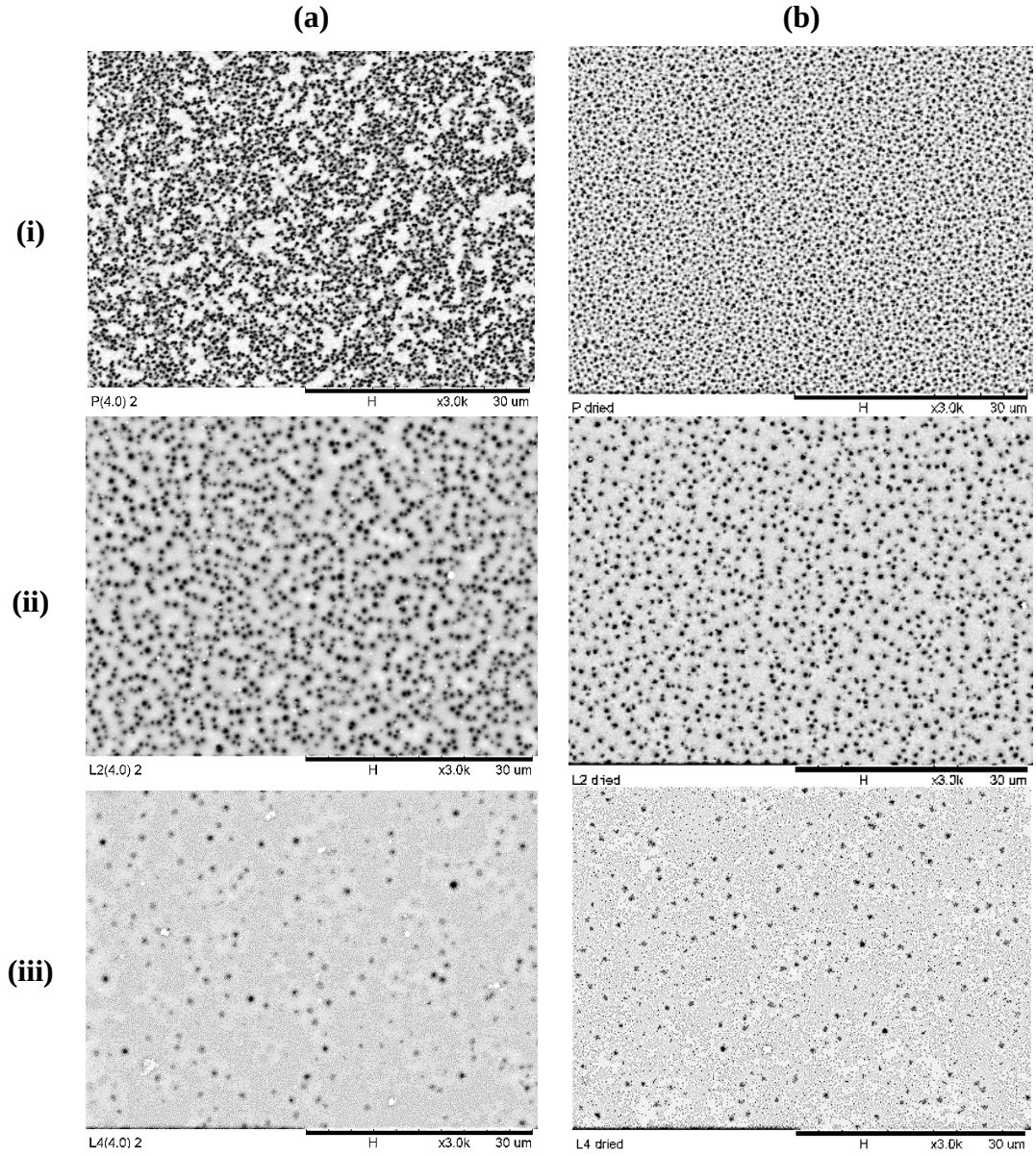

Figure 4.14: Comparison of SEM micrograph of (a) peeled PES-PDMS composite membrane (PES substrate surface) and (b) precoated PES substrate (post-oven) at x3K magnification. (i) Pristine, (ii) LiCl_2% and (iii) LiCl_4%

Nevertheless, it is worth to note that defect control in commercial membranes utilize high permeable polymer to plug defects or to be casted as protective layer (Yoo *et al.*, 2018b). Thin coating of this high permeable polymer would penetrate the pinhole defects and enhance the performance of the composite membrane near to

its perfect, non-defective performance. This approach has also been notable in various literatures and perhaps best known in the work of Henis and Tripodi (1980) for the commercial Monsanto membranes. In a way, the use of gutter layer would follow this approach, and creates a conflicting narrative with the current discussion. Perhaps in a multi-layer's system, low penetration of PDMS as gutter layer may not be that influential as compared to the benefit gained from thinner, non-penetrating selective layer. This has been suggested from the literature result such as in Salih *et al.* (2014) and in patent by Castro *et al.* (1991).

4.2.4 Gas Permeance Analysis

The composite samples were tested for N_2 and CO_2 single gas permeance, as represented by Figure 4.15. All the composite samples exhibit similarly reducing trends with increasing PDMS coating solution mass, which is expected considering a thinner PDMS would exhibit lower gas flow resistance. Nevertheless, composites with pristine substrate exhibiting the highest permeance, followed by LiCl_2% composites and LiCl_4% composites, much like its substrates' performance. Composite sample of 0.5g PDMS on pristine substrate [P(0.5)] exhibit the highest permeance overall at 26.6 ± 2.6 GPU for N_2 and 354.4 ± 27.9 GPU for CO_2, while L4(4.0) sample exhibit the lowest permeance at 0.9 ± 0.3 GPU for N_2 and 15.4 ± 3.9 GPU for CO_2. These results have a significantly lower permeance compared to the non-coated substrates reported in Figure 4.7 and Figure 4.9. It is however, lower than the one registered in literature, such as by Li *et al.* (2019). Much lower base permeance was also registered for the PSf substrate at 20 700 ± 400 GPU and 16 900 ± 300 GPU for N_2 and CO_2 respectively, as compared to this work. Yet, permeance for the composite structure was much higher at 811 ± 12 GPU and 7 780 ± 120 GPU for N_2 and CO_2 respectively, despite of using the same PDMS coating. While the differences were expected considering a much

thinner PDMS at 80 nm, back calculating the permeance and thickness to permeability in the work, however, also gave a higher value at 64.9 Barrer and 622.4 Barrer for N_2 and CO_2, as compared to 31.4 Barrer and 419.4 Barrer for P(0.5) in this work. Similar observation could be concluded when compared to other literature (Hu *et al.*, 2017, Merkel *et al.*, 1999).

Meanwhile, the CO_2/N_2 selectivity ranges between 12-21, suggesting that the PDMS dense coating has successfully been fabricated without significant defects. The thinnest PDMS layer for all substrates made using 0.5g solution possess the lowest selectivity between 13.5 ± 0.5 for P(0.5) and 13.8 ± 1.1 for L4(0.5). Interestingly, the selectivity was noted to be higher for thicker PDMS for all cases of substrates. These values were also much higher than the reported PDMS CO_2/N_2 ideal selectivity in numerous literatures, which is usually between 9-12 (Merkel *et al.*, 1999, Li *et al.*, 2019, Hu *et al.*, 2017, Dong *et al.*, 2020, Yasuda and Rosengren, 1970).

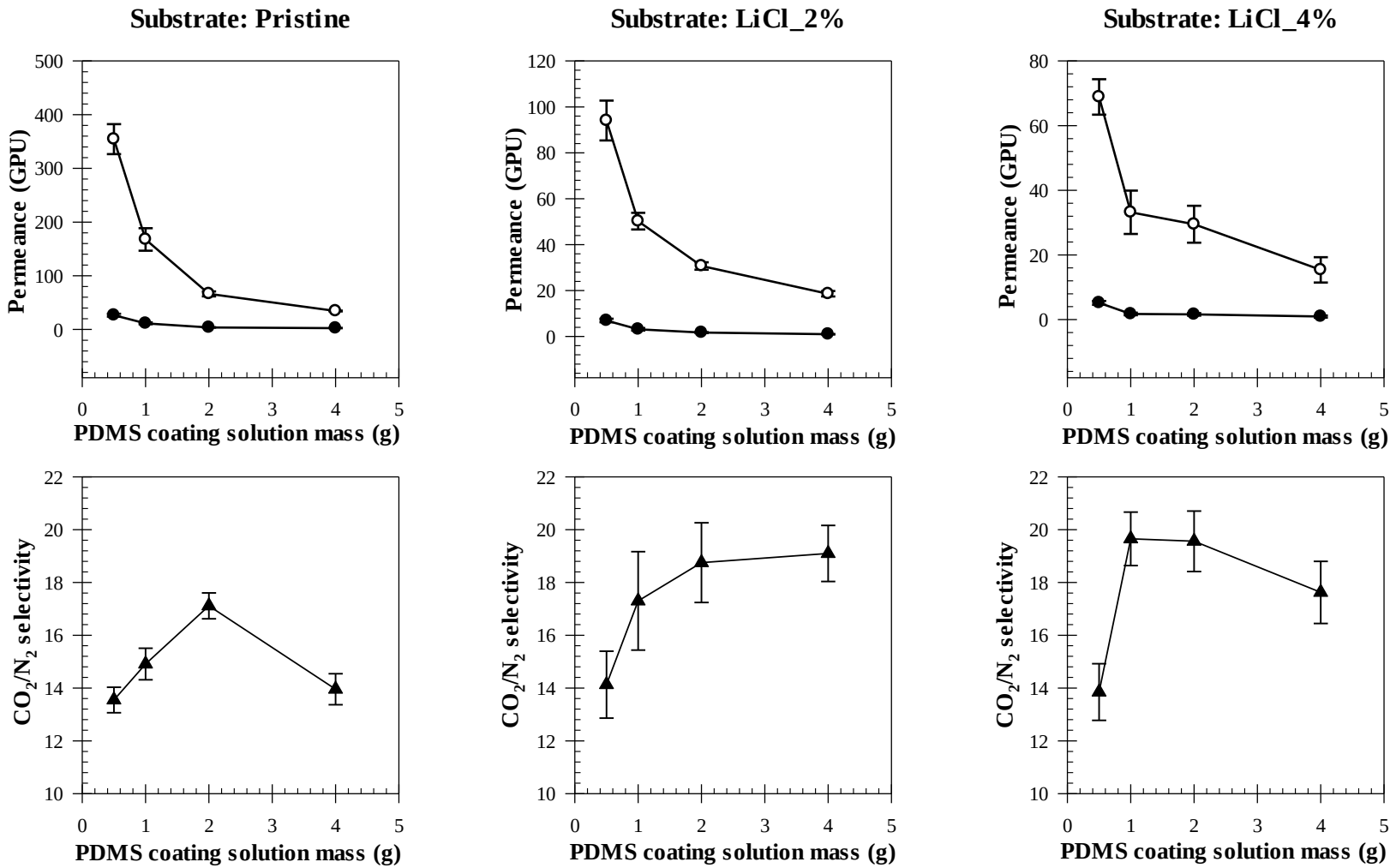

Figure 4.15: N_2 and CO_2 permeances (top) and CO_2/N_2 selectivity (bottom) of pristine, LiCl_2%, and LiCl_4% substrate samples, coated with PDMS of various solution's mass. Solid circle = N_2 permeance, hollow circle = CO_2 permeance

Performance changes of the composite membrane due to difference in shelf time was also studied briefly to elucidate possible effect on the composite membrane performances over 2-months' time, as presented in Figure 4.16. Small reduction in both CO_2 and N_2 permeance of the aging membrane can be found. For example, N_2 permeances were reduced from 26.6 ± 2.6 GPU to 17.4 GPU for P(0.5) sample and from 2.5 ± 0.1 GPU to 1.3 GPU for P(4.0) sample. Similarly, the selectivity was reduced from 13.5 ± 0.5 to 12.8 for P(0.5) sample, but increased from 14.0 ± 0.6 to 16.8 for P(4.0) sample. Nevertheless, these differences were minor, and not significant as it was noticed on both thick (50.7 µm) and thin (1.2 µm) samples.

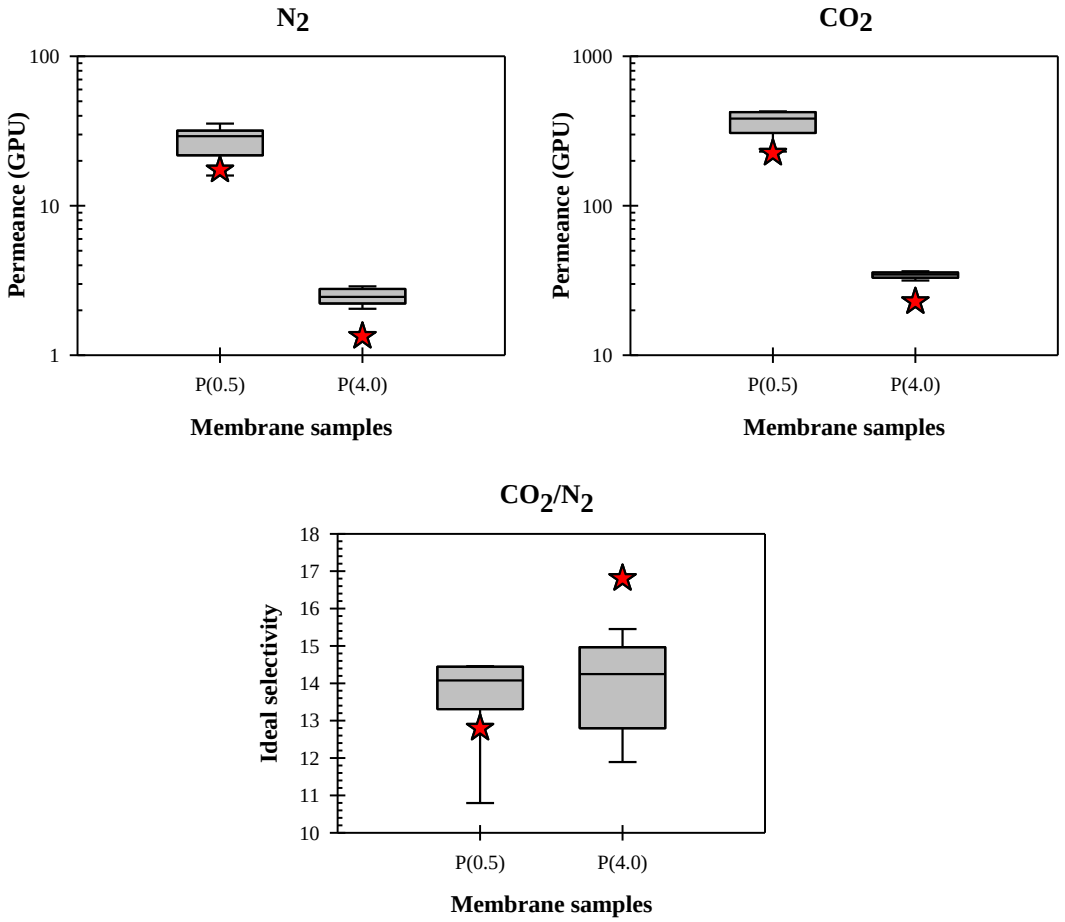

Figure 4.16: Comparison of PES-PDMS composite permeance (2-months aged, red stars) with the average permeance results (time-independent samples) for P(0.5) and P(4.0) samples

Lab scale fabrication of thin layers usually neglects the possible variation of flux performance caused by phenomenon such as physical aging. Thinner dense structures are prone to rearrangement of polymer networks which reduces the permeance of the same membrane over time, which sometimes can be in less than a week for a thin structure (Baker and Low, 2014). Although this is true mainly for glassy polymer, this variation can still be important to be elucidated in this work as the time gap between membrane fabrication and membrane performance test might influence the results.

The composite permeances did not differ much over the two-months' time difference and selectivity remain comparatively similar, suggesting that any fabrication-to-performance time effect over this work would be negligible. Hence, it was concluded that physical aging was not a concern in the time range of two months, a probable time delay between fabrication period and performance testing period in this work. Possible significant effect by densification of the layers, runaway crosslinking, and insufficient drying time can also be excluded.

So far, it was noted that both permeance and selectivity of this work differs quite significantly from the literature. Lower permeance and higher selectivity than predicted suggested that the impact of PES substrate in gas separation performance is much higher than expected. Hence, to further elucidate the performance results, the layers of the 4.0g PDMS made on all three substrates were separated (from now on will be called free or peeled PDMS) and tested individually for CO_2 and N_2 gas, as represented in Figure 4.17. Free PDMS dense layer registered higher permeance as compared to their composites for all cases. However, in contrary to the composite results, free PDMS permeances were comparable between each other regardless of their original substrates used at 3.7 ± 0.1 GPU for N_2 and 38.4 ± 1.8 GPU for CO_2.

This in turns gave a resulting PDMS CO_2/N_2 selectivity of 10.3 ± 0.2; a value expected for PDMS as discussed before (and later shown in Table 4.5). As it has been proven in Figure 4.7 that the substrate lacks dense selectivity, it is safe to say that the increased selectivity in composites were caused by the layering with the substrate, originating from the CO_2/N_2 selectivity of PES. This will be discussed further later.

Meanwhile, free PES substrates (resulting substrates from the peeled composites) gave higher permeances as compared to the corresponding composite and free PDMS layers. This is expected considering that these free PES layers were supposed to be porous and should return to its original permeances as noted in Figure 4.7 and Figure 4.9. However, the current values were much lower than the original non-coated substrate permeances by several folds. In fact, the CO_2/N_2 selectivity was noted in the order of 1.6-2.5. As post-drying N_2 permeance without the PDMS in Figure 4.9 has been confirmed to be far higher than the values noted in Figure 4.17 for free PES substrates, this suggested that solution penetration occurred and blocked some of the substrate surface pores.

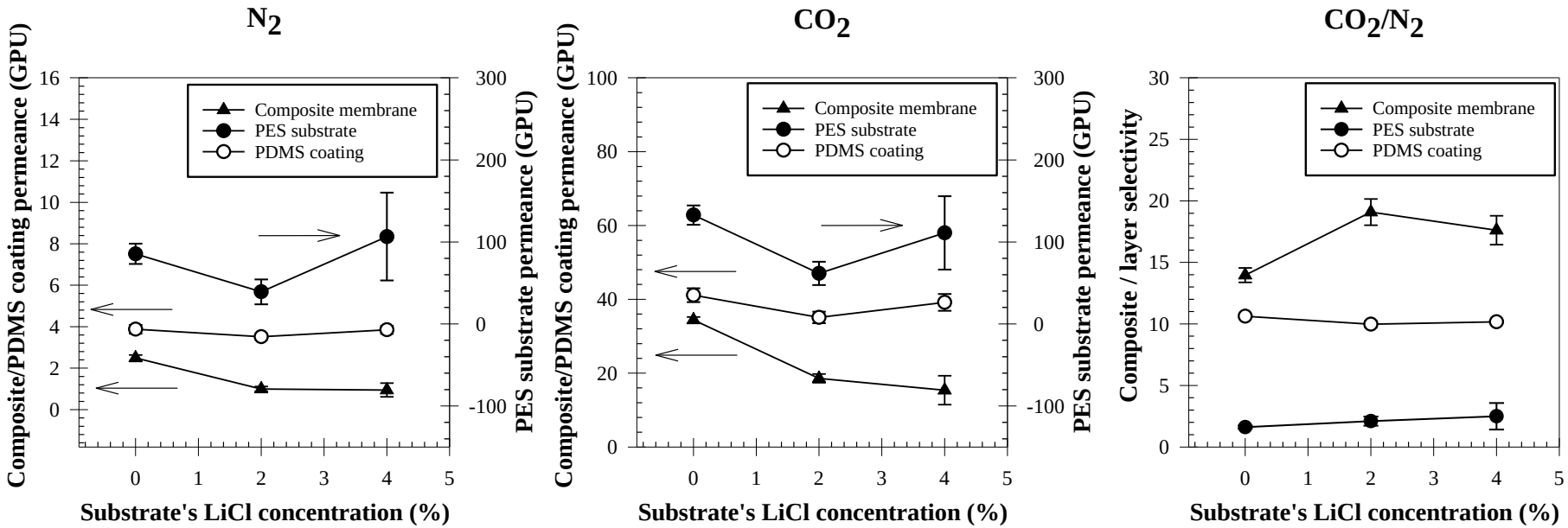

Figure 4.17: N_2-CO_2 permeances and CO_2/N_2 selectivity of the composites, compared to the separated PDMS dense and PES porous substrate for 4.0g PDMS coating sample

Free PDMS permeance of 4.0g PDMS coating with thickness at average of 49.7 µm gave a comparatively stable value at an average permeability of 186.3 Barrer and 1 912.1 Barrer for N_2 and CO_2, respectively. As noted in Table 4.5, these values are much lower than the reported intrinsic PDMS permeability by Merkel *et al.* (1999) at 400 Barrer and 3 800 Barrer for N_2 and CO_2, respectively. Nevertheless, this is arguable due to the different crosslinking reaction used. Permeability values of other works using the same PDMS fabrication chemistry as in the current work were also low. Studies on PDMS crosslinking temperature by Berean *et al.* (2014) have suggested that permeability is only weakly dependent on it. Meanwhile, Hu *et al.* (2018) which dip coated TEOS/DBD catalysed PDMS onto PAN fiber found that TEOS concentration, solution stirring time, and solution standing could affect the permeance and selectivity of the resulting membrane. Nevertheless, all their results were eventually plateaued at CO_2/N_2 selectivity of 9-11, much like the free PDMS layer in this work. Hence, minor differences in mixing methodology or ratio should not be the reason for lower permeability of TEOS/DBD catalysed PDMS when its selectivity has reached the maximum free-standing value. Dong *et al.* (2020) discussed two types of PDMS crosslinking, namely (i) addition type, which utilized PDMS with vinyl groups and (ii) condensation type, which utilized PDMS with hydroxyl groups. It is possible that these two crosslinking methods would give different intrinsic permeability. However, so far, no reliable literature has been found to note or address on this. Possible effect by densification or insufficient drying period in this work has also been rebutted before from results in Figure 4.16 and can be excluded.

Table 4.5: Comparison of PDMS CO_2 and N_2 permeability in literature

PDMS fabrication	Permeance (GPU)		ℓ (μm)	Permeability (Barrer) [a]		Selectivity (CO_2/N_2)	Ref.
	CO_2	N_2		CO_2	N_2		
Wacker Silicones Corp. (proprietary)	-	-	35	3800	400	9.5	(Merkel *et al.*, 1999)
Sylgard 184 (proprietary)	-	-	155	3180	360	8.8	(Berean *et al.*, 2014)
Sylgard 184 (proprietary)	-	-	1000	4541.6	-	-	(Firpo *et al.*, 2015)
Specialty Silicone Products Inc. (proprietary)	-	-	250	3100	290	10.7	(Houston *et al.*, 2002)
PDMS (unspecified, proprietary)	280	-	12	3360	280	12	(Hao *et al.*, 2020)
PDMS (unspecified, proprietary)	6100	-	0.082	500.2	41.7	12	(Hao *et al.*, 2020)
PDMS/ TEOS/DBD in heptane	7780	811	0.08	622.4	64.9	9.6	(Li *et al.*, 2019)
PDMS/ TEOS/DBD in heptane	2370	230.1	0.49	1161.3	112.7	10.3	(Hu *et al.*, 2017)
PDMS/ TEOS/DBD in heptane	34.4	2.5	50.7	1746.5	126.3	13.8	This work [sample P(4.0)]
PDMS/ TEOS/DBD in heptane	41.1	3.87	50.7	2086.26	196.6	10.6	This work [free PDMS layer of sample P(4.0)]

[a] For results reported in GPU, permeability was calculated based on the permeance divided by the thickness of the PDMS layer

The loss in permeability might also be caused by the dependence of PDMS permeability on its thickness. Firpo *et al.* (2015) using the model developed by Islam and Buschatz (2005) to evaluate the permeability of PDMS and found that the PDMS permeability become thickness dependent below 50 μm due to restricted surface reaction. The apparent permeability, P_{app} dependency on the thickness ℓ is given by the equation:

$$P_{app} = \frac{(\frac{k_1}{2})\ell}{1 + (\frac{k_2}{2D})\ell} \tag{4.1}$$

Where D is diffusion coefficient, and k_1, k_2 is the sorption and desorption rate, respectively. In turn, the intrinsic permeability, P_{int} can be determined from the equation:

$$P_{int} = \frac{1}{2} k_1 \frac{2D}{k_2} \tag{4.2}$$

This concept is also quite similar to the loss of permeance by lateral diffusion for composite thin films in the work of Wijmans and Hao (2015) and Hao *et al.* (2020), albeit through different mechanisms. The apparent permeance, $\mathcal{P}_{app}$ is related to the intrinsic permeance, $\mathcal{P}_{int}$ by the equation:

$$\mathcal{P}_{app} = \Psi \mathcal{P}_{int} \tag{4.3}$$

$$\Psi = \frac{\varepsilon_s + 1.6 N_R^{1.1}}{1 + 1.6 N_R^{1.1}} \tag{4.4}$$

$$N_R = \frac{\sigma . \tau . \varepsilon_s}{1 - \varepsilon_s} \tag{4.5}$$

$$\tau = \ell / r \tag{4.6}$$

Where Ψ is called restriction factor, ε_s is the substrate surface porosity, N_R is dimensionless Restriction Number, σ is the uniformity coefficient, ℓ is the thickness of the thin layer, and r is pore radius. $\mathcal{P}_{int}$ can then be related to the P_{int} as $P_{int} = \mathcal{P}_{int}\, x\, \ell$.

As noted in Table 4.5, PDMS membrane made with TEOS/DBD in heptane in the cited literature were all less than 1 μm, which could be significantly affected by either of these phenomena. By comparing literature data with results from Equation (4.1), or by calculating $\mathcal{P}_{int}$ from the substrate data in the literature using Equation (4.3), PDMS permeability can be compared between each other, as presented in Table 4.6. In all cases, only CO_2 was compared, and the reported permeability in literature was taken as the apparent value, as $P_{app} \approx P_{int}$ as $\ell \to \infty$. Using the literature's experimentally fitted coefficient for Equation (4.1), P_{app} was overestimated for thick membranes and underestimated for thin membranes, even when using the error upper limit of k_1 and error lower limit of $\frac{k_2}{2D}$ value to obtain the least P_{int} at 5 179 Barrer (Firpo *et al.*, 2015). While this value is comparable with their own experimental P_{int} range between 3 330.5 and 5 752.6 Barrer, the error was too large for this work to predict or gain significant conclusion on the effect of thickness.

On the other hand, Equation (4.3) was limited only to those literature with available substrate data. Nevertheless, Li *et al.* (2019) gave quite a similar P_{int} at 2256 Barrer as compared to the permeability of free PDMS layer in the current work at 2086 Barrer. With experimentally verified degree of penetration at 0.009, this suggested that PDMS/TEOS/DBD in heptane have a different P_{int} as compared to the known PDMS P_{int} at 3800 Barrer.

Table 4.6: Comparison of apparent CO_2 permeability, P_{app} from Equation (4.1) and calculated CO_2 intrinsic permeability, P_{int} from Equation (4.3) with experimental CO_2 permeability, P_{exp}

PDMS fabrication	**CO_2 P_{exp} (Barrer)**	**ℓ (μm)**	**CO_2 P_{app} (Barrer, Eq. (4.1))** [a]	**CO_2 P_{int} (Barrer, Eq. (4.3))** [#]	**Reference**
Wacker Silicones Corp. (proprietary)	3800	35	2956.2	-	(Merkel *et al.*, 1999)
Sylgard 184 (proprietary)	3180	155	4427.3	-	(Berean *et al.*, 2014)
Sylgard 184 (proprietary)	4541.6	1000	5046.2	-	(Firpo *et al.*, 2015)
Specialty Silicone Products Inc. (proprietary)	3100	250	4685.7	-	(Houston *et al.*, 2002)
PDMS (unspecified, proprietary)	3360	12	1622	3378.4 [b]	(Hao *et al.*, 2020)
PDMS (unspecified, proprietary)	500.2	0.082	16.1	1126.3 [b]	(Hao *et al.*, 2020)
PDMS/ TEOS/DBD in heptane	622.4	0.08	15.7	2256.0 [c]	(Li *et al.*, 2019)
PDMS/ TEOS/DBD in heptane	1161.3	0.49	94.7	-	(Hu *et al.*, 2017)
PDMS/ TEOS/DBD in heptane	419.4	1.2	225.9	446.3 [d]	This work [sample P(0.5)]
PDMS/ TEOS/DBD in heptane	1746.5	50.7	3409.35	1748.4 [d]	This work [sample P(4.0)]
PDMS/ TEOS/DBD in heptane	2086.26	50.7	3409.35	-	This work [free PDMS layer of sample P(4.0)]

[a] For Equation (4.1): $k_1 = 13\ x\ 10^{-8}$ mol.m^{-2}.s^{-1}.Pa^{-1}, $\frac{k_2}{2D} = 3.8\ x10^4$ m^{-1}. Data from Firpo *et al.* (2015).
[#] For Equation (4.4) - (4.6): [b] $\varepsilon_s = 0.040$, $\ell = 12$ and $0.082\ \mu m$, $r = 0.007\ \mu m$. [c] $\varepsilon_s = 0.048$, $\ell = 0.080\ \mu m$, $r = 0.018\ \mu m$. [d] $\varepsilon_s = 0.282$, $\ell = 1.2$ and $50.7\ \mu m$, $r = 0.082\ \mu m$.

Meanwhile, results from Hao *et al.* (2020) were mixed with significantly lower P_{int} for thin coating but comparable P_{int} for thick coating. This is however, expected as both Hao *et al.* (2020) and Ghadimi *et al.* (2018) have noted that initial N_R calculation did not consider the pore size distribution or surface pore uniformity. Nevertheless, while its theoretical origin is proven through CFD and the resulting uniformity coefficient, σ was introduced to include this effect (Hao *et al.*, 2020), determining σ value is currently still arbitrary through error minimization (Ghadimi *et al.*, 2018) with no empirical or first-principle model for accurate prediction. Considering this uncertainty, P_{int} from the work of Li *et al.* (2019) using PDMS/TEOS/DBD in heptane might have a much higher value. On the other hand, calculation from the current work was highly underestimated, probably due to the significant solution intrusion effect as noted from Figure 4.17 for post-coated PES substrate, compared to the permeance of pre-coated PES substrate. As such, reason for discrepancy of the current work's P_{int} with the known acceptable PDMS P_{int} could not be concluded without further data availability. Notwithstanding, while the differences in P_{int} could be important, it should not affect the subsequent analysis in this work. Hence, the free standing PDMS permeability value calculated in this work should be used instead as the intrinsic base PDMS permeability for further analysis.

Similar approach to quantify a composite membrane by separating the layer has also been reported by Li *et al.* (2019), but by dissolving PSf substrate in NMP instead of manually separating the PDMS layer from its substrate. This allows for manipulation of thinner PDMS layer, which is impossible to be made in this work. However, the authors only utilize this approach for thickness measurement, and with the assumption that PDMS solution penetration is a mixture of complete filling of small pores, and division of larger pores into smaller ones. This is agreeable based on

the SEM micrographs in Figure 4.14 and permeation results in Figure 4.17 for separated PES substrates, where increased CO_2/N_2 selectivity and reduction in permeances suggested that the solution penetration was not completely filling all the pores to register selectivity on par to a dense structure, yet the degree of solution penetration were high enough to cause separation above the Knudsen selectivity values.

4.2.5 Contribution of Solution Intrusion and Lateral Diffusion

N_2 gas flow resistance of the precoated substrates (after dried at 70 °C as in Section 4.2.1, but before PDMS coating), pre-dried substrates (substrate as in Section 4.1), composite membranes, and its derivatives were calculated from permeation test result, as represented in Figure 4.18. Composite membranes exhibit an increasing resistance with increased PDMS mass coating for all type of substrates used. The lowest increment is for composites of pristine substrates, ranging from 0.003 ± 0.001 $(GPU.cm^2)^{-1}$ for P(0.5) to 0.034 ± 0.002 $(GPU.cm^2)^{-1}$ for P(4.0), while the highest increment is for composites of LiCl_4% substrates, ranging from 0.018 ± 0.002 $(GPU.cm^2)^{-1}$ for L4(0.5) to 0.117 ± 0.021 $(GPU.cm^2)^{-1}$ for L4(4.0). This is expected considering that resistance is the reciprocal to the permeance of the composite membrane, and permeance is expected to be reduced with increasing thickness. Nevertheless, the resistance was also increasing based on the type of substrates used in the order of LiCl_4% > LiCl_2% > pristine substrate. In fact, composite membranes have a much higher resistance as compared to the sum of the resistance by free PDMS and free PES substrate, up to an extra of 0.09 $(GPU.cm^2)^{-1}$; a value equal to almost 4x the resistance imposed by the free PDMS layer. Considering that the same thickness of PDMS layer was involved, this suggested that lateral diffusion have some contribution towards the total resistance of the composites, which is more severe for

LiCl_4% substrate with dispersed surface pore distribution. This is further supported by the consistent resistance of free PDMS dense layer of 4.0g sample at about 0.023 ± 0.001 $(GPU.cm^2)^{-1}$ regardless of the original substrate used to fabricate it.

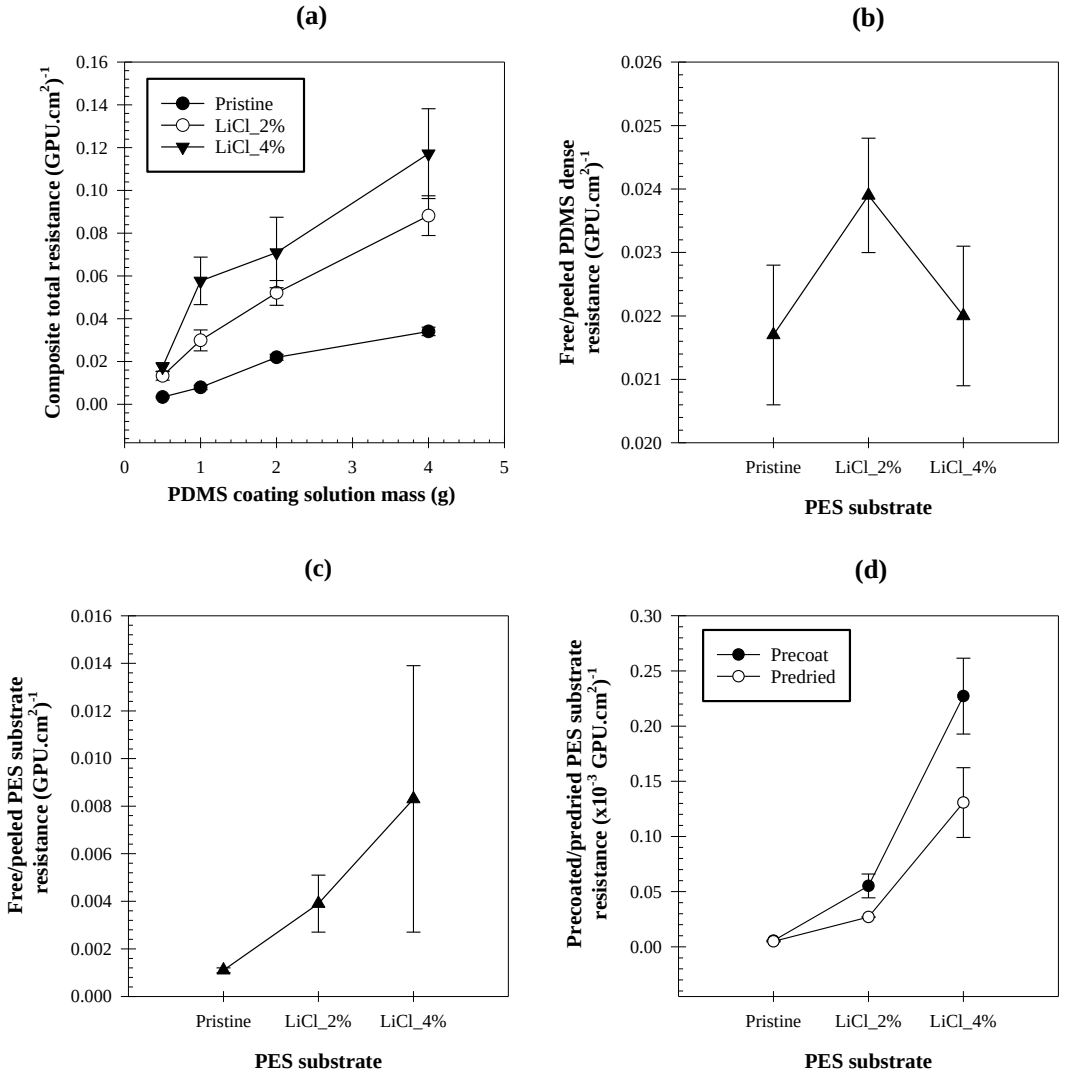

Figure 4.18: N_2 gas flow resistance of the (a) PES/PDMS composite membranes, (b) free/peeled PDMS dense layer from 4.0g PDMS samples, (c) free/peeled PES substrate layer from 4.0g PDMS samples, and (d) precoated and pre-dried PES substrates

It is also interesting to note that the resistance of free substrates was also increasing in the order of LiCl_4% > LiCl_2% > pristine substrate at 0.008 ± 0.006 $(GPU.cm^2)^{-1}$, 0.004 ± 0.001 $(GPU.cm^2)^{-1}$ and 0.001 ± 0.001 $(GPU.cm^2)^{-1}$ respectively, supporting the hypothesis above. However, the deviation is increasing quite

significantly for LiCl_2% substrate and especially for LiCl_4% substrate, suggesting that solution penetration is inconsistent throughout the composite membrane. These values on the other hand, are far higher than the resistance of all precoated PES substrates. Pristine substrate has the highest increment of at least 19 000 % from initial resistance at 0.000006 ± 0.000001 $(GPU.cm^2)^{-1}$ while LiCl_4% substrate has the lowest increment of at least 3 600 % from initial resistance at 0.00023 ± 0.00003 $(GPU.cm^2)^{-1}$. Minimal differences were also seen between precoated and pre-dried substrate, especially for pristine sample. Drying of the substrates at 70 °C in a way could increase the resistance of the pre-dried sample especially for LiCl_4% substrate but it still needs to be at least 85x higher to reach the value obtained from the separated substrate layer. Hence, it is safe to assume that the drying methodology used in this work have negligible effect on the increase of substrate resistance.

Similarly, CO_2 gas flow resistance of the pre-dried substrates, composite membranes, and its derivatives were calculated from permeation test result, as represented in Figure 4.19. The same CO_2 resistances trend as in N_2 resistances were noted for all cases with substrates used in the order of pristine < LiCl_2% < LiCl_4%, although with a lower value of resistances except for pre-dried substrates. Lowering of composite and free dense PDMS resistances are self-explanatory as CO_2 is more permeable in PDMS compared to N_2. On the other hand, pre-dried substrate's CO_2 resistance are higher than N_2 resistance as Knudsen flow in the porous substrate is more restrictive towards CO_2 with larger molecular weight as compared to N_2. However, lower free substrate CO_2 resistance compared to N_2 resistance, and the increment of the resistance value from its pre-dried value would only occur when PDMS intruded into the substrate. Meanwhile, lower resistance gains by the composite as compared to the sum of the resistance by free PDMS and free PES substrate at only

0.002 $(GPU.cm^2)^{-1}$; a value equal to only 1x the resistance imposed by the free PDMS layer suggest that lateral diffusion is less severe when measured using CO_2. With PES permeability of 3.22 Barrer for CO_2 and 0.07 Barrer for N_2 (Chen *et al.*, 2017) some of the restricted CO_2 might pass through the dense part of the PES substrate instead, contributing to the increased composite selectivity noted in Figure 4.15.

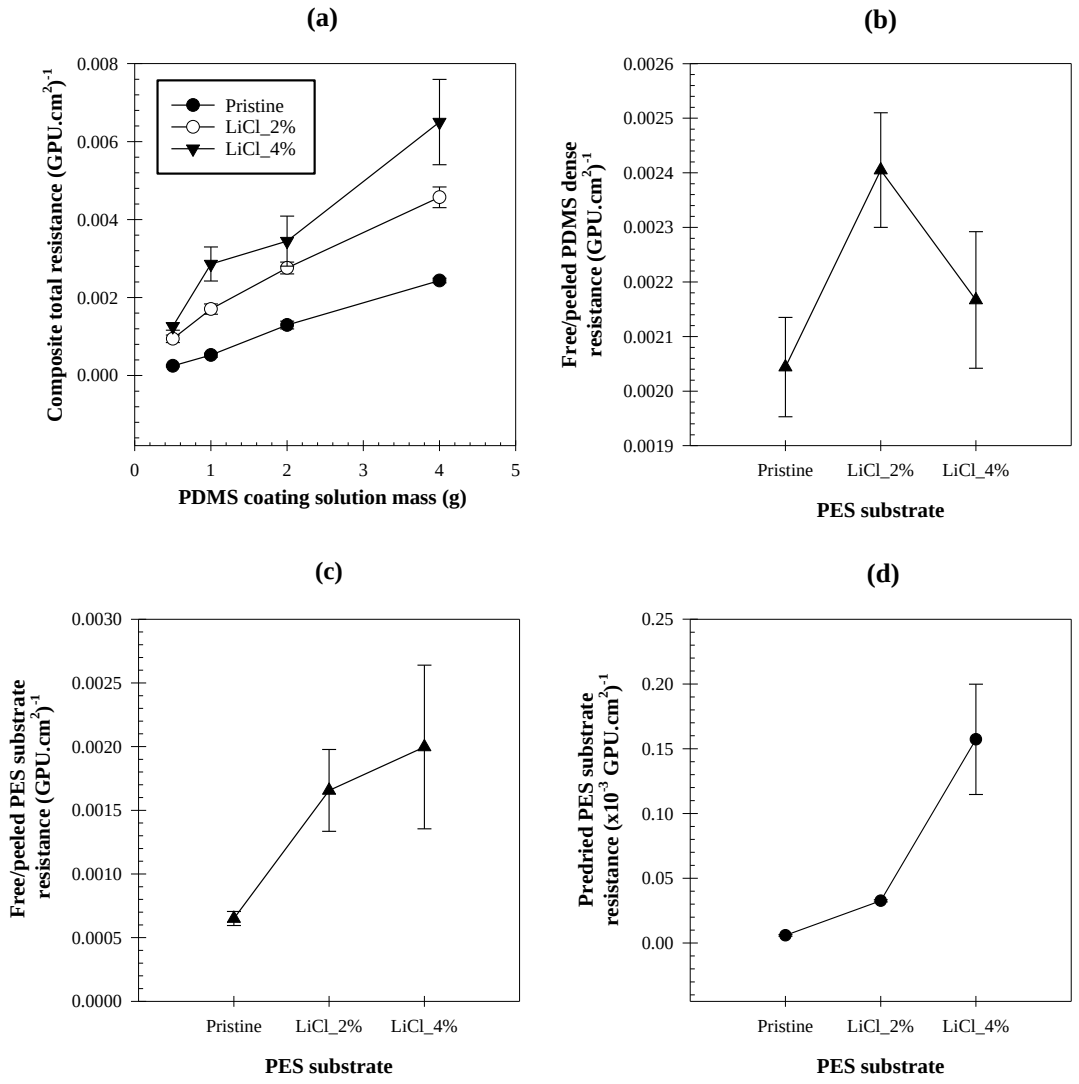

Figure 4.19: CO_2 gas flow resistance of the (a) PES/PDMS composite membranes, (b) free/peeled PDMS dense layer, (c) free/peeled PES substrate layer, and (d) pre-dried PES substrate

From the resistance calculated, two observations can be made: (i) sum of the individual peeled PDMS and peeled PES layers did not equal to the composite total resistances, and (ii) resistances of peeled PES layers are far higher than its precoated

values. These two observations suggested that both lateral diffusion and solution penetration contributed to the increased resistance above their ideal values, which can also occur for any composite membrane structures.

4.3 PMP Based Membrane – Self-Supporting Asymmetric Membrane Performance as Co-Substrate/Gutter Layer

As discussed earlier, composite structures with dense-porous interface would have additional possible problems mainly through lateral diffusion and pore intrusion. In this subchapter, interest is given towards the possibility of dense skin asymmetric membrane as both substrate and gutter layer. Nevertheless, using only a single material means that the role of mechanical strength of substrate and high permeability of gutter layer needs to be considered at the same time, limiting possible material choices. PDMS for example, has mainly been used as the gutter layer due to its high permeability (Dai *et al.*, 2016). However, being a rubbery polymer, it is unsuitable for self-supporting purposes, requiring PDMS thin film to be supported on top of another porous layer; hence the work conducted in the previous subchapter.

In this sense, possibility of high permeability glassy polymer as co-substrate-gutter was elucidated. Poly(4-methyl-1-pentene) (PMP) for example, has not been reported as a gutter layer, despite of its relatively high permeability at about 9.87 and 128 Barrer for N_2 and CO_2 respectively (Yasuda and Rosengren, 1970). Indeed, the value is below the permeability of PDMS, but PMP is advantageous as its high permeability, yet glassy structure should allow it to be used as both support and gutter layer. With thin enough dense layer, the performance of asymmetric PMP could compete with a composite PDMS membrane but without their complications. Hence, prospect from studying the base performance of asymmetric PMP membrane will determine the feasibility of it as support-gutter layer for subsequent studies.

4.3.1 Morphological and Chemical Validation

The morphology of the membrane was examined through FE-SEM for both surface and cross section, represented in Figure 4.20. Dense surface layer was noted from the surface micrograph with no visible sign of pores. Meanwhile the cross section of the membranes was noted to exhibit finely porous substructure. However, the cross section of the dense skin layer is barely visible.

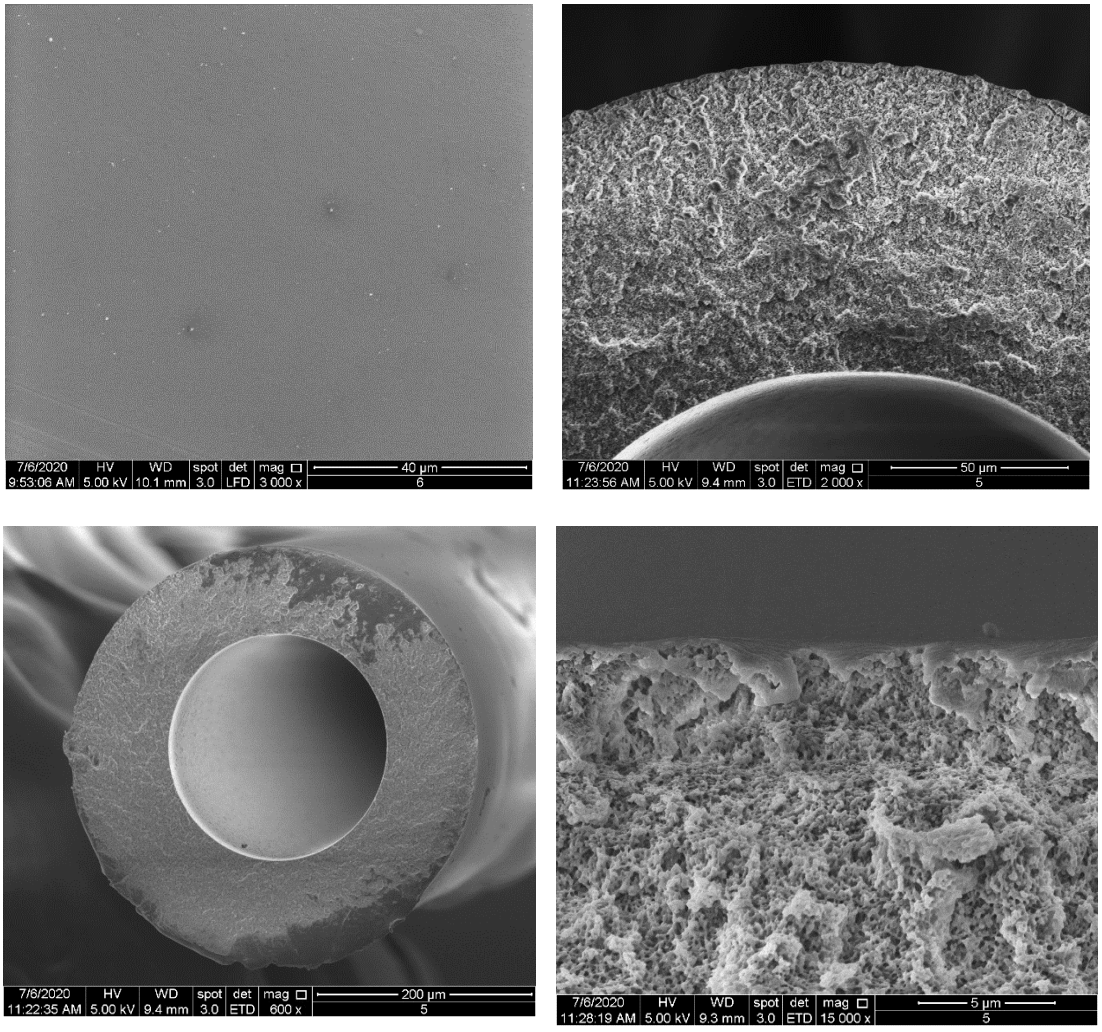

Figure 4.20: (Top, left) surface micrograph at x3K magnification, (top, right) cross-sectional micrograph at x2K magnification, (bottom, left) overall cross-sectional micrograph at x600 magnification, and (bottom, right) cross sectional micrograph near the surface at x15K magnification of commercial PMP hollow fiber membrane

With measured outer membrane radius of 193.8 ± 0.2 μm, inner radius of 103.6 ± 0.2 μm, and resulting membrane thickness of 90.2 ± 0.1 μm, these values are comparable to the specification sheet provided by the supplier (3M, 2019). The thickness of the PMP membrane is also comparable to the thickness of PES substrates at 82-98 μm in the previous subsection. However, the dense skin thickness is too thin to be measured accurately using SEM. This will thus be approximated later from gas permeation data of this work and permeability results from the literature.

To validate the materials of the membrane, FTIR was employed for the hollow fiber (HF) sample and was compared with the PMP pellets, as represented in Figure 4.21. For all samples, peaks were noted at around 1380 and 1470 cm^{-1} due to bending of CH_2-CH_2 bond, and in the ranges of 2800-3000 cm^{-1} due to symmetric and asymmetric stretching vibration of CH_2 and CH_3 (Michaljaničová *et al.*, 2016, James Jebaseelan Samuel and Mohan, 2004). Similarity between the PMP pellets and PMP HF spectra suggested that the membrane is made only from PMP. However, being polyolefin, polymer such as polypropylene (PP) would also possess similar spectra as PMP. This is important to be elucidated as PP and PMP possess different intrinsic permeability. Meanwhile, there has been mixed report in literature on the nature of the membrane, whether being a composite membrane with PP porous substrate (Chabanon *et al.*, 2011, Villeneuve *et al.*, 2018) or an integral asymmetric single material structure (Madhani *et al.*, 2016, Faria *et al.*, 2018).

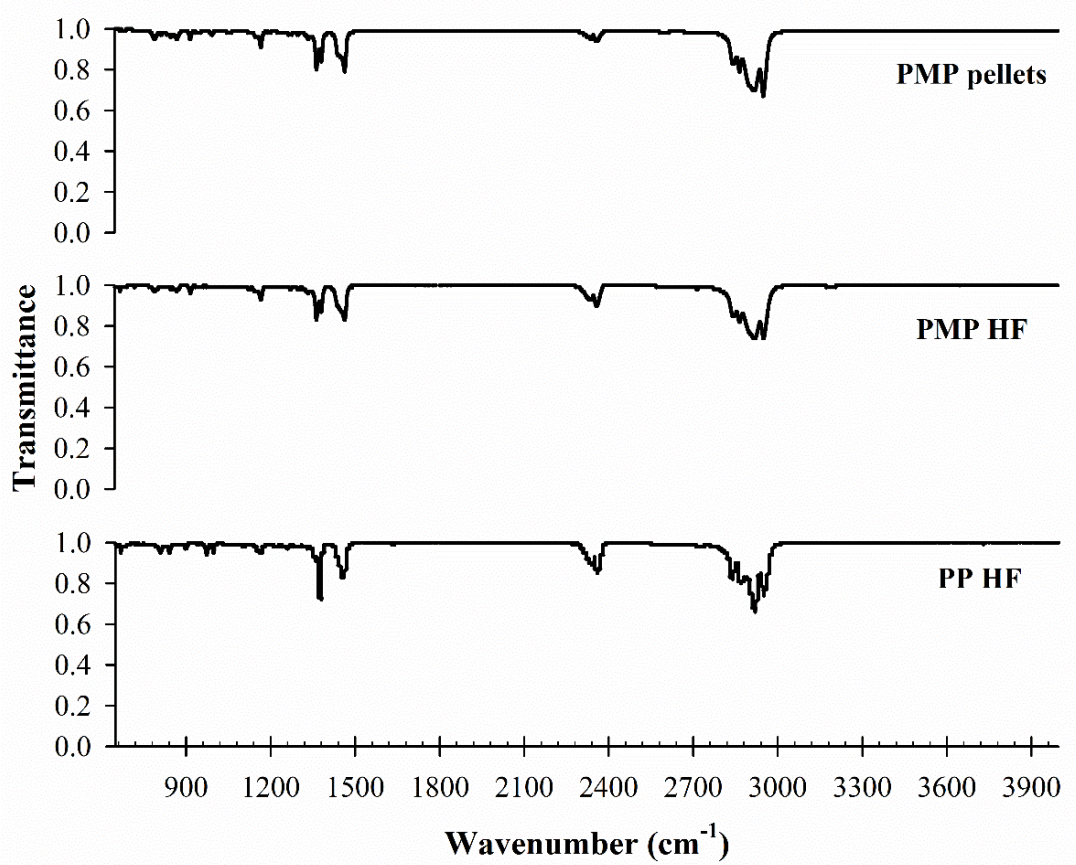

Figure 4.21: PMP pellets full range FTIR spectra against dense skin asymmetric PMP hollow fiber and porous polypropylene (PP) hollow fiber

However, detailed analysis between 1300 and 1500 cm^{-1} in Figure 4.22 suggested some minor differences, especially where only a single peak at 1375 cm^{-1} was noted for PP sample as compared to PMP sample, which possess two peaks at 1365 and 1380 cm^{-1}. Reasons for the differences are out of the scope and interest of the thesis, but with dense skin thickness of 0.1 ± 0.1 µm (to be measured later in Table 4.8), and with expected FTIR depth resolution of at least 0.4-0.7 µm at these wavenumber range (Shimadzu, 2021), the PMP membrane would possess the PP spectrum should it be a composite membrane. As it is absent, the membrane is thus an asymmetric membrane made up of only PMP.

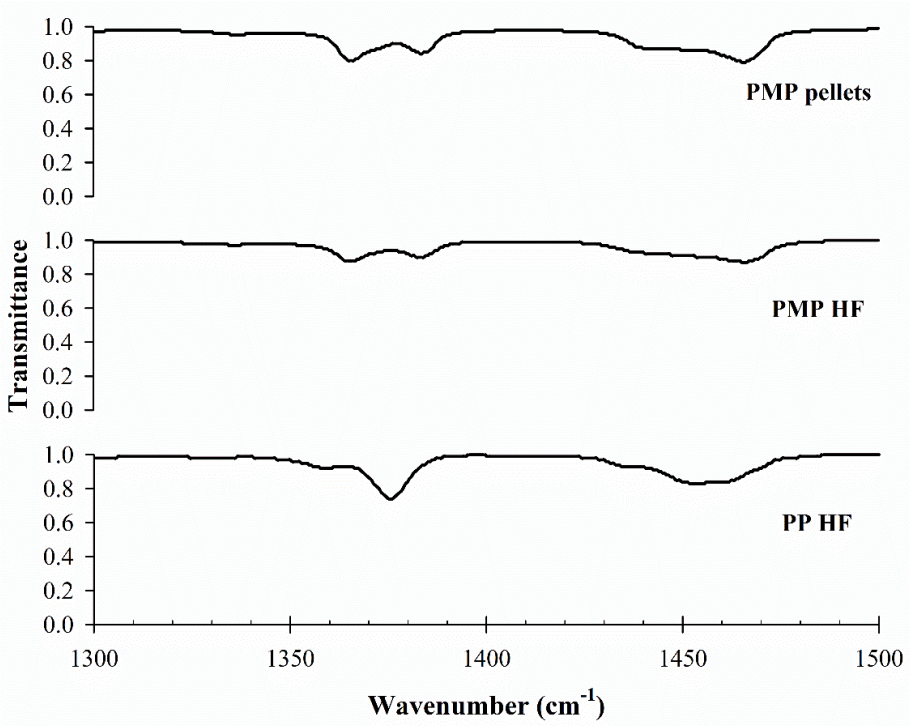

Figure 4.22: Zoom-in spectra at 1300-1500 cm^{-1} of the PMP pellets against dense skin asymmetric PMP hollow fiber and porous polypropylene (PP) hollow fiber

4.3.2 Gas Separation Performance and Overall Resistance

The commercial dense skin asymmetric PMP HF membrane used for this study was originally developed for blood oxygenation application. Hence, for the PMP membranes repurpose from O_2 diffusion to other gases, single gas permeation test was done for N_2, CO_2, and CH_4, as noted in Table 4.7. Samples were tested at 5 bar to ensure the reliability of the membrane at an elevated pressure. Permeance results suggested the suitability of this membrane as both support and gutter layer in terms of its high permeance with increment in the order of $CO_2 > CH_4 > N_2$. On the other hand, the comparatively low CO_2/N_2 and CO_2/CH_4 selectivity means that the substrate-gutter layer will be relatively less selective; properties needed as a good gutter. The permeance value reported for PMP membrane here is also higher than the highest PDMS permeance reported earlier in Figure 4.15 for P(0.5) sample. The N_2 permeance

was also in the range reported in the data sheet of the supplier between 45-445 GPU (3M, 2019).

Table 4.7: Base performance of asymmetric PMP hollow fiber membrane

Gas	Permeance (GPU)	Selectivity		
		CO_2/N_2	N_2/CH_4	CO_2/CH_4
N_2	84.6 ± 6.2			
CO_2	607.3 ± 31.3	7.4 ± 0.4	0.6 ± 0.1	4.0 ± 0.2
CH_4	156.0 ± 13.1			

Indeed, the relatively high permeance value of PMP was achieved thanks to the thin dense skin layer obtained from the asymmetric membrane fabrication. While the same effect should be achieved for a composite membrane with thinner surface dense layer, the effect of lateral diffusion and possible solution penetration, however, cannot be completely removed (Li *et al.*, 2019, Wijmans and Hao, 2015). Meanwhile, pinhole defects would still be available as the composite coating layer becomes thinner. Hence, it is safe to say that a truly defect free thin dense skin asymmetric membrane would exhibit an ideal permeability and free from these limitations. The only thing that would limit the use of asymmetric membrane for this purpose is the material properties itself.

As mentioned before, the dense PMP layer thickness was too thin and thus cannot be measured accurately through SEM. However, this can be predicted from intrinsic permeability data from literature. Thickness ℓ, permeability P, and permeance $\mathcal{P}$ are related by the equation:

$$P = \mathcal{P}\ell \tag{4.7}$$

Using the permeation data in Table 4.7, thickness of the dense layer can then be approximated. Table 4.8 represents the permeability values reported in literature for PMP, and this work's expected thickness to achieve these permeabilities. The

thickness value is quite consistent even between different permeability value sources. Similar values have also been reported in literature that utilized this commercial membrane at 0.1 µm (Villeneuve *et al.*, 2018, Makhloufi *et al.*, 2014).

Table 4.8: PMP dense skin thickness approximation from literature permeability data, compared to permeance of this work

Permeability (Barrer)			**Theoretical skin thickness, µm**	**Reference**
N_2	**CO_2**	**CH_4**		
9.87	128	-	0.16 ± 0.04	(Yasuda and Rosengren, 1970)
7.4	99.1	-	0.13 ± 0.04	(Makhloufi *et al.*, 2013)
-	129.14	16.1	0.16 ± 0.05	(Nematollahi *et al.*, 2015)
6.7	84.6	14.9	0.10 ± 0.02	(Nunes and Peinemann, 2006)
9.26	107.5	19.8	0.14 ± 0.02	(Puleo *et al.*, 1988)
5.02	67.9	10.5	0.08 ± 0.02	(Puleo *et al.*, 1988)
5.93	73.8	13	0.09 ± 0.02	(Puleo *et al.*, 1988)
6.7	84.6	14.9	0.10 ± 0.02	(Mohr and Paul, 1990)
6.5	83	13.1	0.10 ± 0.02	(Mohr and Paul, 1990)
5.36	-	12.1	0.07 ± 0.01	(Roux and Paul, 1992)
7.6	84	12.7	0.10 ± 0.02	(Markova *et al.*, 2020b)
7.03	94.16	14.12	0.11 ± 0.01	Average thickness

Nevertheless, thickness calculation through this method highly depends on the hypothesis that the permeability of the asymmetric membrane is the same as its intrinsic value. Hence, it is also interesting to compare the performance results noted here with the results in the literature, which is represented by Table 4.8. In average, CO_2/N_2 selectivity of PMP was reported at 12.6 ± 0.3 while CO_2/CH_4 selectivity was reported at 6.2 ± 0.3, quite high as compared to the selectivity in this work. On the other hand, N_2/CH_4 selectivity was reported at an average of 0.5 ± 0.1, which is comparable to the current work. While this may increase the skin thickness error, by considering lower actual permeance of N_2 and CH_4 in this work to reach the intrinsic selectivity in the literature, the skin thickness should still be in the range of ± 0.1 µm.

Comparable ideal permeability and selectivity between asymmetric and dense membrane has been reported in literature (Kumazawa *et al.*, 1993, Chen *et al.*, 2017, Barsema, 2003). Nevertheless, significant deviation has also been reported elsewhere (Han *et al.*, 2010, Kawakami *et al.*, 1996). One of the most common explanations for the discrepancy is due to defect formation as at very low dense thickness, defect-free membrane is hard to be made. This can be partially proven when selectivity of the asymmetric membrane is lower than the intrinsic value, such as in this case. On the other hand, considering that the PMP membrane is commercial, it is common for the membrane to be post-processed or for the PMP to be blended with proprietary co-monomer (Puleo *et al.*, 1988), which may have a different intrinsic permeability value. Nevertheless, no traces of both claims were noted from the FTIR and SEM analysis.

To mitigate this discrepancy, attempts were also made to fabricate dense PMP flat sheet membrane, with permeation results as in Table 4.9. The dense membranes, ranged between 10.3-16.1 μm in thickness (see Appendix H for thickness calibration), unfortunately exhibited even lower permeance and selectivity as compared to the commercial membrane and as compared to the literature. This suggested that fabrication of dense PMP through solvent casting is harder than expected due to weak solvation of PMP in cyclohexane around the room temperature. Therefore, pinhole defects could still be formed even for thick dense membrane. Nevertheless, separation still occurred and the permeances in Table 4.9 were comparatively high considering its high thickness. For application as co-substrate-gutter layer, the use of the current commercial PMP membrane is still beneficial as the thinner asymmetric membrane would possess much higher permeance. The defects, if any, should be very minimal since the selectivity is comparatively higher than the

casted membrane. Hence, further modification work was conducted on the commercial membrane instead while the development and optimization of PMP membrane as co-substrate-gutter layer will be left for future research work.

Table 4.9: Permeance and selectivity of PMP dense membrane

Casting method	Thickness (μm)	Permeance (GPU)			Selectivity		
		N_2	CO_2	CH_4	CO_2/N_2	CO_2/CH_4	N_2/CH_4
Petri dish, 2 wt. %	10.9 ± 0.6	2.4 ± 1.4	6.9 ± 2.6	2.9 ± 1.5	3.4 ± 0.9	2.6 ± 0.4	0.8 ± 0.1
Petri dish, 2 wt. %	15.7 ± 0.4	1.2 ± 0.4	3.3 ± 0.7	1.6 ± 0.5	3.0 ± 0.5	2.1 ± 0.1	0.7 ± 0.1
Glass plate, 3 wt.%	-[#]	1.7 ± 0.9	2.9 ± 0.7	-	2.1 ± 0.7	-	-

[#] Casted using 500 μm blades. Final thickness not measured

On the other hand, mechanical and performance stability of the self-supporting HF membrane may be compromised as PMP possess glass transition temperature, T_g at around 30-40 °C (Lopez and Wilkes, 1992, Roux and Paul, 1992). To elucidate this problem, the normalized permeance of N_2 between 25-35 °C was recorded and presented in Figure 4.23. It was noted that the permeance was stable below 30 °C but starts to degrade when tested above 30 °C. This reduction was noted to be irreversible upon the second set of testing, where 12% of permeance loss was noted between 35 °C (1st test) and 25 °C (2nd test). The permeance then increased with permeation temperature for the 2nd test, with final permeance loss of about 8% between 35 °C (1st test) and 35 °C (2nd test). Despite of this, the reduction in permeance is still manageable as the base performance reported in Table 4.7 was conducted at 35 °C.

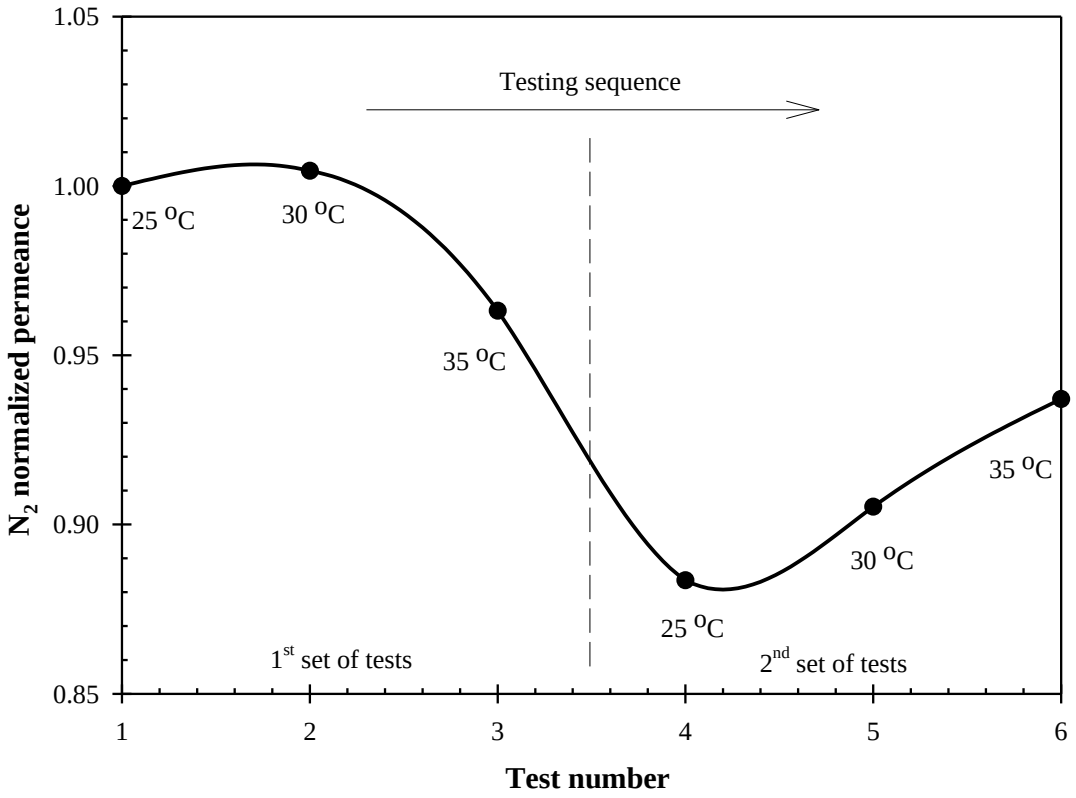

Figure 4.23: N_2 normalized permeances across the PMP asymmetric hollow fiber membranes at temperature range between 25-35 °C

Physical properties of polymer start to change when it reached its T_g. Dramatic loss of PMP's tensile strength has been reported in Reddy *et al.* (1997) at around 45 °C, which could also affects the membrane's performance. Hence, changes in permeance values were also expected when the membrane was studied near to this temperature. It is possible that the rearrangement of the polymer molecules near to the membrane surface caused the decrease in permeance, and later was fixed when the fibers were tested again (2nd test) at lower temperature. This is also supported by the increased permeance during the 2nd set of tests from 25 °C to 35 °C. The explanation of polymer rearrangement is also supported by the work of Fu *et al.* (2016) on the degree of crystallinity and Lopez and Wilkes (1992) on crystal rearrangement, as discussed earlier in Table 2.7.

Finally, total resistance of the membranes was calculated, as represented in Figure 4.24. As resistance is a function of permeability or permeance, the increased resistance of N_2, followed by CH_4 and lastly CO_2 is expected. The resistance of N_2 and CO_2 in PMP was lower than that of the PES/PDMS substrate-gutter layer in previous subchapter at (0.0034 ± 0.0004 $(GPU.cm^2)^{-1}$ and 0.0002 ± 0.0001 $(GPU.cm^2)^{-1}$ for N_2 and CO_2 respectively, for P(0.5) sample). It is suggested that the integral asymmetric dense skin membrane is much suited or at least comparable as co-substrate-gutter layer in terms of layer resistance contribution.

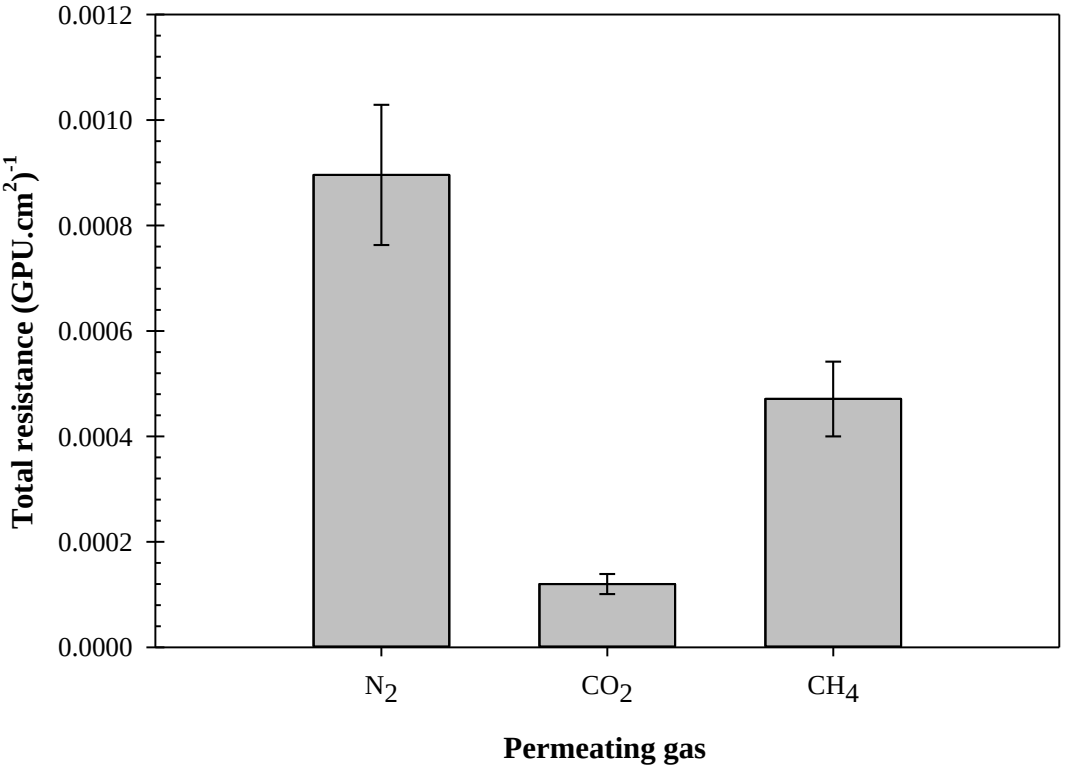

Figure 4.24: Resistance contribution of asymmetric PMP membranes by N_2, CO_2, and CH_4

Nevertheless, literature work such as by Pinnau and Koros (1991) has noted that high resistance of the underlying porous structure of an asymmetric membrane may still significantly affecting the membrane's performance. The overall selectivity could become substructure dependent even when the surface skin layer is defect free. Consequently, selectivity decreased significantly towards Knudsen

selectivity of the substructure. Influence of the porous base is also true for composite membranes, such as in the work of Wu *et al.* (2018) where 5% of resistance was contributed by the PES substrate. Pinnau and Koros (1991) has suggested that the substructure layer to have at least 10x permeability for the fast-permeating gas than the skin layer to avoid being substrate dependent. In this work, high porosity of the PMP asymmetric membrane substructure reported at ≥50% (3M, 2019) and high permeability of the commercial PMP membrane material should allow for the overall membrane to exhibit very low resistance. However, one can also deduce that the reduction in selectivity noted in Table 4.7 and Table 4.9 is due to the substructure resistance as mentioned earlier. Resistance contribution by lateral diffusion in composite membranes remains much higher at 25-30% as compared to the Knudsen resistance contribution of the substrate (Wu *et al.*, 2018). In this sense, asymmetric dense skin membrane should pose to be a better substrate-gutter structure for composite membrane fabrication. Hence, the effect by lateral diffusion and solution penetration of composite membranes, and comparison of these effects with asymmetric membranes will be elucidated in the next subchapter.

4.4 Influence of Geometric Restriction and Solution Intrusion Using Resistances-in-Series Model and CFD Across Substrate-Gutter Layer

Previous subchapters have shown that both composite and asymmetric configurations are suited to be used as substrate and gutter layer. Nevertheless, both approaches have their own specific limitations. In summary:

(i) Composite structure requires at least two materials and hence increased fabrication complexity, and susceptible to resistance increase due to lateral diffusion and solution intrusion.

(ii) Asymmetric structure limits the choice of material to those that can cope to function as both substrate and gutter layer.

In this subchapter, the contribution of solution penetration and geometric restriction that increased the resistance of composite membrane in Section 4.2 above its ideal minimum values were quantified. This was then compared to the resistance of asymmetric membrane in Section 4.3. By using the data from actual experiment, the limitations of the material properties itself can be considered. The effect of lateral diffusion and solution intrusion was also studied through 2D CFD across the dense-porous interface. Results from these theoretical evaluations would give a better understanding on how the resulting permeances and resistances were affected by the composite and asymmetric structures, and what can be done to minimize these effects.

4.4.1 Ideal Composite Permeance and Permeance Efficiency Factor

The permeability of PDMS in this work was fixed at 186.4 ± 7.6 Barrer and 1 914.1 ± 109.3 Barrer for N_2 and CO_2 respectively, based on the permeance results of peeled 4.0g PDMS dense layer from different substrates in Figure 4.17 and their corresponding thickness in Figure 4.11. As PDMS intrinsic permeability is constant regardless of the thickness, it can be used to calculate the corresponding ideal permeance of the coating at a specified thickness. Using this assumption and the thickness of other PES/PDMS composites, the ideal permeance of the composite, $\mathcal{P}_T^{ideal}$ can be determined using Equation (3.16). To recall:

$$\mathcal{P}_{T,i}^{ideal} = \left(\frac{\ell_1}{P_{c,i}} + \frac{1}{\mathcal{P}_{s,i}} \right)^{-1} \tag{3.16}$$

Where ℓ_1 is the thickness of the coating layer taken from Figure 4.11, P_c is the intrinsic permeability of the coating layer, and $\mathcal{P}_s$ is the permeance of the substrate taken from Figure 4.7.

Figure 4.25 represents the deviation of the measured permeance values from the ideal permeance noted from Equation (3.16), for both N_2 and CO_2 gas. Ideal permeances fitted well in a straight line across the log-log scale graph at R^2 of 0.99 for both gases, regardless of the substrates or the coating thickness. This suggested that the substrate's permeance did not contribute much resistance to the composite in an ideal condition. On the other hand, larger deviations between the measured and the ideal permeance values were noted as the coating thickness decreased in both cases. This trend is similar to the prediction in Wijmans and Hao (2015) which was later experimentally validated in Hao *et al.* (2020). As discussed in Section 4.2.4, the depreciation in permeance below its ideal value for thin coating was suggested to be contributed by lateral diffusion through the equation:

$$\mathcal{P}_{app} = \Psi \mathcal{P}_{int} \tag{4.3}$$

Where $\mathcal{P}_{app}$ is the apparent or measured permeance, Ψ is the correction factor called restriction factor, and $\mathcal{P}_{int}$ is the intrinsic permeance of the coating layer. The value of Ψ would be 1 when no lateral diffusion occurred and would be limited by the substrate's porosity at the value of $\Psi = \varepsilon_s$. This seems to be the case for all samples as the permeance reduction is noted to be plateaued on a line of similar gradient as the ideal permeance line (at m = -0.997 and -0.965 for N_2 and CO_2 respectively), as noted from the figure (dotted line). This lower limit, however, is different for pristine substrate but comparable for LiCl_2% and LiCl_4% composite. This is probably due to the difference in surface porosity.

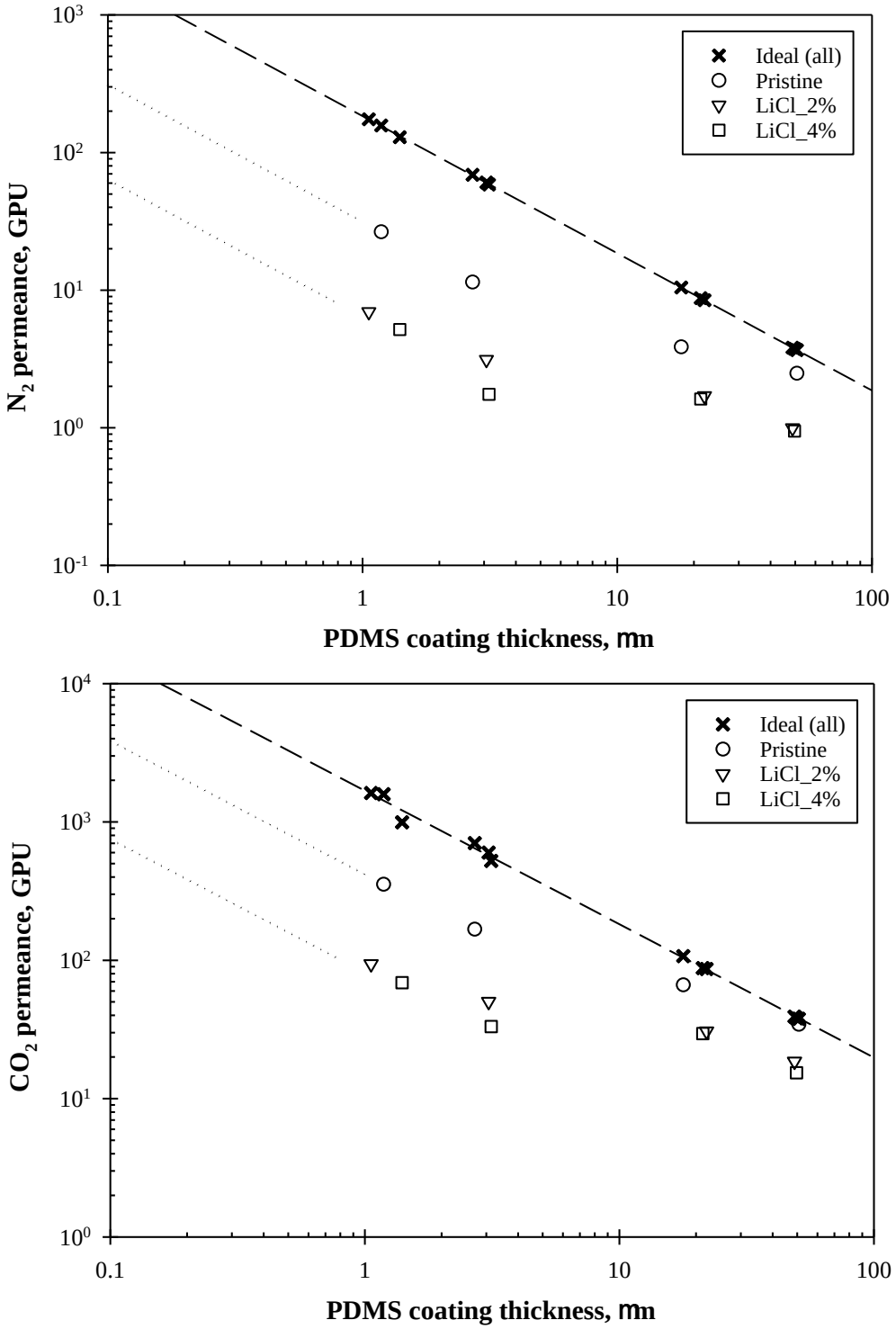

Figure 4.25: Deviation of measured composite permeance from the ideal value for N_2 and CO_2 gas

Nevertheless, Equation (4.3) neglects the influence of solution intrusion, which can also depreciate the measured permeance below the ideal value. Despite that there are no significant changes in coating thickness across different substrates in

Figure 4.11, effect of solution intrusion is still visible through reduction of peeled PES substrate's permeance in Figure 4.17 and increment of peeled PES substrate's resistance in Figure 4.18 and Figure 4.19. Work by Li *et al.* (2019) suggested that solution intrusion cannot be completely removed, and hence should also be considered in this case. Thus, the degree of permeance reduction or permeance efficiency, β were determined. To recall:

$$\beta = \frac{\mathcal{P}_{T,i}}{\mathcal{P}_{T,i}^{ideal}} \tag{3.17}$$

Where $\mathcal{P}_T$ is the measured or apparent composite permeance. β can then represents the actual depreciation of permeance value, based on the experimental data in this work. β will also be a factor of both solution intrusion and lateral diffusion.

Figure 4.26 represents the calculated β on different coating thickness and substrate used, for both N_2 and CO_2 gas. As $\beta = 1$ represents measured permeance which are equal to its ideal value, this suggested that the combined effect of solution intrusion and lateral diffusion is much severe in thinner coating. Nevertheless, as solution penetration should be maximum for thick coating (more mass or solution to penetrate), this suggested that lateral intrusion is much more dominant, at least for thin coating samples. Interestingly, β value of CO_2 is higher than the corresponding N_2 when compared between those of similar coating thickness and substrates used. This is especially true at higher coating thickness, but much less severe when the coating is thin. Li *et al.* (2019) which calculate the β value for both CO_2 and N_2 did noted negligible differences between the gases, in which they studied for selective layer thickness up to 0.20 nm. Meanwhile, Zhu *et al.* (2016b) also suggested a comparable β measured between CO_2, H_2, and N_2 for selective layer thickness up to 0.37 µm. For

the thinnest coating layer in the current work (at 1.0-1.4 μm), β was relatively comparable too, but starkly different at higher thickness.

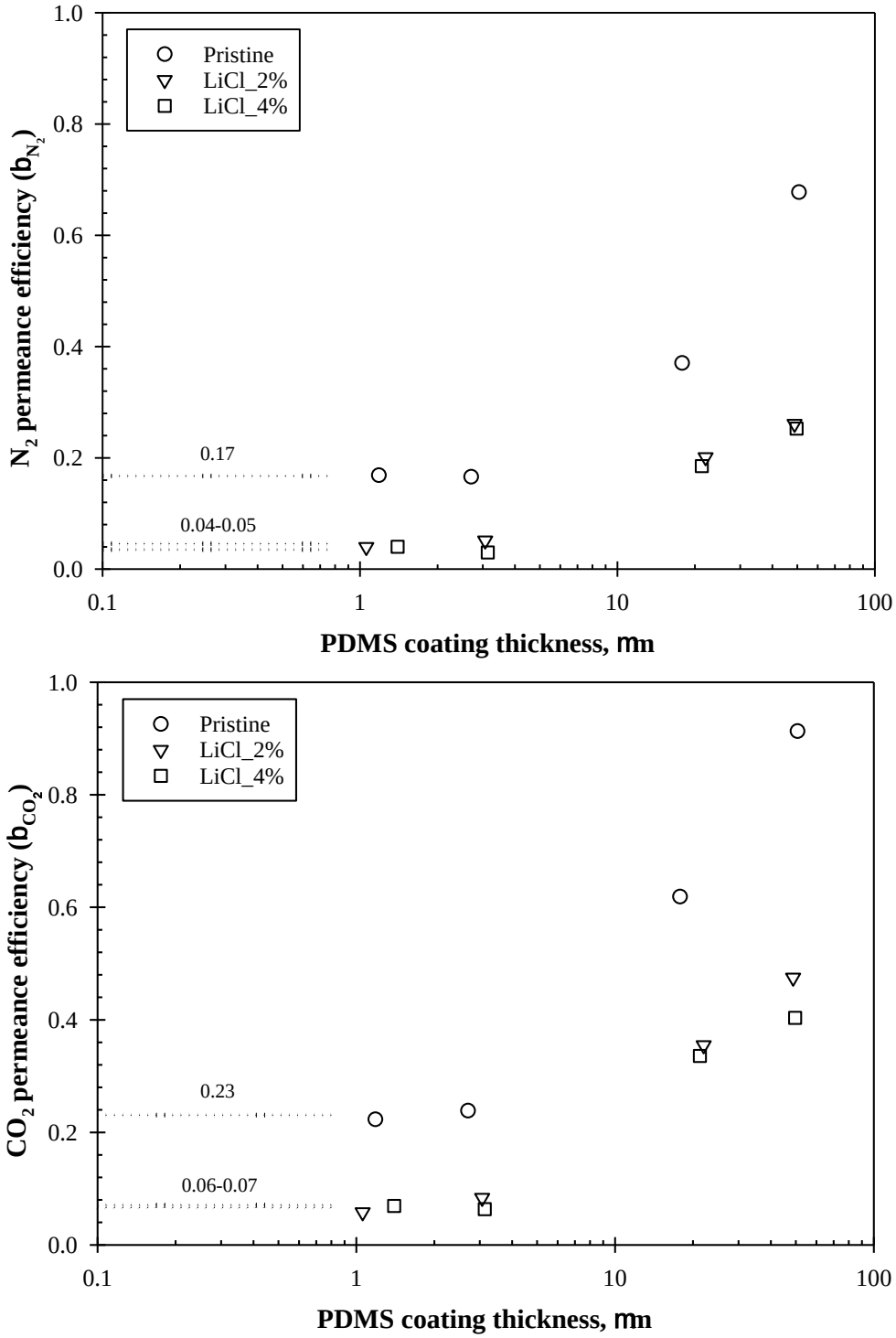

Figure 4.26: Calculated β of PES/PDMS composite membrane against the coating thickness on different substrates

As discussed previously, permeance reduction is noted to be plateaued on a certain line when the coating thickness is low. This is also noted in Figure 4.26 where

β become almost constant at low coating thickness. This value, however, differs depending on the substrate used, at about 0.17 for pristine substrates and 0.04-0.05 for LiCl_2% and LiCl_4% substrates for measurement using N_2. Neglecting the effect of solution intrusion at low coating thickness, the lower limit of β should be contributed only by lateral diffusion through Ψ, where $\Psi = \varepsilon_s$. A slightly increased lower β limit was also noted when using CO_2 at 0.23 for pristine substrates and 0.06-0.07 for LiCl_2% and LiCl_4% substrates, which is still comparable to the values obtained from N_2. These lower β limit was somehow comparable to the results in Table 4.4 for the back calculated substrate surface porosity using Knudsen equation. This is interesting as it suggested that the calculated surface porosity from the image analysis of the surface pore in Table 4.2 did not represent the true nature of the substrate. It is possible that the increased skin layer thickness of the substrate with LiCl content also increased the number of dead pores which do not contribute to the gas permeation (Zhu *et al.*, 2016b).

Calculation of $\mathcal{P}_T^{ideal}$ and β so far has been made directly using experimental permeation data in subchapter 4.1 and 4.2, with the assumption that permeability of the PDMS remains constant for thin layer. However, measured permeance and thus, β for thick coating in Figure 4.25 and Figure 4.26 seems to still be far from the ideal composite permeance line, despite that the free-standing 4.0g PDMS layer has been measured directly in subchapter 4.2 and is the basis of the intrinsic permeability value used so far. With coating of ~50 µm, lateral diffusion should be minimal theoretically at this thickness. Nevertheless, β value as low as 0.26 for L4(4.0) composite sample was reported; too small to be contributed only by solution intrusion, which the evidence so far also suggested to be minimal. On the other hand, higher CO_2/N_2 selectivity of the composites noted from the measurement

in Figure 4.15 is becoming more perplexing as the calculated ideal composite permeance of CO_2 and N_2 using Equation (3.16) suggested the lowering of CO_2/N_2 selectivity as the resistance contribution by the substrate becomes higher. This is supported by the work of Pinnau and Koros (1991) which shows that larger resistance of the substrate would instead reduce composite selectivity below the intrinsic selectivity value of the separating layer.

One hypothesis of this discrepancy is that as the substrate pores were plugged with the coating solution, the dense part of the PES contributed to the separation, hence increasing the selectivity above a value normally seen on PDMS. This has been observed by Henis and Tripodi (1981) which leads to the early commercialization of polymeric gas separation membranes. Figure 4.26 have suggested that this might be the actual case. Nevertheless, this is only possible when the surface porosity of the substrate is very low, which did not explain the results posed by the pristine composites of the current work. The work by Fouda *et al.* (1991) was the first one to suggest the possible increase in selectivity for composite membranes not predicted by RiS model and proposed an alternative called Wheatstone Bridge model, which considers the possible resistance contribution by lateral diffusion flow. Nevertheless, Wheatstone Bridge model never took a mainstream interest, probably due to its complexity. In the recent years, Hao *et al.* (2020) proposed the use of RiS to combine lateral diffusion and solution penetration as a possibility for reduced permeance in composite structure, yet did not consider the possibility for increased selectivity. However, work by Selyanchyn *et al.* (2020) again shows the deviation of selectivity from the prediction by RiS model, but put the reason is due to interfacial nano blending which creates a high selectivity region in the composite membranes.

Sure enough, any increase in selectivity needs to originate from the material's increased permeability for CO_2 as compared to N_2, and RiS model would need to be modified to consider this. Hence, to elucidate all these discrepancies, contribution of solution intrusion and lateral diffusion of the composites are quantified, using the permeance and resistance data of the peeled composite layer in subchapter 4.2.

4.4.2 Quantification of Geometric Restriction and Solution Intrusion

To recall, lateral diffusion and solution penetration contributes to the overall resistance of the composite membrane (R_T) through the following equation:

$$R_{T,i} = R_{1,i} + R_{2,i} = \frac{\ell_1}{\Psi P_{c,i} A_1} + \frac{\ell_2}{f P_{s,i} A_1} = \frac{1}{\Psi \mathcal{P}_{c,i} A_1} + \frac{1}{f \mathcal{P}_{s,i} A_1} \tag{3.23}$$

Where the subscript 1 and 2 represents the component resistance of dense PDMS layer and PES substrate respectively, ℓ is the thickness of the layer, P is the permeability, $\mathcal{P}$ is the permeance, A is the surface area, Ψ is the adjustment factor for lateral diffusion called restriction factor, and f is the adjustment factor for solution penetration called penetration factor. Subscript c and s represents the coating layer and substrate layer respectively. For the coating layer, it would be the intrinsic permeability/permeance of free standing dense PDMS measured by Equation (3.9) while for the substrate layer, it would be the Knudsen permeability/permeance of the PES porous substrate measured by Equation (3.11).

Contribution of lateral diffusion for the 4.0g PDMS coating on PES substrate can be calculated from the experimental resistance of peeled composite layers through Equation (3.20):

$$\Psi = \frac{R_{c,i}}{R_{1,i}} = \frac{R_{c,i}}{R_{T,i} - R_{2,i}}, R_{1,i} \geq R_{c,i} \tag{3.20}$$

The value of Ψ is thus presented in Figure 4.27. The results showed decrease in Ψ with substrate trend of pristine > LiCl_2% > LiCl_4% for both cases of N_2 and CO_2. As the substrate becomes more restrictive, Ψ should be lower, which is the view followed by the trend in this work. Ψ however, is higher by CO_2 than N_2. This is probably because CO_2 is more permeable than N_2 in both PDMS and PES (Ψ of 1 means no effect by lateral diffusion). These values on the other hand, are higher or comparable to the β values calculated earlier. Without the influence of solution intrusion which has been summed together with the substrate resistance and removed by the term R_2, Ψ will need to be higher than or equal to β, as the total permeance loss by β is contributed by the loss of permeance by Ψ and by solution penetration.

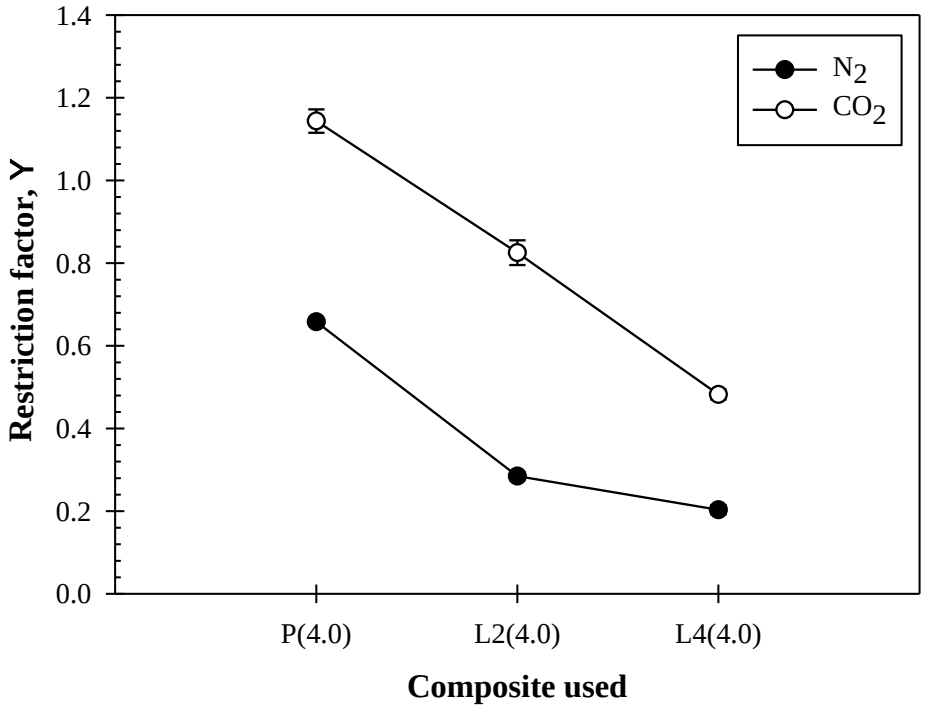

Figure 4.27: Measured contribution of lateral diffusion (restriction factor, Ψ) for 4g PDMS coating solution on PES porous substrate

Interestingly, Ψ by CO_2 for pristine substrate noted a value of more than 1, which means the R_1 component of the composite possesses lower resistance (and higher apparent permeance) than the free standing dense PDMS of the same thickness.

Value of $\Psi > 1$ should not be possible as the resistance across a free-standing layer should be fixed for a certain thickness, which is defined by its intrinsic permeability, as noted by Equation (3.9). It is generally accepted that thick dense polymer structures, such as for 4.0g PDMS at 49.7 ± 0.6 μm would exhibit a constant permeability value for each gas (Firpo *et al.*, 2015, Baker and Low, 2014, Wijmans and Hao, 2015). Hence, $\Psi > 1$ would means that the composite structure, particularly the substrate in some way helps to increase the permeance, which is physically impossible. One possibility of this result is due to higher attachment of PDMS on the pristine substrate compared to the other substrate as noted previously in Figure 4.14. Method of peeling the composite layers could gave two possibilities: (i) removal of certain portion of intruded PDMS near the pore opening, and (ii) adhering of PDMS layers on the substrate. R_2 value could thus be overestimated as adhering PDMS would increase its resistance and hence, reducing the resulting R_1 value (see Equation (3.16)). Similarly, adhered PDMS on the PES substrate would also decrease the thickness of the free PDMS layer, hence decreasing its resistance. This would in turn underestimate the measured R_c value of PDMS peeled from pristine substrate. Nevertheless, results from Figure 4.18(b) suggested negligible free PDMS resistance across different substrate used. This means even if significant amount of PDMS were adhered on the substrate surface, the resulting error is consistent over the different substrates. On the other hand, CO_2 resistance of the free PDMS layer, R_c casted on the pristine substrate would need to be around 0.0018 ± 0.0001 $(GPU.cm^2)^{-1}$ for Ψ to be equal to 1, while currently calculated R_c is at 0.0020 ± 0.0001 $(GPU.cm^2)^{-1}$. With calculated Ψ at 1.14 ± 0.03, resulting $\mathcal{P}_1$ would also be at 46.9 ± 1.2 GPU; an addition of 6 GPU from the $\mathcal{P}_c$ measured on free PDMS layer from pristine substrate at 41.1 ± 1.9 GPU. Similar hypothesis was also proposed by Hao *et al.* (2020) for the possibility of $\Psi > 1$ due to

variation in coating thickness above the mean value. Hence, the reported $\Psi > 1$ from P(4.0) sample using CO_2 is insignificant.

The value of Ψ for both gases in this work can also be compared with the results from the semi-empirical equation developed by Wijmans and Hao (2015) and later modified by Ghadimi *et al.* (2018) and Hao *et al.* (2020), as noted in Equation (4.3)-(4.6). To recall:

$$\mathcal{P}_{app} = \Psi \mathcal{P}_{int} \tag{4.3}$$

$$\Psi = \frac{\varepsilon_s + 1.6N_R^{1.1}}{1 + 1.6N_R^{1.1}} \tag{4.4}$$

$$N_R = \frac{\sigma.\tau.\varepsilon_s}{1 - \varepsilon_s} \tag{4.5}$$

$$\tau = \ell/r \tag{4.6}$$

Where ε_s is the substrate surface porosity, N_R is dimensionless Restriction Number, σ is the uniformity coefficient, ℓ is the thickness of the thin coating layer, and r is surface pore radius. The comparison results are presented in Table 4.10. For the calculation, $\sigma = 1$ and two values of ε_s were used: 0.20 and 0.05. The ε_s values were taken based on the measured ε_s from Table 4.2 which ranges in between 0.12-0.20 for all samples and suggested ε_s results from Figure 4.26 which ranges in between 0.04-0.07 for LiCl_2% and LiCl_4% substrates. In any cases, lower calculated Ψ was noted at lower ε_s, but all are in between 0.92-0.99, suggesting supposedly minimal effect by lateral diffusion at this PDMS thickness. This is far different from the experimental Ψ values in Figure 4.27. As experimental Ψ from Equation (3.20) and calculated Ψ from Equation (4.3)-(4.6) should have ignored the effect of solution intrusion, differences in Ψ would be due to a different factor. Equation (4.3)-(4.6) depends on a few measurable dimensions, notably ℓ, r, and ε_s. Influence of ε_s has been discussed as above, while thickness of the PDMS layer, ℓ is unlikely to be the problem as it was directly measured, on top of the comparable permeance results in Figure 4.17 of peeled

4g PDMS over different substrates also suggesting comparable PDMS thickness. Meanwhile pore radius, r is unlikely to be larger than the one measured through surface SEM for Ψ to be reduced. Sensitivity analysis on ℓ and r also confirms that the resulting Ψ will not drop below 0.9 in all cases, for ℓ and r values in the range of ± 20%.

Table 4.10: Comparison of Ψ of 4g PDMS coating solution of this work with calculated value from Equation (4.3)-(4.6)

Composite	Ψ_{N_2} [This work]	Ψ_{CO_2} [This work]	Ψ [$\sigma = 1, \varepsilon_s = 0.20$]	Ψ [$\sigma = 1, \varepsilon_s = 0.05$]
P(4.0)	0.66 ± 0.01	1.14 ± 0.03	0.99	0.96
L2(4.0)	0.28 ± 0.01	0.83 ± 0.03	0.99	0.94
L4(4.0)	0.20 ± 0.01	0.48 ± 0.01	0.99	0.92

Differences in experimental and calculated Ψ can thus be hypothesised to be originated from two sources: (i) uniformity coefficient, $\sigma < 1$ and (ii) contribution of dense portion of the substrate when in composite structure. For case (i), the initial version of the Equation (4.5) took σ equals to 1, which later was modified by Ghadimi *et al.* (2018) and Hao *et al.* (2020) to include the effect of substrate pore randomness or pore uniformity, which normally observed to be non-uniform for porous membranes from phase inversion process. The expected value of uniformity coefficient, σ is presented in Table 4.11. This was calculated by adjusting the value of σ to reduce calculated Ψ to the value of experimental Ψ. σ was calculated for the case of both N_2 and CO_2, and ε_s of 0.20 and 0.05. With the exception of P(4.0) composite which has experimental $\Psi > 1$, others can be calculated to obtain significantly low σ. Very low σ has also been calculated by Ghadimi *et al.* (2018) at 0.0483 for track-etch polycarbonate substrate by Zhu *et al.* (2016a), which possess very low surface porosity (ε_s = 0.0059). Meanwhile, track-etch polycarbonate substrate from the same work also suggested σ of 0.256 at ε_s = 0.011, suggesting increased σ at higher ε_s. This is the

opposite to the CFD study by Hao *et al.* (2020), where σ increase at lower ε_s, a view similar to this work. It is said that these differences are due to how the distribution in pore location differs between the membrane type. Hence, it is concluded that real membrane is much more nonuniform than expected from simulation studies, although further simulation studies with much more unorthodox pore location distribution will be needed to confirm this claim, as the work by Hao *et al.* (2020) only predicts the effect of 5 pore patterns with σ ranging from 0.72 to 1. Nevertheless, as σ should be a factor of the substrate's pore, σ should be the same for lower coating thickness composites of the same substrate.

Table 4.11: Expected value of uniformity coefficient, σ based on different surface porosity and permeation gas type

Composite	**Expected σ $[\varepsilon_s = 0.20]$, N_2**	**Expected σ $[\varepsilon_s = 0.05]$, N_2**	**Expected σ $[\varepsilon_s = 0.20]$, CO_2**	**Expected σ $[\varepsilon_s = 0.05]$, CO_2**
P(4.0)	0.015	0.094	1.000*	1.000*
L2(4.0)	0.003	0.034	0.063	0.361
L4(4.0)	0.001	0.025	0.014	0.095

* σ from CO_2 for P(4.0) composite is taken as 1 as experimental Ψ is more than 1

On the other hand, as for case (ii), it is interesting to note that Equation (4.3)-(4.6) did not consider the type of gas used, but instead is only a factor of the composite membrane's physical dimensions. This is different from the results noted by the current work where Ψ changed based on the gases used. Equation (4.3)-(4.6) was developed based on the assumptions that the solid part of the substrate is impenetrable, which may not be always true. As noted by the original work of RiS model in Henis and Tripodi (1981), selectivity of multilayer composite membrane would be dictated by the substrate material when ε_s is low. However, owing to the higher permeability of CO_2 than N_2 in PES at 0.07 and 3.22 Barrer for N_2 and CO_2 respectively (Chen *et al.*, 2017), Ψ by N_2 should reflect the impermeability

assumptions of the equations better than Ψ by CO_2. Further discussions on these discrepancies will be made in the next section.

Moving on, the contribution of solution intrusion for the 4.0g PDMS coating on PES substrate can also be calculated from the experimental resistance of peeled composite layers through Equation (3.22):

$$f = \frac{R_{s,i}}{R_{2,i}}, R_{2,i} \geq R_{s,i} \tag{3.22}$$

The value of f is thus presented in Figure 4.28. The results showed increase in f with substrate trend of pristine > LiCl_2% > LiCl_4% for both cases of N_2 and CO_2. Increase in f means lower effect by solution intrusion. For the same amount of coating solution, this suggested that more PDMS penetrated in pristine substrate than in LiCl modified substrates, a view supported by the observation in Figure 4.14. This is however, against the expected trend of reduced f with higher skin thickness, which should allow larger effect by solution penetration for the thicker skin LiCl_4% substrate. Smaller surface pores noted in pristine substrate could in fact generate larger capillary forces that increase the penetration depth of the coating solution into the substrate. Again, f is also lower by N_2 as compared to CO_2, identical to the observation for Ψ as noted previously.

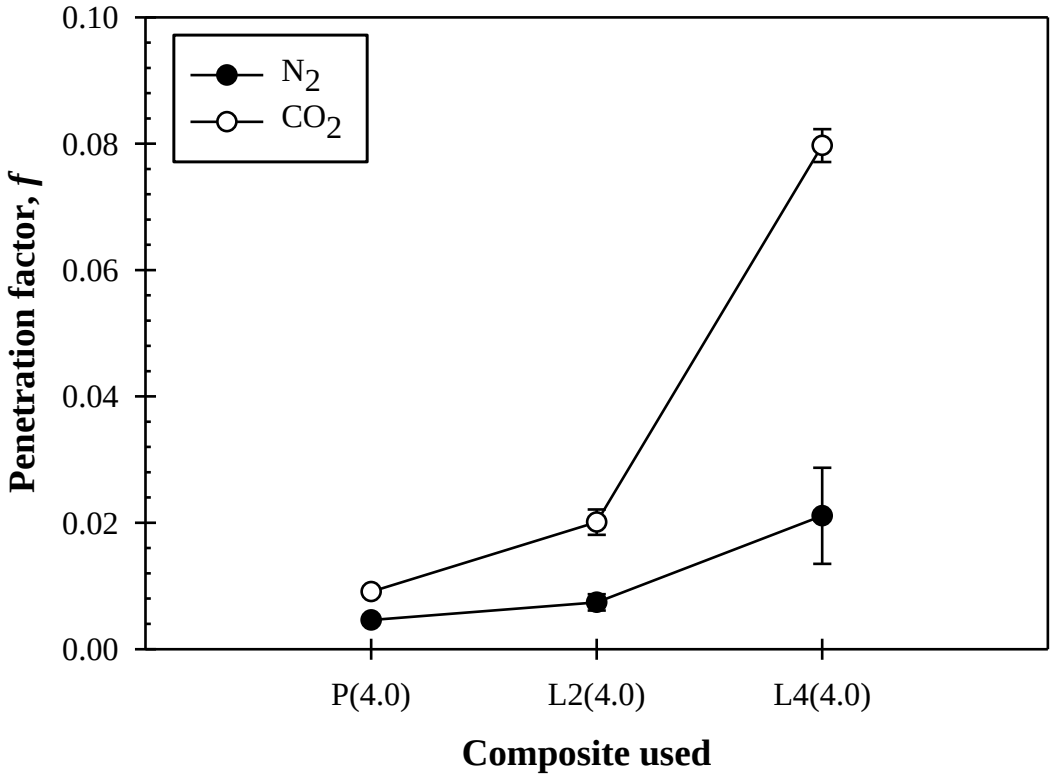

Figure 4.28: Measured contribution of solution penetration for 4g PDMS coating solution on PES porous substrate

It is also worth to note that f for all cases are quite low, suggesting significant influence of solution penetration. This is notable for example, from the reduction of pre-coated permeance of pristine substrate at 86 420 GPU to peeled permeance of the same substrate at 132.75 GPU. Considering that results in Section 4.2 where PDMS intrusion is visually not severe or solidly plugging all the pores from SEM and EDX, this suggested that small amount of penetration would significantly increase the resistance of the composite. This is indeed the case as noted by Hao *et al.* (2020), where they find out penetration of 1 nm adds resistance equivalent to the resistance of 160 nm top layer in their CFD analysis. Li *et al.* (2019) suggested that effect of solution penetration on the gas transport resistance is stronger at the early stage of penetration, meaning even a small penetration would have significantly large effect on increasing the resistance. This is shown by Chung (1997) to be in between 10-100 nm where normalized permeance drop from 0.9 down to 0.4, although this

might differ based on the composites studied. For the current work, relationship between f and penetration depth is not elucidated. However, penetration depth should also be relatively low, bounded by a maximum of the substrate's skin thickness in Table 4.1.

Experimentally measured β values in Figure 4.26 is a factor of Ψ and f. To recall, β is related to Ψ and f through Equation (3.25):

$$\beta = \frac{(\Psi f)(\mathcal{P}_s + \mathcal{P}_c)}{f\mathcal{P}_s + \Psi\mathcal{P}_c}, 0 \leq \beta \leq 1 \tag{3.25}$$

As β measured from composite samples (from now on called experimental β) is the actual permeance efficiency of the composite while β from Equation (3.25) (from now on called calculated β) is determined from Ψ, f, $\mathcal{P}_s$, and $\mathcal{P}_c$ measured from free-standing/peeled samples, the validity of the relationship can be verified. Table 4.12 represents the comparison of experimental β against the calculated β for both N_2 and CO_2. Except for L2(4.0) sample for β_{CO_2}, all the calculated β values are comparable to the experimental β. Significant differences in β of L2(4.0) from CO_2 permeation may originated from the variation in penetration depth, as noted by the large error bar for peeled PES substrate resistance of LiCl_2% and LiCl_4% in Figure 4.19. Nevertheless, as the calculated β is barely different from the measured Ψ in Figure 4.27, this suggested that β is mainly contributed by Ψ rather than f in the current work, a rather peculiar observation considering the experiments were done for thick PDMS coatings. However, the same observation was also noted by Hao *et al.* (2020) using almost similar concept through CFD simulation where the calculated β slightly reduced when penetration depth increased. In the mentioned work, both σ and penetration depth were theoretically studied to discuss the source of error between experiment and calculation when using the original correlation for Ψ developed in

Wijmans and Hao (2015). Here in the current work, it is believed that Ψ, or more specifically the pore uniformity, σ plays an important role in determining the efficiency of the composite permeance.

Table 4.12: Comparison of β from composite samples and β from free-standing layers through Equation (3.25) for both N_2 and CO_2 for 4g PDMS coating composite

Composite	β_{N_2} (composite)	β_{N_2} (free-standing)	β_{CO_2} (composite)	β_{CO_2} (free-standing)
P(4.0)	0.68	0.65	0.91	1.08
L2(4.0)	0.26	0.28	0.48	0.76
L4(4.0)	0.25	0.20	0.40	0.46

Equation (3.25) together with Equation (4.3)-(4.6) can be used to create a generalize correlation for calculating β of composite membranes with known ε_s, σ, ℓ, r, f, $\mathcal{P}_s$, and $\mathcal{P}_c$; all are measurable either directly or indirectly through experimental means as proven throughout the current work. Hence, calculated β of thinner PDMS coated samples can also be made and compared to their experimental β. Other than the original assumption that the PDMS intrinsic permeability remains constant at different thickness, two additional assumptions need to be considered: (i) Any reduction in f (increased effect by solution penetration) should be maximum at thicker coatings. Hence similar f values will be used for thinner coatings, assuming that penetration is only due to capillary forces (see discussions in Section 4.2.3), and (ii) Ψ is a factor of coating thickness and thus cannot be constant. However, σ should be the same for the same substrate even with different coating thickness (see discussions for Table 4.11). Comparison of calculated β and experimental β for both N_2 and CO_2 gas is presented in Figure 4.29. Ψ was calculated using the experimentally measured values of ℓ (Figure 4.11) and r (Table 4.2), while theoretical ε_s from Table 4.4 was used based on the discussions in Section 4.4.1. Meanwhile, σ was determined from solving Equation

(4.3)-(4.6) to obtain the experimental Ψ values of 4.0g PDMS coating samples as in Table 4.10. The data fits well with R^2 of 0.95 (red dotted line), with slight deviation to the left against the diagonal line was noted at high β comparison. This also confirms the validity of σ as a function of substrates regardless of coating thickness, although the origin of differences noted between gas type is yet to be explained.

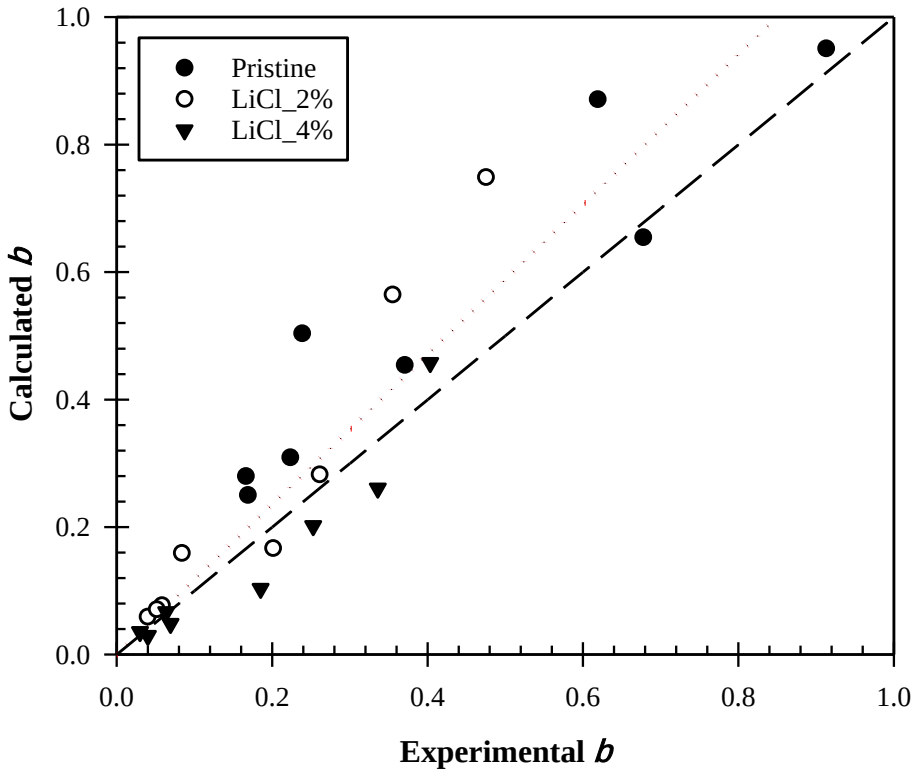

Figure 4.29: Comparison of experimental β and calculated β from Equation (3.25) for both N_2 and CO_2 of all PES/PDMS samples

The validity of the calculated β line plot was also made using experimental β values for pristine PES composites by N_2 permeation as an example. The line and experimental data points are compared to several other theoretical lines, i.e., assuming no penetration (f = 1), uniform substrate pores (σ = 1), and both (f = σ = 1), as presented in Figure 4.30. Calculated β line (solid line) follows near to the experimental β plot, although with slight overestimation at lower coating thickness. This, however, are far better than other theoretical lines mentioned as all, especially for those assumed for uniform pores, are far deviated from the experimental β plot. The line that assumes

$f = \sigma = 1$, which represents the theoretically achievable ideal condition (where only lateral diffusion with uniform pores took place) was significantly skewed from the experimental β plot. Meanwhile, by considering only the influence of solution penetration ($\sigma = 1$), calculated β was significantly reduced especially for thin coatings, suggesting higher impact at lower coating thickness. Although, this is still not fitting towards the experimental β plot. Only when the pores are considered as non-uniform ($f = 1$) that the calculated β line starts to fit with the experimental β plot.

Better fittings can be found by decreasing f by a factor of 0.1, or by reducing the ε_s down to 0.17, which is the value found from experimental β assuming no penetration occurred (or $f = 1$, see Figure 4.26). It is however shown from the experiment and from literature that f is highly unlikely to be 1 (no solution penetration), even when proper pre-wetting care is given (Jin *et al.*, 2017, Cay-Durgun *et al.*, 2020, Chung, 1997). Hence, it is hypothesised that the actual solution penetration is in fact higher than the one measured here (hence lower f), although still not as influential as the effect by σ. A correlation between f and penetration depth, and better methodology to quantify nanoscale penetration such as in the work of Li *et al.* (2019) would be interesting to further validate this. While the influence of σ is validated, more experiments are needed to confirm the trend at lower coating thickness and with controlled coating penetration.

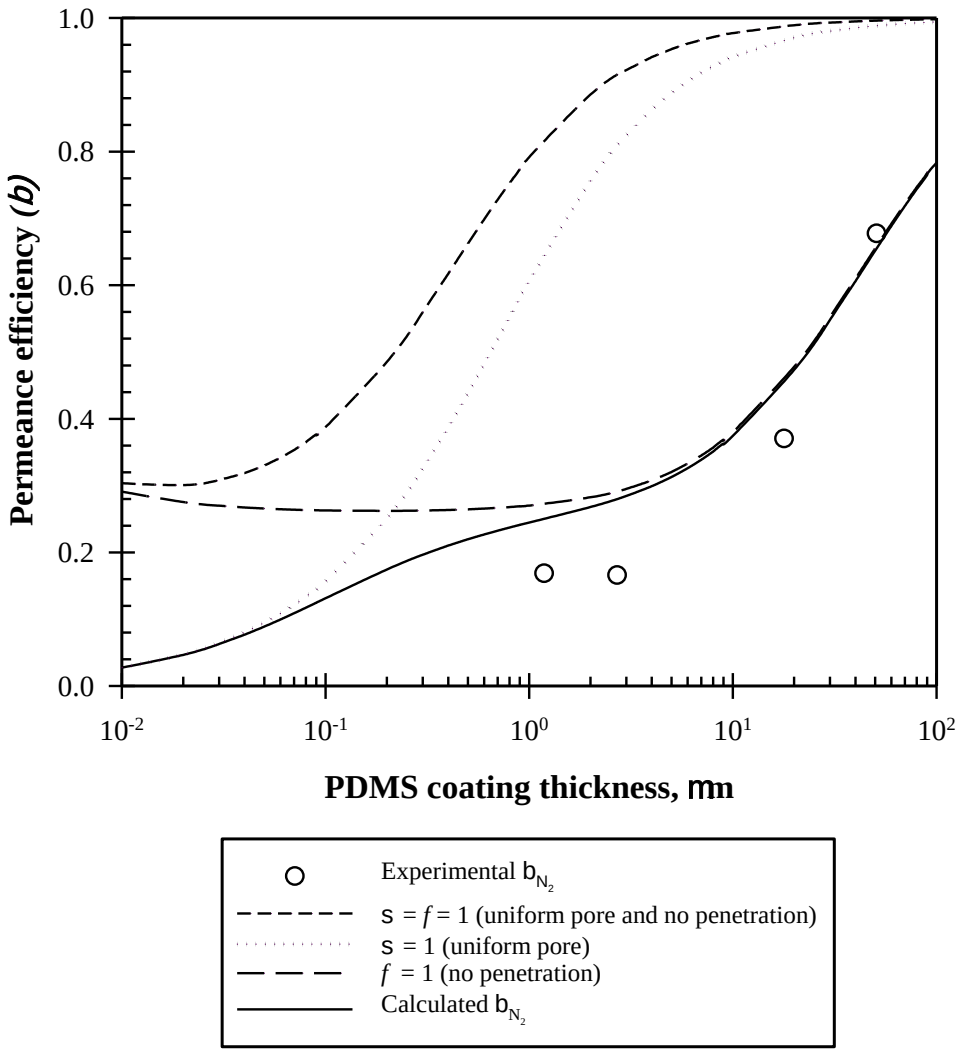

Figure 4.30: Comparison of experimental β data points from PES/PDMS composite with pristine substrate with calculated β lines at various conditions: (i) $\sigma = f = 1$, (ii) $\sigma = 1$, $f = 0.0046$ (iii) $\sigma = 0.0097$, $f = 1$, (iv) $\sigma = 0.0097$, $f = 0.0046$ (experimentally measured value from N_2 permeation)

Results so far have shown that composite permeation across dense-porous layers are more complicated than expected. In some instance, such as in Table 4.7, high permeable polymer such as PMP in dense form can exceed the permeance of PDMS composite membrane (Figure 4.15). Here, N_2 permeance comparison is made between a hypothetical PES/PDMS composite with 1 µm PDMS thickness and using pristine substrate, and asymmetric PMP at different uniformity coefficient and penetration factor. The results are presented in Figure 4.31. Asymmetric PMP, while being inferior in intrinsic permeability as compared to PDMS, observed a better

permeance when certain conditions are met as asymmetric PMP is unaffected by the non-ideality of the dense-porous interface in PES/PDMS composite. At an achievable ideal condition ($f = \sigma = 1$), maximum apparent permeance at 147.3 GPU can be reached. However, the true ideal N_2 permeance of the PES/PDMS composite at 186.08 GPU will never be reached because of restriction factor, Ψ, which limits the maximum permeance efficiency, β at 0.79. As Ψ is a factor of coating thickness, increasing the PDMS thickness to about 2.3 µm would bypass the limit imposed by Ψ with β of 0.9 in an achievable ideal condition ($f = \sigma = 1$). This, however, would reduce the apparent permeance to 72.6 GPU, lower than the permeance observed by PMP.

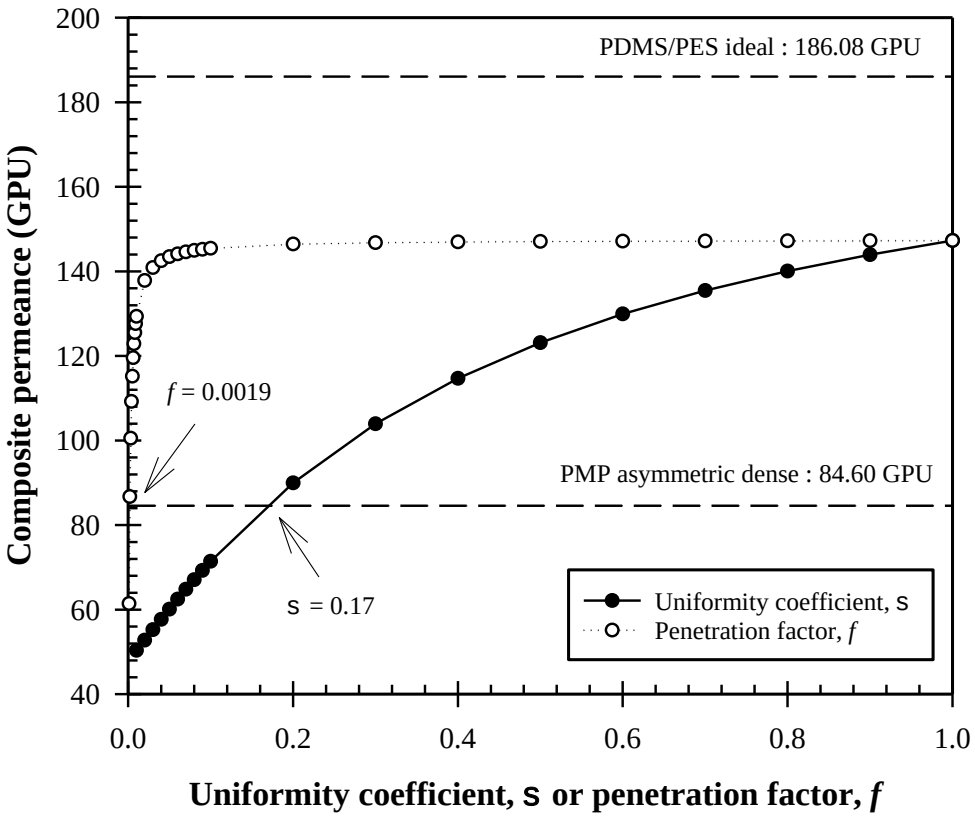

Figure 4.31: Comparison between hypothetical composite PES/PDMS with 1 µm PDMS thickness and using pristine substrate and asymmetric PMP at different uniformity coefficient and penetration factor

As noted from the experiment, the achievable ideal condition at $f = \sigma = 1$, while being theoretically achievable, is hard to reach. Reduction of f or σ

independently would reduce the apparent permeance, crossing the PMP permeance line at f = 0.0019, σ = 1 or σ = 0.17, f = 1. f is less affected by the reduction in apparent permeance at high value, which probably corresponds to non-complete penetration where the pore size are reduced by the coating material, but not being filled up (Li *et al.*, 2019). This is also supported by the results in Figure 4.17 as peeled PES substrate permeance was significantly reduced compared to its pre-coating permeance, but the selectivity remains low in the order of 2-3 for CO_2/N_2, although above the Knudsen selectivity. As more pores are being filled, f would decrease rapidly due to the significant resistance differences through solid PDMS versus through porous structure. Apparent permeance on the other hand, reduced steadily with decreasing σ.

While improvement in coating technique through pre-wetting the substrate could increase f, this however would not completely be removing the effect of solution penetration, as discussed before. Meanwhile, fundamental aspects of σ is still in its infancy, which from the experiment so far is seen as an intrinsic property of the substrate. Indeed, the phase inversion method used to fabricate the substrate is also a random process in which while the pore dimensions can be relatively controlled, the pore locations are not. Theoretical study such as by Hao *et al.* (2020) have produce surface pores with σ of 0.72, but such uniform surface as in the simulation is not practically possible with the current technology. The discrepancy is further confirmed when the observation of the theoretical study is compared to the calculated σ of track-etch substrate by Ghadimi *et al.* (2018), using the results of Zhu *et al.* (2016a). In the current work, with σ of 0.0097 for the pristine substrate, apparent permeance of the PES/PDMS composite would not surpass the PMP permeance line, even if f = 1. Thinner PDMS coating of 0.58 μm at f = 1, or 0.48 μm at f = 0.0046 (f value assumed

for pristine substrate in the current work; see Figure 4.28) would be needed to achieve similar permeance as the PMP.

4.4.3 2D-CFD Near Porous-Dense Layer Interface

Based on the discussions so far, one of the discrepancies found in the current work is the differences in the value of experimentally measured Ψ, as noted in Figure 4.27. Equation (4.3)-(4.6) which was used for calculating Ψ did not consider the type of gas used, but instead is only a factor of the composite membrane's physical dimensions. Here it is hypothesised to be caused by the non-zero permeability of the substrate, which in turn helps to reduce the effect of lateral diffusion. This hypothesis was based on the discrepancy between the original work of RiS model in Henis and Tripodi (1981) where selectivity of multilayer composite membrane would be dictated by the substrate material when ε_s is low, yet most composite layered work propose to reduce solution penetration to avoid loss of permeance while assuming the dense substrate area to be impenetrable (Chung, 1997, Wijmans and Hao, 2015).

Figure 4.32 represents the 2D-CFD simulation of flow across membrane materials at various conditions. The streamline arrows are set to be at the same local time, to represent the restriction posed on the composites of different configurations. In example (i), when the substrate dense area is assumed to be impermeable, decrease of coating thickness would indeed constrict the flow towards the pores, which is the source of inefficiency by lateral diffusion. While incoming flow directly above the pore opening would pass easier through the coating as the coating thickness is reduced, flow from above the dense substrate area would be heavily curved to go to the porous part of the substrate. This in turn, is reflected in Equation (4.3)-(4.6), where in a theoretical case of σ = 1 and coating thickness of 1 µm, halving the coating thickness would reduce Ψ, but when the ε_s is doubled at this half thickness, Ψ would increase

much more than the original value. This would also be worsened when solution intrusion is considered, as noted in example (ii). Increased penetration would restrict incoming flow even from those directly above the pore opening. Detailed observations on these phenomenon have been discussed in detail in the work of Wijmans and Hao (2015) and Kattula *et al.* (2015).

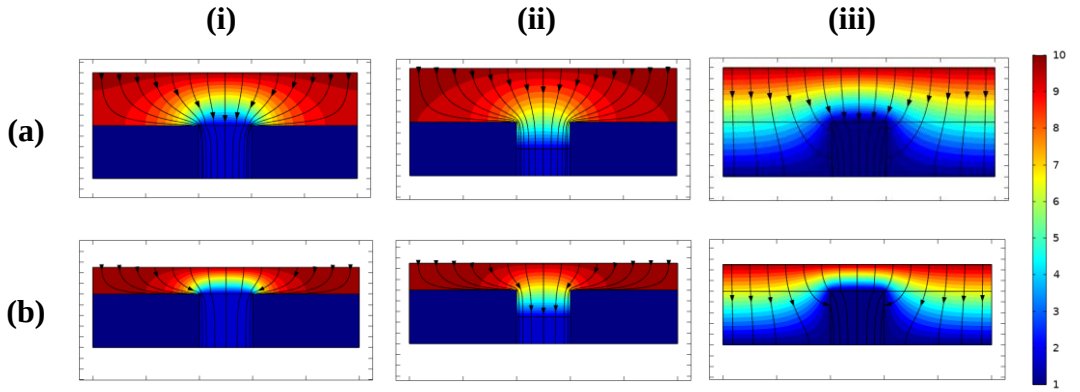

Figure 4.32: CFD flow across the membrane. (a) dense layer of 1 µm, (b) dense layer of 0.5 µm. (i) Composite with no solution intrusion, (ii) composite with solution intrusion, (iii) asymmetric. Colour intensity represents the local permeate concentration, while the streamline represents the flux of the permeating species. All streamlines are at the same local time while the materials are with the same diffusion coefficient

While subsequent study in Hao *et al.* (2020) have taken note on the effect of pore uniformity and solution intrusion, the work neglects the possible influence of non-zero substrate permeability. As noted in the extreme case of example (iii), by allowing the substrate part to be of similar diffusion coefficient, geometric restriction can be alleviated with minimum deviation of the streamline from flowing towards x-axis. Meanwhile, flux across the composite's depth is much more uniform when the substrate didn't restrict the flow. Composite design with similar diffusion coefficient, as in the case of example (iii), can be considered as asymmetric membrane. Hence, in layered composite membrane of different materials with non-zero substrate permeability, similar observations could be seen as the substrate would also acts as a

conduit to flow gas towards the porous section, albeit at a lesser degree. How the flow across the membrane evolves between the extreme cases (i) and (iii) would thus be interesting for further studies. Nevertheless, as the substrate material also possess its own intrinsic selectivity, it is expected that more permeable gas would exhibit less restrictions and thus lower restriction factor, as noted from the experimental results in Figure 4.27. The influence of substrate permeability could also be one of the factors that governs σ, where value of σ would increase when substrate material is more permeable towards the penetrating gas. This could explain the higher σ value by CO_2 as compared to N_2, as noted from Table 4.11. However, more studies would be needed to validate this correlation.

In the meantime, thickness of asymmetric dense skin should not be a problem as a gutter layer, given that the substrate portion of the membrane possess high enough porosity. This is unlike a composite substrate-gutter structure which the apparent permeance is governed by various factors, as noted in Figure 4.31. The limitation of using asymmetric dense skin membrane would be the availability of the material, which needs to possess strong enough mechanical strength yet being highly permeable such as PMP. This will be used in the next part of the study.

4.5 P84 Polyimide Coating as Selective Layer

PMP asymmetric dense skin membrane has the potential to be used as co-substrate-gutter layer, as noted in the previous subchapters. Thin film coating of the selective layer can become much easier and effective when there is no influence of solution intrusion, while lateral diffusion can be mitigated through the dense skin of the co-substrate-gutter layer. Despite of PMP's lower permeability than PDMS, under suitable condition, the asymmetric structure can perform much better than its composite counterpart. Nevertheless, these advantages are limited to the suitability of

the material, which should possess high permeability and high mechanical strength. On the other hand, the processability and compatibility of the co-substrate-gutter to form composite structure with another layer will also be important. Hence, compatibility of PMP with P84 polyimide (PI), a candidate material as selective layer was elucidated. PMP, being a polyolefin, is supposed to possess better resistance to the usual aprotic solvent used for dissolving polymer such as N-methyl-2-pyrrolidone (NMP). Hence, this gives an added advantage for fabrication of thin composite coating with most of the polymers known to exhibit good performance in gas separation. On the other hand, P84 PI was chosen due to its recent success in commercialization for CO_2 gas separation (Visser *et al.*, 2016), suggesting its feasibility and reliability as the selective layer.

4.5.1 P84 PI Performance and Preliminary Gutter-Selective Layer Evaluation

The base performance of dense P84 PI flat sheet membrane was quantified as presented in Table 4.13. Permeability of P84 PI was the highest for CO_2, while the difference in permeability of N_2 and CH_4 is negligible. This gives comparatively high CO_2/N_2 and CO_2/CH_4 selectivity, and quite small N_2/CH_4 selectivity. In comparison, CO_2 performance in the patent of Visser *et al.* (2016) is higher at CO_2/CH_4 selectivity of 63.9. Although, the fibers formed were annealed near to P84 PI glass transition temperature at around 300 °C. The current work's result is more in line with other literature that casted flat sheet dense membrane from P84 PI solution such as by Tin *et al.* (2004) with CO_2 and CH_4 permeability of 1.2 and 0.02 Barrer respectively, and CO_2/CH_4 ideal selectivity of 50, using DMF as solvent. Meanwhile, work that utilize NMP as solvent, like in the current work, reported N_2, CO_2, and CH_4 permeability of 0.05, 1.37, and 0.028 Barrer respectively (Hosseini and Chung, 2009), comparable to

the previously mentioned literature. The ideal selectivity for CO_2/CH_4 and N_2/CH_4 was reported at 48.93 and 1.78 respectively. CO_2/N_2 selectivity, however, was at 27.4, much lower than the result of the current work.

Table 4.13: Base performance of self-supporting dense P84 PI flat sheet membrane made from 10 wt.% solution in NMP (thickness: 7.8 ± 0.3 µm)

Gas	Permeability (Barrer)	Ideal selectivity		
		CO_2/N_2	N_2/CH_4	CO_2/CH_4
N_2	0.04 ± 0.01			
CO_2	1.88 ± 0.30	46.4 ± 9.7	1.4 ± 0.3	53.8 ± 6.4
CH_4	0.036 ± 0.006			

To compare the base performance of P84 PI for gas separation application, the position of P84 PI in the upper bound graph of CO_2/N_2 and CO_2/CH_4 was plotted, as presented in Figure 4.33. The upper bound line was taken from the correlation reported in Robeson (2008) through the equation:

$$P_i = h\alpha_{ij}^m \quad (4.8)$$

Where P is the permeability of the gas, α is the selectivity of the material, subscript i and j refers to the gas of interest, and h and m is the line variable, noted from the literature. For CO_2/N_2, h = 30967000 and $m = -2.888$ while for CO_2/CH_4, h = 5369140 and $m = -2.636$. On the other hand, data from literature, previously presented in Table 2.6 and Table 2.8 is also compared in the same graphs. Indeed, all the reported results were located beneath these lines, which is expected considering that they are mostly pristine polymer results. Hence, it would be surprising if P84 PI would be able to surpass the line easily without modification such as through nanoparticle incorporation. Overall, there are no literature on mixed matrix membrane (MMM) with P84 PI as the polymer matrix found to surpass the line, with almost all the MMM to have comparable results with the unmodified polymeric membrane. Although, with

limited literature data found between the year 2011-2021, it is expected that more P84 PI MMM will be reported in the future. On the other hand, recent work for P84 PI based MMM has shown improvement in performance as compared to their non-MMM standards, e.g., CO_2 permeance from 2.66 Barrer to 11.02 Barrer, CO_2/CH_4 from 54.1 to 92.3 in the work by Guo *et al.* (2018) and CO_2 permeance from 0.72 Barrer to 1.3 Barrer, CO_2/CH_4 from 44 to 67 in the work by Sheng *et al.* (2020a). These results did not surpass the upper bound line, unfortunately, but it is an improvement nonetheless as compared to their base standard. On the other hand, dispersion of graphene oxide has been noted to be very good in NMP (Paredes *et al.*, 2008) and might be advantageous for dispersion in the thin P84 PI coating for subsequent studies due to its two-dimensional structure. It is also important to note that surpassing the upper bound line is not the only requirements for a MMM to become industrially attractive, as noted early in the introduction.

Interestingly, the position of the dense membrane performance in the current work is also comparable to the results in Visser *et al.* (2016), a patented P84 PI asymmetric membrane for CO_2/CH_4 separation. This position suggesting its potential impact for improved performance into the attractive region through subsequent MMM study (Ding, 2019, Koros and Mahajan, 2000). For now, with P84 PI CO_2/CH_4 selectivity of >50 reported in the current work, this is far higher than the suggested selectivity of 20-25 for polyimides to be a viable contender of cellulose acetate membranes in this domain of separation (Baker, 2002). Although, mixed gas performance of P84 PI should be elucidated to confirm this view in a more realistic condition. Meanwhile, the potential from the point of view of practical industrial application of high selectivity membrane for CO_2/CH_4 application such as in biogas upgrading has been noted by Ding (2019). Although CO_2/N_2 performance is a bit weak

with base P84 PI performance a bit far from the upper bound line, it should still be acceptable for preliminary studies in the current work.

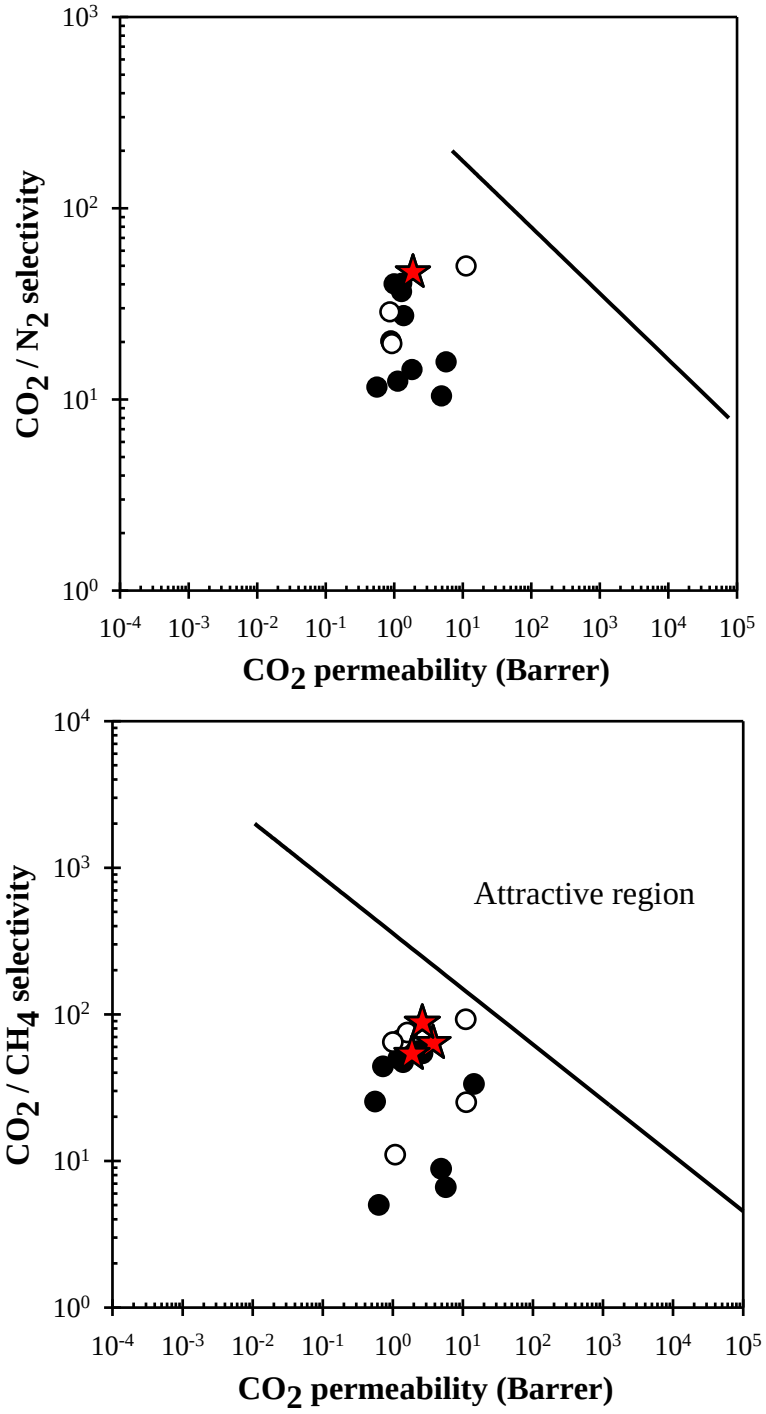

Figure 4.33: Position of P84 PI in literature and in the current work compared to the upper bound graph of CO_2/N_2 and CO_2/CH_4. —— 2008 upper bound, ● dense/asymmetric (non-modified), ○ mixed matrix, ★ current work and patent results in Visser *et al.* (2016)

In order to justify the suitability of PMP as gutter layer with P84 PI as selective layer, the permeance ratio ($\mathcal{P}_{gutter}/\mathcal{P}_{selective}$), the ratio between the gutter's ($\mathcal{P}_{gutter}$) and selective layer's permeance ($\mathcal{P}_{selective}$) was calculated, as presented in Table 4.14. The ratio should be high so that the resulting permeance of the composite would be as near to the intrinsic permeance of the selective layer, maximizing the performance improvements (Wijmans and Hao, 2015). With the assumption that 0.1 and 0.5 µm thickness of P84 PI thin film can be coated onto the PMP, $\mathcal{P}_{gutter}/\mathcal{P}_{selective}$ was noted to be limited by CO_2 with the lowest permeance ratio of 32 for 0.1 µm P84 PI. So far, there has been limited work on P84 PI composite layer reported in literature, such as by Shen and Lua (2010) which was able to spin coated P84 PI onto poly(methyl methacrylate) (PMMA) substrates down to 6 µm. On the other hand, Escorihuela *et al.* (2018a) has reported dip coated P84 PI onto ceramic support at 4.73 µm. While no literature on P84 PI thickness below 1 µm was found, another commercial PI (Matrimid) has been reported with final coating thickness as low as 0.4 µm by spin coating on a silicon wafer (Huang and Paul, 2007). Hence it is safe to say that the thickness assumption is in the achievable range, with 0.1 µm being the lower thickness limit for the preliminary evaluation.

Table 4.14: Expected permeance of P84 PI and permeance ratio between asymmetric PMP HF and P84 PI, for hypothetical 0.1 µm and 0.5 µm P84 PI thickness

Gas	P84 PI expected permeance (GPU), 0.1 µm	$\mathcal{P}_{gutter}/\mathcal{P}_{selective}$, P84 PI = 0.1 µm	P84 PI expected permeance (GPU), 0.5 µm	$\mathcal{P}_{gutter}/\mathcal{P}_{selective}$, P84 PI = 0.5 µm
N_2	0.45	189	0.09	943
CO_2	18.79	32	3.76	162
CH_4	0.36	435	0.07	2176

Expected permeance was calculated by dividing the permeability with the chosen thickness of the P84 PI layer

For triple layer composite with distinct substrate and gutter layer, Kattula *et al.* (2015) have suggested that the resulting composite permeance efficiency factor, β depends on the $\mathcal{P}_{gutter}/\mathcal{P}_{selective}$ value at a constant scaled gutter layer thickness and are highly affected by the porosity of the substrate. This is different than in the current case, as the asymmetric nature of the gutter-substrate layer means that substrate porosity and gutter thickness would be less important as permeating gas could also be channelled through the solid part of the substrate, as noted in the previous subchapter. To ensure that the gutter and substrate layer would not detriment the performance of the composite membrane, similar relationship between $\mathcal{P}_{gutter}/\mathcal{P}_{selective}$ against β was calculated. Ideal composite permeance, $\mathcal{P}_T^{ideal}$ definition in Equation (3.16) can be modified for this case as:

$$\mathcal{P}_{T,i} = \left(\frac{1}{\mathcal{P}_{selective,i}} + \frac{1}{\mathcal{P}_{gutter,i}} \right)^{-1} \tag{4.9}$$

$$\beta = \frac{\mathcal{P}_{T,i}}{\mathcal{P}_{T,i}^{ideal}} \tag{4.10}$$

Where $\mathcal{P}_T$ is the composite permeance, and $\mathcal{P}_T^{ideal}$ is taken when $\mathcal{P}_{gutter} \to \infty$, hence $\mathcal{P}_T^{ideal} = \mathcal{P}_{selective}$. $\mathcal{P}_{gutter}$ is thus taken as the total permeance of co-substrate-gutter layer. The relationship can thus be simplified as:

$$\beta = \frac{\mathcal{P}_{gutter}}{\mathcal{P}_{gutter} + \mathcal{P}_{selective}} \tag{4.11}$$

This can be plotted as presented in Figure 4.34, with lower limit at $\mathcal{P}_{gutter}/\mathcal{P}_{selective}$ = 1. This is true as $\mathcal{P}_{gutter}$ cannot be lower than $\mathcal{P}_{selective}$, otherwise the gutter layer would become the separating layer. The relationship suggested that β is affected by $\mathcal{P}_{gutter}/\mathcal{P}_{selective}$ value but the trend is indifferent regardless of the gas used. This also means that β is not affected by the individual permeance value of the layers, but

only by the ratio of it. Indeed, as $\mathcal{P}_{gutter}/\mathcal{P}_{selective}$ increased, β also increase, just as predicted by Kattula *et al*. (2015). However, without the influence of lateral diffusion, porosity of the 'substrate' becomes irrelevant and thus the trend become much more direct. From the figure, $\mathcal{P}_{gutter}/\mathcal{P}_{selective}$ of at least 9 is needed to achieve β of at least 0.9. In the current work, the minimum $\mathcal{P}_{gutter}/\mathcal{P}_{selective}$ of 32 noted at a hypothetical 0.1 µm selective layer thickness means that the resulting β would be at 0.970. Hence, the PMP co-gutter-substrate layer would have negligible effect on the composite performance. In fact, P84 PI thickness as low as 31 nm can be theoretically made and the resulting composite would still retain the performance above 90% of the selective layer intrinsic permeance. This gives a lot of room for optimization or improvement, for the gutter layer and for the selective layer alike.

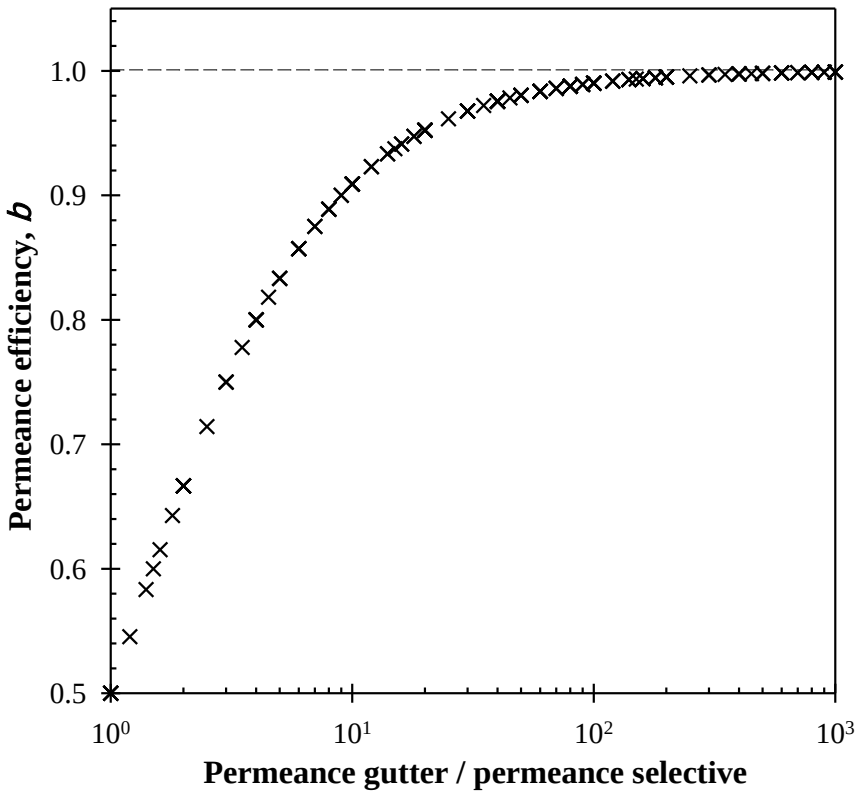

Figure 4.34: Relationship between $\mathcal{P}_{gutter}/\mathcal{P}_{selective}$ against permeance efficiency factor, β

Similarly, in terms of selectivity, α, the definition can be extended from Equation (4.9) as:

$$\alpha_{i,j} = \frac{\mathcal{P}_{T,i}}{\mathcal{P}_{T,j}} = \frac{\left(\frac{1}{\mathcal{P}_{selective,i}} + \frac{1}{\mathcal{P}_{gutter,i}}\right)^{-1}}{\left(\frac{1}{\mathcal{P}_{selective,j}} + \frac{1}{\mathcal{P}_{gutter,j}}\right)^{-1}} \tag{4.12}$$

Where i and j is the gas of interest. In a similar fashion, the ideal selectivity can be defined as:

$$\alpha_{i,j}^{ideal} = \frac{\mathcal{P}_{T,i}^{ideal}}{\mathcal{P}_{T,j}^{ideal}} = \frac{\mathcal{P}_{selective,i}}{\mathcal{P}_{selective,j}} \tag{4.13}$$

Hence, the degree of selectivity reduction or selectivity efficiency, ω can be defined as:

$$\omega_{i,j} = \frac{\alpha_{i,j}}{\alpha_{i,j}^{ideal}} \tag{4.14}$$

By knowing the intrinsic selectivity of the selective layer ($\alpha_{selective}$) and the gutter layer (α_{gutter}), ω can be expanded into:

$$\omega_{i,j} = \frac{\mathcal{P}_{gutter,i}.\alpha_{selective,i,j} + \mathcal{P}_{selective,i}.\alpha_{gutter,i,j}}{\alpha_{selective,i,j}(\mathcal{P}_{gutter,i} + \mathcal{P}_{selective,i})} \tag{4.15}$$

This can also be plotted as presented in Figure 4.35, with lower limit at $\mathcal{P}_{gutter}/\mathcal{P}_{selective} = \alpha_{selective}/\alpha_{gutter}$ = 1. Lower limit of $\mathcal{P}_{gutter}/\mathcal{P}_{selective}$ is true as discussed before, and in a similar fashion, $\alpha_{selective}$ cannot be lower than α_{gutter}, otherwise the gutter layer would become the separating layer. The relationship also suggested that ω is affected by $\mathcal{P}_{gutter}/\mathcal{P}_{selective}$ of gas i and $\alpha_{selective}/\alpha_{gutter}$ of gas pair i/j, but the trend is indifferent regardless of the gas used. Similarly, ω is also unaffected by the individual permeance value of the layers, but only by the ratio of it. ω is also independent of the individual selectivity of the selective layer or gutter layer. Increase in $\alpha_{selective}/\alpha_{gutter}$ would have a reduced ω at lower $\mathcal{P}_{gutter}/\mathcal{P}_{selective}$.

This is also similar to the prediction by Kattula *et al.* (2015) for triple layer composite membrane.

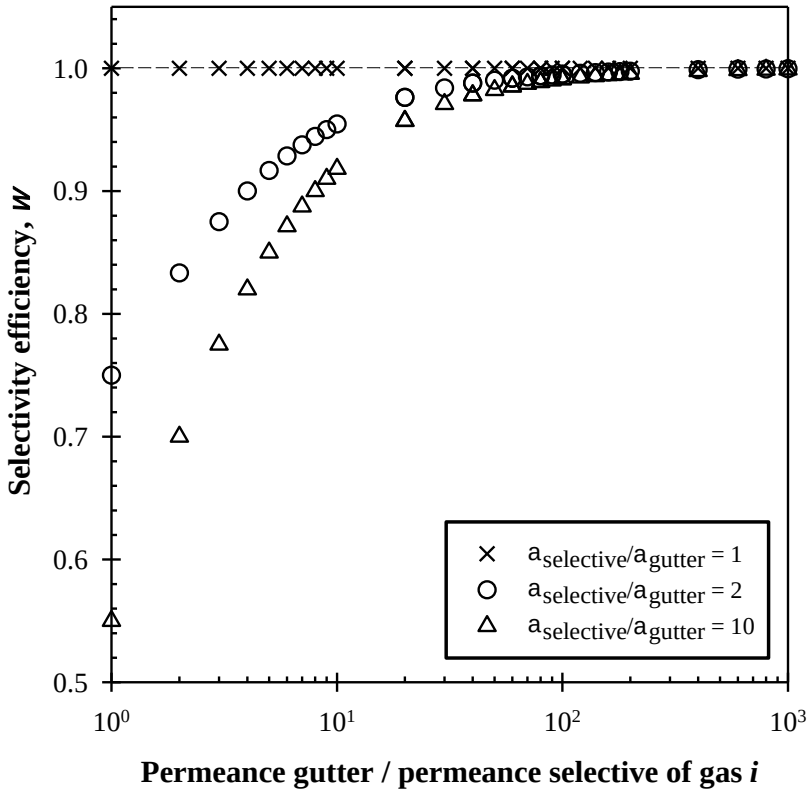

Figure 4.35: Relationship between $\mathcal{P}_{gutter}/\mathcal{P}_{selective}$ of gas i against the selectivity efficiency of gas pair i/j, $\omega_{i,j}$

On the other hand, Figure 4.34 and Figure 4.35 combined gives a good reference point for a dense-dense composite membrane fabrication. As discussed before, $\mathcal{P}_{gutter}/\mathcal{P}_{selective}$ needs to be at least 9 to achieve β = 0.9. At this condition, ω will always be more than 0.9 for $\alpha_{selective}/\alpha_{gutter}$ above 1. Lower $\alpha_{selective}/\alpha_{gutter}$ would give higher ω. But maintaining $\alpha_{selective}/\alpha_{gutter}$ = 1 would be counterproductive as gutter material with high selectivity usually would have low permeability as limited by the upper bound line and hence, high permeance would be hard to achieve. Thus, it would be very hard to achieve the targeted $\mathcal{P}_{gutter}/\mathcal{P}_{selective}$ of at least 9. Hence, dense-dense composite fabrication is limited by the possible material properties and selection such as their intrinsic permeance ratio, intrinsic

selectivity ratio, and their wetting properties to form thin layer onto each other. In the current work, with $\mathcal{P}_{gutter}/\mathcal{P}_{selective}$ for CO_2 at 32 and β = 0.970 for hypothetical 0.1 µm P84 PI, α_{gutter} at 7.4 and $\alpha_{selective}$ at 46.4 for CO_2/N_2 would give ω = 0.975. Similarly, α_{gutter} at 4.0 and $\alpha_{selective}$ at 53.8 for CO_2/CH_4 would also give ω = 0.972, a negligible loss for both permeance and selectivity in all cases.

4.5.2 PMP Hollow Fiber Membrane Performance Stability in Selective Layer's Coating Environment

One limitation with the fabrication of composite structure, especially in the case of polymer-polymer composite layer is the instability of the substrate with the solvent and fabrication condition (temperature, post-treatment, etc.) of the dense selective layer. This limits the composite fabrication only between polymers with dissimilar solvent or with modest fabrication condition. Hence, the PMP hollow fiber membrane's stability was tested versus the drying temperature and solvent used, i.e., NMP, a strong aprotic polar solvent used for P84 PI dissolution and coating for composite fabrication. The choice of this temperature was based on the pre-studies conducted for P84 PI drying condition, where at least 50 °C is needed to avoid phase inversion of the P84 PI with the humidity due to the hygroscopic nature of NMP. Figure 4.36 represents the FTIR spectra of the heat treatment at 60 °C and NMP soaked (3h and 3 days) PMP hollow fiber, to detect any chemical changes on the polymers. All the samples exhibit similar spectra with the same peaks as the original, untreated PMP fibers as in Figure 4.21. Peaks were noted at around 1 380 and 1 470 cm^{-1} for all samples due to bending of CH_2-CH_2 bond, and in the ranges of 2 800-3 000 cm^{-1} due to symmetric and asymmetric stretching vibration of CH_2 and CH_3 (Michaljaničová *et al.*, 2016, James Jebaseelan Samuel and Mohan, 2004). Hence, soaking in NMP and heat treating at 60 °C did not alter the bonding or chemical structure of the PMP fibers.

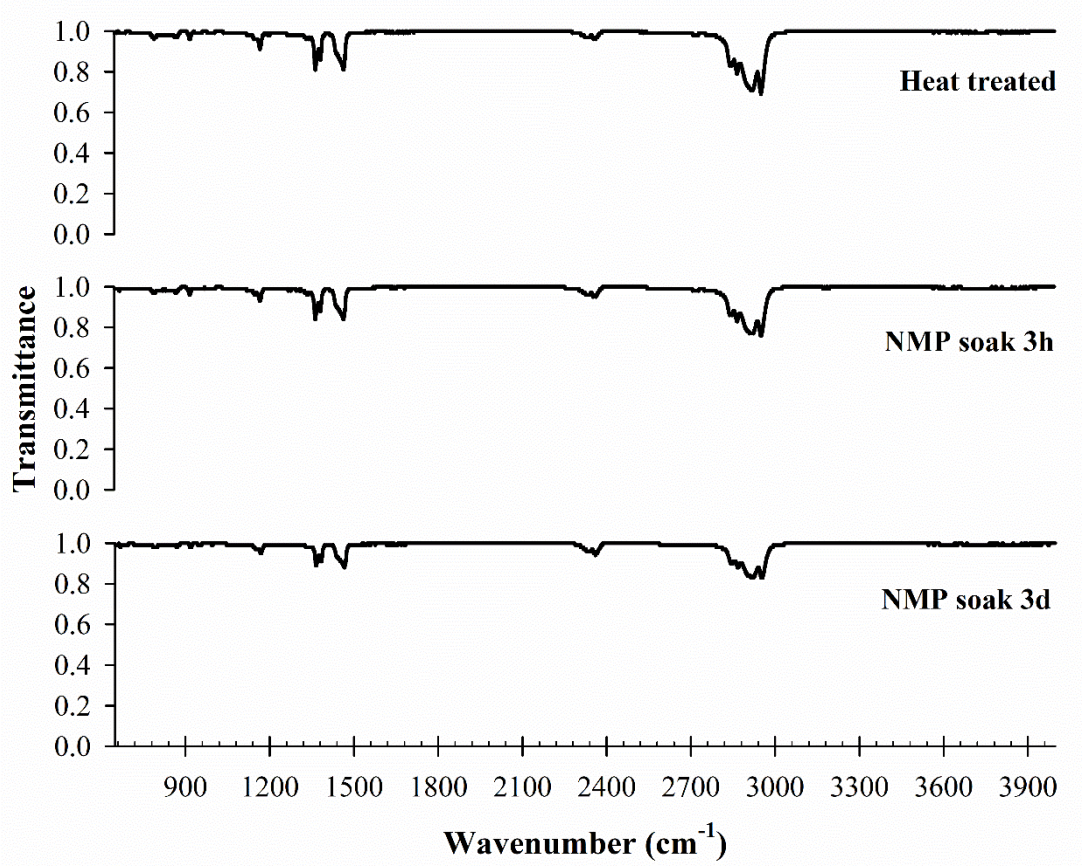

Figure 4.36: FTIR spectrum comparison of heat treated and NMP soaked PMP hollow fiber membrane (3h and 3 days)

Similarly, the treated fibers were analysed using SEM for surface (x3K magnification) and cross section (x1K and x300 magnification), as presented in Figure 4.37. No visual defects were detected for all samples, while the surface remains dense with no noticeable cracks formed. Circularity and dimensions of the fiber remains intact as before and between the different treatments. Hence, heat and solvent treatment conducted also did not change the morphology and structure of the PMP fibers.

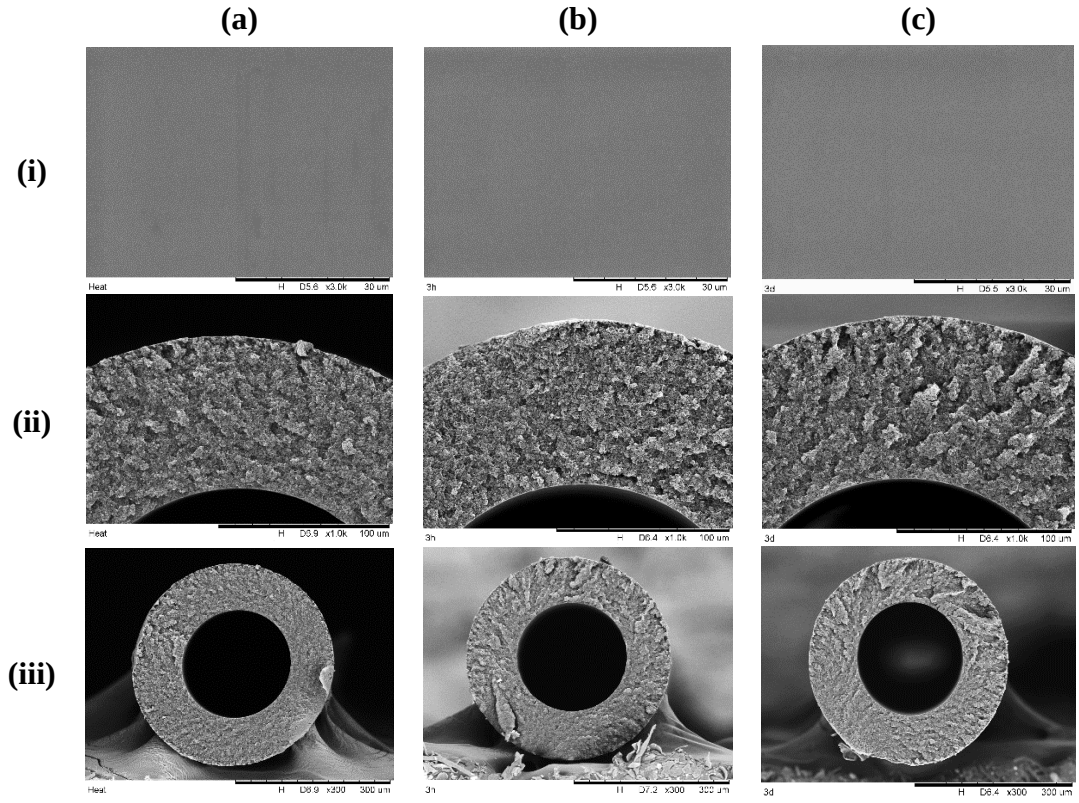

Figure 4.37: SEM micrograph of (a) heat treated and NMP soaked PMP hollow fiber membrane [(b) 3 hours and (c) 3 days]. (i) Surface at x3K magnification, (ii) cross section at x1K magnification, (iii) cross section at x300 magnification

While results so far suggested that the treatments conducted did not have any effect on the fibers, what is important would be the performance of the fibers post-treatment, which could affect the final composite performance. The results on the effect of heat treatment are presented in Table 4.15. Being dried at 60 °C, it was shown that the permeance decreased by about 11-12 % for CO_2 and N_2, and by about 16 % for CH_4 as compared to the base performance of pre-treated fibers. This is in line with the results in Figure 4.23 on the effect of permeance temperature of pre-treated PMP fibers, which showed reduced N_2 permeance as temperature increased. This, however, did not correspond to changes in selectivity as reported differences are negligible. Hence, the drying temperature may have certain effects on the rearrangement of

polymer molecules, but these changes are minimal and should not affect the resulting composite membranes performance.

Table 4.15: Influence of heat treatment (60 °C, 18h) on PMP substrate-gutter layer's permeance and selectivity

Gas	Permeance (GPU)		
	Base performance	**After treatment**	**Differences (%)**
N_2	80.3 ± 3.9	71.4 ± 4.9	- 11.1
CO_2	563.0 ± 19.2	497.4 ± 25.2	- 11.7
CH_4	132.2 ± 9.0	111.7 ± 5.1	- 15.6

Gas	Selectivity		
	Base performance	**After treatment**	**Differences (%)**
CO_2/N_2	7.1 ± 0.3	7.1 ± 0.3	- 0.5
CO_2/CH_4	4.3 ± 0.1	4.5 ± 0.1	3.1
N_2/CH_4	0.6 ± 0.1	0.6 ± 0.1	2.8

On the other hand, Table 4.16 represents the effect of 3h NMP solvent soak and Table 4.17 represents the effect of 3 days NMP solvent soak respectively. Soaking in NMP for extend time have significant effect on the permeance and selectivity of the PMP fibers. Limited decrease of 5-8% of CO_2 permeance was noted, while N_2 and CH_4 permeance were highly increased, up to 83-99% for N_2 and 43-49% for CH_4, as compared to the base performance. As a result, these permeances increment led to decrease in selectivity values for CO_2, between 48-54% for CO_2/N_2 and 34-38% for CO_2/CH_4. The dense PMP layer, however, can be said to be unaffected or minimally affected as the selectivity values are still significantly higher than the gas pair's Knudsen selectivity (at 0.8 for CO_2/N_2 and 0.6 for CO_2/CH_4). This confirms that the HF remain dense after the treatment.

Table 4.16: Influence of coating solvent (NMP) on PMP substrate-gutter layer's permeance and selectivity (3h soak and dried at 60 °C, 18h)

Gas	Permeance (GPU)		
	Base performance	**After treatment**	**Differences (%)**
N_2	93.8 ± 5.4	185.8 ± 6.2	98.8
CO_2	768.1 ± 21.9	709.0 ± 23.3	- 7.7
CH_4	195.3 ± 7.2	289.9 ± 7.2	48.4

Gas	Selectivity		
	Base performance	**After treatment**	**Differences (%)**
CO_2/N_2	8.2 ± 0.2	3.8 ± 0.1	- 53.5
CO_2/CH_4	3.9 ± 0.1	2.4 ± 0.1	- 37.9
N_2/CH_4	0.5 ± 0.1	0.6 ± 0.1	33.6

Table 4.17: Influence of coating solvent (NMP) on PMP substrate-gutter layer's permeance and selectivity (3 days soak and dried at 60 °C, 18h)

Gas	Permeance (GPU)		
	Base performance	**After treatment**	**Differences (%)**
N_2	101.8 ± 3.8	187.2 ± 1.7	83.8
CO_2	631.8 ± 9.7	597.7 ± 16.0	- 5.4
CH_4	195.1 ± 7.3	279.1 ± 7.7	43.0

Gas	Selectivity		
	Base performance	**After treatment**	**Differences (%)**
CO_2/N_2	6.2 ± 0.2	3.2 ± 0.1	- 48.6
CO_2/CH_4	3.2 ± 0.1	2.1 ± 0.1	- 34.0
N_2/CH_4	0.5 ± 0.1	0.7 ± 0.1	28.6

NMP has been reported as nonsolvent additive for PMP phase inversion (Lai *et al.*, 1996, Wang *et al.*, 2000). Phase diagram of PMP also suggested that there are no single-phase region for PMP-NMP pair (Kikkawa *et al.*, 2020), suggesting that PMP would not be affected by NMP immersion. Nevertheless, PMP based labware has been reported to have some effect after 7 days of constant exposure at 20 °C and suggested immediate danger for usage and hence not recommended for continuous use at 50 °C (ThermoFisher, 2016). This suggested that NMP did have some negative

effect on the PMP's morphology when exposed for more than 3 days conducted in the current work and at an augmented temperature, although the extended effect on gas permeability is unknown. These observations are hypothesised to be caused by PMP swelling by NMP. While no literature on PMP swelling was found, similar effect is expected as in gas permeation across water-swollen membranes, where the swelling molecules cause the rearrangement of the polymer chain, increasing the free volume (Liu *et al.*, 2008). Combined effect with heat treatment afterwards to dried up the NMP decreased the CO_2 permeance, but the plasticization effect by NMP is high enough to increase the N_2 and CH_4 permeances even after drying period. Nevertheless, despite of the harsh treatment applied to the HF, i.e., 3h and 3 days soaking in NMP, the HF appeared to be very stable with minimal differences between the soaking time. Pre-studies conducted suggesting that thin P84 PI coating was able to solidify in less than 1h, which is shorter than the time in this experiment. Hence it can be said that the reported permeance and selectivity here would be the maximum changes possible on the base PMP performance after P84 PI coating, assuming no other effects took place.

To compare the influence of these changes on the composite fabrication feasibility as in Table 4.14, the same calculation was also made here. The results are presented as in Table 4.18. Significant changes in $\mathcal{P}_{gutter}/\mathcal{P}_{selective}$ can be noted in the case of N_2 and CH_4, with increment as high as 120% and 82% for N_2 and CH_4 respectively. However, $\mathcal{P}_{gutter}/\mathcal{P}_{selective}$ of CO_2 was only slightly increased, by 8% from 32 to 35. As permeance efficiency factor, β has been shown to be a factor of $\mathcal{P}_{gutter}/\mathcal{P}_{selective}$ with lower $\mathcal{P}_{gutter}/\mathcal{P}_{selective}$ being less efficient in Figure 4.34, changes in β is negligible (from 0.970 to 0.972 for CO_2). Meanwhile, increment of $\alpha_{selective}/\alpha_{gutter}$ for CO_2/N_2 and CO_2/CH_4 (due to lowering of the α_{gutter} for both gas pairs in Table 4.16 and Table 4.17) was also negligible as selectivity efficiency, ω

barely changes at $\mathcal{P}_{gutter}/\mathcal{P}_{selective}$ above 20, and $\alpha_{selective}/\alpha_{gutter}$ above 10. This consequently reduced the theoretical P84 PI minimum thickness to 26 nm from the previous 31 nm. This effect is identical to the observation noted by Wijmans and Hao (2015) for PDMS gutter on a non-permeable porous substrate, where high permeability, low selectivity gutter layer is needed to minimize selectivity and permeance loss.

Table 4.18: Expected permeance of P84 PI and permeance ratio between NMP soaked PMP HF and hypothetical 0.1 µm thickness P84 PI, and changes in permeance efficiency, β and minimum theoretical P84 PI thickness with pre-treated fibers

Gas	P84 PI expected permeance (GPU), 0.1 µm	$\mathcal{P}_{gutter}/\mathcal{P}_{selective}$, P84 PI = 0.1 µm	Permeance efficiency, β [% changes]	Minimum P84 PI thickness (nm) [% changes]
N_2	0.45	416	0.998 [0.3]	
CO_2	18.79	35	0.972 [0.2]	0.26 [7.1]
CH_4	0.36	794	0.9998 [0.01]	

Expected permeance was calculated by dividing the permeability with the chosen thickness of the P84 PI layer

4.5.3 Influence of P84 Polyimide Concentration on Coating Thickness

The minimum theoretical P84 PI thickness calculated in Table 4.18 is based on the idea to maximize the composite permeance with β and ω of at least 90%. Nevertheless, the actual minimum thickness of P84 PI possible is really depends on the fabrication methodology and control to obtain the thinnest, defect free coating possible. Hence, the PMP HF was coated with P84 PI of 2, 6, and 10 wt.% using dip coating method with controlled dipping speed and coating temperature (single dipping). The surface (x1K magnification) and cross sectional (x5K magnification) micrographs of the P84 PI coated PMP HF membrane are presented in Figure 4.38. Both 6 and 10 wt.% suggested dense surfaces identical to the results in Figure 4.37,

suggesting no apparent defects and cross-sectional views verified the formation of the P84 PI coating. However, defect formation was noted for the 2 wt. % coating along the presumably interface between the P84 PI coating and the dense PMP surface. This suggested that coating of P84 PI solution somehow damages the surface structure of the PMP skin layer, despite that drying and NMP soaking stability test conducted earlier in Section 4.5.2 did not show sign of surface defects formation. One hypothesis is due to the shrinking of the low concentration P84 PI coating which tore the thin PMP dense surface. This claim is supported by the defect formation being formed along the presumably layer-layer interface, and the lack of noticeable damage to the underlying PMP substrate from the cross-sectional micrograph.

Shrinkage of thin film polymer solution during drying process is a common phenomenon observed, which caused reduction in coating size and increased coating tensile stress (Brinker, 2013). As more solvent is removed, polymer chain in the coating layer starts to concentrate and reduced in wet thickness. However, at a critical concentration, the polymer solution solidifies, and stress starts to build up in the coating film. Stress formation is to increase with thicker coating (Grosso *et al.*, 2015), which is in contrary to this work where no visible cracks were noticeable for higher concentration, thicker coating samples. In fact, the micrograph presented for 2 wt.% coating did not show cracks of P84 PI coating, but instead a tear along the interfaces. This suggested that the tear is instead due to shear stress on the thin dense PMP layer as the coating shrunk. Indeed, as coating solidifies, stress formed by further shrinkage needs to be released somewhere. As the coating shrinkage is constrained by the adhesion with the substrate, failure to supress the stress build up may be translated to either coating failure through cracking/delamination, or through substrate deformation (Francis *et al.*, 2002, Tomar *et al.*, 2020). For the latter, normally flat

configuration of the composite in literature would induce upward curling which stretched the substrate and shrunk the coating. Nevertheless, the fiber nature of this work and the thin PMP dense surface may instead rip the PMP surface, exposing the underlying porous network. Substrate deformation has also been discussed in the case of wetting on soft solid, which may be identical to the current proposed phenomenon (Rio and Boulogne, 2017).

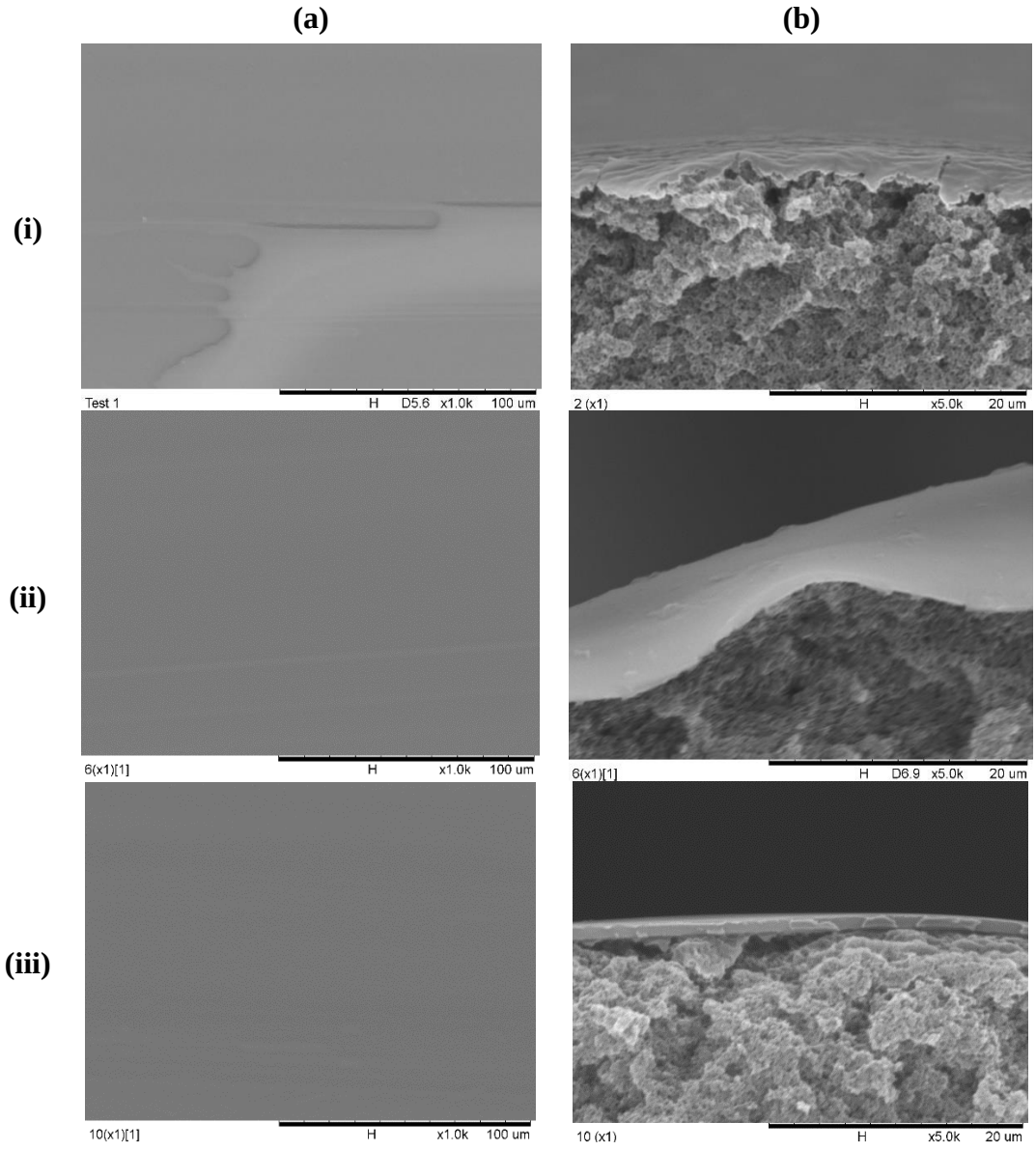

Figure 4.38: SEM micrographs (a) surface at x1K magnification, (b) coating cross section at x5K magnification of P84 PI coated PMP hollow fiber membranes. (i) 2 wt.%, (ii) 6 wt.%, (iii) 10 wt.% P84 PI solution with single dipping

For P84 PI layer to tear the PMP dense surface, two conditions need to be met; (i) P84 PI and PMP layer need to exhibit a strong layer-layer interaction/adhesion, otherwise shrinking of P84 PI would just slide on top of the dense PMP layer, and (ii) P84 PI solution dewets prior to reaching the critical concentration and hence creating the layer-layer interface, otherwise shrinking of P84 PI layer would either implode the fibers or cracks upon reaching its stress threshold. For condition (i), while no P84 PI-PMP layer-layer adhesion strength has been found in literature, the strong adhesion has been confirmed through the preliminary study conducted whereby P84 PI / PMP composite is able to withstand at least 0.12 N/mm^2 of constant pull force between the layer overnight or hanging 4 kg of water across a composite layer 2 cm in diameter. In comparison, Kapton tape with silicone adhesive and UV-ozone treated PDMS layer adhesion has been reported at 0.072 N/mm through peel test (Hoang *et al.*, 2016). Nevertheless, more studies are needed before conclusion can be made on the mechanism of the adhesion.

On the other hand, PMP exhibit low surface energy at 21.0 mJ/m^2, below the surface tension of NMP solvent at 40.8 mN/m at room temperature. Wettability of NMP on PMP can be predicted from the spreading coefficient, S, given by:

$$S = \gamma_{SV} - \gamma_{LV} - \gamma_{SL} \tag{4.16}$$

Where γ_{SV} is the surface energy of the solid, γ_{LV} is the surface tension of the liquid, and γ_{SL} is the interfacial tension between the solid and the liquid. Coated surface will always be stable when $S > 0$ (fully wetting) and can underwent dewetting if certain conditions are met when $S < 0$ (partial wetting) (Gennes *et al.*, 2004). Dewetting refers to the process of the liquid minimizing its surface energy and forming droplets and is the opposite of wetting phenomenon. For PMP-NMP system, with γ_{SV} and γ_{LV}

given the value as above, γ_{SL} can be determined from the contact angle measurement by rearranging the Young's formula:

$$\gamma_{SL} = \gamma_{SV} - \gamma_{LV}\, cos(\theta_Y) \quad (4.17)$$

Where θ_Y is called Young's contact angle. Measurement of PMP-NMP contact angle gives a value of 64.4 ± 1.5°, which gives γ_{SL} of 3.4 mN/m and S of -23.2 mN/m. Assuming minimal to negligible increment on surface tension of P84 PI-NMP polymer solution over the range of concentration used (Lasseuguette *et al.*, 2013, Ryck and Quéré, 1998), as $S < 0$, dewetting is possible to occur for PMP-NMP system.

Despite of the partial wetting condition, proper control of dip coating and solution parameters can allow an even coating of nonwetting solution when withdrawn vertically from a reservoir above a critical velocity (Shing Chan *et al.*, 2011). This phenomenon, called forced wetting is confirmed from the cross-sectional SEM micrographs of Figure 4.38 where P84 PI coating of consistent thickness can be observed clearly, at least for 6 wt.% and 10 wt.% coating. It is however, limited by what is called as dry regime, where below a certain thickness or withdrawal speed threshold, no wet film will be formed (Shing Chan *et al.*, 2011, Gennes *et al.*, 2004, Quéré, 1999). Dewetting by speed threshold is due to the resistance of liquid wedge close to the contact line (line where solid, liquid and vapor coexist) from viscous dissipation at low coating speed, while dewetting by minimum thickness is due to the increased action of van der Waals (vdW) force between the atoms at the liquid-solid and liquid-gas interfaces in nano thin film below 100 nm (Alizadeh Pahlavan *et al.*, 2018, Fondecave and Wyart, 1997, Quéré, 1999). As coating was visually formed for 6 and 10 wt.% solution, dewetting due to reaching the critical withdrawal speed is unlikely. However, it is possible that 2 wt.% coating P84 PI solution has reached the

critical thickness prior to reaching the critical solidification concentration, and hence undergoes dewetting.

Discussions so far were made on the assumption that P84 PI coating, especially for the 2 wt.% concentration was successfully formed. To confirm the formation of this thin coating layer, FTIR was employed for all coatings, as presented in Figure 4.39. Comparison of the spectra with PMP HF and P84 PI flakes suggested that 2, 6 and 10 wt.% coatings exhibit a mix of both PMP and P84 PI spectra, with the PMP peaks notably at 2 800-3 000 cm^{-1} due to symmetric and asymmetric stretching vibration of CH_2 and CH_3 (Michaljaničová *et al.*, 2016, James Jebaseelan Samuel and Mohan, 2004) diminished with increased P84 PI concentration. This is due to the increased thickness of the P84 PI coating, which is in line with the observation noted in Figure 4.38 from the cross-sectional SEM. Meanwhile, P84 PI peaks were noticeable especially as P84 PI coating concentration increased. These peaks are at 1360, 1715 and 1780 cm^{-1}, corresponding to the stretching mode of C=N, and the symmetric and asymmetric stretching mode of C=O from imide groups respectively (Guo *et al.*, 2018, Lua and Shen, 2013b, Favvas *et al.*, 2014). Peaks of 2 wt.% P84 PI coating barely have any spectrum of P84 PI, with only minor peaks at around 1715 cm^{-1} from the symmetric stretching mode of C=O. This, however, confirms that P84 PI was successfully coated on the PMP fibers in all cases, albeit to varying degrees.

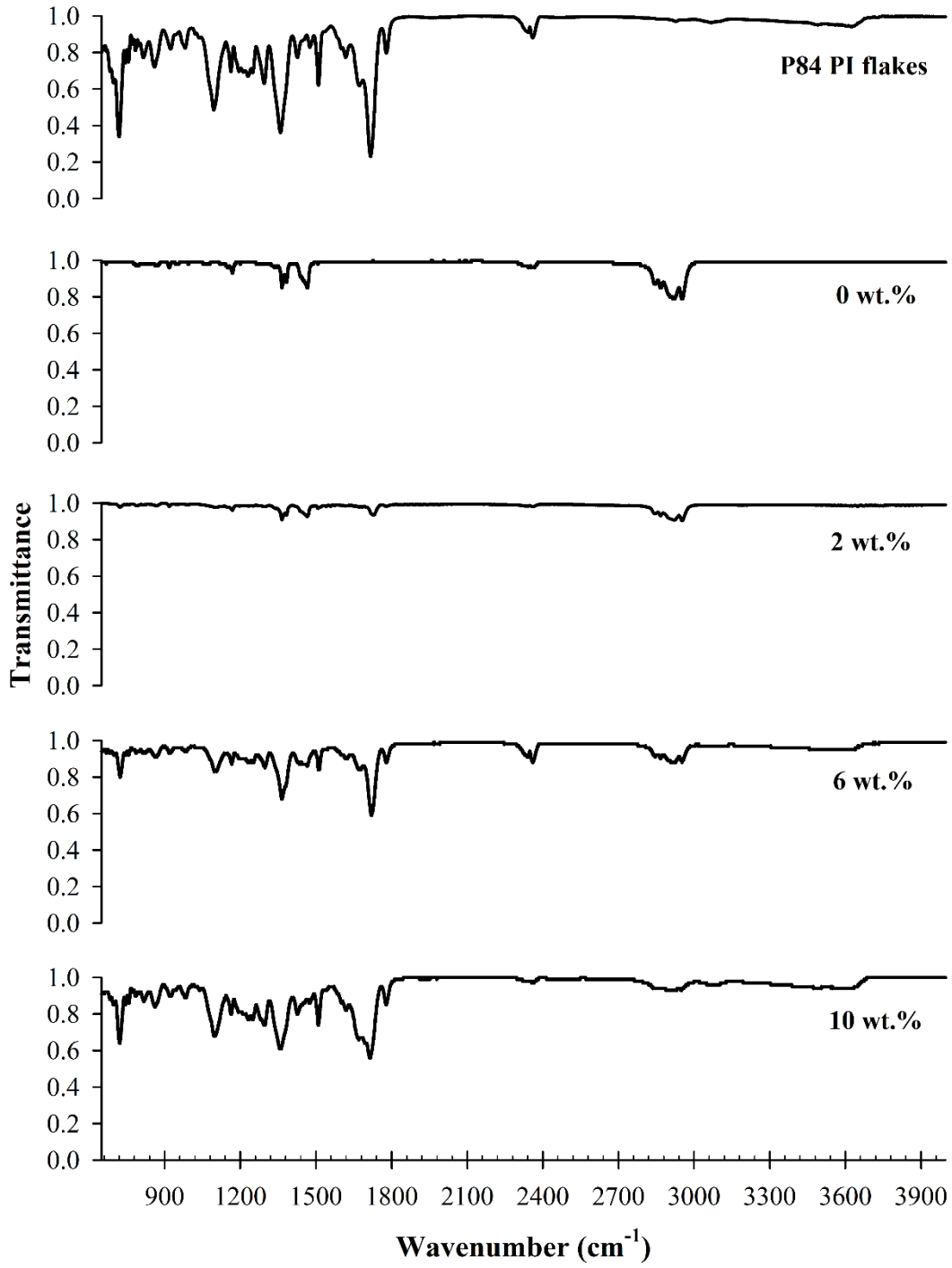

Figure 4.39: FTIR spectrum comparison between P84 PI flakes and P84 PI coated PMP HF made of different coating concentrations (0, 2, 6, and 10 wt.%)

While FTIR can confirm that P84 PI has been coated, it could not confirm the existence of defect formation nor the uniformity of the P84 PI coating as it is still localized to a small region. In all cases, FTIR was also employed along the fibers for every 1 mm. While the results have been consistent for the other fibers, it was found

that 2 wt.% coating was prone to a mix of coated and non-coated region, suggesting the dewetting phenomenon mentioned earlier. Out of 16 mm coated length tested, it was found that 13 locations of the coating detected P84 PI peaks while another 3 didn't (at 2, 3, and 7 mm), in the case of 2 wt.% P84 PI coating. Although most of the fibers were coated, the uncoated portion or defects formed such as the one seen in Figure 4.38 may cause significant reduction in performance. This, however, did not confirm if the coating was uniform for the other parts as random small uncoated surfaces or defects maybe formed in between the scan location or on the other side of the fibers.

Contrary to the common intuition, forces that governed the thin film deposition for dip coating is during the pulling of the substrate out of the solution bath, not during the immersion process. The equilibrium between entrainment of the coating solution and drainage of the solution from the surface predicts the wet thickness of the coating, while evaporation of the coating solvent dictates the dry thickness and stability of the coating. In most low speed, low viscosity coating cases, wet coating thickness, h_0 is governed by the Landau-Levich-Derjaguin (LLD) equation. To recall:

$$h_0 = 1.34bCa^{2/3} \tag{3.29}$$

$$Ca = \frac{\eta U_0}{\gamma_{LV}} \tag{3.30}$$

Where b is the fiber outer radius, and Ca is the capillary number, η is solution's viscosity, U_0 is coating velocity, and γ_{LV} is the solution's surface tension. Meanwhile, assuming that P84 PI is well dispersed in the NMP, all coated NMP is evaporated while P84 PI is not, and P84 PI solidify into a layer of equal density with the pre-coated P84 flakes, the theoretical dry thickness, h_f of the P84 PI coating can be determined. To recall:

$$h_f = h_0 \left(\frac{w_{polymer}}{w_{solution}}\right) \frac{\rho_{solution}}{\rho_{polymer}} \quad (3.32)$$

Where $w_{polymer}/w_{solution}$ is the weight fraction of the P84 PI solution, and ρ would be the density.

Figure 4.40 represents the evolution of theoretical wet and dry coating thickness of the P84 PI/PMP HF composites in the current work with different coating solution concentration. Using the SEM micrographs, experimental thickness of the P84 PI coating was also measured and compared with the theoretical thickness, as labelled in the figure. Indeed, P84 coating thickness increased with increasing P84 PI concentration when coated at the same withdrawal speed, drying temperature, and holding time. Differences between dry and wet coating thickness diminished as P84 PI concentration increased, as less solvent will be evaporated, and more polymers will be retained. However, experimental thickness at 6 and 10 wt.% P84 PI was a bit overestimated, but within less than 350 nm from the theoretical value. At this thickness, it can be considered significant should a stricter requirement is needed. Nevertheless, it should be close enough for relative comparison.

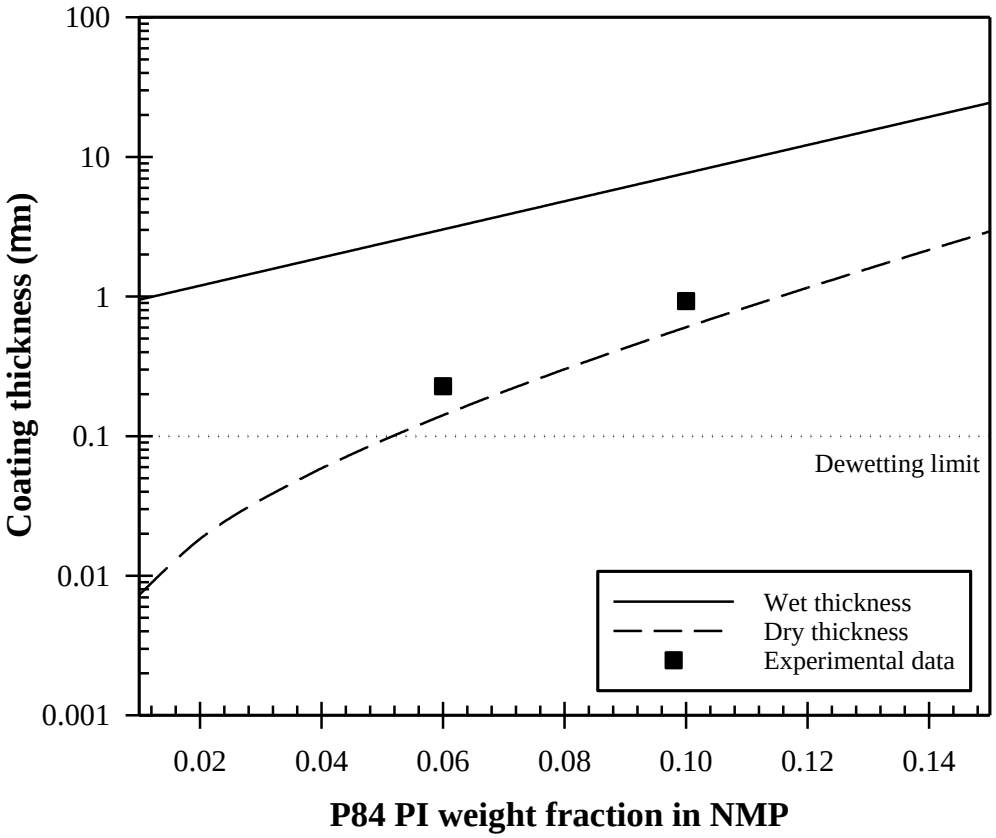

Figure 4.40: Evolution of coating thickness with P84 PI concentration and comparison with the measured experimental thickness

The theory behind dip-coating and wetting process is complex and will be outside of the scope of the thesis. Nevertheless, it is good to be understood, at least in the context of the experiment. In the range of the experiment (low speed, low viscosity solution), called visco-capillary regime, viscous drag entrains the liquid while capillary force tries to retrain and destabilize the coating, taking the liquid back into the coating reservoir (Quéré, 1999). Hence, LLD equation used in this calculation is limited by several factors. The first one is the negligibility of gravity over the capillary force, the two forces that would retrain the coated solution. This is limited by the capillary length, κ^{-1} given by Equation (3.34), where gravity is negligible if total thickness $(b + h_0)$ is much lower than κ^{-1}, or Bond number, $Bo < 1$, as given by Equation (3.33) (Lasseuguette *et al.*, 2013, Gennes *et al.*, 2004). The second limitation would be Ca < 0.64, where above this value LLD equation needs to be corrected to its

more generalized form (Quéré, 1999). This will be needed if the coating thickness is approaching the fiber's radius, either by increased coating speed, increased coating viscosity, or reduced coating solution's surface tension (see Equation (3.35)). In these cases, the limit of LLD validity was not surpassed for wet coating, with Bo within 0.0091-0.0093, and Ca within 0.001-0.03.

The first two limitations are the upper LLD limit that governs thicker coating. On the lower end of the spectrum, another limitation that needs to be considered is the effect of intermolecular forces (Quéré, 1999, Gennes *et al.*, 2004). This is the increased action of van der Waals (vdW) force at thin film below 100 nm for partial wetted surfaces, as discussed previously (Alizadeh Pahlavan *et al.*, 2018, Fondecave and Wyart, 1997, Quéré, 1999). For the current work, dry thickness drops below the 100 nm limit at about P84 PI concentration of 5.3%, suggesting the possibility for spontaneous dewetting (or spinodal dewetting) at concentrations below this limit. This is in line with the SEM results noted in Figure 4.38 for 2 wt.% coating solutions, and discussions made previously. Further validation of the effect on the PMP dense surface will be made based on the permeation results in the next subsection.

As noted earlier, experimental thickness in Figure 4.40 was overestimated as compared to the theoretical dry thickness. These are probably due to several simplifications made in this theoretical analysis, particularly other limitations of LLD equation which was purposely ignored. First, polymer solution is usually a non-Newtonian, shear thinning (pseudoplastic) fluids, where the viscosity decreases as shear rate increases. Nevertheless, at low concentration and low flow rate (hence low shear or coating speed), viscosity of these solutions would typically followed Newtonian behaviour (Sorbie, 1991, Larson, 1999). The concentration limit is expected to be limited at 4.3% for P84 PI-NMP system (Escorihuela *et al.*, 2018a).

Above this concentration, shear thinning condition will be observed. However, owing to the slow coating speed, deviation might be minor. Although, at higher concentration, deviations might become larger as coating thickening occurred (Ryck and Quéré, 1998). Similar assumption was also made for surface tension where it is assumed to be constant, as previously mentioned (Lasseuguette *et al.*, 2013, Ryck and Quéré, 1998). Second, coating was made at 60 °C, but most of the data used was taken at 25 °C. This would decrease the dynamic viscosity, surface tension, and density of the coating solution. Adjusting the values accordingly might increase the wet coating thickness nearer to the experimental value. This is highly likely to be the source of deviation in the current work. Another consideration would be the interaction between P84 PI-PMP. Fondecave and Wyart (1998) have studied the effects of antagonistic wetting interaction between solvent-polymer mixture with the substrate (solvent wets the substrate but the polymer did not). It was found that dewetting occurred in different regimes below a critical thickness, which is a factor of the polymer concentration. For the current work, it is known that the solvent is partial wetting, but the polymer's interaction is unknown. Meanwhile, drying of polymer solution can become complex due to viscosity change, formation of skin layer, and non-uniform polymer dispersion. For thin film, this might affect the resulting coating morphology (Schaefer *et al.*, 2015). Nevertheless, the last two considerations are most probably would affect the lower limit of LLD equation rather than explaining the source of deviation in this work.

4.5.4 Single Gas Permeation Performance

Figure 4.41 represents the permeation and selectivity results of CO_2/N_2 over the PMP HF composites, coated with different concentration of P84 PI for single dipped coating at 5 mm/s. Only a single fiber was tested per run in this test. NMP coated composite (0 wt.% P84 PI) suggested a comparable permeance and selectivity

for all gases, on par with the base PMP results in Table 4.7. This confirms that the NMP was completely evaporated below 3h limit imposed in Table 4.16, although higher coating concentration may have a slower evaporation rate due to higher coating viscosity. Meanwhile, permeance of 2 wt.% coating solutions were significantly increased for both CO_2 and N_2 with reduced selectivity down to 1.1, confirming the formation of tears on the substrate, exposing the porous nature of the bulk PMP layer as discussed earlier.

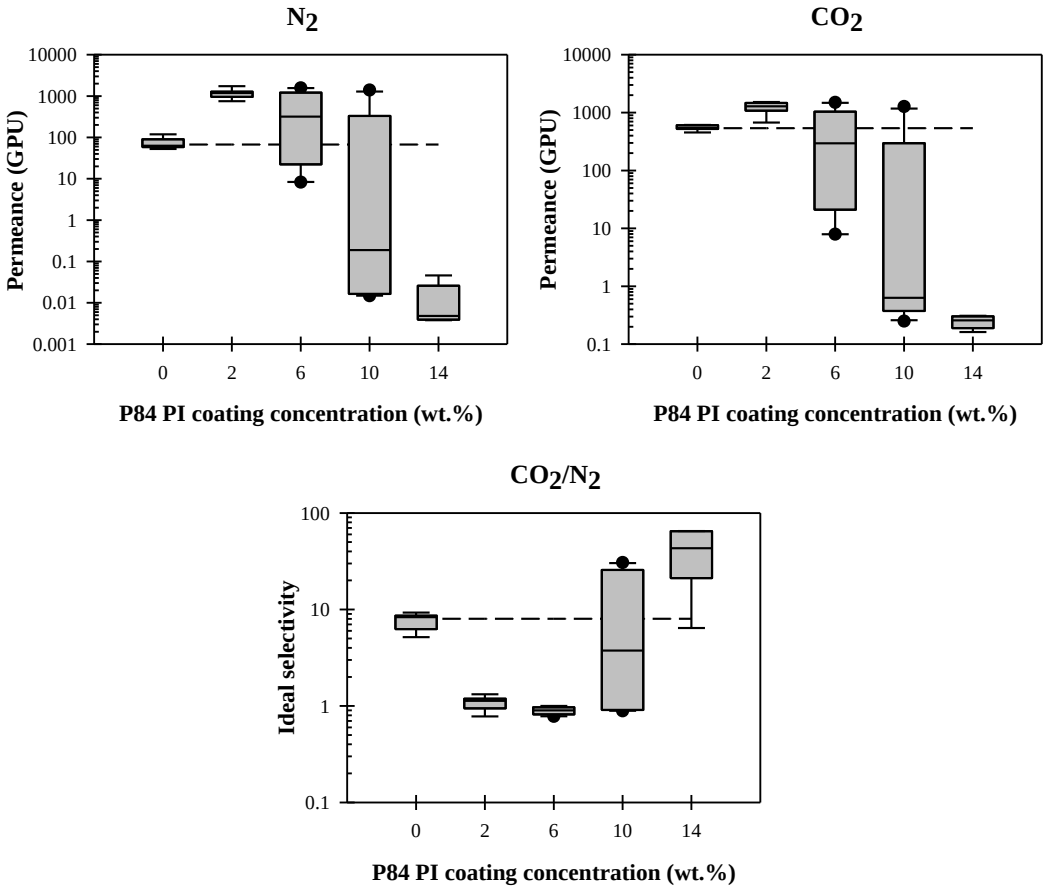

Figure 4.41: Influence of P84 PI polymer concentration (0-14 wt.%) on single composite fiber's permeance and selectivity (single dipped). Dash line represents the neat (untreated and uncoated) fiber's performance

As for higher polymer concentration coatings, 6 and 10 wt.% still exhibit an increased permeance for both CO_2 and N_2, although with varying degrees. At 6 wt.%, selectivity reduced to 0.8-0.9 suggesting smaller tears (due to Knudsen selectivity), although this was not observed from the SEM. Meanwhile, increase in

polymer concentration increased the range of permeances of CO_2 and N_2, with 10 wt.% coating exhibit the largest range. Only at 14 wt.% that permeance drops tremendously to an average of 0.013 ± 0.001 GPU for N_2, and 0.25 ± 0.03 GPU for CO_2. This gives an average selectivity of 42.99 ± 10.80, where the large error bar range is due to one of the data exhibit the selectivity of PMP, signifying the possibility for defects to occur even at this concentration. Nevertheless, this value is comparable to the ideal selectivity results of free-standing P84 PI in Table 4.13. Consequently, using Figure 4.40, theoretical dry thickness of 14 wt.% coating is given at 2.16 µm, which gives permeability of 0.03 and 0.54 Barrer for N_2 and CO_2 respectively. This is a bit lower than the intrinsic permeability results noted in Table 4.13, while back calculating using the intrinsic permeability gives a thickness between 3.5-7.6 µm. Interestingly, evolution of permeance range with coating solution concentration can be seen at 10 wt.%, where the permeance and selectivity reaches both ends of the limit (defective 2 wt.% coating and relatively good 14 wt.% coating).

As discussed previously, partial wetting coatings are prone to dewetting and are being governed by the minimum critical thickness. However, there are two critical thickness to be considered. The first critical thickness, usually at around 1 mm, is the true limit of stability of a partial wetted surface (Redon *et al.*, 1991, Gennes *et al.*, 2004). Below this limit, partially wetted surface is metastable and will always exhibit dewetting tendency up to a second critical thickness (the one at around 100 nm). It is below this second critical thickness that the coating solution will always undergo spinodal dewetting (Redon *et al.*, 1991). In the metastable region, wet thin film coating is sensitive to contaminants, air pockets, and forced instability due to movements or jiggering during coating process, which can randomly formed nucleation sites to cause dewetting (Gennes *et al.*, 2004), creating either non-coated

region or defects. This dewetting, called dewetting by nucleation and growth, expands from a nucleus of dry patch, which can occur due to the factors mentioned before. Nevertheless, the nucleation site will only expands when the radius is above a certain threshold, and took time to happen (Redon *et al.*, 1991). This is easier to occur as coating is thinner as the driving force (minimization of the total energy) would be higher (Thompson, 2012), on top of the possibility of more dry patches due to covering by dust and contaminants or air bubbles introduced during immersion process. Higher coating concentration would also have higher viscosity, hence should slows down any expansion of nucleation site.

Indeed, SEM results so far did not suggest any defects except for 2 wt.% coating. Nevertheless, even for a dense membrane, gas permeation is highly sensitive to even a tiny defects, much more than RO membranes (Baker, 2004). Hence, while defects (dry patch) that did not damage the PMP dense layer would be acceptable (as for the case of 14 wt.%), damage to the PMP layer should be avoided. Indeed, dewetting of the coating layer would also reduce the composite's selectivity as the PMP layer was no longer being coated. However, minimum selectivity should be limited by the value measured in Table 4.17, which is defined by the PMP layer. At a controlled dewetting without dense PMP tearing, permeance and selectivity might also be adjustable to suit the process needs.

The permeation results so far suggested that 14 wt.% coating solutions would be the minimum concentration needed for the current work to avoid PMP surface tearing. However, the tearing could be governed by two factors, (i) thickness of the coating which increased as coating concentration increases, or (ii) shrinkage of the coating, which is higher at low coating concentration. Hence, permeation test was conducted at varying coating speed (1, 3, and 5 mm/s) for 14 wt.% P84 PI coating

solution, single dipped, and 4 fibers per run for CO_2, N_2, and CH_4 gas, as represented in Figure 4.42. For 5 mm/s coating speed, average permeance was increased when 4 fibers were used as compared to the single fiber test previously, suggesting that defects were still formed. Nevertheless, the selectivity remains comparatively high; quite comparable in the case of CO_2/CH_4 but reduced by almost half for CO_2/N_2. As the coating speed was lowered, permeance value increased while selectivity decreased, suggesting even higher number of defect formation. Nevertheless, ideal selectivity remains high suggesting no tearing of PMP dense layer. The lowest speed at 1 mm/s found the highest permeance and the lowest selectivity for all gas pairs, suggesting even higher number of defects. With N_2/CH_4 selectivity at less than 1, this suggested that the defects are comparatively severe. Although, the selectivity for all gas pairs is still in the order of 2-3, which is less damage than the coating at 6 wt.%, 5 mm/s conducted earlier. This value is also comparable to the 3h and 3 days NMP soaked selectivity in Table 4.16 and Table 4.17. It is possible that the dense PMP was not teared, but longer immersion time imposed by slow coating speed have reduced the base PMP performance. Combined with the severe dry patch formation, overall composite selectivity was governed by the PMP rather than by P84 PI.

Theoretical dry coating thickness, using Equation (3.32) suggested that 1 and 3 mm/s speed gave a value of 178 and 370 nm respectively. This is lower than the experimental coating thickness reported in Figure 4.40 at 228 and 929 nm for 6 and 10 wt.% coating solution respectively, which also exhibit worse permeation and selectivity results. This suggested that the dense PMP tearing is mostly caused by the higher degree of shrinking at low polymer concentration, although contribution by thinner coatings which are much more prone to dewetting cannot be completely ignored.

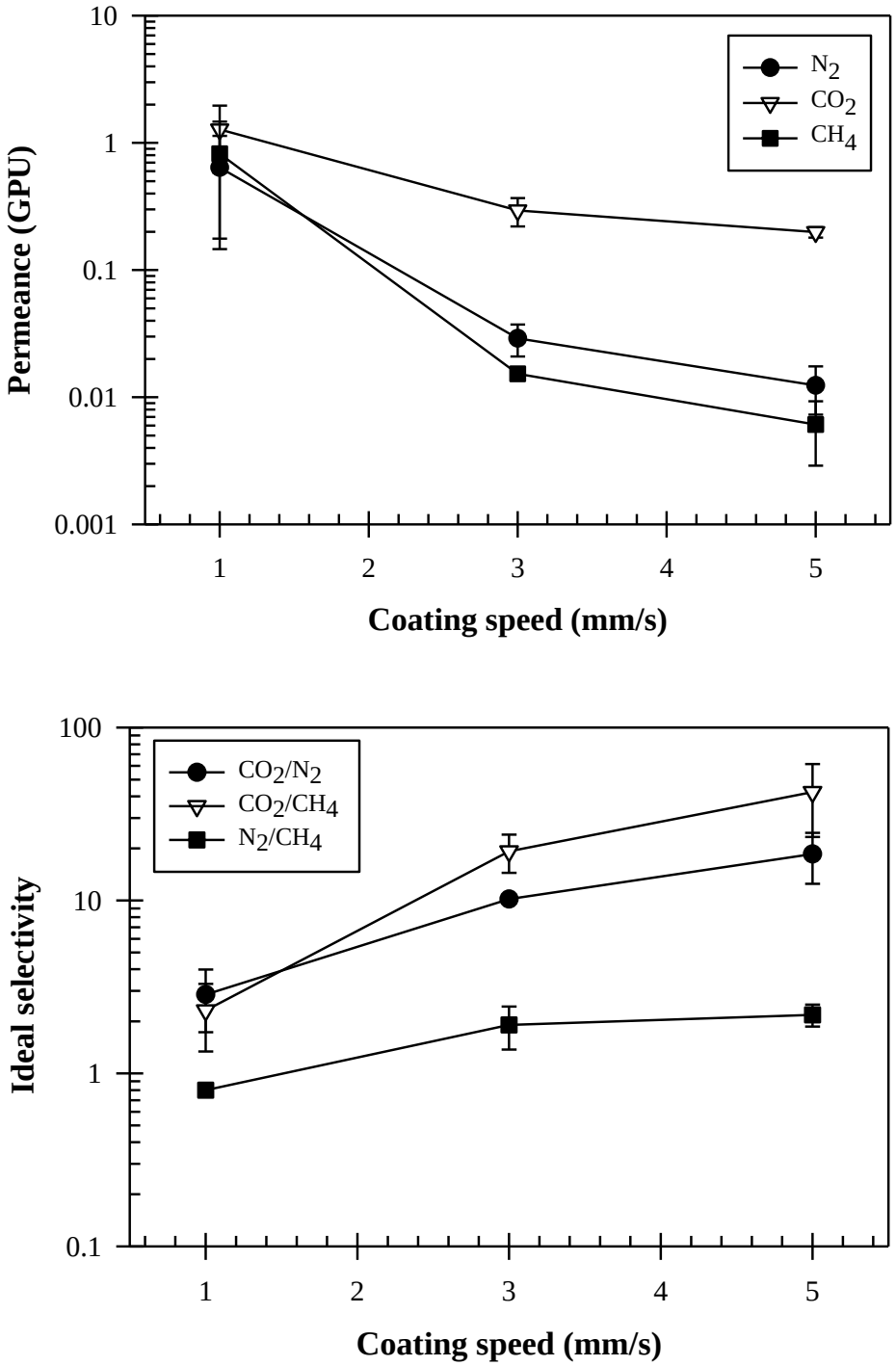

Figure 4.42: Influence of coating speed (1-5 mm/s) in 14 wt.% P84 PI polymer solution on composite fiber's permeance and selectivity (single dipped, 4 fibers)

CHAPTER FIVE

CONCLUSION AND RECOMMENDATIONS

5.1 Conclusion

In the current work, attempt has been made to elucidate the influence of substrate-gutter design (composite vs asymmetric) on the porous-dense interfacial phenomenon across the layered composite membrane (namely lateral diffusion and solution intrusion) using experimental, theoretical modelling and computational fluid dynamics (CFD) simulation through PES/PDMS composite and PMP asymmetric membranes. Significant drop in permeance from its ideal value was noted for PES/PDMS composite membranes especially at lower coating thickness. This is seen by the experimentally measured permeance of about 1.2 μm PDMS on a pristine PES substrate at 26.6 ± 2.6 GPU for N_2 and 354.4 ± 27.9 GPU for CO_2, as compared to their ideal permeance at about 186 GPU for N_2 and 1882 GPU for CO_2, a permeance loss of about 80-85%. Even though the substrate being highly permeable, its design played an important role particularly its surface architectures, which defines the permeance drop, or permeance efficiency of the selective layer. This includes the pore size, porosity, pore density, and pore uniformity on top of the permeability of the substrate material itself. On the other hand, the use of asymmetric PMP in this work was able to obtain permeance of 84.6 ± 6.2 GPU, 607.3 ± 31.3 GPU, and 156.0 ± 13.1 GPU for N_2, CO_2, and CH_4 respectively. This is much higher as compared to the results by PES/PDMS composite membrane despite of PMP's lower permeability as compared to PDMS, as asymmetric membrane removes the hurdle of geometric restriction and solution penetration noted across porous-dense composite structures. The concept is however limited by the number of possible materials that can act as substrate-gutter layer as it would require high permeance values to be used as a gutter layer, yet mechanically

strong enough to support the gas permeation process at elevated pressure. PMP is particularly interesting on this aspect especially since it is compatible with NMP; typical solvent used for polymeric membrane formation. Layer-layer compatibility between PMP and P84 PI as substrate-gutter and selective layer respectively was noted to be good, with possible P84 PI thickness as low as 0.26 nm before its permeance became high enough that PMP resistance would be detrimental towards the composite design. Meanwhile, the asymmetric PMP fibers were able to maintain its performance at an acceptable level when being dipped in NMP for about 3 days or heat treated at high as 60 °C overnight. This enables the use of mature dip coating methodology of P84 PI on PMP as its substrate-gutter layer. With intrinsic dense P84 PI permeability at 0.04 ± 0.01 Barrer, 1.88 ± 0.30 Barrer, and 0.036 ± 0.006 Barrer for N_2, CO_2, and CH_4 respectively, this gives an ideal selectivity of 46.4 ± 9.7, 1.4 ± 0.3, and 53.8 ± 6.4 for CO_2/N_2, N_2/CH_4, and CO_2/CH_4 respectively. Nevertheless, while PMP/P84 PI composite membrane can be fabricated, high shrinkage of low concentration P84 PI can cause tearing of the thin PMP skin layer especially at 2 wt.% P84 PI, exposing the porous substrate underneath and render the composite non-selective. Nevertheless, at 14 wt.% P84 PI and 5 mm/s dip coating speed, the composite gives a good separation performance with no major defects on the PMP layer at an average permeance of 0.013 ± 0.001 GPU for N_2, 0.25 ± 0.03 GPU for CO_2, and average selectivity of 42.99 ± 10.80 for CO_2/N_2, quite comparable to the selectivity of the intrinsic dense P84 PI membrane. Attempt to create thinner P84 PI at this concentration by using slower dip coating speed at 3 mm/s was able to maintain the P84 PI selectivity relatively high at 10.19 ± 0.32, 19.24 ± 4.79, and 1.90 ± 0.53 for CO_2/N_2, CO_2/CH_4, and N_2/CH_4 respectively. Nevertheless, this shows that dewetting still occurred as fabricated thickness is decreased by slower coating speed, which increasing the permeance up to 0.64 ± 0.49

GPU, 0.82 ± 0.65 GPU, and 1.27 ± 0.69 GPU for N_2, CH_4, and CO_2 respectively with ideal selectivity reduced to 2.86 ± 1.13, 2.31 ± 0.98, and 0.80 ± 0.03 for CO_2/N_2, CO_2/CH_4, and N_2/CH_4 respectively when conducted at 1 mm/s.

5.2 Recommendations

Several recommendations are proposed beyond the work of this thesis:

i. Most of the fillers used for CO_2 separation are soluble in polar solvent such as NMP. Hence, elucidation on the coating performance of suitable nanofillers should be elucidated.

ii. The use of 0.1 µm skin thickness asymmetric PMP layer may be too thin which caused the tearing upon drying of the P84 PI layer. Increase of PMP layer thickness, lowering surface energy of PMP, or using lower surface tension solvent may help to fabricate P84 PI with lower thickness without tearing effects at lower concentration.

iii. Relationship between the penetration factor and average coating penetration depth should be elucidated. Similarly, the factors influencing the uniformity coefficient should be elucidated so a better understanding can be made on the flow across composite membranes.

iv. Adhesion mechanism between P84 PI and PMP should be elucidated.

v. Fabricated PMP/P84 PI composite membranes should be tested with simulated mixed gas and actual biogas feed condition to better understand the system.

REFERENCES

3M 2019. Data Sheet for 3M™ Membrana™ OXYPLUS™, capillary membrane, type PMP 90/200. 3M™ Membrana™.

Abetz, V., Brinkmann, T., Dijkstra, M., Ebert, K., Fritsch, D., Ohlrogge, K., Paul, D., Peinemann, K. V., Pereira-Nunes, S., Scharnagl, N. & Schossig, M. 2006. Developments in Membrane Research: from Material via Process Design to Industrial Application. *Advanced Engineering Materials,* 8**,** 328-358.

Agrawal, A. 2005. *Surface Tension of Polymers* [Online]. Hatsopoulos Microfluids Laboratory, Department of Mechanical Engineering, Massachusetts Institute of Technology. Available: http://web.mit.edu/nnf/education/wettability/summerreading-2005short.pdf [Accessed 28 June 2021].

Ahmadpour, E., Shamsabadi, A. A., Behbahani, R. M., Aghajani, M. & Kargari, A. 2014. Study of CO2 separation with PVC/Pebax composite membrane. *Journal of Natural Gas Science and Engineering,* 21**,** 518-523.

Ahmed, I., Idris, A. & Pa, N. F. C. 2010. Novel method of synthesizing poly(ether sulfone) membranes containing two solvents and a lithium chloride additive and their performance. *Journal of Applied Polymer Science,* 115**,** 1428-1437.

Alizadeh Pahlavan, A., Cueto-Felgueroso, L., Hosoi, A. E., McKinley, G. H. & Juanes, R. 2018. Thin films in partial wetting: stability, dewetting and coarsening. *Journal of Fluid Mechanics,* 845**,** 642-681.

Alkan, M. H. & Groves, M. J. 1978. The measurement of membrane filter pore size by a gas permeability technique. *Drug Development and Industrial Pharmacy,* 4**,** 225-241.

AlMarzooqi, F. A., Bilad, M. R., Mansoor, B. & Arafat, H. A. 2015. A comparative study of image analysis and porometry techniques for characterization of porous membranes. *Journal of Materials Science,* 51**,** 2017-2032.

Armstrong, J. K., Wenby, R. B., Meiselman, H. J. & Fisher, T. C. 2004. The hydrodynamic radii of macromolecules and their effect on red blood cell aggregation. *Biophys J,* 87**,** 4259-70.

Baker, R. W. 2002. Future Directions of Membrane Gas Separation Technology. *Industrial & Engineering Chemistry Research,* 41**,** 1393-1411.

Baker, R. W. 2004. *Membrane Technology and Applications,* England, John Wiley & Sons.

Baker, R. W. 2008. Vapor and Gas Separation by Membranes. *In:* Li, N. N., Fane, A. G., Ho, W. S. W. & Matsuura, T. (eds.) *Advanced Membrane Technology and Applications.* John Wiley & Sons, Inc.

Baker, R. W. & Low, B. T. 2014. Gas Separation Membrane Materials: A Perspective. *Macromolecules,* 47**,** 6999-7013.

Bakhtiari, O., Mosleh, S., Khosravi, T. & Mohammadi, T. 2011. Synthesis and Characterization of Polyimide Mixed Matrix Membranes. *Separation Science and Technology,* 46**,** 2138-2147.

Barsema, J. 2003. Preparation and characterization of highly selective dense and hollow fiber asymmetric membranes based on BTDA-TDI/MDI co-polyimide. *Journal of Membrane Science,* 216**,** 195-205.

BASF. 2019. *Ultrason, Membrane Applications - Properties of Ultrason E, S and P* [Online]. BASF. Available: https://documents.basf.com/4ad3a7ce592532c830e59ad971b811a5173a0e3/Ultrason_Membran_Br_e_16.pdf [Accessed 28 June 2021].

Berean, K., Ou, J. Z., Nour, M., Latham, K., McSweeney, C., Paull, D., Halim, A., Kentish, S., Doherty, C. M., Hill, A. J. & Kalantar-zadeh, K. 2014. The effect of crosslinking temperature on the permeability of PDMS membranes: Evidence of extraordinary CO2 and CH4 gas permeation. *Separation and Purification Technology,* 122**,** 96-104.

Bernardo, P., Drioli, E. & Golemme, G. 2009. Membrane Gas Separation: A Review/State of the Art. *Industrial & Engineering Chemistry Research,* 48**,** 4638-4663.

Brinker, C. J. 2013. Dip Coating. *Chemical Solution Deposition of Functional Oxide Thin Films.*

C&EN 1980. Composite Membrane: Key to Gas Separators. *Chemical & Engineering News Archive,* 58**,** 57-60.

Cadotte, J. E. & Petersen, R. J. 1981. Thin-Film Composite Reverse-Osmosis Membranes: Origin, Development, and Recent Advances. *ACS Symposium Series,* 153**,** 305-326.

Car, A., Stropnik, C., Yave, W. & Peinemann, K.-V. 2008. Pebax®/polyethylene glycol blend thin film composite membranes for CO2 separation: Performance with mixed gases. *Separation and Purification Technology,* 62**,** 110-117.

Castro-Muñoz, R., Martin-Gil, V., Ahmad, M. Z. & Fíla, V. 2017. Matrimid® 5218 in preparation of membranes for gas separation: Current state-of-the-art. *Chemical Engineering Communications,* 205**,** 161-196.

Castro, R. P., Baker, R. W. & Wijmans, J. G. 1991. Multilayer Interfacial Composite Membrane. 5,049,167.

Cay-Durgun, P., Herrera, S. C. & Lind, M. L. 2020. Filler materials to prevent polymer intrusion into mesoporous substrates during thin film formation. *Microporous and Mesoporous Materials,* 296.

Ceratti, D. R., Louis, B., Paquez, X., Faustini, M. & Grosso, D. 2015. A New Dip Coating Method to Obtain Large-Surface Coatings with a Minimum of Solution. *Adv Mater,* 27**,** 4958-62.

Chabanon, E., Bouallou, C., Remigy, J. C., Lasseuguette, E., Medina, Y., Favre, E., Nguyen, P. T. & Roizard, D. 2011. Study of an innovative gas-liquid contactor for CO2 absorption. *Energy Procedia,* 4**,** 1769-1776.

Chen, X. Y., Kaliaguine, S. & Rodrigue, D. 2017. A Comparison between Several Commercial Polymer Hollow Fiber Membranes for Gas Separation. *Journal of Membrane and Separation Technology,* 6**,** 1-15.

Chen, X. Y., Vinh-Thang, H., Ramirez, A. A., Rodrigue, D. & Kaliaguine, S. 2015. Membrane Gas Separation Technologies for Biogas Upgrading. *RSC Advances,* 5**,** 24399-24448.

Chuah, C. Y., Goh, K., Yang, Y., Gong, H., Li, W., Karahan, H. E., Guiver, M. D., Wang, R. & Bae, T. H. 2018. Harnessing Filler Materials for Enhancing Biogas Separation Membranes. *Chem Rev,* 118**,** 8655-8769.

Chung, T.-S., Jiang, L. Y., Li, Y. & Kulprathipanja, S. 2007. Mixed matrix membranes (MMMs) comprising organic polymers with dispersed inorganic fillers for gas separation. *Progress in Polymer Science,* 32**,** 483-507.

Chung, T. S. 1997. Calculation of the intrusion depth and its effects on microporous composite membranes. *Separation and Purification Technology,* 12**,** 17-23.

Comesaña-Gándara, B., Chen, J., Bezzu, C. G., Carta, M., Rose, I., Ferrari, M.-C., Esposito, E., Fuoco, A., Jansen, J. C. & McKeown, N. B. 2019. Redefining the Robeson upper bounds for CO2/CH4 and CO2/N2 separations using a series of ultrapermeable benzotriptycene-based polymers of intrinsic microporosity. *Energy & Environmental Science,* 12**,** 2733-2740.

Cong, H., Radosz, M., Towler, B. & Shen, Y. 2007. Polymer–inorganic nanocomposite membranes for gas separation. *Separation and Purification Technology,* 55**,** 281-291.

Dai, Z., Ansaloni, L. & Deng, L. 2016. Recent advances in multi-layer composite polymeric membranes for CO_2 separation: A review. *Green Energy & Environment,* 1**,** 102-128.

Day, J. C., Alince, B. & Robertson, A. A. 1978. Interaction of polymers in solution with porous solids. I. Penetration of porous glass by dextran. *Canadian Journal of Chemistry,* 56.

Ding, X. & Harris, T. A. L. 2017. Review on penetration and transport phenomena in porous media during slot die coating. *Journal of Polymer Science Part B: Polymer Physics,* 55**,** 1669-1680.

Ding, Y. 2019. Perspective on Gas Separation Membrane Materials from Process Economics Point of View. *Industrial & Engineering Chemistry Research,* 59**,** 556-568.

Dong, S., Wang, Z., Sheng, M., Qiao, Z. & Wang, J. 2020. Scaling up of defect-free flat membrane with ultra-high gas permeance used for intermediate layer of multi-layer composite membrane and oxygen enrichment. *Separation and Purification Technology,* 239.

El-Kafrawy, A. 1982. Investigation of the Cellulose/LiCl/Dimethylacetamide and Cellulose/LiC1/N-Methyl-2-Pyrrolidinone Solutions by 13C NMR Spectroscopy. *Journal of Applied Polymer Science,* 27**,** 2435-2443.

Escorihuela, S., Tena, A., Shishatskiy, S., Escolastico, S., Brinkmann, T., Serra, J. M. & Abetz, V. 2018a. Gas Separation Properties of Polyimide Thin Films on Ceramic Supports for High Temperature Applications. *Membranes (Basel),* 8.

Escorihuela, S., Valero, L., Tena, A., Shishatskiy, S., Escolástico, S., Brinkmann, T. & Serra, J. M. 2018b. Study the Effect of Inorganic Particles on the Gas Transport Propeerties of Glassy Polyimides for Selective CO2 and H2O Seperation. *membranes,* 8**,** 128.

Etxeberria-Benavides, M., Karvan, O., Kapteijn, F., Gascon, J. & David, O. 2019. Fabrication of Defect-Free P84(R) Polyimide Hollow Fiber for Gas Separation: Pathway to Formation of Optimized Structure. *Membranes (Basel),* 10.

Faria, M., Moreira, C., Mendonça Eusébio, T., de Pinho, M. N., Brogueira, P. & Semião, V. 2018. Oxygen mass transfer in a gas/membrane/liquid system surrogate of membrane blood oxygenators. *AIChE Journal,* 64**,** 3756-3763.

Favvas, E. P., Katsaros, F. K., Papageorgiou, S. K., Sapalidis, A. A. & Mitropoulos, A. C. 2017. A review of the latest development of polyimide based membranes for CO 2 separations. *Reactive and Functional Polymers,* 120**,** 104-130.

Favvas, E. P., Papageorgiou, S. K., Nolan, J. W., Stefanopoulos, K. L. & Mitropoulos, A. C. 2013. Effect of air gap on gas permeance/selectivity performance of BTDA-TDI/MDI copolyimide hollow fiber membranes. *Journal of Applied Polymer Science***,** n/a-n/a.

Favvas, E. P., Stefanopoulos, K. L., Nolan, J. W., Papageorgiou, S. K., Mitropoulos, A. C. & Lairez, D. 2014. Mixed Matrix Hollow Fiber Membranes with enhanced gas permeation properties. *Separation and Purification Technology,* 132**,** 336-345.

Filiatrault, D., Phuong-Nguyen, H. & Delmas, G. 1981. Intrinsic viscosities of four homopolymers and one copolymer in nonpolar solvents. I. Effect of correlations of molecular orientations. *Journal of Polymer Science: Polymer Physics Edition,* 19**,** 763-771.

Firpo, G., Angeli, E., Repetto, L. & Valbusa, U. 2015. Permeability thickness dependence of polydimethylsiloxane (PDMS) membranes. *Journal of Membrane Science,* 481**,** 1-8.

Flick, E. W. 1998. *Industrial Solvents Handbook,* New Jersey, Noyes Data Corporation.

Fondecave, R. & Wyart, F. B. 1997. Wetting laws for polymer solutions. *Europhysics Letters,* 37**,** 115-120.

Fondecave, R. & Wyart, F. B. 1998. Polymers as dewetting agents. *Macromolecules,* 31**,** 9305-9315.

Fouda, A., Chen, Y., Bai, J. & Matsuura, T. 1991. Wheatstone bridge model for the laminated polydimethylsiloxane/polyethersulfone membrane for gas separation. *Journal of Membrane Science,* 64**,** 263-271.

Fox, H. W. & Zisman, W. A. 1952. The Spreading of Liquids on Low-Energy Surfaces. II. Modified Tetrafluoroethylene Polymers. *Journal of Colloid Science,* 7.

Francis, L. F., McCormick, A. V., Vaessen, D. M. & Payne, J. A. 2002. Development and measurement of stress in polymer coatings. *Journal of Materials Science,* 37**,** 4717-4731.

Francis, P. S., Luzio, F. C. D., Gilla, W. S. & Kotch, A. 1966. Fabrication and Evaluation of New Ultrathin Reverse Osmosis Membranes. *Research and Development Progress Report.* Office of Saline Water United States Department of the Interior.

Freeman, B. D. 1999. Basis of Permeability/Selectivity Tradeoff Relations in Polymeric Gas Separation Membranes. *Macromolecules,* 32**,** 375-380.

Fu, Y.-J., Lai, C.-L., Hu, C.-C., Sun, Y.-M., Wu, S.-Y., Chen, J.-T., Huang, S.-H., Hung, W.-S. & Lee, K.-R. 2016. Extraordinary transport behavior of gases in isothermally annealed poly(4-methyl-1-pentene) membranes. *Journal of Polymer Science Part B: Polymer Physics,* 54**,** 2368-2376.

Galizia, M., Chi, W. S., Smith, Z. P., Merkel, T. C., Baker, R. W. & Freeman, B. D. 2017. 50th Anniversary Perspective: Polymers and Mixed Matrix Membranes for Gas and Vapor Separation: A Review and Prospective Opportunities. *Macromolecules,* 50**,** 7809-7843.

Gao, J. & Chung, T.-S. 2019. Influence of contaminants in glycerol/water mixtures during post-treatment on physicochemical properties and separation performance of air-dried membranes. *Journal of Membrane Science,* 572**,** 223-229.

Gennes, P.-G. d., Brochard-Wyart, F. & Quéré, D. 2004. *Capillarity and wetting phenomena: Drops, bubbles, pearls, waves*, Springer-Verlag New York Inc.

Ghadimi, A., Norouzbahari, S., Lin, H., Rabiee, H. & Sadatnia, B. 2018. Geometric restriction of microporous supports on gas permeance efficiency of thin film composite membranes. *Journal of Membrane Science,* 563**,** 643-654.

Ghalei, B., Sakurai, K., Kinoshita, Y., Wakimoto, K., Isfahani, Ali P., Song, Q., Doitomi, K., Furukawa, S., Hirao, H., Kusuda, H., Kitagawa, S. & Sivaniah, E. 2017. Enhanced selectivity in mixed matrix membranes for CO2 capture through efficient dispersion of amine-functionalized MOF nanoparticles. *Nature Energy,* 2**,** 17086.

Gholami, M., Nasseri, S., Feng, C. Y., Matsuura, T. & Khulbe, K. C. 2003. The effect of heat-treatment on the ultrafiltration performance of polyethersulfone (PES) hollow-fiber membranes. *Desalination,* 155**,** 293-301.

Ghosh, A. K., Jeong, B.-H., Huang, X. & Hoek, E. M. V. 2008. Impacts of reaction and curing conditions on polyamide composite reverse osmosis membrane properties. *Journal of Membrane Science,* 311**,** 34-45.

Goh, P. S., Ismail, A. F., Sanip, S. M., Ng, B. C. & Aziz, M. 2011. Recent advances of inorganic fillers in mixed matrix membrane for gas separation. *Separation and Purification Technology,* 81**,** 243-264.

Grosso, D., Boissière, C. & Faustini, M. 2015. Thin film deposition techniques. *In:* Levy, D. (ed.) *The Sol-Gel Handbook: Synthesis, Characterization, and Applications.* Wiley-VCH Verlag GmbH.

Guillen, G. R., Pan, Y., Li, M. & Hoek, E. M. V. 2011. Preparation and Characterization of Membranes Formed by Nonsolvent Induced Phase Separation: A Review. *Industrial & Engineering Chemistry Research,* 50**,** 3798-3817.

Guillen, G. R., Ramon, G. Z., Kavehpour, H. P., Kaner, R. B. & Hoek, E. M. V. 2013. Direct microscopic observation of membrane formation by nonsolvent induced phase separation. *Journal of Membrane Science,* 431**,** 212-220.

Gunawan, T., Widiastuti, N., Fansuri, H., Wan Salleh, W. N., Ismail, A. F., Lin, R., Motuzas, J. & Smart, S. 2021. The utilization of micro-mesoporous carbon-based filler in the P84 hollow fibre membrane for gas separation. *R Soc Open Sci,* 8**,** 201150.

Guo, A., Ban, Y., Yang, K. & Yang, W. 2018. Metal-organic framework-based mixed matrix membranes: Synergetic effect of adsorption and diffusion for CO2/CH4 separation. *Journal of Membrane Science,* 562**,** 76-84.

Guo, L. & Santschi, P. H. 2007. Ultrafiltration and its Applications to Sampling and Characterisation of Aquatic Colloids. *In:* Wilkinson, K. J. & Lead, J. R. (eds.) *Environmental Colloids and Particles : Behaviour, Separation and Characterisation.* England: John Wiley & Sons Ltd.

Halim, A., Fu, Q., Yong, Q., Gurr, P. A., Kentish, S. E. & Qiao, G. G. 2014. Soft polymeric nanoparticle additives for next generation gas separation membranes. *Journal of Materials Chemistry A,* 2.

Han, J., Lee, W., Choi, J. M., Patel, R. & Min, B.-R. 2010. Characterization of polyethersulfone/polyimide blend membranes prepared by a dry/wet phase inversion: Precipitation kinetics, morphology and gas separation. *Journal of Membrane Science,* 351**,** 141-148.

Hao, P., Wijmans, J. G., He, Z. & White, L. S. 2020. Effect of pore location and pore size of the support membrane on the permeance of composite membranes. *Journal of Membrane Science,* 594.

Hapgood, K. P., Litster, J. D., Biggs, S. R. & Howes, T. 2002. Drop penetration into porous powder beds. *J Colloid Interface Sci,* 253**,** 353-66.

He, G., Huang, X., Xu, R. & Zhu, B. 1996. An improved resistance model for gas permeation in composite membranes. *Journal of Membrane Science,* 118**,** 1-7.

Henis, J. M. S. 2018. Commercial and Practical Aspects of Gas Separation Membranes. *In:* Paul, D. R. & Yampol'skii, Y. P. (eds.) *Polymeric Gas Separation Membranes.* Florida, USA: CRC Press.

Henis, J. M. S. & Tripodi, M. K. 1980. A Novel Approach to Gas Separations Using Composite Hollow Fiber Membranes. *Separation Science and Technology,* 15**,** 1059-1068.

Henis, J. M. S. & Tripodi, M. K. 1981. Composite hollow fiber membranes for gas separation: the resistance model approach. *Journal of Membrane Science,* 8**,** 233-246.

Hoang, M. V., Chung, H.-J. & Elias, A. L. 2016. Irreversible bonding of polyimide and polydimethylsiloxane (PDMS) based on a thiol-epoxy click reaction. *Journal of Micromechanics and Microengineering,* 26.

Hosseini, S. S. & Chung, T. S. 2009. Carbon membranes from blends of PBI and polyimides for N_2/CH_4 and CO_2/CH_4 separation and hydrogen purification. *Journal of Membrane Science,* 328**,** 174-185.

Hosseini, S. S., Omidkhah, M. R., Moghaddam, A. Z., Pirouzfar, V., Krantz, W. B. & Tan, N. R. 2014. Enhancing the properties and gas separation performance of PBI–polyimides blend carbon molecular sieve membranes via optimization of the pyrolysis process. *Separation and Purification Technology,* 122**,** 278–289.

Houston, K. S., Weinkauf, D. H. & Stewart, F. F. 2002. Gas transport characteristics of plasma treated poly(dimethylsiloxane) and polyphosphazene membrane materials. *Journal of Membrane Science,* 205**,** 103-112.

Hu, L., Cheng, J., Li, Y., Liu, J., Zhou, J. & Cen, K. 2017. Amino-functionalized surface modification of polyacrylonitrile hollow fiber-supported polydimethylsiloxane membranes. *Applied Surface Science,* 413**,** 27-34.

Hu, L., Cheng, J., Li, Y., Liu, J., Zhou, J. & Cen, K. 2018. Optimization of coating solution viscosity of hollow fiber-supported polydimethylsiloxane membrane for CO2/H2separation. *Journal of Applied Polymer Science,* 135.

Huang, Y. & Paul, D. R. 2007. Effect of film thickness on the gas-permeation characteristics of glassy polymer membranes. *Industrial Engineering Chemistry Research,* 46**,** 2342 - 2347.

Idris, A., Ahmed, I. & Limin, M. A. 2010. Influence of lithium chloride, lithium bromide and lithium fluoride additives on performance of polyethersulfone membranes and its application in the treatment of palm oil mill effluent. *Desalination,* 250**,** 805-809.

Islam, M. A. & Buschatz, H. 2005. Assessment of thickness-dependent gas permeability of polymer membranes. *Indian Journal of Chemical Technology,* 12**,** 88-92.

Ismail, N. H., Salleh, W. N. W., Sazali, N., Mohamed, M. A., Rosman, N. & Yusof, N. 2017. Effect of P84 (BTDA-TDI/MDI) Composition Towards the Performance of the Disk Supported Carbon Membrane. *Jurnal Teknologi,* 79**,** 41-45.

J. Puetz & Aegerter, M. A. 2004. Dip Coating Technique. *Sol-Gel Technologies for Glass Producers and Users.* Springer Science.

James Jebaseelan Samuel, E. & Mohan, S. 2004. FTIR and FT Raman spectra and analysis of poly(4-methyl-1-pentene). *Spectrochimica Acta Part A: Molecular and Biomolecular Spectroscopy,* 60**,** 19-24.

Jawad, Z. A., Ahmad, A. L., Low, S. C., Chew, T. L. & Zein, S. H. S. 2015. Influence of solvent exchange time on mixed matrix membrane separation performance for CO2/N2 and a kinetic sorption study. *Journal of Membrane Science,* 476**,** 590-601.

Jeong, B.-H., Hoek, E. M. V., Yan, Y., Subramani, A., Huang, X., Hurwitz, G., Ghosh, A. K. & Jawor, A. 2007. Interfacial polymerization of thin film nanocomposites: A new concept for reverse osmosis membranes. *Journal of Membrane Science,* 294**,** 1-7.

Jiang, X., Chuah, C. Y., Goh, K. & Wang, R. 2021. A facile direct spray-coating of Pebax® 1657: Towards large-scale thin-film composite membranes for efficient CO2/N2 separation. *Journal of Membrane Science,* 638.

Jiao, C., Song, X., Zhang, X., Sun, L. & Jiang, H. 2021. MOF-Mediated Interfacial Polymerization to Fabricate Polyamide Membranes with a Homogeneous Nanoscale Striped Turing Structure for CO2/CH4 Separation. *ACS Appl Mater Interfaces,* 13**,** 18380-18388.

Jin, M.-Y., Liao, Y., Loh, C. H., Tan, C.-H. & Wang, R. 2017. Preparation of Polydimethylsiloxane–Polyvinylidene Fluoride Composite Membranes for Phenol Removal in Extractive Membrane Bioreactor. *Industrial & Engineering Chemistry Research,* 56**,** 3436-3445.

Johnson, L. M., Gao, L., Shields, I. C., Smith, M., Efimenko, K., Cushing, K., Genzer, J. & Lopez, G. P. 2013. Elastomeric microparticles for acoustic mediated bioseparations. *J Nanobiotechnology,* 11**,** 22.

Kapantaidakis, G. C., Koops, G. H., Wessling, M., Kaldis, S. P. & Sakellaropoulos, G. P. 2003. CO2 plasticization of polyethersulfone/polyimide gas-separation membranes. *Aiche Journal,* 49**,** 1702-1711.

Karkhanechi, H., Kazemian, H., Nazockdast, H., Mozdianfard, M. R. & Bidoki, S. M. 2012. Fabrication of Homogenous Polymer-Zeolite Nanocomposites as Mixed-Matrix Membranes for Gas Separation. *Chemical Engineering & Technology,* 35**,** 885-892.

Kattula, M., Ponnuru, K., Zhu, L., Jia, W., Lin, H. & Furlani, E. P. 2015. Designing ultrathin film composite membranes: the impact of a gutter layer. *Scientific Reports,* 5**,** 15016.

Kawakami, H., MIkawa, M. & Nagaoka, S. 1996. Gas permeability and selectivity through asymmetric polyimide membranes. *Journal of Applied Polymer Science,* 62**,** 965-971.

Kenarsari, S. D., Yang, D., Jiang, G., Zhang, S., Wang, J., Russell, A. G., Wei, Q. & Fan, M. 2013. Review of recent advances in carbon dioxide separation and capture. *RSC Advances,* 3.

Khare, V. P., Greenberg, A. R., Kelley, S. S., Pilath, H., Juhn Roh, I. & Tyber, J. 2007. Synthesis and characterization of dense and porous cellulose films. *Journal of Applied Polymer Science,* 105**,** 1228-1236.

Khulbe, K. C., Feng, C. Y. & Matsuura, T. 2008. Pore Size, Pore Size Distribution, and Roughness at the Membrane Surface. *In:* Pasch, H. (ed.) *Synthetic Polymeric Membranes.* Springer.

Kiesow, I., Marczewski, D., Reinhardt, L., Muhlmann, M., Possiwan, M. & Goedel, W. A. 2013. Bicontinuous zeolite polymer composite membranes prepared via float casting. *Journal of American Chemical Society,* 135**,** 4380-8.

Kikkawa, K., Hsu, Y.-I., Cui, X., Mizuno, S., Asoh, T.-A. & Uyama, H. 2020. Surface Oxidation of Polymer 3D Porous Structures Using Chlorine Dioxide Radical Gas. *ACS Applied Polymer Materials,* 2**,** 4964-4972.

Kim, J.-H. & Lee, K.-H. 1998. Effect of PEG additive on membrane formation by phase inversion. *Journal of Membrane Science,* 138**,** 153-163.

Koros, W. J. & Mahajan, R. 2000. Pushing the limits on possibilities for large scale gas separation: which strategies? *Journal of Membrane Science,* 175**,** 181-196.

Koros, W. J. & Pinnau, I. 2008. Membrane Formation for Gas Separation Processes. *In:* Paul, D. R. & Yampol'skii, Y. P. (eds.) *Polymeric Gas Separation Membranes.* FL, USA: CRC Press.

Koros, W. J. & Pinnau, I. 2018. Membrane Formation for Gas Separation Processes. *In:* Paul, D. R. & Yampol'skii, Y. P. (eds.) *Polymeric Gas Separation Membranes.* Florida, USA: CRC Press.

Koros, W. J. & Zhang, C. 2017. Materials for next-generation molecularly selective synthetic membranes. *Nat Mater,* 16**,** 289-297.

Kouketsu, T., Duan, S., Kai, T., Kazama, S. & Yamada, K. 2007. PAMAM dendrimer composite membrane for CO2 separation: Formation of a chitosan gutter layer. *Journal of Membrane Science,* 287**,** 51-59.

Kumazawa, H., Wang, J. S. & Sada, E. 1993. Gas Transport through Homogeneous and Asymmetric Polyethersulfone Membranes. *Journal of Polymer Science: Part B: Polymer Physics,* 31.

Kuo, A. C. M. 1999. Poly(dimethylsiloxane). *In:* Mark, J. E. (ed.) *Polymer Data Handbook.* Oxford University Press Inc.

Kusworo, T. D., Utomo, D. P., Aryanti, N. & Qudratun 2017. Synergistic effect of UV irradiation and thermal annealing to develop high performance polyethersulfone-nano silica membrane for produced water treatment. *Journal of Environmental Chemical Engineering,* 5**,** 3290-3301.

Lai, J.-Y., Lin, F.-C., Wang, C.-C. & Wang, D.-M. 1996. Effect of nonsolvent additives on the porosity and morphology of asymmetric TPX membranes. *Journal of Membrane Science,* 118**,** 49-61.

Landau, L. & Levich, B. 1988. Dragging of a Liquid by a Moving Plate. *Dynamics of Curved Fronts***,** 141-153.

Langan, J. R. & Salmon, G. A. 1987. Physical Properties of N-Methylpyrrolidinone as Functions of Temperature. *Journal of Chemical Engineering Data,* 32**,** 420-422.

Larson, R. G. 1999. Polymers. *The structure and rheology of complex fluids.* New York: Oxford University Press.

Lasseuguette, E., Rouch, J.-C. & Remigy, J.-C. 2013. Hollow-Fiber Coating: Application to Preparation of Composite Hollow-Fiber Membrane for Gas Separation. *Industrial & Engineering Chemistry Research,* 52**,** 13146-13158.

Lau, W. J., Gray, S., Matsuura, T., Emadzadeh, D., Chen, J. P. & Ismail, A. F. 2015. A review on polyamide thin film nanocomposite (TFN) membranes: History, applications, challenges and approaches. *Water Res,* 80**,** 306-24.

Lee, H. J., Won, J., Lee, H. & Kang, Y. S. 2002. Solution properties of poly(amic acid)–NMP containing LiCl and their effects on membrane morphologies. *Journal of Membrane Science,* 196**,** 267-277.

Lee, J. N., Park, C. & Whitesides, G. M. 2003a. Solvent compatibility of poly(dimethylsiloxane)-based microfluidic devices. *Anal Chem,* 75**,** 6544-54.

Lee, K.-W., Seo, B.-K., Nam, S.-T. & Han, M.-J. 2003b. Trade-off between thermodynamic enhancement and kinetic hindrance during phase inversion in the preparation of polysulfone membranes. *Desalination,* 159**,** 289-296.

Lee, W. H., Seong, J. G., Hu, X. & Lee, Y. M. 2020. Recent progress in microporous polymers from thermally rearranged polymers and polymers of intrinsic microporosity for membrane gas separation: Pushing performance limits and revisiting trade-off lines. *Journal of Polymer Science,* 58**,** 2450-2466.

Li, H.-B., Shi, W.-Y., Zhang, Y.-F., Liu, D.-Q. & Liu, X.-F. 2014. Effects of Additives on the Morphology and Performance of PPTA/PVDF in Situ Blend UF Membrane. *Polymers,* 6**,** 1846-1861.

Li, S., Wang, Z., Yu, X., Wang, J. & Wang, S. 2012. High-performance membranes with multi-permselectivity for CO2 separation. *Adv Mater,* 24**,** 3196-200.

Li, S., Zhang, H., Yu, S., Hou, J., Huang, S. & Liu, Y. 2019. Pore structure characterization and gas transport property of the penetrating layer in composite membranes. *Separation and Purification Technology,* 211**,** 252-258.

Li, Y., Cao, C., Chung, T.-S. & Pramoda, K. P. 2004. Fabrication of dual-layer polyethersulfone (PES) hollow fiber membranes with an ultrathin dense-selective layer for gas separation. *Journal of Membrane Science,* 245**,** 53-60.

Li, Y., Wang, S., He, G., Wu, H., Pan, F. & Jiang, Z. 2015. Facilitated transport of small molecules and ions for energy-efficient membranes. *Chemical Society Reviews,* 44**,** 103-118.

Lin, H. & Yavari, M. 2015. Upper bound of polymeric membranes for mixed-gas CO2/CH4 separations. *Journal of Membrane Science,* 475**,** 101-109.

Liu, C. & Martin, C. R. 1991. Composite Membranes from Photochemical-Synthesis of Ultrathin Polymer-Films. *Nature,* 352**,** 50-52.

Liu, L., Chakma, A. & Feng, X. 2008. Gas permeation through water-swollen hydrogel membranes. *Journal of Membrane Science,* 310**,** 66-75.

Liu, M., Xie, K., Nothling, M. D., Gurr, P. A., Tan, S. S. L., Fu, Q., Webley, P. A. & Qiao, G. G. 2018. Ultrathin Metal-Organic Framework Nanosheets as a Gutter Layer for Flexible Composite Gas Separation Membranes. *ACS Nano,* 12**,** 11591-11599.

Liu, T.-Y., Liu, Z.-H., Zhang, R.-X., Wang, Y., Bruggen, B. V. d. & Wang, X.-L. 2015. Fabrication of a thin film nanocomposite hollow fiber nanofiltration membrane for wastewater treatment. *Journal of Membrane Science,* 488**,** 92-102.

Liu, Y., Liu, Z., Liu, G., Qiu, W., Bhuwania, N., Chinn, D. & Koros, W. J. 2020. Surprising plasticization benefits in natural gas upgrading using polyimide membranes. *Journal of Membrane Science,* 593.

Loeb, S. & Sourirajan, S. 1963. Sea Water Demineralization by Means of an Osmotic Membrane. *Advances in Chemistry,* 38**,** 117-132.

Lopez, L. C. & Wilkes, G. L. 1992. Synthesis, structure, and properties of poly(4-methyl-1-pentene). *Journal of Macromolecular Science, Part C: Polymer Reviews,* 32**,** 301-406.

Louie, J., Pinnau, I. & Reinhard, M. 2008. Gas and liquid permeation properties of modified interfacial composite reverse osmosis membranes. *Journal of Membrane Science,* 325**,** 793-800.

Lua, A. C. & Shen, Y. 2013a. Preparation and characterization of asymmetric membranes based on nonsolvent/NMP/P84 for gas separation. *Journal of Membrane Science,* 429**,** 155-167.

Lua, A. C. & Shen, Y. 2013b. Preparation and characterization of polyimide–silica composite membranes and their derived carbon–silica composite membranes for gas separation. *Chemical Engineering Journal,* 220**,** 441-451.

Ma, D., Peh, S. B., Han, G. & Chen, S. B. 2017. Thin-Film Nanocomposite (TFN) Membranes Incorporated with Super-Hydrophilic Metal-Organic Framework (MOF) UiO-66: Toward Enhancement of Water Flux and Salt Rejection. *ACS Appl Mater Interfaces,* 9**,** 7523-7534.

Madhani, S. P., D'Aloiso, B. D., Frankowski, B. & Federspiel, W. J. 2016. Darcy Permeability of Hollow Fiber Membrane Bundles Made from Membrana Polymethylpentene Fibers Used in Respiratory Assist Devices. *ASAIO J,* 62**,** 329-31.

Makhloufi, C., Lasseuguette, E., Remigy, J. C., Belaissaoui, B., Roizard, D. & Favre, E. 2014. Ammonia based CO2 capture process using hollow fiber membrane contactors. *Journal of Membrane Science,* 455**,** 236-246.

Makhloufi, C., Roizard, D. & Favre, E. 2013. Reverse selective NH3/CO2 permeation in fluorinated polymers using membrane gas separation. *Journal of Membrane Science,* 441**,** 63-72.

Mansourizadeh, A. & Ismail, A. F. 2010. Effect of LiCl concentration in the polymer dope on the structure and performance of hydrophobic PVDF hollow fiber membranes for CO2 absorption. *Chemical Engineering Journal,* 165**,** 980-988.

Markova, S., Shalygin, M., Pelzer, M., Gries, T. & Teplyakov, V. 2020a. Application prospects of dense gas separation hollow fibers based on poly(4-methyl-1-pentene). *Chemical Papers,* 74**,** 1917-1921.

Markova, S., Zhmakin, V., Gries, T. & Teplyakov, V. 2020b. Combination of the Experimental and Theoretical Approaches for the Estimation of the C1–C4 Alkane Permeability Parameters in Poly (4-Methyl-2-Pentyne) and Poly (4-Methyl-1-Pentene). *Applied Sciences,* 10.

Merck 2021a. IR Spectrum Table & Chart. Merck.

Merck. 2021b. *Poly(dimethylsiloxane), hydroxy terminated Product Comparison Guide* [Online]. Merck KGaA. Available: https://www.sigmaaldrich.com/MY/en/substance/polydimethylsiloxanehydroxyterminated1234570131678?context=product [Accessed 24 June 2021].

Merkel, T. C., Bondar, V. I., Nagai, K., Freeman, B. D. & Pinnau, I. 1999. Gas Sorption, Diffusion, and Permeation in Poly(dimethylsiloxane). *Journal of Polymer Science Part B: Polymer Physics,* 38**,** 415-434.

Michaljaničová, I., Slepička, P., Hadravová, J., Rimpelová, S., Ruml, T., Malinský, P., Veselý, M. & Švorčík, V. 2016. High power plasma as an efficient tool for polymethylpentene cytocompatibility enhancement. *RSC Advances,* 6**,** 76000-76010.

Misdan, N., Lau, W. J., Ismail, A. F., Matsuura, T. & Rana, D. 2014. Study on the thin film composite poly(piperazine-amide) nanofiltration membrane: Impacts of physicochemical properties of substrate on interfacial polymerization formation. *Desalination,* 344**,** 198-205.

Moch, I. J. 2004. Hollow Fiber Membranes. *Encyclopedia of Desalination and Water Resources (DESWARE).*

Mohr, J. M. & Paul, D. R. 1990. Effect of casting solvent on the permeability of poly(4-methyl-1-pentene). *Polymer,* 32**,** 1236 - 1243.

Mohsenpour, S., Safekordi, A., Tavakolmoghadam, M., Rekabdar, F. & Hemmati, M. 2016. Comparison of the membrane morphology based on the phase diagram using PVP as an organic additive and TiO 2 as an inorganic additive. *Polymer,* 97**,** 559-568.

Mojsiewicz-Pienkowska, K. 2008. Size exclusion chromatography with evaporative light scattering detection: Method for the determination of polydimethylsiloxanes. II. Application of TSK-GEL H HR GMH HR -M column to determine and separate molecular weight of linear polydimethylsiloxanes. *J Chromatogr B Analyt Technol Biomed Life Sci,* 865**,** 7-12.

Mojsiewicz-Pienkowska, K. 2012. Size exclusion chromatography with evaporative light scattering detection as a method for speciation analysis of polydimethylsiloxanes. III. Identification and determination of dimeticone and simeticone in pharmaceutical formulations. *J Pharm Biomed Anal,* 58**,** 200-7.

Moretto, H.-H., Schulze, M. & Wagner, G. 2005. Silicones. *Ullmann's Encyclopedia of Industrial Chemistry.* 7th Edition ed. Weinheim, Germany: Wiley-VCH Verlag GmbH & Co.

Morgan, P. W. 2002. Interfacial Polymerization. *Encyclopedia of Polymer Science and Technology.* John Wiley & Sons, Inc.

Morgan, P. W. 2011. Interfacial Polymerization. *In:* Mark, H. F. (ed.) *Encyclopedia of Polymer Science and Technology.* Wiley Inc.

NanoH_2O, L. C. s. 2017. LG Water Solutions: Seawater, Brackish Water RO Membranes Application Flyer. *In:* Chem, L. (ed.). LG Chem.

Nematollahi, M. H., Dehaghani, A. H. S. & Abedini, R. 2015. CO2/CH4 separation with poly(4-methyl-1-pentyne) (TPX) based mixed matrix membrane filled with Al2O3 nanoparticles. *Korean Journal of Chemical Engineering,* 33**,** 657-665.

Nunes, S. P. & Peinemann, K.-V. 2006. *Membrane Technology in the Chemical Industry,* Weinheim, Germany, Wiley-VCH.

Paredes, J. I., Villar-Rodil, S., Martinez-Alonso, A. & Tascon, J. M. 2008. Graphene oxide dispersions in organic solvents. *Langmuir,* 24**,** 10560-4.

Park, H. B., Kamcev, J., Robeson, L. M., Elimelech, M. & Freeman, B. D. 2017. Maximizing the right stuff: The trade-off between membrane permeability and selectivity. *Science,* 356.

Park, H. C., Moon, Y. S., Rhee, H. W., Won, J., Kang, Y. S. & Kim, U. Y. 1999. Effect of Solvent Exchange on the Morphology of Asymmetric Membranes. *Membrane Formation and Modification.*

Park, S.-H., Kim, S. H., Park, S.-J., Ryoo, S., Woo, K., Lee, J. S., Kim, T.-S., Park, H.-D., Park, H., Park, Y.-I., Cho, J. & Lee, J.-H. 2016. Direct incorporation of silver nanoparticles onto thin-film composite membranes via arc plasma deposition for enhanced antibacterial and permeation performance. *Journal of Membrane Science,* 513**,** 226-235.

Perreault, F., Tousley, M. E. & Elimelech, M. 2014. Thin-Film Composite Polyamide Membranes Functionalized with Biocidal Graphene Oxide Nanosheets. *Environmental Science & Technology Letters,* 1**,** 71-76.

Peter, J. & Peinemann, K. V. 2009. Multilayer composite membranes for gas separation based on crosslinked PTMSP gutter layer and partially crosslinked Matrimid® 5218 selective layer. *Journal of Membrane Science,* 340**,** 62-72.

Pinnau, I. & Freeman, B. D. 1999. Formation and Modification of Polymeric Membranes: Overview. *Membrane Formation and Modification.* American Chemical Society.

Pinnau, I. & Koros, W. J. 1991. Relationship between Substructure Resistance and Gas Separation Properties of Defect-Free Integrally Skinned Asymmetric Membranes. *Industrial & Engineering Chemistry Research,* 30**,** 1837-1840.

Pixton, M. R. & Paul, D. R. 2018. Relationships between Structure and Transport Properties for Polymers with Aromatic Backbones. *In:* Paul, D. R. & Yampol'skii, Y. P. (eds.) *Polymeric Gas Separation Membranes.* Florida, USA: CRC Press.

Puleo, A. C., Paul, D. R. & Wong, P. K. 1988. Gas sorption and transport in semicrystalline poly(4-methyl-1-pentene). *Polymer,* 30.

Pulyalina, A., Polotskaya, G., Rostovtseva, V., Pientka, Z. & Toikka, A. 2018. Improved Hydrogen Separation Using Hybrid Membrane Composed of Nanodiamonds and P84 Copolyimide. *Polymers (Basel)*, 10.

Qin, L., Mergos, I. A. & Verweij, H. 2015. Obtaining accurate cross-section images of supported polymeric and inorganic membrane structures. *Journal of Membrane Science,* 476**,** 194-199.

Quéré, D. 1999. Fluid coating on a fiber. *Annual Review of Fluid Mechanics,* 31**,** 347 - 384.

Rahman, M. M., Filiz, V., Shishatskiy, S., Abetz, C., Neumann, S., Bolmer, S., Khan, M. M. & Abetz, V. 2013. PEBAX® with PEG functionalized POSS as nanocomposite membranes for CO2 separation. *Journal of Membrane Science,* 437**,** 286-297.

Reddy, S., Desai, P., Abhiraman, A. S., Beckham, H. W., Kulik, A. S. & Spiess, H. W. 1997. Structure and Temperature Dependent Properties of Poly(4-methyl-1-pentene) Fibers. *Macromolecules,* 30.

Redon, C., Brochard-Wyart, F. & Rondelez, F. 1991. Dynamics of dewetting. *Phys Rev Lett,* 66**,** 715-718.

Rio, E. & Boulogne, F. 2017. Withdrawing a solid from a bath: how much liquid is coated? *Advances in Colloid and Interface Science,* 247**,** 100-114.

Robeson, L. M. 1991. Correlation of separation factor versus permeabiity for polymeric membranes. *Journal of Membrane Science,* 62**,** 165-185.

Robeson, L. M. 2008. The upper bound revisited. *Journal of Membrane Science,* 320**,** 390-400.

Rosenholm, J. B. 2015. Liquid spreading on solid surfaces and penetration into porous matrices: Coated and uncoated papers. *Adv Colloid Interface Sci,* 220**,** 8-53.

Roux, J. D. L. & Paul, D. R. 1992. Preparation of composite membranes by a spin coating process. *Journal of Membrane Science,* 74**,** 233 - 252.

Rukhlya, E. G., Litmanovich, E. A., Dolinnyi, A. I., Yarysheva, L. M., Volynskii, A. L. & Bakeev, N. F. 2011. Penetration of Poly(ethylene oxide) into the Nanoporous Structure of the Solvent-Crazed Poly(ethylene terephthalate) Films. *Macromolecules,* 44**,** 5262-5267.

Ryck, A. d. & Quéré, D. 1998. Fluid coating from a polymer solution. *Langmuir,* 14**,** 1911-1914.

Sadrzadeh, M. & Bhattacharjee, S. 2013. Rational design of phase inversion membranes by tailoring thermodynamics and kinetics of casting solution using polymer additives. *Journal of Membrane Science,* 441**,** 31-44.

Salih, A. A. M., Yi, C., Peng, H., Yang, B., Yin, L. & Wang, W. 2014. Interfacially polymerized polyetheramine thin film composite membranes with PDMS inter-layer for CO_2 separation. *Journal of Membrane Science,* 472**,** 110-118.

Schaefer, C., van der Schoot, P. & Michels, J. J. 2015. Structuring of polymer solutions upon solvent evaporation. *Phys Rev E Stat Nonlin Soft Matter Phys,* 91**,** 022602.

Scriven, L. E. 1988. Physics and Applications of Dip Coating and Spin Coating. *Materials Research Society symposium proceedings,* 121**,** 717–729.

Selyanchyn, O., Selyanchyn, R. & Fujikawa, S. 2020. Critical Role of the Molecular Interface in Double-Layered Pebax-1657/PDMS Nanomembranes for Highly Efficient CO2/N2 Gas Separation. *ACS Applied Materials & Interfaces,* 12**,** 33196-33209.

Shen, Y. & Lua, A. C. 2010. Effects of membrane thickness and heat treatment on the gas transport properties of membranes based on P84 polyimide. *Journal of Applied Polymer Science***,** NA-NA.

Shen, Y. & Lua, A. C. 2012. Structural and transport properties of BTDA-TDI/MDI co-polyimide (P84)–silica nanocomposite membranes for gas separation. *Chemical Engineering Journal,* 188**,** 199-209.

Sheng, L., Guo, Y., Zhao, D., Ren, J., Wang, S. & Deng, M. 2020a. Enhanced CO2/CH4 separation performance of BTDA-TDI/MDI (P84) copolyimide mixed-matrix membranes by incorporating submicrometer-sized [Ni3(HCOO)6] framework crystals. *Journal of Natural Gas Science and Engineering,* 75.

Sheng, L., Ren, J., Hua, K., Li, H., Feng, Y. & Deng, M. 2020b. The enhancement of mechanical properties of P84 hollow fiber membranes by thermally annealing below and above Tg. *Journal of Membrane Science,* 595.

Shi, L., Wang, R., Cao, Y., Liang, D. T. & Tay, J. H. 2008. Effect of additives on the fabrication of poly(vinylidene fluoride-co-hexafluropropylene) (PVDF-HFP) asymmetric microporous hollow fiber membranes. *Journal of Membrane Science,* 315**,** 195-204.

Shih, H. C., Yeh, Y. S. & Yasuda, H. 1990. Morphology of Microporous Poly(vinylidene fluoride) Membranes Studied by Gas Permeation and Scanning Electron Microscopy. *Journal of Membrane Science,* 50**,** 299-317.

Shimadzu. 2021. *FTIR Analysis Q&A: How deep does the infrared light penetrate at the position of contact between the prism and sample during ATR measurements?* [Online]. Shimadzu Corporation. [Accessed 21 July 2021].

Shin, C., Jiang, X., Ko, W. & Balsara, N. P. 2017. Effect of pore penetration on transport through supported membranes studied by electron microscopy and pervaporation. *Journal of Membrane Science,* 542**,** 18-23.

Shing Chan, T., Gueudré, T. & Snoeijer, J. H. 2011. Maximum speed of dewetting on a fiber. *Physics of Fluids,* 23.

SigmaAldrich. 2021a. *Price of Basolite Z1200 (ZIF-8)* [Online]. [Accessed 12 April 2021].

SigmaAldrich. 2021b. *Price of graphene oxide powder, 15-20 sheets, 4-10% edge-oxidized* [Online]. [Accessed 12 April 2021].

Slepička, P., Trostová, S., Slepičková Kasálková, N., Kolská, Z., Malinský, P., Macková, A., Bačáková, L. & Švorčík, V. 2012. Nanostructuring of polymethylpentene by plasma and heat treatment for improved biocompatibility. *Polymer Degradation and Stability,* 97**,** 1075-1082.

Sorbie, K. S. 1991. *Properties of polymer solutions,* Springer, Dordrecht.

SpectraBase 2020. Polydimethylsiloxane, hydroxy terminated. John Wiley & Sons, Inc.

Sridhar, S., Veerapur, R. S., Patil, M. B., Gudasi, K. B. & Aminabhavi, T. M. 2007. Matrimid polyimide membranes for the separation of carbon dioxide from methane. *Journal of Applied Polymer Science,* 106**,** 1585-1594.

Subrahmanyan, S. 2003. *An Investigation of Pore Collapse in Asymmetric Polysulfone Membranes.* Doctor of Philosophy, Virginia Polytechnic Institute and State University.

Sun, M., Li, M., Zhang, X., Wu, C. & Wu, Y. 2020. Graphene oxide modified porous P84 co-polyimide membranes for boron recovery by bipolar membrane electrodialysis process. *Separation and Purification Technology,* 232.

Tanigami, T., Suzuki, H., Yamaura, K. & Matsuzawa, S. 1985. Gelation and crystallization of Poly(4-methyl-1-pentene) in Cyclohexane Solution. *Macromolecules,* 18**,** 2595-2600.

ThermoFisher 2016. Thermo Scientific™ Nalgene™ Plastic Labware Chemical Resistance Reference Guide. ThermoFisher Scientific Inc.

Thompson, C. V. 2012. Solid-State Dewetting of Thin Films. *Annual Review of Materials Research,* 42**,** 399-434.

Tin, P. S., Chung, T.-S., Liu, Y. & Wang, R. 2004. Separation of CO2/CH4 through carbon molecular sieve membranes derived from P84 polyimide. *Carbon,* 42**,** 3123-3131.

Tiraferri, A., Yip, N. Y., Phillip, W. A., Schiffman, J. D. & Elimelech, M. 2011. Relating performance of thin-film composite forward osmosis membranes to support layer formation and structure. *Journal of Membrane Science,* 367**,** 340-352.

Tomar, B. S., Shahin, A. & Tirumkudulu, M. S. 2020. Cracking in drying films of polymer solutions. *Soft Matter,* 16**,** 3476-3484.

Tsai, F. J., Kang, D. & Anand, M. 1995. Thin-Film-Composite Gas Separation Membranes: On the Dynamics of Thin Film Formation Mechanism On Porous Substrates. *Separation Science and Technology,* 30**,** 1639-1652.

Vanherck, K., Cano-Odena, A., Koeckelberghs, G., Dedroog, T. & Vankelecom, I. 2010. A simplified diamine crosslinking method for PI nanofiltration membranes. *Journal of Membrane Science,* 353**,** 135-143.

Verma, S. K., Modi, A. & Bellare, J. 2019. Polyethersulfone-carbon nanotubes composite hollow fiber membranes with improved biocompatibility for bioartificial liver. *Colloids Surf B Biointerfaces,* 181**,** 890-895.

Villeneuve, K., Roizard, D., Remigy, J.-C., Iacono, M. & Rode, S. 2018. CO2 capture by aqueous ammonia with hollow fiber membrane contactors: Gas phase reactions and performance stability. *Separation and Purification Technology,* 199**,** 189-197.

Visser, T., Ungerank, M., Balster, J. & Fuhrer, C. 2016. *Method for Producing Polyimide Membranes*. United States patent application 14/900,012.

Vrbová, V. & Ciahotný, K. 2017. Upgrading Biogas to Biomethane Using Membrane Separation. *Energy & Fuels,* 31**,** 9393-9401.

Wang, D.-M., Wu, T.-T., Lin, F.-C., Hou, J.-Y. & Lai, J.-Y. 2000. A novel method for controlling the surface morphology of polymeric membranes. *Journal of Membrane Science,* 169**,** 39-51.

Wang, D., Xu, R., Jiang, G. & Zhu, B. 1990. Determination of surface dense layer structure parameters of the asymmetric membrane by gas permeation method. *Journal of Membrane Science,* 52**,** 97-108.

Ward III, W. J., Browall, W. R. & Salemme, R. M. 1976. Ultrathin Silicone/Polycarbonate Membranes for Gas Separation Processes. *Journal of Membrane Science,* 1**,** 99-108.

Wessling, M., Lopez, M. L. & Strathmann, H. 2001. Accelerated plasticization of thin-film composite membranes used in gas separation. *Separation and Purification Technology,* 24**,** 223-233.

Wijmans, J. G. & Hao, P. 2015. Influence of the porous support on diffusion in composite membranes. *Journal of Membrane Science,* 494**,** 78-85.

Winn, E. B. 1950. The Temperature Dependence of the Self-Diffusion Coefficients of Argon, Neon, Nitrogen, Oxygen, Carbon Dioxide, and Methane. *Physical Review,* 80**,** 1024-1027.

Wittbecker, E. L. & Morgan, P. W. 1959. Interfacial Polycondensation. *Journal of Polymer Science,* 40**,** 289-297.

Wong, K. C., Goh, P. S. & Ismail, A. F. 2015. Gas separation performance of thin film nanocomposite membranes incorporated with polymethyl methacrylate grafted multi-walled carbon nanotubes. *International Biodeterioration & Biodegradation,* 102**,** 339-345.

Wong, K. C., Goh, P. S. & Ismail, A. F. 2016. Thin film nanocomposite: the next generation selective membrane for CO2 removal. *Journal of Materials Chemistry A,* 4**,** 15726-15748.

Wu, D., Han, Y., Salim, W., Chen, K. K., Li, J. & Ho, W. S. W. 2018. Hydrophilic and morphological modification of nanoporous polyethersulfone substrates for composite membranes in CO2 separation. *Journal of Membrane Science,* 565**,** 439-449.

Yampolskii, Y. 2012. Polymeric Gas Separation Membranes. *Macromolecules,* 45**,** 3298-3311.

Yan, F., Ding, A., Girones, M., Lammertink, R. G., Wessling, M., Borger, L., Vilsmeier, K. & Goedel, W. A. 2012. Hierarchically structured assembly of polymer microsieves, made by a combination of phase separation micromolding and float-casting. *Adv Mater,* 24**,** 1551-7.

Yanagishita, H., Kitamoto, D., Haraya, K., Nakane, T., Okada, T., Matsuda, H., Idemoto, Y. & Koura, N. 2001. Separation performance of polyimide composite membrane prepared by dip coating process. *Journal of Membrane Science,* 188**,** 165-172.

Yang, T., Wan, C. F., Zhang, J., Gudipati, C. & Chung, T.-S. 2021. Optimization of interfacial polymerization to fabricate thin-film composite hollow fiber membranes in modules for brackish water reverse osmosis. *Journal of Membrane Science,* 626.

Yasuda, H. & Rosengren, K. 1970. Isobaric measurement of gas permeability of polymers. *Journal of Applied Polymer Science,* 14**,** 2839-2877.

Ying, Y., Yang, Z., Shi, D., Peh, S. B., Wang, Y., Yu, X., Yang, H., Chai, K. & Zhao, D. 2021. Ultrathin covalent organic framework film as membrane gutter layer for high-permeance CO2 capture. *Journal of Membrane Science,* 632.

Yoo, M. J., Kim, K. H., Lee, J. H., Kim, T. W., Chung, C. W., Cho, Y. H. & Park, H. B. 2018a. Ultrathin gutter layer for high-performance thin-film composite membranes for CO2 separation. *Journal of Membrane Science,* 566**,** 336-345.

Yoo, M. J., Lee, J. H., Yoo, S. Y., Oh, J. Y., Roh, J. M., Grasso, G., Lee, J. H., Lee, D., Oh, W. J., Yeo, J.-g., Cho, Y. H. & Park, H. B. 2018b. Defect control for large-scale thin-film composite membrane and its bench-scale demonstration. *Journal of Membrane Science,* 566**,** 374-382.

Yoshimizu, H., Fukatsu, H., Suzuki, T., Tsujita, Y. & Kinoshita, T. 1998. CO2 permeation and diffusion properties of semicrystalline poly(4-methyl pentene-1) membranes. *Polymer Journal,* 30**,** 981-984.

Young, T.-H. & Chen, L.-W. 1995. Pore formation mechanism of membranes from phase inversion process. *Desalination,* 103**,** 233-247.

Yuan, F., Wang, Z., Li, S., Wang, J. & Wang, S. 2012. Formation–structure–performance correlation of thin film composite membranes prepared by interfacial polymerization for gas separation. *Journal of Membrane Science,* 421-422**,** 327-341.

Zeynali, R., Ghasemzadeh, K., Sarand, A. B., Kheiri, F. & Basile, A. 2018. Performance evaluation of graphene oxide (GO) nanocomposite membrane for hydrogen separation: Effect of dip coating sol concentration. *Separation and Purification Technology,* 200**,** 169-176.

Zhang, Z., Salamatin, A., Peng, F. & Kornev, K. G. 2021. Dip coating of cylinders with Newtonian fluids. *Journal of Colloid and Interface Science*.

Zheng, L., Wu, Z., Wei, Y., Zhang, Y., Yuan, Y. & Wang, J. 2016. Preparation of PVDF-CTFE hydrophobic membranes for MD application: Effect of LiCl-based mixed additives. *Journal of Membrane Science,* 506**,** 71-85.

Zhou, C., Hou, Z., Lu, X., Liu, Z., Bian, X., Shi, L. & Li, L. 2010. Effect of Polyethersulfone Molecular Weight on Structure and Performance of Ultrafiltration Membranes. *Industrial & Engineering Chemistry Research,* 49**,** 9988–9997.

Zhou, W., Apkarian, R., Wang, Z. L. & Joy, D. 2007. Fundamentals of Scanning Electron Microscopy (SEM). *In:* Zhou, W. & Wang, Z. L. (eds.) *Scanning Microscopy for Nanotechnology: Techniques and Applications.* New York, NY: Springer New York.

Zhu, L., Jia, W., Kattula, M., Ponnuru, K., Furlani, E. P. & Lin, H. 2016a. Effect of porous supports on the permeance of thin film composite membranes: Part I. Track-etched polycarbonate supports. *Journal of Membrane Science,* 514**,** 684-695.

Zhu, L., Yavari, M., Jia, W., Furlani, E. P. & Lin, H. 2016b. Geometric Restriction of Gas Permeance in Ultrathin Film Composite Membranes Evaluated Using an Integrated Experimental and Modeling Approach. *Industrial & Engineering Chemistry Research,* 56**,** 351-358.

APPENDICES

APPENDIX A Validity of Permeate Pressure Linear Increase with Time for Constant Volume Permeation Method

Figure A.1 represents the linearity of permeate pressure and the time in the range of 0-0.1 bar for the dense PMP sample. Most of the data was concentrated on the ideal line with minimal deviation from some of the samples. The same linearity can also be extended for other samples utilizing constant volume permeation method.

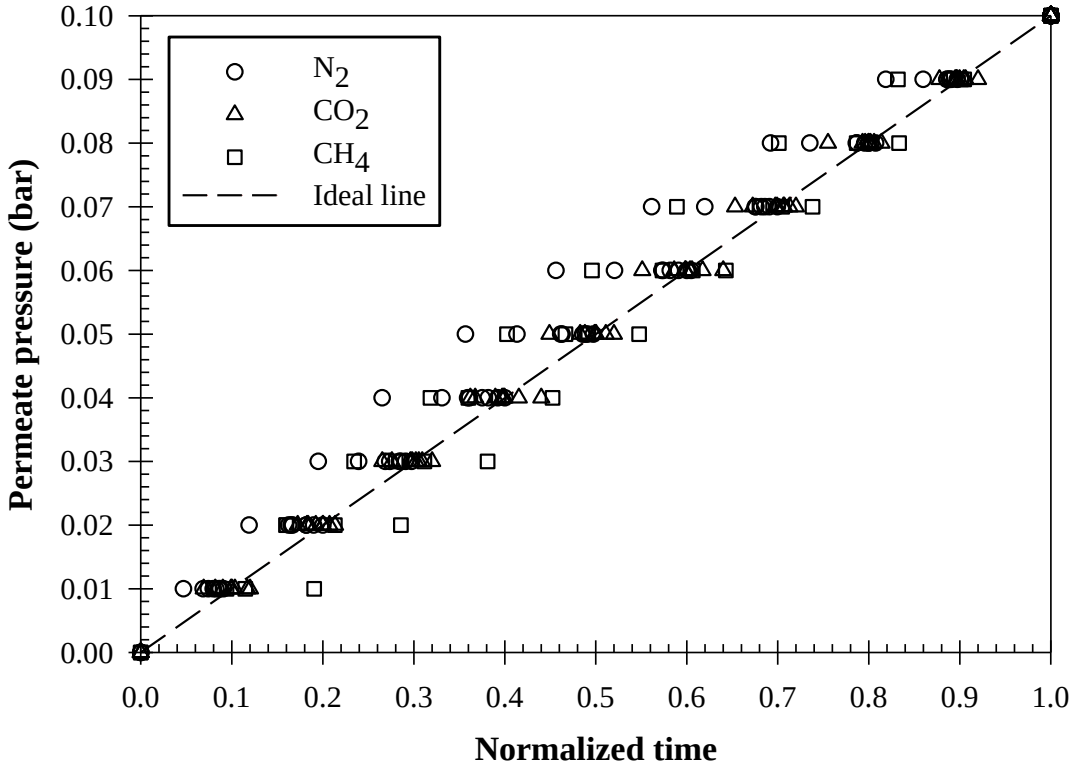

Figure A.1: Permeate pressure increase (0.00-0.10 bar) in constant downstream volume with normalized time for CO_2, N_2, and CH_4 across dense PMP membrane

APPENDIX B Viscosity of P84 PI Solution in NMP in Literature

Figure B.1 represents the relationship between P84 PI's solution concentration with its viscosity. Viscosity data was taken from several literature, all was taken at around 25 °C (Ismail *et al.*, 2017, Langan and Salmon, 1987, Vanherck *et al.*, 2010, Flick, 1998). R^2 of the plot fitting is at 0.91.

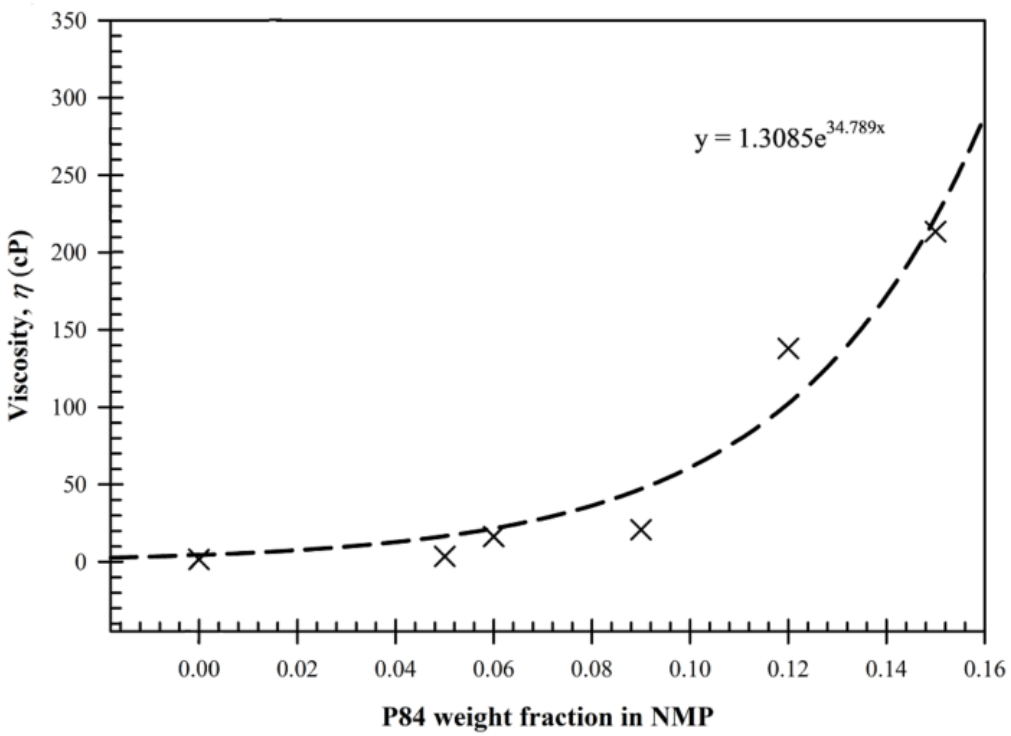

Figure B.1: Relationship between P84 PI's solution concentration with its viscosity

APPENDIX C Validation of Image Processing in Determining Surface Pore Size Distribution

Image processing is a powerful tool to obtain data from images. However, it is limited by the degree of manipulation of the user and the quality of the original images as significantly altered data could be obtained during the processing. Figure C.1 represent the comparison of the threshold images with the original SEM images. For pristine substrate, some low intensity structures were omitted during the threshold setup. Nevertheless, these structures might be the deeper pores recorded due to the very thin skin layer of pristine samples (at 0.21 ± 0.02 µm). Hence, only highly shaded structures were measured. On the other hand, some background pixels were recorded when using 'Yen' threshold for LiCl_4% substrate due to its dispersed pore structures.

In all samples, edge structures were excluded, while the threshold includes the silhouette noted around the pores which in some instances merged pores that are very close to each other. This is further confirmed by adjusting the lookup table (LUT)

of the original images from greyscale to ‘fire’ which gave a better contrast overall and compared to the outlines of the threshold pores. As a result, some of the pore sizes were exaggerated. However, as the pore counts are very high (at least 500 pores for LiCl_4% substrate and more than 3 000 for pristine substrate), the reported pore size distribution and values would be averaged over and gave a comparable result to manual pore size measurement (for pristine substrate, pore diameter was at 429 ± 1 nm for image analysis against 411 ± 7 nm for manual measurement of 15 random pores).

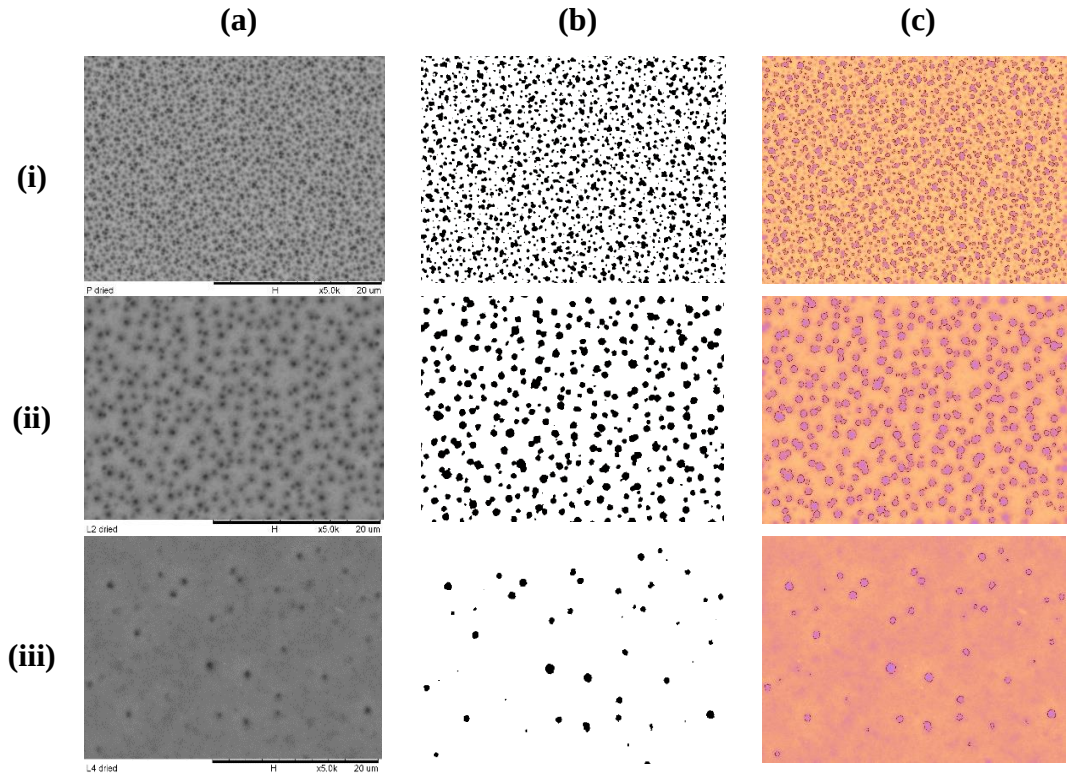

Figure C.1: Validation of image processing in determining surface pore size distribution. (a) Original surface SEM at 5kx magnification, (b) Threshold image after applying bandpass filter between 3-100 pixels and suppressed horizontal stripes (c) Overlay of the particle outline with the original SEM adjusted to ‘fire’ LUT for comparison

APPENDIX D Pristine PES Substrate N_2 Gas Flux Comparison between Test Rig and Porometer

The use of test rig to determine the N_2 flux across the substrate was limited for pristine sample for transmembrane pressure above 3 bar as the permeate flow rate was too fast to be measured using the bubble flow setup (50 ml maximum). Hence, the N_2 flux for pristine sample was verified using the gas permeation function of Porolux 1000 porometer. Figure D.1 represent the comparison between these two methods. Gas flux by porometer was recorded slower than the test rig. Nevertheless, the measurement by porometer is increasing linearly with transmembrane pressure up to 10 bar, suggesting no compaction occurred during the short testing period.

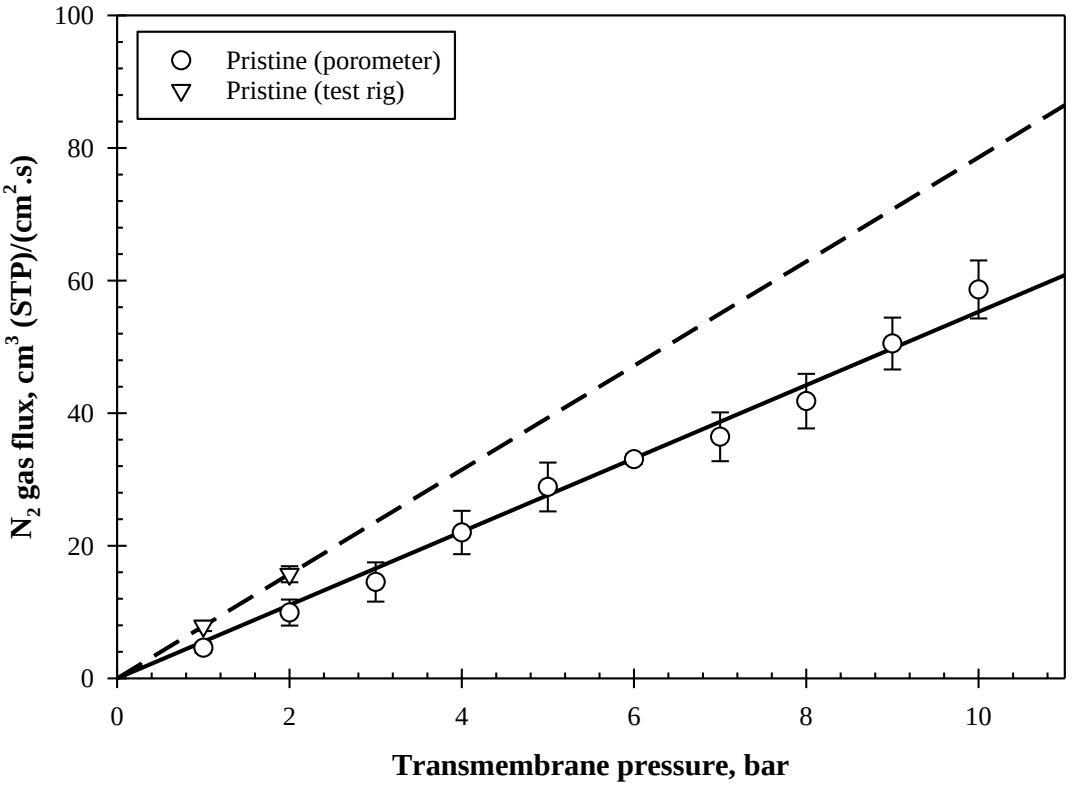

Figure D.1: Pristine PES substrate layer's N_2 gas flux over different transmembrane pressures for test conducted using test rig and porometer

APPENDIX E Preliminary Study on the Mass of PDMS Coating on Pristine PES Substrate

Thickness of PDMS coating on the PES substrate can be controlled through various methodologies. In this work however, the thickness was mainly controlled through the mass of the solution layered onto the substrates. In this sense, a minimum solution mass can be found before the resulting coating became unreliable due to defect formation. Figure E.1 represents the N_2 & CO_2 gas permeance and CO_2/N_2 selectivity across PES-PDMS composite membrane made from various PDMS solution mass between 0.25 to 4.0g. Both N_2 and CO_2 permeances were increasing with decreased PDMS coating solution's mass (hence its thickness), which is expected and comparable to the full permeance results in Figure 4.15. However, CO_2/N_2 selectivity were lost for 0.25g PDMS solution, down to 5.38 against the PDMS-only layer average at 10.20 ± 0.12. This was observed over the 1 to 4 bar transmembrane pressure tested (with selectivity ranging from 5.19 to 6.65), suggesting that significant defects formed at this thickness. Despite that the PDMS layer would later act as a gutter and thus, less selective, more permeable gutter layer would be preferred, the formation of defects at 0.25g might introduce further complications when a new selective layer (hence much less permeable) is introduced and intruded into the defects. Hence, the subsequent studies and repeats were only done for 0.5g-4.0g PDMS solutions.

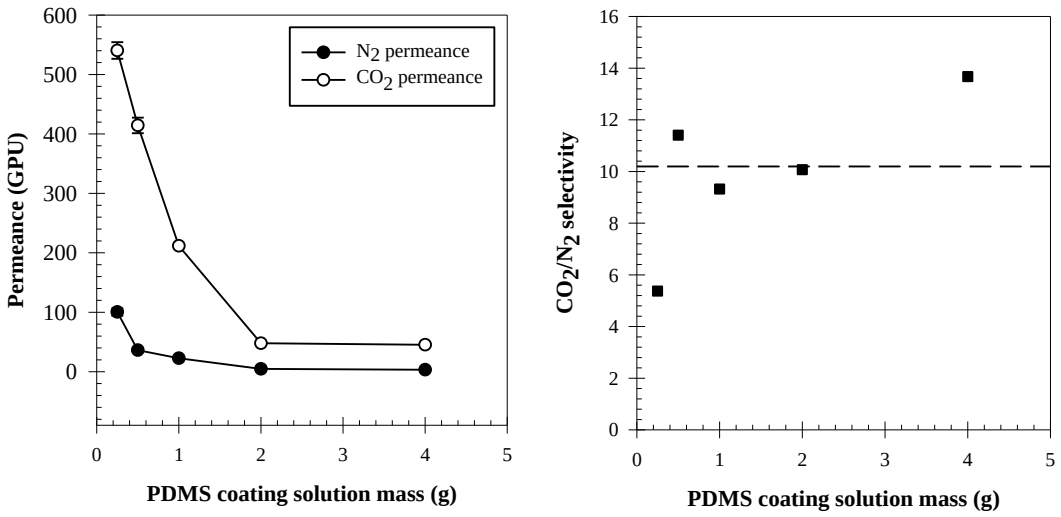

Figure E.1: Preliminary N_2 & CO_2 permeances and CO_2/N_2 selectivity of pristine substrate samples, coated with PDMS of various solution's mass between 0.25g to 4.0g. Dashed line represents the base CO_2/N_2 selectivity of standalone PDMS layer

APPENDIX F Estimation of Capillary Pressure by n-Heptane on the Porous PES Substrates

Capillary pressure, p_c can be estimated through Young-Laplace equation:

$$p_c = \frac{2\gamma_\ell cos\theta}{r_c} \tag{F.1}$$

Where γ_ℓ is the surface tension of the liquid, θ is the contact angle of the liquid with the capillary's surface, and r_c is the radius of the pore. Meanwhile, surface energy of the solid, γ_s can be approximated to be equal to the critical surface tension, γ_{cr} of the solid for polymer, and hence any liquid with $\gamma_\ell < \gamma_{cr}$ will wet the surface (Agrawal, 2005, Fox and Zisman, 1952). With PES surface energy at 44.8 mJ/m^2 (BASF, 2019) and n-heptane surface tension at 20.14 mJ/m^2, this suggested that complete wetting of PES will occur for n-heptane (θ = 0° and $cos\theta = 1$). Fitting into Equation (F.1) gives the corresponding P_c. For r_c between 100-500 nm (approximated range of PES pore size from the surface pore data available), resulting P_c would hence be between 0.81-4.03 bar.

APPENDIX G Molecular Weight of PDMS against its Kinematic viscosity and Hydrodynamic Radius

Molecular weight of PDMS (Mw_{PDMS}) can be approximated from its dynamic viscosity (η) based on the equation (Moretto *et al.*, 2005):

$$Mw_{PDMS} = \frac{464.(\eta_{25})^{0.825}}{2 + 0.0905.(\eta_{25})^{0.555}} \quad \text{(G.1)}$$

Where the subscript under η_{25} represents the measurement temperature. By comparing this equation with data obtained from other literatures (Mojsiewicz-Pienkowska, 2008, Mojsiewicz-Pienkowska, 2012, Kuo, 1999, Merck, 2021b), the equation can be verified for application in this work, as presented in Figure G.1. Do note that the literature data were presented in kinematic viscosity (ν) instead of η, where $\nu = \eta/\rho$ (ρ is the density of the fluid). By taking the average density at 0.96 g/mL, the resulting correlation as compared to the literature data is as follows.

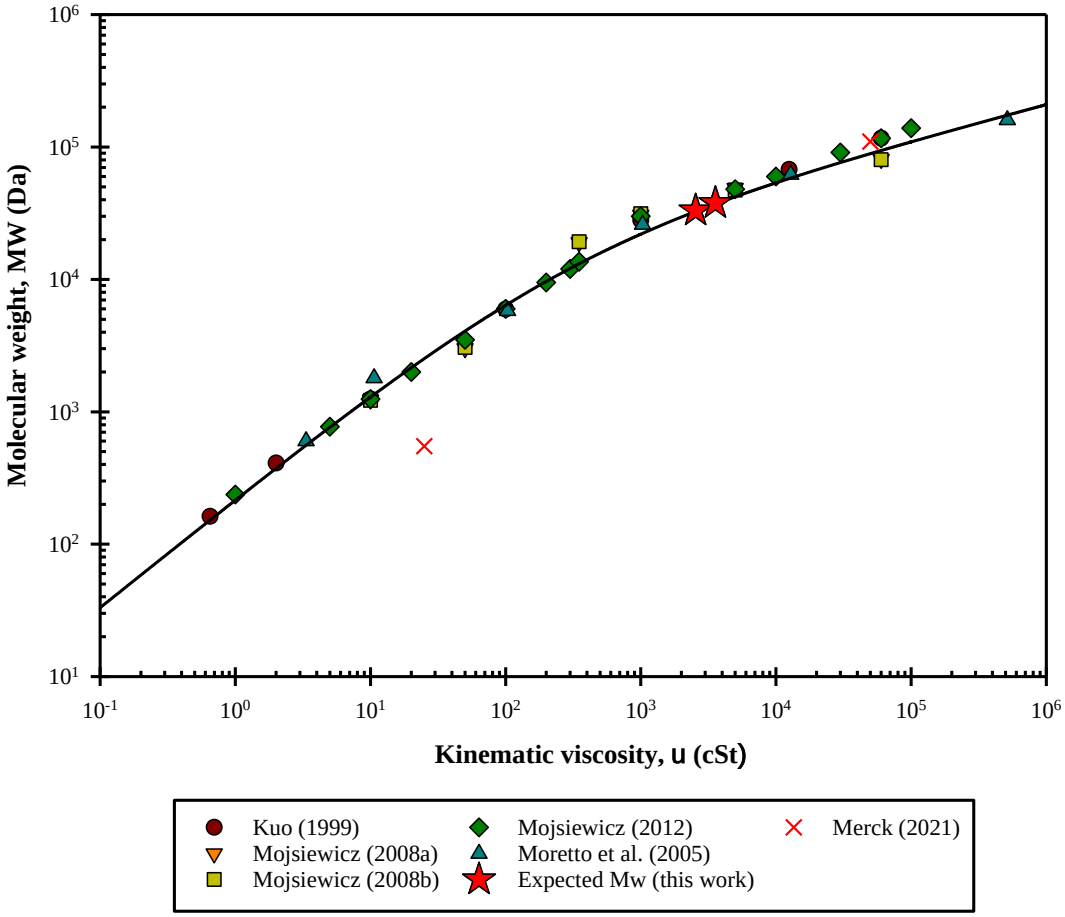

Figure G.1: Average molecular weight of PDMS against its kinetic viscosity compared to the correlation by Moretto *et al.* (2005)

The data distribution from literature corresponds well with the correlation proposed by Moretto *et al.* (2005). Significant deviation can be seen however for data from Merck (2021b) for 25 cSt hydroxy terminated PDMS, which is for hydroxy terminated PDMS. However, the data was taken in terms of number averaged molecular weight, which can be lower than the weight averaged molecular weight used in the graph. Taking this into account, hence, for this work, the hydroxy terminated PDMS used (viscosity 2550-3570 cSt) should have molecular weight of around 33.2-37.8 kDa.

Using the correlation by Armstrong *et al.* (2004), the equivalent hydrodynamic radius, R_h (in cm) can be approximated.

$$R_h = \left(\frac{3[\eta]MW}{10\pi N}\right)^{1/3} \quad \text{(G.2)}$$

Where $[\eta]$ is the intrinsic viscosity assumed at 1.04 (for PDMS MW 250 kDa) in heptane (Filiatrault *et al.*, 1981) and N is Avogadro's number (6.022×10^{23} mol^{-1}). This gives the pre-crosslinked PDMS R_h in the range of 1.76-1.84 nm, which is comparable to the molecular weight cut off-pore size relation noted for ultrafiltration membrane at about 2.0-2.3 nm (Guo and Santschi, 2007).

APPENDIX H Calibration of Casted Dense PMP Thickness

Thickness of the fabricated dense PMP membrane was measured using micrometre screw gauge, as presented in Figure H.1. PMP solution could only be flattened into the petri dish down to the solution's mass of 2g, which corresponds to the thickness of 10.9 ± 0.6 μm. Nevertheless, the two thickness values obtained is quite linear passing through the origin with an R^2 of 0.9997. Comparison with the theoretical thickness calculated found that the measured thickness is a bit higher than expected. Back calculating the PMP solution's concentration suggested that the theoretical thickness would be equal to the measured value when PMP solution is at 2.4-2.5 wt.%. This discrepancy could be due to the high volatility of cyclohexane which evaporates during solution preparation, increasing the final solution concentration prior to the pouring into the petri dishes.

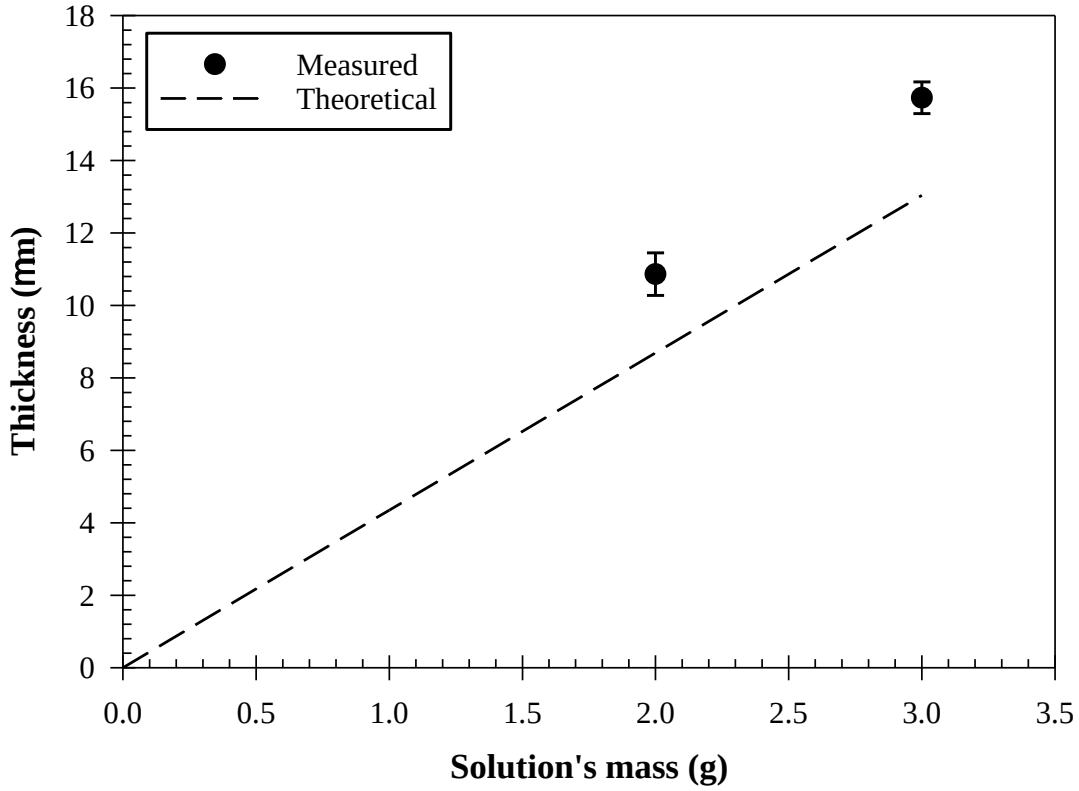

Figure H.1: Comparison of calculated and measured thickness of casted dense PMP membrane

LIST OF PUBLICATIONS

Publications

1. **Z. M. H**. **Mohd Shafie,** A. L. Ahmad, S. Rode, B. Belaissaoui, D. Roizard, & S. C. Low, 2019. Prospect of Oxyplus Hollow Fibre Membrane with Dense Polymethylpentene (PMP) Skin as Support-gutter Layer of Thin Film Composite (TFC) for Biogas upgrading. *Journal of Physical Science*, 30, 179-189.
2. **Z. M. H. Mohd Shafie**, A. L. Ahmad, S. C. Low, S. Rode, & B. Belaissaoui, 2020. Lithium chloride (LiCl)-modified polyethersulfone (PES) substrate surface pore architectures on thin poly(dimethylsiloxane) (PDMS) dense layer formation and the composite membrane's performance in gas separation. *RSC Advances*, 10, 9500-9511.

Conference / seminar

1. **Z.M.H. Mohd Shafie**, S. Rode, B. Belaissaoui, A.L. Ahmad, S.C. Low. Prospect of Oxyplus Hollow Fiber Membrane with Dense Polymethylpentene Skin as Support-Gutter Layer for CO_2 / N_2 Gas Separation. *Journée Scientifique de L'École Doctorale SIMPPÉ 2019 : 'L'Économie Circulaire'*, Nancy, 12 March 2019
2. **Z.M.H. Mohd Shafie**, A.L. Ahmad, S.C. Low, S. Rode, B. Belaissaoui, D. Roizard. Preliminary Study on the Compatibility of P84 Polyimide (PI) Coated Polymethylpentene (PMP) Thin Composite Membrane. *2nd USM SChE Postgraduate Colloquium 2020*, Penang Malaysia, 23 September 2020
3. **Z.M.H. Mohd Shafie**, A.L. Ahmad, S.C. Low, S. Rode, B. Belaissaoui. Influence of Lateral Diffusion in Gas Permeation Resistance through Thin Composite Membrane. *International Congress on Membranes & Membrane Processes (ICOM) 2020*, Online, 7 – 11 December 2020

Awards

1. 2nd runner up, USM 3-Minute Thesis (3MT) Competition (Engineering Category), Penang Malaysia, 4 March 2020
2. Best presenter, 2nd USM SChE Postgraduate Colloquium 2020, Penang Malaysia, 23 September 2020

RÉSUMÉ DÉTAILLÉ DE LA THÈSE EN FRANÇAIS

Élaboration de membranes composites á fibres creuses á base de poly-4-méthyl-1-pentène et polydiméthylsiloxane comme couche intermédiaire revêtues d'une couche sélective de polyimide P84 pour la séparation de CO_2/N_2 et CO_2/CH_4

1. Introduction

Pour la séparation membranaire des gaz dans un contexte commercial, les membranes à matrices mixtes (MMM) ne sont pas encore économiquement viables pour rivaliser avec les membranes à matrice simple. Ceci malgré leurs meilleures performances de séparation documentées dans la littérature. Outre l'éventuelle incompatibilité des différents polymères et le risque de présence de défauts interfaciaux, le coût élevé des additifs spécifiques caractérisant les MMM peut notablement réduire le potentiel de commercialisation de ces nouvelles membranes (Galizia *et al.*, 2017, Bernardo *et al.*, 2009). Une solution simple à ce problème consiste à disperser les additifs uniquement sur la fine couche sélective de la membrane, ce qui peut être réalisé grâce à des membranes composites multicouches. Dans cette conception, il est possible de supporter les coûts élevés des matériaux dispersés dans la couche sélective mince. Ce coût peut aller jusqu'à 25 000 $ à 50 000 $/kg tout en étant économiquement viable (Baker and Low, 2014).

Ainsi, pour que tout MMM avec des additifs coûteux soit compétitive, la conception composite serait la voie la plus attrayante (Pixton and Paul, 2018). Toutefois, en regardant la chronologie de l'histoire de la fabrication des membranes pour la séparation des gaz (Koros and Pinnau, 2008), il s'avère que la fabrication de la membrane stratifiée composite est particulièrement complexe. En résumé, il y a trois problèmes principaux associés aux membranes composites :

(i) Diffusion latérale à l'interface séparant la couche composite de la couche sélective mince. Lorsque l'épaisseur de la couche sélective se rapproche de la taille des pores de surface du support poreux, le flux de gaz traversant la couche sélective s'écarte du flux idéalement observé, ce qui réduit la perméance de la membrane (Ghadimi *et al.*, 2018, Wijmans and Hao, 2015, Kattula *et al.*, 2015).

(ii) Pénétration de la couche sélective dense dans les pores du support poreux lors de la fabrication de la membrane composite. Cette pénétration augmente la résistance de la membrane, en raison de l'augmentation de la longueur de diffusion dans la couche dense à faible perméabilité (Henis and Tripodi, 1981, Salih *et al.*, 2014, Pixton and Paul, 2018).

(iii) Limitations de la conception et de la fabrication de la membrane composite. Ces limitations sont dues à la nécessité d'une compatibilité entre le solvant utilisé pour déposer la couche sélective et le support sur lequel la couche est déposée

(Pixton and Paul, 2018). Ainsi, en cas de non compatibilité, on peut par exemple observer la formation d'un hydrogel dans le support poreux lors de la polymérisation interfaciale (Baker, 2004).

Alors que le troisième problème est explicite et sans solution spécifique, les deux premiers problèmes peuvent être minimisés. Ceci, d'une part, par un contrôle approprié des caractéristiques des pores de surface du support et, d'autre part, par l'introduction d'une couche intermédiaire entre la couche sélective et la couche de support. Les deux stratégies peuvent être utilisées simultanément. La fabrication du support poreux peut être réalisée de différentes manières, mais la technique la plus courante est basée sur un processus d'inversion de phase pour produire une membrane asymétrique avec une morphologie de surface microporeuse (Baker, 2002). Le polydiméthylsiloxane (PDMS) a principalement été utilisé comme matériaux pour la couche intermédiaire. Ceci en raison de sa grande perméabilité (Dai *et al.*, 2016). Afin de fabriquer une bonne structure composite, une bonne conception des différentes étapes de sa fabrication est indispensable. L'objectif final est de garantir que la plus grande fraction de la résistance au transfert est localisée dans la couche sélective mince. Le traitement adéquat de ces différents aspects nécessite une compréhension approfondie de la chimie de la formation des membranes pour les structures poreuses et denses, ainsi qu'une compréhension de la dynamique des écoulements à travers la membrane composite et enfin des connaissances dans la science de la formation de dépôts minces. Outre les problèmes spécifiques notés pour la membrane composite ci-dessus, il est important de noter que les membranes composites doivent toujours respecter les limitations de la structure de membrane asymétrique. Les couches sélectives doivent être aussi fines que possible tout en étant exemptes de défauts pour éviter la perte de sélectivité (Yampolskii, 2012).

Les deux premiers problèmes peuvent également être résolus en fabriquant une membrane asymétrique, constituée d'une peau dense et d'une couche intermédiaire fabriquées avec un même matériau. L'utilisation d'un même matériau évite à la fois la diffusion latérale et la pénétration du matériau de la couche dense intermédiaire dans la sous-structure poreuse. De plus, la présence d'une couche dense intermédiaire peut faciliter la formation d'une couche sélective très mince (Salih *et al.*, 2014). Toutefois, de nombreux matériaux utilisés pour la fabrication de membranes asymétriques n'ont pas la perméabilité élevée nécessaire pour former une bonne couche dense intermédiaire. De plus, ces matériaux peuvent être attaqués et dissous par le solvant utilisé pour déposer la couche mince sélective, qui peut être constituée de polysulfones ou de polyimides (PI). Par ailleurs, les polymères caoutchouteux à haute perméabilité n'ont pas la résistance mécanique nécessaire pour former des membranes asymétriques autosupportées, ce qui rend les matériaux tels que le PDMS inadaptés à cet effet. Cependant, le poly(4-méthyl-1-pentène) (PMP) convient à cette description. Le PMP, un polymère vitreux à volume libre relativement élevé, n'a pas été utilisé comme couche intermédiaire dense dans la littérature, malgré sa perméabilité modérément élevée d'environ 9,87 et 128 Barrer pour l'azote (N_2) et le dioxyde de carbone (CO_2) respectivement (Yasuda and Rosengren, 1970). Bien que la valeur de la perméabilité

soit inférieure à la perméabilité du PDMS, le PMP est avantageux, car sa structure vitreuse devrait lui permettre d'être utilisé à la fois comme couche de support et comme couche dense intermédiaire. Cependant, le PMP a une faible énergie de surface (Slepička *et al.*, 2012), ce qui peut limiter sa mouillabilité avec une autre solution de polymère, nécessaire à la formation de la membrane composite. Par conséquent, la possibilité d'utiliser le PMP comme support et comme couche intermédiaire, ainsi que ses performances devront être élucidées et comparées à une structure composite de PDMS. Une couche sélective appropriée avec une fiabilité industrielle connue sera choisie telle que le PI et appliquée sur le support ou sur la couche intermédiaire. Des tests de performance seront effectués pour les gaz $N_2/CO_2/CH_4$, qui sont des gaz industriels courants. En effet, ces gaz sont séparés lors de la valorisation du biogaz, la séparation du gaz naturel et la capture du dioxyde de carbone dans les gaz de combustion (Ding, 2019).

Ce travail de thèse vise à proposer le développement d'une membrane composite multicouches, adaptée à la fabrication d'une membrane MMM. La dynamique de l'écoulement à travers la membrane sera étudiée. Pour y parvenir, trois objectifs sont à atteindre :

i) Élucider l'influence de la conception du support et de la couche intermédiaire (composite ou asymétrique) sur le phénomène de diffusion latérale et d'intrusion de solution à travers la membrane composite, étudiée par étude expérimentale, théorique et simulation numérique de dynamique des fluides (CFD).

ii) Élucider la compatibilité entre la couche intermédiaire choisie (PMP) et la couche sélective P84 PI.

iii) Quantifier la performance de perméation de la membrane composite multicouche avec P84 PI comme couche sélective réalisée par revêtement par immersion et la comparer avec son homologue à membrane dense.

2. Méthodologie

2.1 Matériaux et produits chimiques

Les matériaux et produits chimiques utilisés dans ce travail sont répertoriés dans le Tableau 1.

Tableau 1: Liste des matériaux et produits chimiques

Matériau / Produit	**Qualité**	**Fournisseur**	**Rôle dans l'étude**
Polyéthersulfone (PES)	Ultrason E6020P	BASF	Polymère du support poreux
N-méthyl-2-pyrrolidone (NMP)	EMPLURA	Merck	Solvant du PES & polyimide P84 (P84 PI)
Chlorure de lithium (LiCl)	ACS Reag., Ph Eur.	Merck	Additif du PES
Polydiméthylsiloxane (PDMS)	Terminé par fonction hydroxy, viscosité 2550 – 3570 cSt	Sigma	Polymère de la couche intermédiaire dense
N-heptane	Anhydre, 99%	Sigma	Solvant du PDMS
Orthosilicate de tétraéthyle (TEOS)	Qualité du réactif, 98%	Sigma	Réticulant du PDMS
Dilaurate de dibutylétain (DBD)	95%	Sigma	Catalyseur de réticulation du PDMS
Membrane capillaire Oxyplus	PMP 90/200	3M Membrana	Membrane à peau dense asymétrique commerciale
Polyimide P84 (P84 PI)	Granulaire, qualité solution	HP Polymer GmbH	Polymère de la couche de sélective

2.2 Plan des travaux de recherche

Le travail a été divisé en quatre parties : (1) fabrication et performances des membranes composites PES/PDMS, (2) performance de la membrane PMP à peau dense asymétrique commerciale, (3) modélisation des résistances en série (RiS) et CFD au voisinage de l'interface entre la couche intermédiaire et le support poreux, et (4) fabrication d'une fine couche sélective de P84 PI par dépôt par immersion et performance de la membrane composite. Le plan général de la recherche est résumé dans la Figure 1. Les détails et la façon dont chaque partie a été réalisée peuvent être trouvés dans le texte principal de la thèse (Chapter 3 : Methodology).

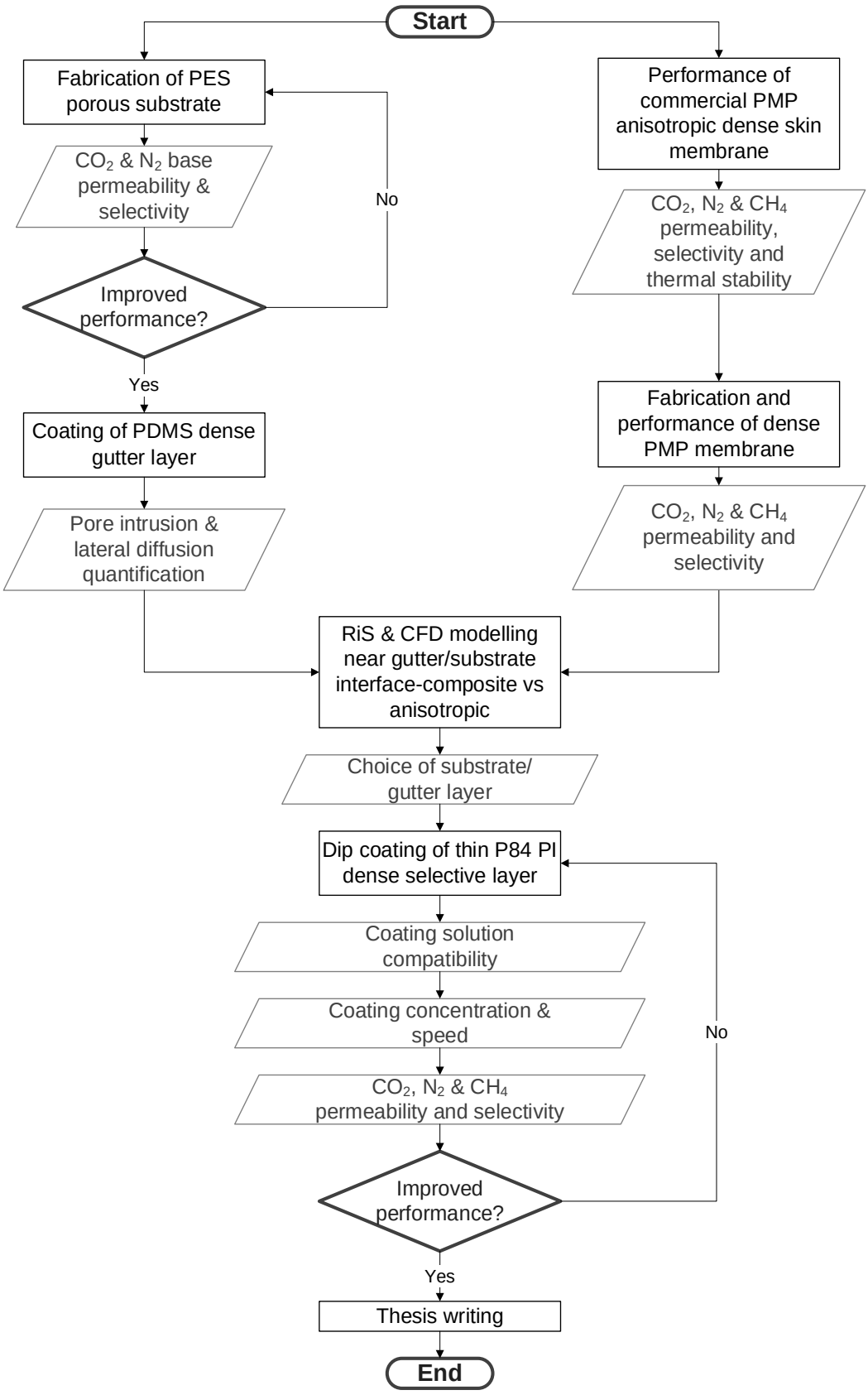

Figure 1: Le plan général de la recherche

3. Résultats et discussions

3.1 Membrane poreuse PES modifiée au LiCl - formation du support

Les performances de la couche de support peuvent avoir un impact significatif sur les performances globales de la membrane composite. Par conséquent, l'influence de la couche de support sur les performances de perméation des gaz doit être élucidée. La Figure 2 représente la perméance CO_2/N_2 des supports et leur sélectivité idéale. Une tendance similaire a été notée pour les deux gaz, pour lesquels la perméance diminue avec la teneur en LiCl. Les mesures ont confirmées que le transfert des gaz dans le support est principalement régi par le régime de Knudsen. En effet, on observe une sélectivité moyenne d'environ 0,8 pour le binaire CO_2/N_2, ce qui est en accord avec la sélectivité d'une diffusion de Knudsen pour ces gaz. Toutes les perméances étaient dans deux écarts types par rapport à la moyenne de l'échantillon. Une large variation de perméance peut être notée pour tous les échantillons (différence de 100 000 GPU de N_2 entre le support vierge et LiCl_4%). La diminution de la perméance entre les différents échantillons pourrait être due à l'augmentation de l'épaisseur de la peau et à la diminution de la porosité de surface, qui est liée à la porosité de la peau (voir texte principal, chapitre 4.1.3 pour plus de détails).

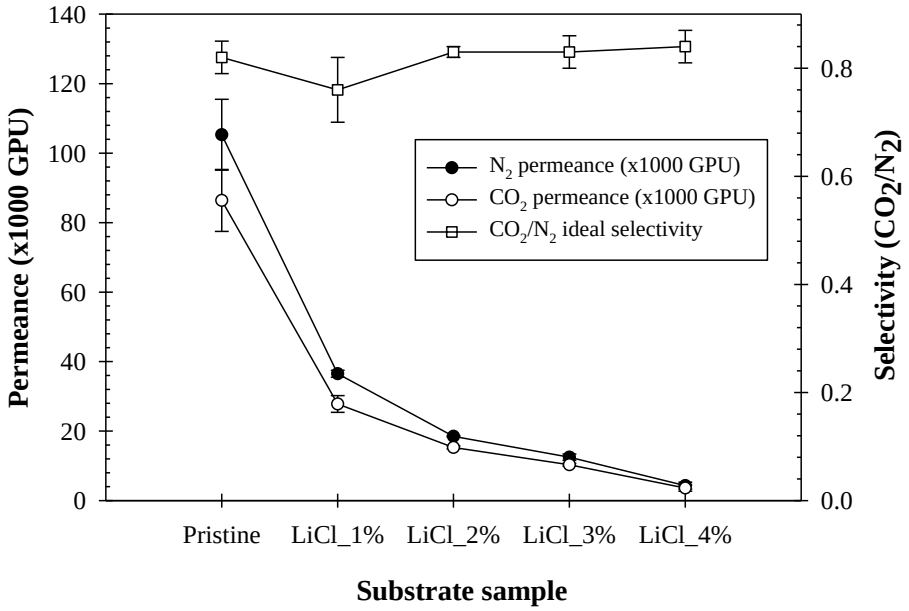

All permeance and selectivity was taken at 6 bars transmembrane pressure value except for pristine due to equipment limitation (1 bar)

Figure 2: Perméances du CO_2/N_2 et sélectivité idéale des supports

Afin d'être utilisé comme support, les échantillons de membrane devraient avoir une perméance d'au moins 2 900 GPU. En effet, dans la littérature, il est recommandé que le support soit au moins 5 à 10 fois plus perméable que la couche sélective dense, ceci afin d'assurer une résistance minimale au transfert (Kattula *et al.*, 2015, Baker, 2004). Par conséquent, la perméance intrinsèque maximale de la couche sélective

adaptée à la fabrication d'une membrane composite avec ce support devrait être d'environ 290 GPU, ce qui est réalisable pour de nombreux matériaux connus.

3.2 Composite PES/PDMS – Impact de la pénétration de la solution et de la diffusion latérale

3.2.1 Épaisseur de la couche dense

L'épaisseur de la couche dense de PDMS déposée a été mesurée à l'aide d'une technique d'analyse d'image. Les résultats sont illustrés dans la Figure 3. La nature du support utilisé n'a pas modifié de manière significative l'épaisseur de la couche dense de PDMS, ce qui confirme que la pénétration de la solution de PDMS était, si elle se produisait, limitée au film de surface du support (voir texte principal, chapitre 4.1.3 pour plus de détails). Ceci est acceptable, étant donné que l'épaisseur maximale de ce film de surface est d'environ 1 µm pour le support LiCl_4%, ce qui est inférieur à la plage d'erreur de la mesure de l'épaisseur pour la plupart des échantillons. D'autre part, une augmentation presque linéaire de l'épaisseur de la couche dense déposée a été observée avec l'augmentation du poids de la solution de PDMS utilisée pour la formation du film.

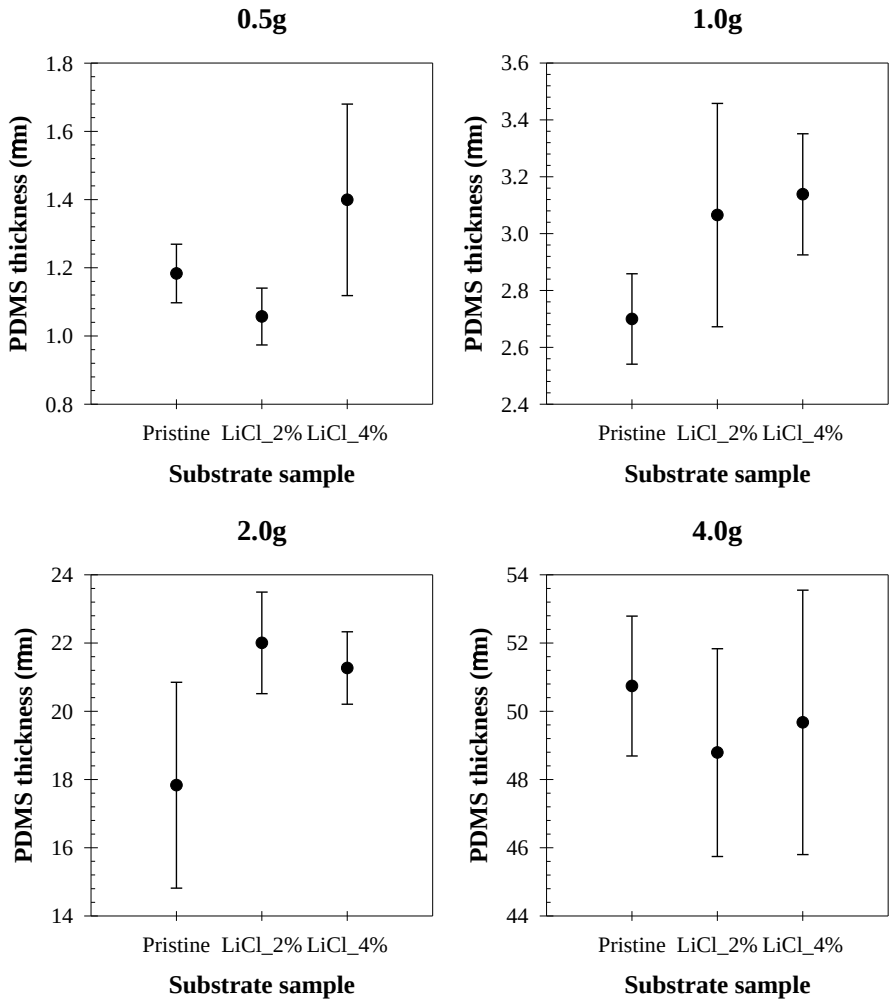

Figure 3: Épaisseur mesurée de la couche de PDMS sur différents échantillons de supports, basée sur la masse versée de la solution de PDMS

L’épaisseur de la couche dense déposée varie entre la moitié de l'épaisseur du support, soit 50,74 ± 2,05 µm, pour une solution de PDMS de 4,0 g lors de la formation de la couche, et environ 1,06 ± 0,08 µm pour une solution de PDMS de 0,5 g utilisée pour le dépôt. Des travaux similaires sur le dépôt d’une couche de PDMS ont conduit à des couches de PDMS plus minces : 550 nm (Salih *et al.*, 2014) et 490 nm (Hu *et al.*, 2017). Toutefois, une étude préliminaire réalisée sur un support PES vierge n'a pas permis de fabriquer un revêtement de PDMS plus mince à une masse inférieure à 0,5 g, sans perte de sélectivité en CO_2/N_2, suggérant soit un recouvrement incomplet par le PDMS, soit une rupture de la couche dense résultante (voir texte principal, Annexe E pour plus de détails). Ceci est probablement dû à la taille des pores de surface du support membranaire, qui est plus grande dans ce travail, par rapport aux études de la littérature. L’épaisseur de la couche de PDMS formée doit être aussi faible que possible, afin de minimiser la résistance au transfert du gaz. Toutefois, comme tout défaut, même petit, sur la couche de PDMS peut contribuer à la pénétration de la solution utilisée pour la couche sélective que l’on souhaite déposer par la suite, la perte de sélectivité mesurée ici, suggère que les couches de PDMS plus minces n'étaient pas suffisamment fiables pour pouvoir être retenues.

3.2.2 Analyse de la perméabilité au gaz

Les échantillons composites ont été testés pour la perméance aux gaz purs N_2 et CO_2, comme représenté sur la Figure 4. Tous les échantillons composites présentent des tendances similaires. On observe la diminution du flux avec l'augmentation de la masse de la solution de dépôt de PDMS, ce qui est attendu étant donné qu'une couche de PDMS plus mince présenterait une résistance au transfert des gaz plus faible. Néanmoins, les composites avec un support sans LiCl présentent la perméance la plus élevée, suivis des composites LiCl_2% et des composites LiCl_4%. Ceci est similaire à ce qui a été observé pour la performance de ces supports. L'échantillon composite de 0,5 g de PDMS sur un support dépourvu de LiCl [P(0,5)] présente la perméance globale la plus élevée à 26,6 ± 2,6 GPU pour N_2 et 354,4 ± 27,9 GPU pour CO_2, tandis que l'échantillon L4(4,0) présente la perméance la plus faible à 0,9 ± 0,3 GPU pour N_2 et 15,4 ± 3,9 GPU pour CO_2. Ces résultats montrent que la perméance est significativement plus faible que celle des supports non revêtus d’un film de PDMS, rapportés sur la Figure 2. La perméance est inférieure à celle enregistrée dans la littérature, comme par Li *et al.* (2019). Une perméance de base beaucoup plus faible a également été enregistrée pour le support PSf à 20 700 ± 400 GPU et 16 900 ± 300 GPU pour N_2 et CO_2 respectivement, par rapport à ce travail. Pourtant, la perméance de la structure composite était beaucoup plus élevée à 811 ± 12 GPU et 7 780 ± 120 GPU pour N_2 et CO_2 respectivement, malgré l'utilisation du même revêtement PDMS. Les différences étaient attendues, compte tenu d'une couche de PDMS beaucoup plus fine, de 80 nm, dans la littérature. Toutefois, l’estimation de la perméabilité de la membrane, qui tient compte de l’épaisseur de la couche dense et de la perméance, a également conduit à une valeur plus élevée dans la littérature, respectivement 64,9 Barrer et 622,4 Barrer pour N_2 et CO_2, par rapport à respectivement 31,4 Barrer et

419,4 Barrer pour P(0,5) dans ce travail. Les résultats sont similaires si l'on considère d'autres publications (Hu *et al.*, 2017, Merkel *et al.*, 1999).

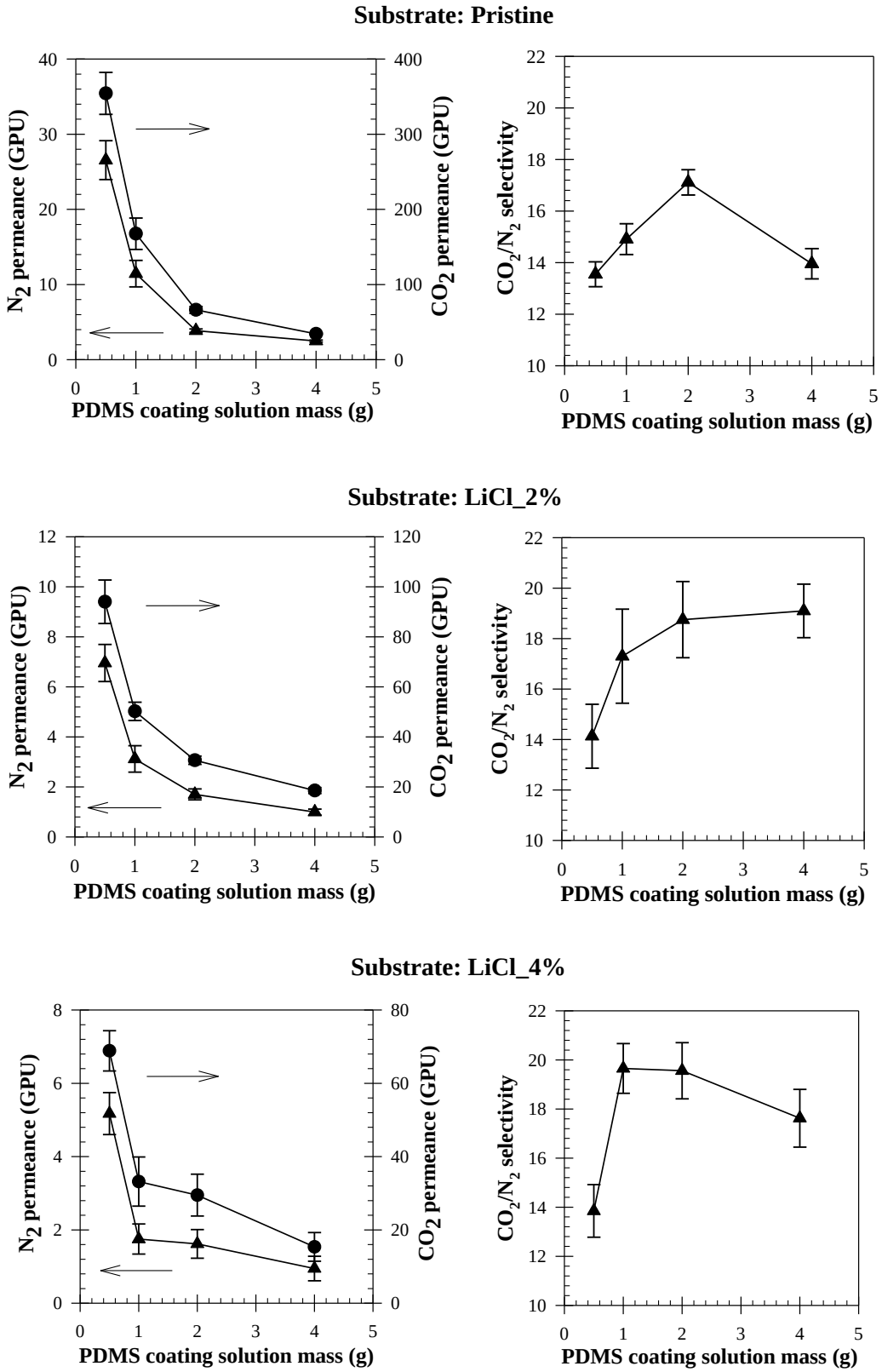

Figure 4: Perméances N_2 & CO_2 et sélectivité CO_2/N_2 d'échantillons de support sans LiCl, LiCl_2% et LiCl_4%, recouverts de PDMS de diverses masses en solution

La sélectivité en CO_2/N_2 se situe entre 12 et 21, ce qui suggère que le revêtement dense en PDMS a été fabriqué avec succès sans défauts significatifs. La couche de PDMS la plus fine pour tous les supports fabriqués avec une solution de 0,5 g possède la sélectivité la plus faible entre 13,5 ± 0,5 pour P(0,5) et 13,8 ± 1,1 pour L4(0,5). Il est intéressant de noter que la sélectivité a été trouvée plus élevée pour le PDMS le plus épais, ceci pour tous les supports étudiés. Ces valeurs étaient également beaucoup plus élevées que la sélectivité idéale du PDMS CO_2/N_2 indiquée dans la littérature, qui se situe généralement entre 9 et 12 (Merkel *et al.*, 1999, Li *et al.*, 2019, Hu *et al.*, 2017, Dong *et al.*, 2020, Yasuda and Rosengren, 1970).

Pour comprendre davantage les résultats de performance, les couches de PDMS de 4,0 g fabriquées sur les trois supports ont été séparées ou pelées (à partir de maintenant, elles seront appelées PDMS libres) et testées séparément pour le gaz CO_2 et N_2. Les résultats sont représentés sur la Figure 5.

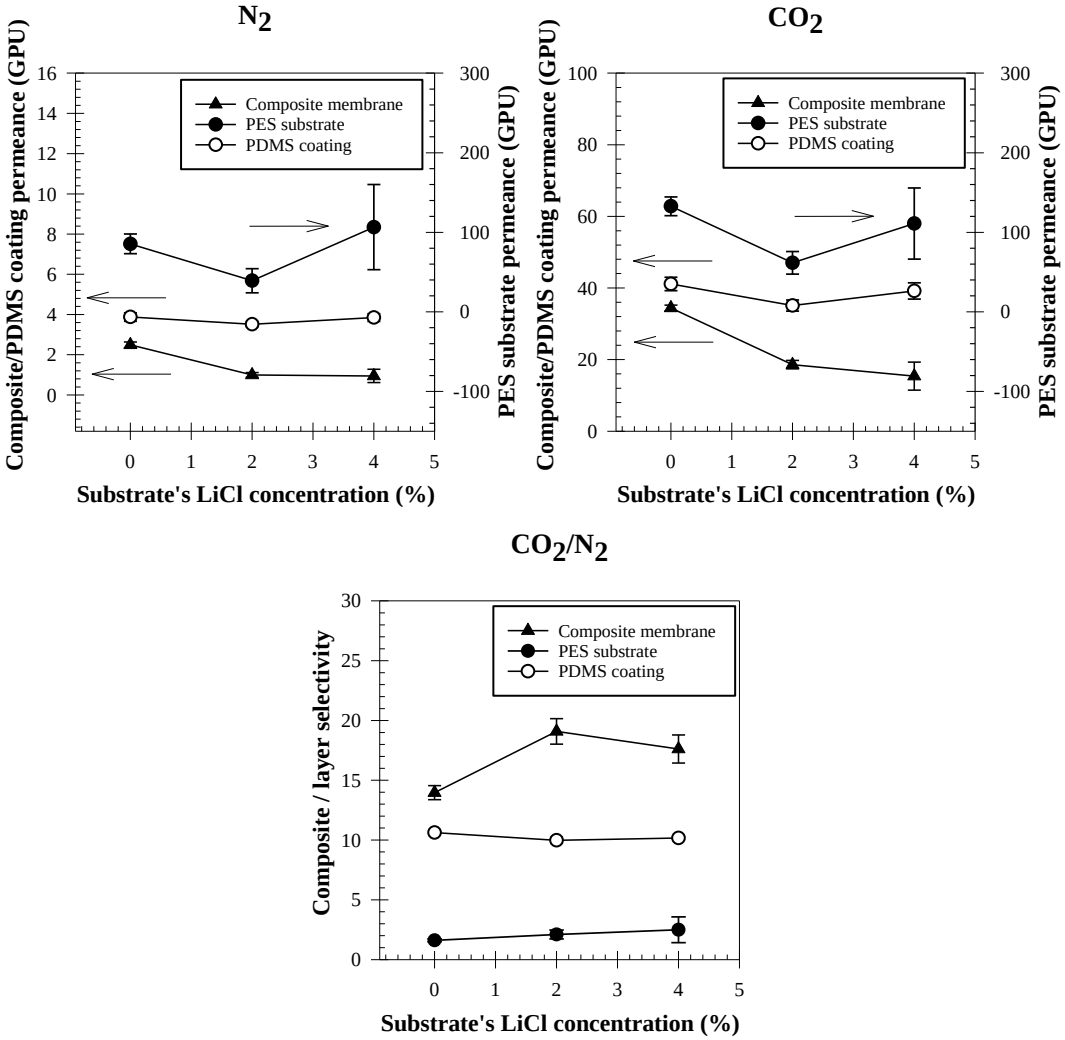

Figure 5: Perméances du N_2 – CO_2 et sélectivité du CO_2/N_2 des membranes composites, par rapport au support poreux du PES et dense PDMS qui á été séparé (les supports PES libres et PDMS libres) pour les échantillons de revêtement PDMS de 4,0 g

Pour toutes les mesures, la perméance mesurée du PDMS libre était plus élevée que celle des membranes composites. Cependant, contrairement aux résultats obtenues pour les membranes composites, les perméances mesurées sur les PDMS libres étaient comparables entre elles, quels que soient leurs supports d'origine utilisés, à 3,7 ± 0,1 GPU pour N_2 et 38,4 ± 1,8 GPU pour CO_2. Ceci correspondait à une sélectivité résultante du PDMS CO_2/N_2 de 10,3 ± 0,2 ; une valeur attendue pour le PDMS (voir texte principal, chapitre 4.2.4 pour plus de détails). Comme il a été montré sur la Figure 2 que le support est poreux et n'a pas la sélectivité d'une couche dense, on peut affirmer que la sélectivité accrue observée dans les membranes composites a été créée par l'interaction entre le PDMS et le PES formant le support. Cette sélectivité accrue provient de la sélectivité CO_2/N_2 du PES. Les supports PES libres (supports résultant des composites qui ont été séparées ou pelées) ont produit des perméances plus élevées que celles des membranes composites et PDMS libres correspondantes. Ceci est attendu étant donné que ces couches de PES libres étaient poreuses et devraient retrouver leurs perméances d'origine comme indiqué sur la Figure 2 (ou la perméance après le séchage du support, voir le texte principal, chapitre 4.2.1 pour plus de détails). Cependant, les flux observés étaient beaucoup plus faibles que les perméances du support avant dépôt du film de PDMS. Par ailleurs, la sélectivité CO_2/N_2 a été notée de l'ordre de 1,6 – 2,5. Cela suggère que la solution de dépôt du PDMS a pénétrée dans les pores situés à la surface du support, conduisant à leur blocage partiel.

3.3 Membrane à base de PMP - performance de membranes asymétrique autosupportées en tant que support et couche intermédiaire unifiée

3.3.1 Performance de séparation des gaz

Les membranes à fibres creuses commerciales en PMP asymétrique à peau dense utilisée pour cette étude ont été initialement développées pour une application d'oxygénation. Par conséquent, pour la réutilisation de la membrane, un test de perméation de gaz unique a été effectué pour le N_2, le CO_2, et le méthane (CH_4), comme indiqué dans le Tableau 2. Des échantillons ont été testés à 5 bars pour garantir la fiabilité de la membrane à une pression élevée. Les résultats de perméance ont suggéré que cette membrane convient comme support et couche intermédiaire unifiés. En effet, sa perméance est élevée, avec une augmentation des flux dans l'ordre : $CO_2 > CH_4 > N_2$. Cependant, les sélectivités CO_2/N_2 et CO_2/CH_4 sont relativement faibles. Toutefois la membrane a les propriétés nécessaires à une membrane support revêtu d'une couche intermédiaire. La valeur des perméances mesurées pour la membrane PMP est plus élevée que la perméance PDMS la plus élevée reportées précédemment dans la Figure 4 pour l'échantillon P(0,5). La perméance à N_2 est dans la plage indiquée dans la fiche technique du fournisseur entre 45 et 445 GPU (3M, 2019).

La valeur de perméance assez élevée du PMP est obtenue grâce à la faible épaisseur de la peau dense, déposée lors de la fabrication asymétrique de la membrane. Alors que le même effet devrait être obtenu pour une membrane composite avec une

couche dense de surface plus mince, l'effet de la diffusion latérale et la pénétration de la solution dans les pores du support, ne peuvent pas être complètement évitées (Li *et al.*, 2019, Wijmans and Hao, 2015). De plus, des défauts apparaissent si l'épaisseur de la couche déposée est diminuée. Il s'avère qu'une membrane asymétrique à peau dense, mince et sans défauts, présente de bonnes caractéristiques de perméabilité et évite les problèmes liés au dépôt de la couche intermédiaire. Ce qui pourrait limiter l'utilisation de la membrane asymétrique est uniquement liée aux propriétés du matériau lui-même.

Tableau 2: Performances de la membrane asymétrique en fibres creuses PMP

Gaz	**Perméance (GPU)**	**Sélectivité**		
		CO_2/N_2	**N_2/CH_4**	**CO_2/CH_4**
N_2	84.6 ± 6.2			
CO_2	607.3 ± 31.3	7.4 ± 0.4	0.6 ± 0.1	4.0 ± 0.2
CH_4	156.0 ± 13.1			

3.4 Influence de la restriction géométrique et de la pénétration de la solution à l'qide d'un modèle de résistances en série et d'un modèle CFD pour le support et la couche intermédiaire

3.4.1 Perméance idéale du composite et facteur d'efficacité de la perméance

La perméabilité du PDMS dans ce travail a été fixée à 186,4 ± 7,6 Barrer et 1914,1 ± 109,3 Barrer pour N_2 et CO_2 respectivement, sur la base des résultats de perméance de la couche dense de PDMS libre de 4,0 g de différents supports sur la Figure 5 et de leur épaisseur correspondante sur la Figure 3. Comme la perméabilité intrinsèque du PDMS est constante, quelle que soit son épaisseur, elle peut être utilisée pour calculer la perméance idéale correspondante du revêtement à une épaisseur spécifiée. En utilisant cette hypothèse et l'épaisseur d'autres composites PES/PDMS, la perméance idéale du composite, $\mathcal{P}_T^{ideal}$ peut être déterminée :

$$\mathcal{P}_{T,i}^{ideal} = \left(\frac{\ell_1}{P_{c,i}} + \frac{1}{\mathcal{P}_{s,i}} \right)^{-1} \tag{1}$$

ℓ_1 est l'épaisseur de la couche intermédiaire, présentée sur la Figure 3, P_c est la perméabilité intrinsèque de la couche intermédiaire et $\mathcal{P}_s$ est la perméance du support, présentée sur la Figure 2. Le taux de réduction de la perméance ou l'efficacité de la perméance, β ont été déterminés par l'équation :

$$\beta = \frac{\mathcal{P}_{T,i}}{\mathcal{P}_{T,i}^{ideal}} \tag{2}$$

$\mathcal{P}_T$ est la perméance composite mesurée ou apparente. β est un facteur à la fois de pénétration de la solution et de diffusion latérale.

La Figure 6 représente la valeur de β calculée pour différentes épaisseurs de la couche intermédiaire et pour différents supports utilisés. Ceci pour N_2 et CO_2. Comme

$\beta = 1$ représente une perméance mesurée qui est égale à sa valeur idéale, cela suggère que l'effet combiné de la pénétration de la solution et de la diffusion latérale est beaucoup plus sévère lorsque l'épaisseur de la couche déposée est faible. Néanmoins, comme la pénétration de la solution devrait être maximale pour un dépôt épais (plus de masse ou de solution à pénétrer), cela suggère que la diffusion latérale est le mécanisme dominant, au moins lorsque la couche déposée est de faible épaisseur. Il est intéressant de noter que la valeur de β caractérisant le CO_2 est supérieure à celle caractérisant le N_2 pour une même membrane composite. La différence de la valeur de β entre ces gaz est particulièrement élevée lorsque les couches de PDMS déposées sont épaisses. Li *et al.* (2019) qui ont estimé la valeur de β pour le CO_2 et le N_2 ont noté des différences négligeables entre les gaz. Mais ils ont étudié une épaisseur de couche sélective faible, jusqu'à 0,20 nm. Zhu *et al.* (2016b) ont également suggéré un β comparable mesuré entre CO_2, H_2, et N_2 pour une épaisseur de couche sélective allant jusqu'à 0,37 µm. Pour la couche déposée la plus mince dans le travail présent (à 1,0 - 1,4 µm), le β caractérisant les deux gaz était également comparable. Toutefois, il était très différent pour une épaisseur de couche dense plus élevée.

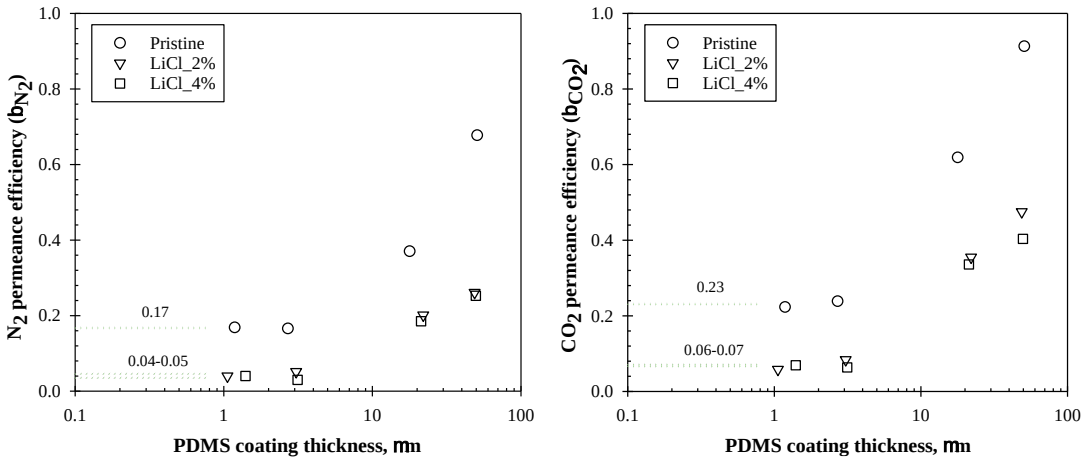

Figure 6: β calculé de la membrane composite PES/PDMS en fonction de l'épaisseur de la couche de PDMS sur différents supports

Le calcul de $\mathcal{P}_T^{ideal}$ et β a été effectué en utilisant des données expérimentales de perméation avec l'hypothèse que la perméabilité du PDMS reste constante pour la couche déposée. Cependant, on voit sur la Figure 6 que, même si l'on dépose une couche épaisse de PDMS, la valeur de β est encore loin de l'unité. Pourtant, avec un revêtement d'environ 50 µm, la diffusion latérale devrait être faible (voir le texte principal, chapitre 4.4.2 pour plus de détails). Expérimentalement, une valeur de β aussi faible que 0,26 pour l'échantillon composite L4(4,0) a été déterminée. Cette valeur est trop faible pour être attribuée uniquement à la pénétration de la solution dans les pores. De plus, cette pénétration ne semble pas être très importante (voir le texte principal, chapitre 4.2.3 pour plus de détails). Par ailleurs, la sélectivité plus élevée en CO_2/N_2 des membranes composites indiquée sur la Figure 4 est déroutante, car la perméance composite idéale calculée du CO_2 et du N_2 à l'aide de l'Équation (1) suggère une diminution de la sélectivité du CO_2/N_2 lorsque la contribution du support à la

résistance totale devient plus élevée. Ceci est soutenu par les travaux de Pinnau and Koros (1991) qui montrent qu'une plus grande résistance du support réduit la sélectivité de la membrane composite en dessous de la valeur de la sélectivité intrinsèque de la couche déposée. Une hypothèse permettant d'expliquer cet écart est que lorsque les pores du support sont remplies avec la solution permettant le dépôt de la couche dense, la partie dense du PES contribue à la séparation, augmentant ainsi la sélectivité de la membrane au-dessus d'une valeur normalement observée pour le PDMS. Ce phénomène a été observé par Henis and Tripodi (1981). Pour qu'il soit observé, il faut que la porosité de surface du support soit très faible. Pour mieux comprendre ces phénomènes, la contribution de la pénétration de la solution de déposition et de la diffusion latérale sur la perméance des membranes composites est quantifiée, en utilisant les données de perméance et de résistance de la couche composite pelée.

3.4.2 Quantification de la restriction géométrique et de l'intrusion de solution

La diffusion latérale et la pénétration de la solution contribuent à la résistance globale de la membrane composite (R_T) à travers l'équation suivante :

$$R_{T,i} = R_{1,i} + R_{2,i} = \frac{\ell_1}{\Psi P_{c,i} A_1} + \frac{\ell_2}{f P_{s,i} A_1} = \frac{1}{\Psi \mathcal{P}_{c,i} A_1} + \frac{1}{f \mathcal{P}_{s,i} A_1} \quad (3)$$

Les indices 1 et 2 représentent respectivement la résistance des composants de la couche PDMS dense et du support PES, ℓ est l'épaisseur de la couche, P est la perméabilité, $\mathcal{P}$ est la perméance, A est la surface membranaire, Ψ est le facteur d'ajustement pour la diffusion latérale appelé facteur de restriction, et f est le facteur d'ajustement pour la pénétration de la solution appelé facteur de pénétration. Les indices c et s représentent respectivement la couche de revêtement (coating en anglais) et la couche de support (substrate en anglais). La contribution de la diffusion latérale pour le revêtement PDMS de 4,0 g sur support PES peut être calculée à partir de la résistance expérimentale des couches composites pelées :

$$\Psi = \frac{R_{c,i}}{R_{1,i}} = \frac{R_{c,i}}{R_{T,i} - R_{2,i}}, R_{1,i} \geq R_{c,i} \quad (4)$$

La contribution de la pénétration de la solution pour le revêtement PDMS de 4,0 g dans le support PES peut également être calculée à partir de la résistance expérimentale des couches composites pelées à travers l'équation :

$$f = \frac{R_{s,i}}{R_{2,i}}, R_{2,i} \geq R_{s,i} \quad (5)$$

Les détails des développements peuvent être trouvés dans le texte principal, chapitre 3.5.2. Les valeurs mesurées de Ψ et de f des échantillons composites de 4,0 g sont présentées à la Figure 7. On observe une diminution du facteur de diffusion latérale,

Ψ, avec l'augmentation de la concentration en LiCl utilisée lors de la fabrication de la membrane support. Ceci pour les deux gaz, N_2 et CO_2. Lorsque la membrane support devient moins poreuse, Ψ devrait diminuer, ce qui est la tendance observée expérimentalement. Ψ est cependant plus élevé pour le CO_2 comparé au N_2. Ceci est probablement dû au fait que la perméabilité du CO_2 est plus élevée que celle du N_2 et ceci à la fois dans le PDMS et dans le PES (Ψ de 1 signifie aucune diffusion latérale). Les valeurs sont supérieures ou comparables aux valeurs de β calculées précédemment. Sans l'influence de la pénétration de la solution, qui a été additionnée à la résistance du support et supprimée par le terme R_2, Ψ devrait être supérieure ou égal à β, car la perte de perméance totale est liée aux contributions des pertes de perméance par Ψ et par la pénétration de la solution. Par ailleurs, les résultats montrent une augmentation de f avec l'augmentation de la concentration en LiCl utilisée lors de la fabrication de la membrane support. Ceci pour les deux gaz, N_2 et CO_2. L'augmentation de f signifie un effet plus faible lié à la pénétration de la solution dans le support. Pour la même qualité de la solution de dépôt, cela suggère que davantage de PDMS pénètre dans le support préparé sans LiCl, comparé aux supports modifiés par LiCl. Ceci est en contradiction avec la tendance attendue, qui est que f diminue avec l'augmentation de l'épaisseur de la couche superficielle de la membrane support. Ceci devrait conduire à un effet plus important par pénétration de la solution pour le support à peau plus épaisse créé pour une solution de préparation comportant LiCl_4%. Des pores de surface plus petits observés dans le support préparé sans LiCl pourraient générer des forces capillaires plus importantes, qui augmenteraient la profondeur de pénétration de la solution de revêtement dans le support. Encore une fois, f est également inférieur pour N_2, comparé à CO_2. Cet effet est identique à l'observation faite pour Ψ , indiquée précédemment.

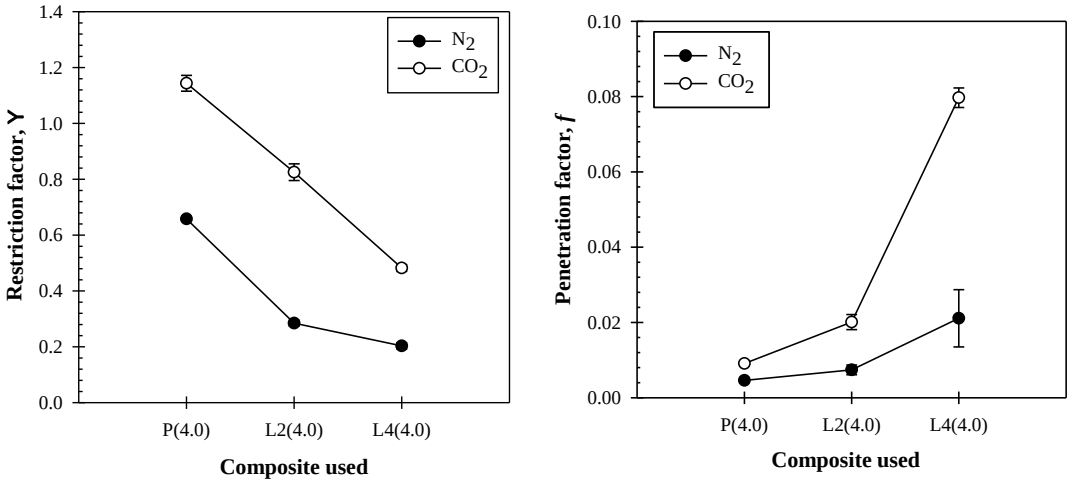

Figure 7: Contribution mesurée de la diffusion latérale (facteur de restriction, Ψ) et de la pénétration de la solution (facteur de pénétration, f) pour 4g de solution de revêtement PDMS sur support poreux PES

Il convient également de noter que f est très faible dans toutes les configurations, suggérant une influence très importante de la pénétration de la solution. Par exemple, on observe une réduction de la perméance du support PES préparé sans LiCl avant

dépôt et après dépôt et pelage de 86 420,00 GPU à 132,75 GPU. Comme la pénétration de PDMS n'est pas détectée visuellement, cela suggère qu'une faible pénétration augmenterait considérablement la résistance du support (voir le texte principal, chapitre 4.2.3 pour plus de détails). Cette observation est cohérente avec les travaux de Hao *et al.* (2020), qui montrent par une analyse CFD que la pénétration de 1 nm ajoute une résistance équivalente à la résistance de la couche supérieure de 160 nm. Li *et al.* (2019) suggèrent que l'effet de la pénétration de la solution sur la résistance au transport du gaz est particulièrement importante au début. Même une petite pénétration aurait un effet très important sur l'augmentation de la résistance. Ceci est aussi montré par Chung (1997) qui montre qu'une profondeur de pénétration comprise entre 10 et 100 nm conduit à une chute de la perméance normalisée de 0,9 à 0,4, selon la membrane composite étudiée. Dans le présent travail, la relation entre f et la profondeur de pénétration n'est pas élucidée.

La valeur de Ψ pour les deux gaz dans ce travail peut également être comparée aux résultats de l'équation semi-empirique développée par Wijmans and Hao (2015) et modifiée plus tard par Ghadimi *et al.* (2018) et Hao *et al.* (2020) :

$$\begin{aligned} \mathcal{P}_{app} &= \Psi \mathcal{P}_{int} \\ \Psi &= \frac{\varepsilon_s + 1.6 N_R^{1.1}}{1 + 1.6 N_R^{1.1}} \\ N_R &= \frac{\sigma . \tau . \varepsilon_s}{1 - \varepsilon_s} \\ \tau &= \ell / r \end{aligned} \tag{6}$$

ε_s est la porosité de la surface du support, N_R est le nombre de restriction sans dimension, σ est le coefficient d'uniformité, ℓ est l'épaisseur de la couche de revêtement mince et r est le rayon des pores de la surface. Les détails de cette comparaison peuvent être trouvés dans le texte principal, chapitre 4.4.2. En résumé, un ε_s plus faible conduit à un Ψ plus faible, mais tous les résultats de calcul sont situés entre 0,92 et 0,99, suggérant un effet très faible de la diffusion latérale pour l'épaisseur de PDMS étudiée. Ceci est très différent des valeurs expérimentales de Ψ présentés sur la Figure 7. Comme la valeur expérimentale de Ψ de l'Équation (4) et la valeur calculée de Ψ de l'Équation (6) ne tiennent pas compte de l'effet de pénétration de la solution dans les pores, la différence entre expérience et théorie doit être due à un phénomène différent. Elle est supposée provenir de deux sources : (i) le coefficient d'uniformité, $\sigma < 1$ et (ii) la contribution de la partie dense du support lorsqu'il est en structure composite. Pour le cas (i), la version initiale de l'Équation (6) prenait σ égal à 1, qui a ensuite été modifié par Ghadimi *et al.* (2018) et Hao *et al.* (2020) pour inclure l'effet du caractère aléatoire des pores du support ou de l'uniformité des pores. La distribution de taille des pores n'est pas uniforme pour les membranes poreuses produites par un procédé d'inversion de phase. L'estimation de σ à partir de la valeur expérimentale de Ψ, conduit à des valeurs très faibles. Des valeurs très faibles de σ ont également été calculées par Ghadimi *et al.* (2018), soit 0,0483, pour un support en polycarbonate utilisé par Zhu *et al.* (2016a), qui possède une très faible porosité de

surface (ε_s = 0,0059). D'autres valeurs pour le même support, une valeur de σ de 0,256 et une valeur de ε_s de 0,011 ont également été proposées, suggérant une augmentation de σ avec ε_s . Ceci est en contradiction avec l'étude CFD de Hao *et al.* (2020), dans laquelle σ augmente lorsque ε_s diminue. Cette dernière évolution est en accord avec nos observations. Les différences entre les travaux pourraient être dues au fait que la distribution spatiale des pores diffère selon le type de membrane. Il convient de conclure que la membrane réelle est bien moins uniforme que ce que suggère des études de simulation. D'autres simulations, avec une distribution spatiale différente des pores sont nécessaires pour confirmer cette affirmation. En effet, le travail de Hao *et al.* (2020) ne prédit que l'effet de cinq modèles de distribution de pores, avec σ allant de 0,72 à 1. Néanmoins, comme σ devrait être lié au support, sa valeur devrait être indépendante de l'épaisseur du dépôt de PDMS.

Comme pour le cas (ii), il est intéressant de noter que l'Équation (6) ne prend pas en compte le type de gaz utilisé, mais n'est qu'un facteur des dimensions physiques de la membrane composite. Ceci est différent des résultats notés par les travaux actuels où Ψ varie selon le gaz utilisé. L'Équation (6) a été développée sur la base des hypothèses selon lesquelles la partie solide du support est impénétrable, ce qui n'est pas nécessairement vrai. Comme indiqué par les travaux originaux du modèle RiS dans Henis and Tripodi (1981), la sélectivité de la membrane composite multicouche serait dictée par le matériau du support lorsque ε_s est faible. Cependant, en raison de la perméabilité plus élevée du CO_2 que du N_2 dans les PES à 0,07 et 3,22 Barrer pour N_2 et CO_2 respectivement (Chen *et al.*, 2017), Ψ par N_2 devrait mieux refléter les hypothèses d'imperméabilité des équations que Ψ par CO_2 (voir texte principal, chapitre 4.4.3 pour plus de détails).

Les valeurs de β mesurées expérimentalement sur la Figure 6 sont liée à un facteur de Ψ et à un facteur f. β est lié à Ψ et f via :

$$\beta = \frac{(\Psi f)(\mathcal{P}_s + \mathcal{P}_c)}{f\mathcal{P}_s + \Psi\mathcal{P}_c}, 0 \leq \beta \leq 1 \qquad (7)$$

β mesuré à partir d'échantillons composites (appelé désormais β expérimental) est l'efficacité de perméance réelle du composite tandis que β de l'Équation (7) (appelé désormais β calculé) est déterminé à partir de Ψ, f, $\mathcal{P}_s$, & $\mathcal{P}_c$ mesurés à partir d'échantillons isolés/pelés/libres (la validité de la relation peut être trouvée dans le texte principal, chapitre 4.4.2). L'Équation (7) et l'Équation (6) peuvent être utilisées pour créer une corrélation généralisée pour le calcul de β de membranes composites avec ε_s, σ, ℓ, r, f, $\mathcal{P}_s$, & $\mathcal{P}_c$; tous sont mesurables soit directement, soit indirectement par des moyens expérimentaux comme cela a été prouvé tout au long des présents travaux. Par conséquent, la valeur de β calculée pour des échantillons recouverts de PDMS plus minces peut être comparée à la valeur de β expérimentale. Outre l'hypothèse initiale, selon laquelle la perméabilité intrinsèque du PDMS reste constante quel que soit l'épaisseur du dépôt, deux hypothèses supplémentaires doivent être faites : (i) toute réduction de f (effet accru par pénétration de la solution) doit être maximale

pour les couches déposées plus épaisses. Par conséquent, des valeurs de f similaires seront utilisées pour des couches plus minces, en supposant que la pénétration est uniquement due aux forces capillaires (voir le texte principal, chapitre 4.2.3 pour plus de détails), et (ii) Ψ est fonction de l'épaisseur de la couche déposée et peut donc varier. Cependant, σ devrait être le même pour le même support même avec une épaisseur de couche déposée différente (comme discuté ci-dessus ou voir le texte principal sur les discussions du Tableau 4.12). La comparaison du β calculé et du β expérimental pour les gaz N_2 et CO_2 est présentée à la Figure 8. La régression est acceptable avec une valeur de R^2 de 0,95 (ligne pointillée rouge). On observe une légère déviation vers la gauche par rapport à la diagonale pour des valeurs élevées de β. Ceci confirme l'indépendance de σ et de l'épaisseur du dépôt. Toutefois, l'origine des différences constatées entre les deux gaz reste à expliquer.

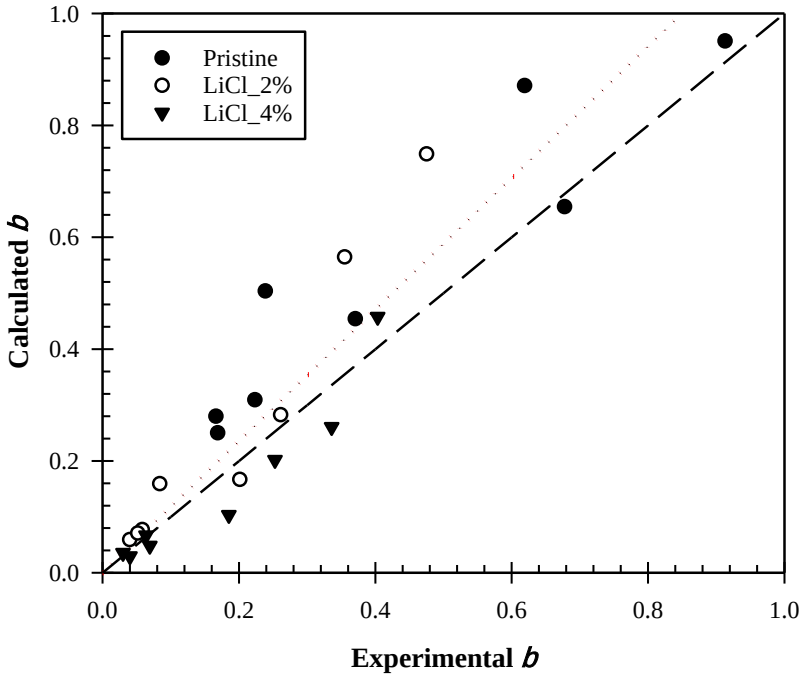

Figure 8: Comparaison du β expérimental et du β calculé à partir de l'Équation (7) pour le N_2 et le CO_2 de tous les échantillons PES/PDMS

Les valeurs expérimentales de β pour les membranes composites du PES/PDMS avec les supports préparées sans LiCl ont été tracées et comparées au β calculée. Ceci pour la perméation de N_2. Sur la Figure 9, les données expérimentales sont comparées à plusieurs autres lignes théoriques, c'est-à-dire en supposant qu'il n'y a pas de pénétration (f = 1), que les pores de supports sont uniformes (σ = 1) et les deux (f = σ = 1). La ligne de β calculée par la corrélation (ligne continue) suit assez bien le tracé expérimental de β, bien qu'avec une légère surestimation pour de faibles épaisseurs de PDMS. La corrélation est cependant bien meilleure que les autres lignes théoriques mentionnées car toutes, en particulier celles supposant des pores uniformes, sont très éloignées du tracé expérimental de β. La ligne qui suppose f = σ = 1, qui représente la condition idéale théoriquement réalisable (où seule la diffusion latérale avec des pores uniformes a eu lieu) dévie significativement du tracé expérimental de β. En ne

considérant que l'influence de la pénétration de la solution (σ = 1), le β calculé est considérablement réduit, en particulier pour un dépôt de faible épaisseur, suggérant un impact plus élevé dans ces conditions. Cependant, cela ne correspond toujours pas au tracé expérimental β. Ce n'est que lorsque les pores sont considérés comme non uniformes (f = 1) que la ligne de β calculée commence à s'adapter au tracé expérimental de β.

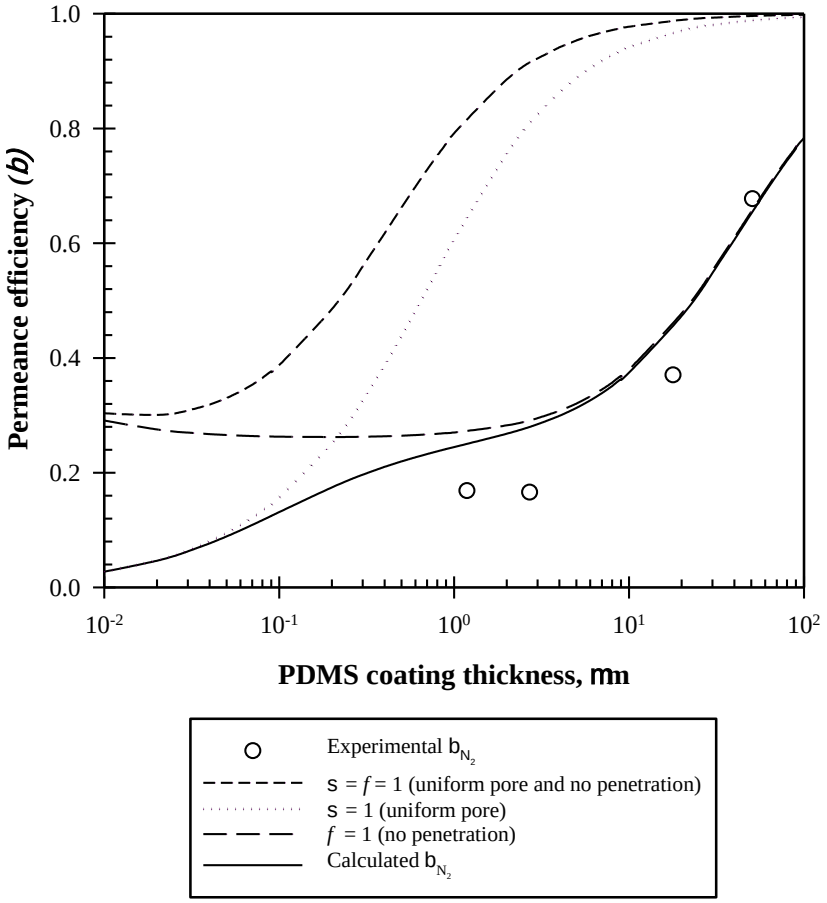

Figure 9: Comparaison des données expérimentales de β de la membrane composite PES/PDMS avec un support préparé sans LiCl avec des lignes de β calculées dans diverses conditions : (i) $\sigma = f = 1$, (ii) $\sigma = 1$, $f = 0.0046$ (iii) $\sigma = 0.0097$, $f = 1$, (iv) $\sigma = 0{,}0097$, $f = 0{,}0046$ (valeur mesurée expérimentalement à partir de la perméation de N_2)

De meilleurs ajustements peuvent être trouvés en diminuant f d'un facteur de 0,1, ou en réduisant ε_s jusqu'à 0,17, qui est la valeur trouvée à partir de β expérimental en supposant qu'aucune pénétration ne s'est produite (ou f = 1, voir le texte principal sur les discussions de la Figure 4.26 pour plus de détails). Il est cependant montré à partir de l'expérience et de la littérature que f est très peu susceptible d'être 1 (pas de pénétration de la solution), même lorsque des soins de pré-mouillage appropriés sont réalisés (Jin *et al.*, 2017, Cay-Durgun *et al.*, 2020, Chung, 1997). Par conséquent, il est supposé que la pénétration réelle de la solution soit en fait supérieure à celle mesurée ici (donc f inférieur), bien que toujours pas aussi influent que l'effet lié à la valeur de

σ. Une corrélation entre f et la profondeur de pénétration, et une meilleure méthodologie pour quantifier la pénétration à l'échelle nanométrique comme dans les travaux de Li *et al.* (2019) seraient intéressants pour valider davantage les différentes hypothèses. Bien que l'influence de σ soit validée, d'autres expériences sont nécessaires pour confirmer la tendance pour des épaisseurs de PDMS plus faibles et pour une pénétration contrôlée lors du dépôt.

Ces différents résultats montrent que la modélisation d'une perméation à travers une membrane composite composée de couches denses et poreuses est plus compliquée que prévu. Dans certains cas, comme dans le Tableau 2, un polymère hautement perméable tel que le PMP sous forme dense peut dépasser la perméance de la membrane composite PES/PDMS (Figure 4). Ici, la comparaison de la perméance N_2 est faite entre un composite PES/PDMS hypothétique avec une épaisseur de PDMS de 1 µm et utilisant un support vierge, et un PMP asymétrique à différents coefficients d'uniformité et facteurs de pénétration. Les résultats sont présentés à la Figure 10. Le PMP asymétrique, tout en étant inférieur en perméabilité intrinsèque par rapport au PDMS, conduit à une meilleure perméance lorsque certaines conditions sont remplies, car le PMP asymétrique n'est pas affecté par la non-idéalité de l'interface dense - poreuse dans le composite PES/PDMS. Dans une condition idéale réalisable ($f = \sigma = 1$), la perméance apparente maximale à 147,3 GPU peut être atteinte. Cependant, la véritable perméance à N_2 idéale du composite PES/PDMS à 186,08 GPU ne sera jamais atteinte en raison du facteur de restriction, Ψ, qui limite l'efficacité de perméance maximale, β à 0,79. Comme Ψ est un facteur lié à l'épaisseur du revêtement, augmenter l'épaisseur du PDMS à environ 2,3 µm contournerait la limite imposée par Ψ avec une valeur de β de 0,9 dans une condition idéale réalisable ($f = \sigma = 1$). Ceci réduirait cependant la perméance apparente de la membrane composite à 72,6 GPU, ce qui est inférieure à la perméance observée par PMP.

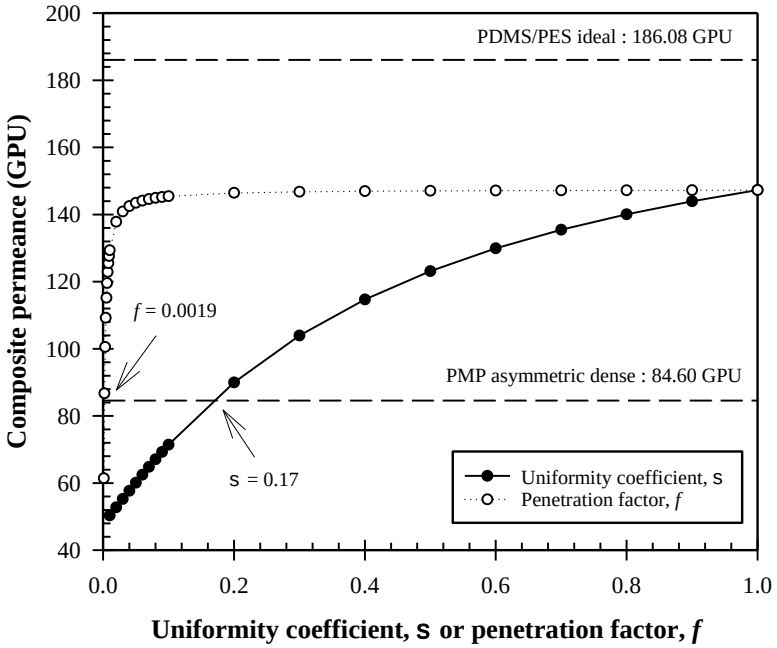

Figure 10: Comparaison entre le composite hypothétique PES/PDMS avec une épaisseur de PDMS de 1 µm et l'utilisation d'un support vierge et d'un PMP asymétrique à différents coefficients d'uniformité et facteur de pénétration

Comme indiqué dans l'expérience, la condition idéale réalisable à $f = \sigma = 1$, bien qu'elle soit théoriquement réalisable, est difficile à atteindre. La réduction de f ou σ indépendamment réduirait la perméance apparente, croisant la ligne de perméance PMP à $f = 0{,}0019$, $\sigma = 1$ ou $\sigma = 0{,}17$, $f = 1$. f est moins affecté par la réduction de la perméance apparente à valeur élevée, ce qui correspond probablement à une pénétration incomplète où la taille des pores est réduite par le matériau de revêtement, mais n'est pas comblée (Li *et al.*, 2019). Ceci est corroboré par les résultats de la Figure 5, car la perméance du support PES libre était considérablement réduite par rapport à sa perméance avant le revêtement, mais la sélectivité reste faible de l'ordre de 2 à 3 pour le CO_2/N_2, bien qu'au-dessus de la sélectivité Knudsen. Au fur et à mesure que davantage de pores sont remplis, f diminuerait rapidement en raison des différences significatives de résistance du gaz à travers le PDMS solide par rapport à la structure poreuse. Cependant, la perméance apparente diminue régulièrement avec la diminution de σ.

Alors que l'amélioration de la technique de revêtement grâce au pré-mouillage du support pourrait augmenter f, cela ne supprimerait cependant pas complètement l'effet de la pénétration de la solution, comme discuté précédemment. En parallèle, les aspects fondamentaux de σ sont encore mal compris, ce qui, d'après l'expérience jusqu'à présent, est considéré comme une propriété intrinsèque du support. En effet, la méthode d'inversion de phase utilisée pour fabriquer le support est également un processus aléatoire dans lequel, si les dimensions des pores peuvent être relativement contrôlées, les emplacements des pores ne le sont pas. Dans une étude théorique telle

que celle menée par Hao *et al.* (2020), les auteurs ont produit des pores de surface avec σ de 0,72, mais une surface aussi uniforme que dans la simulation n'est pratiquement pas possible avec la technologie actuelle. L'écart est encore confirmée lorsque l'observation de l'étude théorique est comparée au σ calculé du support à gravure sur piste par Ghadimi *et al.* (2018), en utilisant les résultats de Zhu *et al.* (2016a). Dans le travail actuel, avec σ de 0,0097 pour le support vierge, la perméance apparente du composite PES/PDMS ne dépasserait pas la ligne de perméance PMP, même si f = 1. Un dépôt en PDMS plus fin, de 0,58 µm à f = 1, ou 0,48 µm à f = 0,0046 (valeur f supposée pour un support vierge dans le travail actuel ; voir la Figure 7) serait nécessaire pour obtenir une perméance similaire à celle du PMP.

3.5 Revêtement polyimide P84 (P84 PI) comme couche sélective

3.5.1 Performance du P84 PI et évaluation préliminaire de la couche sélective et de la couche intermédiaire

La performance de base de la membrane P84 PI à couche plane dense a été quantifiée comme présenté dans le Tableau 3. La perméabilité du P84 PI était la plus élevée pour le CO_2, tandis que la différence de perméabilité entre N_2 et CH_4 est négligeable. Cela donne une sélectivité relativement élevée pour CO_2/N_2 et CO_2/CH_4, et une sélectivité assez faible pour N_2/CH_4. En comparaison, les performances en CO_2 dans le brevet de Visser *et al.* (2016) sont plus élevées avec une sélectivité CO_2/CH_4 de 63,9. Cependant, les fibres formées ont été recuites proche de la température de transition vitreuse du P84 PI, à environ 300 °C. Le résultat du travail actuel est plus conforme à d'autres publications dans lesquelles une membrane dense a été coulée en feuille plane à partir de la solution P84 PI, comme par Tin *et al.* (2004) avec une perméabilité au CO_2 et au CH_4 de 1,2 et 0,02 Barrer respectivement, et une sélectivité idéale au CO_2/CH_4 de 50, en utilisant le diméthylformamide (DMF) comme solvant. En parallèle, les travaux qui utilisent la NMP comme solvant, comme dans ce travail de thèse, ont rapporté une perméabilité au N_2, au CO_2 et au CH_4 de 0,05, 1,37 et 0,028 Barrer respectivement (Hosseini and Chung, 2009). Ceci est comparable à la littérature mentionnée précédemment. La sélectivité idéale pour CO_2/CH_4 et N_2/CH_4 a été rapportée à 48,93 et 1,78 respectivement. La sélectivité en CO_2/N_2 était cependant de 27,4, bien inférieure au résultat des travaux en cours.

Afin de justifier l'adéquation du PMP comme couche intermédiaire avec le P84 PI comme couche sélective, le rapport de perméance ($\mathcal{P}_{gutter}/\mathcal{P}_{selective}$), qui est le rapport entre la couche intermédiaire ($\mathcal{P}_{gutter}$) et la perméance de la couche sélective ($\mathcal{P}_{selective}$) a été calculé. Ce rapport doit être élevé, pour que la perméance résultante du composite soit aussi proche que possible de la perméance intrinsèque de la couche sélective, maximisant ainsi les performances de la membrane (Wijmans and Hao, 2015). Les détails de cette étude se trouvent dans le texte principal, chapitre 4.5.1. En résumé, l'utilisation du PMP comme une couche de support et couche intermédiaire

unifiées aurait un effet négligeable sur les performances du composite avec P84 PI. En fait, une épaisseur de P84 PI aussi faible que 31 nm peut être théoriquement réalisée et le composite résultant conserverait toujours les performances au-dessus de 90 % de la perméance intrinsèque de la couche sélective. Cela laisse beaucoup de place à l'optimisation ou à l'amélioration, tant pour la couche intermédiaire que pour la couche sélective.

Tableau 3: Performance de base de la membrane P84 PI plane dense autosupportée fabriquée à partir d'une solution à 10 % en masse dans du NMP (épaisseur : 7,8 ± 0,3 µm)

Gaz	**Perméabilité (Barrer)**	**Sélectivité idéale**		
		CO_2/N_2	**N_2/CH_4**	**CO_2/CH_4**
N_2	0.04 ± 0.01			
CO_2	1.88 ± 0.30	46.4 ± 9.7	1.4 ± 0.3	53.8 ± 6.4
CH_4	0.036 ± 0.006			

3.5.2 Performance de perméation de gaz seuls pour les membranes composites PMP/P84 PI

La Figure 11 présente les résultats de perméation et de sélectivité du CO_2/N_2 sur les membranes composites à fibres creuses PMP, revêtues avec des solutions de différentes concentrations de P84 PI pour un dépôt par immersion à 5 mm/s. Une seule fibre a été testée par passage dans ce test. La membrane composite de référence, traité avec du NMP (0 % en masse de P84 PI) montre des perméances et des sélectivités comparables pour tous les gaz, égales aux résultats obtenues avec la membrane PMP de base, présentées dans le Tableau 2. Cela confirme que la NMP s'est complètement évaporée après la limite de 3 h imposée. Toutefois une concentration de la solution de déposition plus élevée peut induire une vitesse d'évaporation plus lente, en raison d'une viscosité plus élevée de la solution permettant le dépôt (voir le texte principal, chapitre 4.5.2 pour plus de détails). En parallèle, la perméance des membranes traitées avec des solutions de dépôt à 2 % en masse augmente considérablement. Ceci pour le CO_2 et le N_2, avec une sélectivité réduite jusqu'à 1,1. Ceci indique la formation de déchirures sur la surface de la membrane asymétrique de PMP comportant une couche dense de PMP. Le gaz peut alors passer par les pores de la structure de support de la membrane PMP.

En ce qui concerne les dépôts à concentration de polymère plus élevée, 6 et 10 % en masse, ils conduisent toujours à une perméance accrue pour le CO_2 et le N_2, bien qu'à des degrés divers. À 6 % en masse, la sélectivité a été réduite à 0,8 – 0,9, ce qui suggère des déchirures plus petites (en raison de la sélectivité de Knudsen), bien que cela n'ait pas été observé à partir du microscope électronique à balayage (SEM). En

parallèle, l'augmentation de la concentration en polymère augmente la variabilité des perméances du CO_2 et du N_2. Cette variabilité est maximale pour les essais réalisés à 10 % en masse du polymère. À 14% en masse, la perméance chute de façon importante à une moyenne de 0,013 ± 0,001 GPU pour N_2 et de 0,25 ± 0,03 GPU pour CO_2. Cela conduit à une sélectivité moyenne de 42,99 ± 10,80. La grande plage de barres d'erreur est due à une des données, ce qui indique la possibilité que des défauts se produisent même à cette concentration. Néanmoins, cette valeur est comparable aux résultats de sélectivité idéaux du P84 PI libre du Tableau 3. Il est intéressant de noter que la plage de perméance obtenue avec une concentration de la solution de dépôt de 10 % en masse est particulièrement large. Pour cette teneur en polymère, la perméance et la sélectivité peuvent indiquer, soit un revêtement défectueux, soit un revêtement non défectueux.

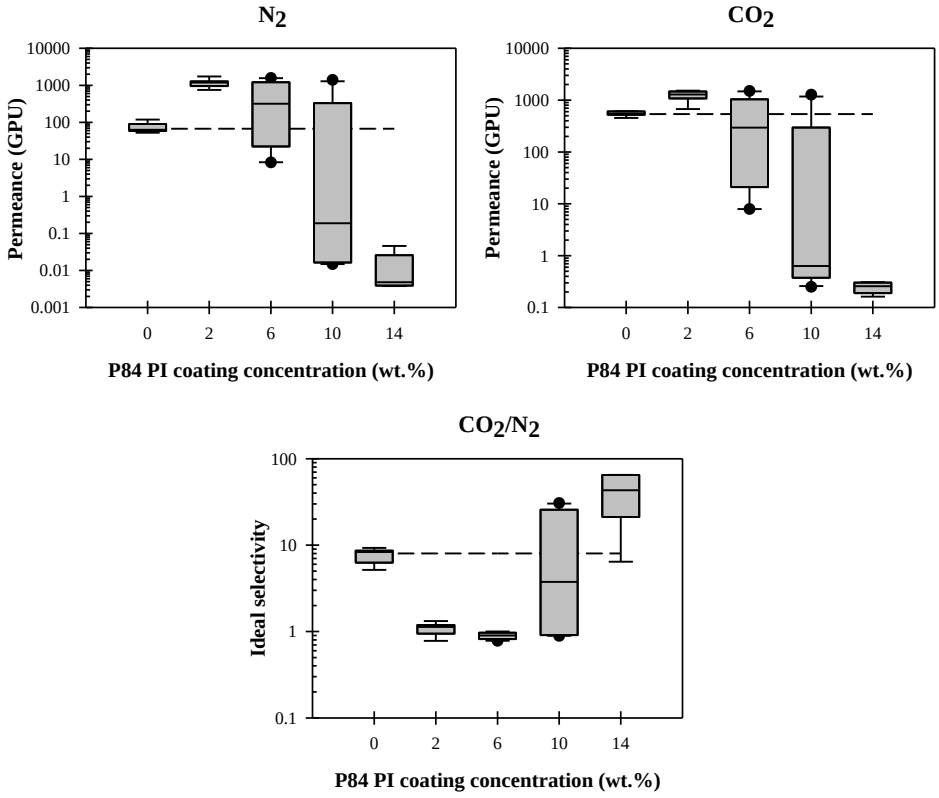

Figure 11: Influence de la concentration en polymère P84 PI (0 – 14 % en masse) sur la perméance et la sélectivité des fibres composites simples (une immersion). La ligne en tirets représente la performance de la fibre non modifiée (non traitée et non revêtue)

Les dépôts dans lesquels le mouillage est partiel sont sujets au démouillage et sont régis par une épaisseur critique minimale. Cependant, il y a deux épaisseurs critiques à considérer. La première épaisseur critique, généralement de l'ordre de 1 mm, est la vraie limite de stabilité d'une surface partiellement mouillée (Redon *et al.*, 1991, Gennes *et al.*, 2004). En dessous de cette limite, la surface partiellement mouillée est métastable et présentera toujours une tendance au démouillage jusqu'à une seconde épaisseur critique (à environ 100 nm). C'est en dessous de cette deuxième

épaisseur critique que la solution d'enrobage subira toujours un démouillage spinodal (Redon *et al.*, 1991). Dans la région métastable, le revêtement en couche mince humide est sensible aux contaminants, aux poches d'air et à l'instabilité forcée due aux mouvements ou au tremblement pendant le processus de revêtement, qui peuvent former de manière aléatoire des sites de nucléation pour provoquer un démouillage (Gennes *et al.*, 2004), créant les régions non-revêtue ou défauts. Ce démouillage, appelé démouillage par nucléation et croissance, se développe à partir de zones sèches, qui peut se produire en raison des facteurs mentionnés précédemment. Néanmoins, le site de nucléation ne s'étend que lorsque le rayon dépasse un certain seuil, et met du temps à se produire (Redon *et al.*, 1991). Ceci est plus facile à réaliser quand le revêtement est plus fin car la force motrice (minimisation de l'énergie totale) serait plus élevée (Thompson, 2012), en plus de la possibilité de plus des zones sèches en raison de la couverture par la poussière et les contaminants ou les bulles d'air introduites pendant le processus d'immersion. Une concentration de revêtement plus élevée aurait également une viscosité plus élevée, ce qui devrait ralentir toute expansion du site de nucléation (voir le texte principal, chapitre 4.5.3 pour de plus de discussions).

En effet, les résultats SEM jusqu'à présent n'ont suggéré aucun défaut, à l'exception d'un des revêtements à 2 % en masse. Néanmoins, même pour une membrane dense, la perméation de gaz est très sensible même à de minuscules défauts, bien plus que les membranes d'osmose inverse (Baker, 2004). Par conséquent, alors que des défauts (zone sèche) qui n'endommagent pas la couche dense de PMP seraient acceptables (comme pour le cas de 14 % en masse), les dommages causés par les déchirures à la couche PMP doivent être évités. En effet, le démouillage de la couche de revêtement réduirait également la sélectivité du composite car la couche de PMP ne serait plus recouverte. Cependant, la sélectivité minimale doit être limitée par la valeur mesurée dans le Tableau 2, qui est définie par la couche PMP. Lors d'un démouillage contrôlé sans déchirure de la couche dense du PMP, la perméabilité et la sélectivité peuvent également être ajustées pour répondre aux besoins du procédé.

Les résultats de perméation suggèrent jusqu'à présent que des solutions de revêtement à 14% en masse seraient la concentration minimale nécessaire pour le travail actuel afin d'éviter le déchirement de la surface du PMP. Cependant, le déchirement pourrait être régi par deux facteurs, (i) l'épaisseur du revêtement qui augmente à mesure que la concentration du revêtement augmente, ou (ii) le retrait du revêtement, qui est plus élevé à faible concentration du revêtement. Par conséquent, un test de perméation a été effectué à différentes vitesses de revêtement (1, 3 et 5 mm/s) pour une solution de revêtement P84 PI à 14 % en masse, à immersion unique, et 4 fibres par cycle pour le gaz CO_2, N_2, et CH_4, comme représenté dans la Figure 12. Pour une vitesse de revêtement de 5 mm/s, la perméance moyenne a augmenté lorsque 4 fibres ont été utilisées par rapport au test de fibre unique précédemment réalisé, suggérant que des défauts étaient toujours formés. Néanmoins, la sélectivité reste relativement élevée ; tout à fait comparable dans le cas du CO_2/CH_4 mais réduit de

près de moitié pour le CO_2/N_2. Au fur et à mesure que la vitesse de revêtement diminuait, la valeur de perméance augmentait tandis que la sélectivité diminuait, suggérant un nombre encore plus élevé de formation de défauts. Néanmoins, la sélectivité idéale reste élevée suggérant l'absence de déchirure de la couche dense de PMP. La vitesse la plus faible à 1 mm/s a donné lieu à la perméance la plus élevée et la sélectivité la plus faible pour toutes les paires de gaz, suggérant un nombre encore plus élevé de défauts. Avec une sélectivité en N_2/CH_4 inférieure à 1, cela suggère que les défauts sont comparativement sévères. Cependant, la sélectivité pour toutes les paires de gaz est toujours de l'ordre de 2 à 3, ce qui est moins dommageable que le revêtement à 6 % en masse, 5 mm/s effectué plus tôt. Cette valeur est également comparable à la sélectivité NMP trempée 3 heures et 3 jours. Par conséquent, il est possible que le PMP dense n'ait pas été déchiré, mais un temps d'immersion plus long imposé par une vitesse de revêtement lente a réduit les performances du PMP de base (voir le texte principal, chapitre 4.5.2 pour plus de détails). Combiné avec la formation de plus de zones sèches, la sélectivité composite globale était régie par le PMP plutôt que par la couche de P84 PI.

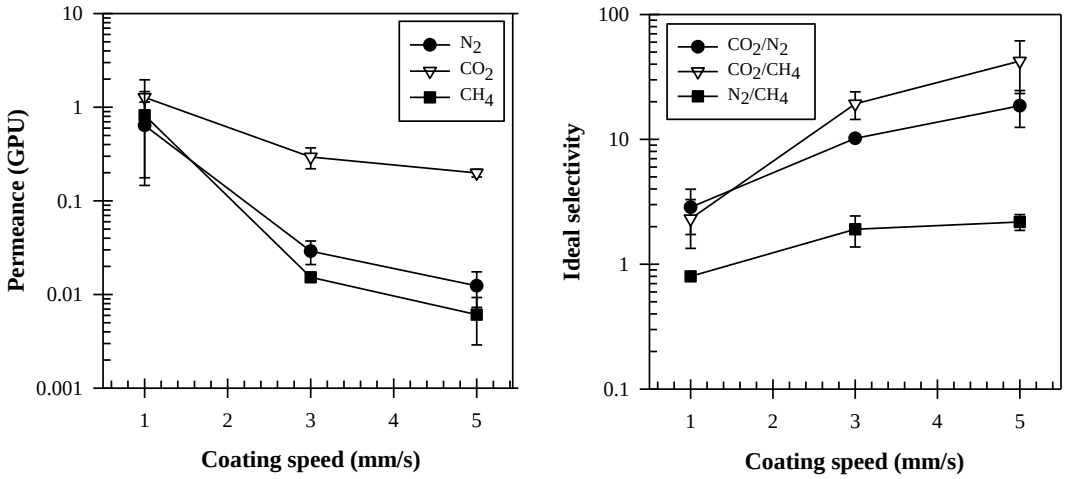

Figure 12: Influence de la vitesse de revêtement (1 à 5 mm/s) dans une solution de polymère P84 PI à 14 % en masse sur la perméabilité et la sélectivité des fibres composites (une immersion, 4 fibres)

L'épaisseur théorique du revêtement sec (voir le texte principal, chapitre 4.5.3 pour plus de détails) a suggéré que la vitesse de 1 et 3 mm/s donnait une valeur de 178 et 370 nm respectivement. Ceci est inférieur à l'épaisseur du revêtement expérimental à 228 et 929 nm pour une solution de revêtement à 6 et 10 % en masse respectivement, qui présente également de moins bons résultats de perméation et de sélectivité. Cela suggère que la déchirure de la couche dense du PMP est principalement causée par le degré de retrait plus élevé à faible concentration de polymère, bien que la contribution des revêtements plus minces qui sont beaucoup plus sujets au démouillage ne puisse être complètement ignorée.

4. Conclusion

Pour faire avancer la recherche dans le domaine de développement de membranes pour la séparation de gaz, en particulier des membranes à matrices mixtes, la fabrication de membranes composites serait une étape indispensable. La compréhension et l'optimisation de la méthodologie de fabrication à la fois de couches poreuse et dense est importante. Les interactions entre les couches doivent être élucidées, pour maximiser les performances de la membrane. Dans le présent travail, une baisse significative de la perméance par rapport à sa valeur idéale a été notée pour les membranes composites PES/PDMS, en particulier à faible épaisseur de revêtement. Même s'il est hautement perméable, la conception du support a joué un rôle important en particulier son architecture de surface, qui impacte l'efficacité de perméance de la couche sélective. L'architecture de surface inclut la taille des pores, la porosité, la densité et les emplacements des pores ainsi que la perméabilité du matériau du support lui-même. Pour cette raison, un revêtement en film mince serait beaucoup plus facile à réaliser sur une couche dense, comme sur une membrane asymétrique à peau dense. L'utilisation de membranes asymétriques élimine l'obstacle de la restriction géométrique et de la pénétration de la solution observé dans les structures composites avec les couches poreuses et denses. Cependant, ceci limite le nombre de matériaux possibles car ces derniers doivent présenter des valeurs de perméance élevées pour être utilisé comme couche intermédiaire (gutter layer en anglais), tout en étant suffisamment résistant mécaniquement pour supporter le processus de perméation de gaz à pression élevée. Le PMP est particulièrement intéressant sur cet aspect, d'autant plus qu'il est compatible avec le NMP ; solvant typique utilisé pour la formation de membranes polymères. Cela permet d'utiliser une méthodologie mature de revêtement par immersion sur certains des polymères les plus prometteurs et testés industriellement, tels que le P84 PI, à utiliser à des fins de fabrication de composites, qui peuvent ensuite être améliorés grâce à l'incorporation de nano additives. Néanmoins, alors que la membrane composite PMP/P84 PI peut être fabriquée, un retrait élevé du P84 PI à faible concentration peut provoquer une déchirure de la fine peau de PMP, exposant le support poreux sous-jacent et rendant le composite non sélectif. Néanmoins, à 14 % en masse de P84 PI, le composite donne une bonne performance de séparation sans défauts majeurs sur la couche de PMP, bien qu'un démouillage se produise encore lorsque l'épaisseur fabriquée est diminuée. Ceci, cependant, peut être une bonne méthode pour contrôler la perméance/sélectivité des composites en fonction des besoins du procédé de séparation.

References

3M 2019. Data Sheet for 3M™ Membrana™ OXYPLUS™, capillary membrane, type PMP 90/200. 3M™ Membrana™.

Baker, R. W. 2002. Future Directions of Membrane Gas Separation Technology. *Industrial & Engineering Chemistry Research,* 41**,** 1393-1411.

Baker, R. W. 2004. *Membrane Technology and Applications,* England, John Wiley & Sons.

Baker, R. W. & Low, B. T. 2014. Gas Separation Membrane Materials: A Perspective. *Macromolecules,* 47**,** 6999-7013.

Bernardo, P., Drioli, E. & Golemme, G. 2009. Membrane Gas Separation: A Review/State of the Art. *Industrial & Engineering Chemistry Research,* 48**,** 4638-4663.

Cay-Durgun, P., Herrera, S. C. & Lind, M. L. 2020. Filler materials to prevent polymer intrusion into mesoporous substrates during thin film formation. *Microporous and Mesoporous Materials,* 296.

Chen, X. Y., Kaliaguine, S. & Rodrigue, D. 2017. A Comparison between Several Commercial Polymer Hollow Fiber Membranes for Gas Separation. *Journal of Membrane and Separation Technology,* 6**,** 1-15.

Chung, T. S. 1997. Calculation of the intrusion depth and its effects on microporous composite membranes. *Separation and Purification Technology,* 12**,** 17-23.

Dai, Z., Ansaloni, L. & Deng, L. 2016. Recent advances in multi-layer composite polymeric membranes for CO_2 separation: A review. *Green Energy & Environment,* 1**,** 102-128.

Ding, Y. 2019. Perspective on Gas Separation Membrane Materials from Process Economics Point of View. *Industrial & Engineering Chemistry Research,* 59**,** 556-568.

Dong, S., Wang, Z., Sheng, M., Qiao, Z. & Wang, J. 2020. Scaling up of defect-free flat membrane with ultra-high gas permeance used for intermediate layer of multi-layer composite membrane and oxygen enrichment. *Separation and Purification Technology,* 239.

Galizia, M., Chi, W. S., Smith, Z. P., Merkel, T. C., Baker, R. W. & Freeman, B. D. 2017. 50th Anniversary Perspective: Polymers and Mixed Matrix Membranes for Gas and Vapor Separation: A Review and Prospective Opportunities. *Macromolecules,* 50**,** 7809-7843.

Gennes, P.-G. d., Brochard-Wyart, F. & Quéré, D. 2004. *Capillarity and wetting phenomena: Drops, bubbles, pearls, waves,* Springer-Verlag New York Inc.

Ghadimi, A., Norouzbahari, S., Lin, H., Rabiee, H. & Sadatnia, B. 2018. Geometric restriction of microporous supports on gas permeance efficiency of thin film composite membranes. *Journal of Membrane Science,* 563**,** 643-654.

Hao, P., Wijmans, J. G., He, Z. & White, L. S. 2020. Effect of pore location and pore size of the support membrane on the permeance of composite membranes. *Journal of Membrane Science,* 594.

Henis, J. M. S. & Tripodi, M. K. 1981. Composite hollow fiber membranes for gas separation: the resistance model approach. *Journal of Membrane Science,* 8**,** 233-246.

Hosseini, S. S. & Chung, T. S. 2009. Carbon membranes from blends of PBI and polyimides for N_2/CH_4 and CO_2/CH_4 separation and hydrogen purification. *Journal of Membrane Science,* 328**,** 174-185.

Hu, L., Cheng, J., Li, Y., Liu, J., Zhou, J. & Cen, K. 2017. Amino-functionalized surface modification of polyacrylonitrile hollow fiber-supported polydimethylsiloxane membranes. *Applied Surface Science,* 413**,** 27-34.

Jin, M.-Y., Liao, Y., Loh, C. H., Tan, C.-H. & Wang, R. 2017. Preparation of Polydimethylsiloxane–Polyvinylidene Fluoride Composite Membranes for Phenol Removal in Extractive Membrane Bioreactor. *Industrial & Engineering Chemistry Research,* 56**,** 3436-3445.

Kattula, M., Ponnuru, K., Zhu, L., Jia, W., Lin, H. & Furlani, E. P. 2015. Designing ultrathin film composite membranes: the impact of a gutter layer. *Scientific Reports,* 5**,** 15016.

Koros, W. J. & Pinnau, I. 2008. Membrane Formation for Gas Separation Processes. *In:* Paul, D. R. & Yampol'skii, Y. P. (eds.) *Polymeric Gas Separation Membranes.* FL, USA: CRC Press.

Li, S., Zhang, H., Yu, S., Hou, J., Huang, S. & Liu, Y. 2019. Pore structure characterization and gas transport property of the penetrating layer in composite membranes. *Separation and Purification Technology,* 211**,** 252-258.

Merkel, T. C., Bondar, V. I., Nagai, K., Freeman, B. D. & Pinnau, I. 1999. Gas Sorption, Diffusion, and Permeation in Poly(dimethylsiloxane). *Journal of Polymer Science Part B: Polymer Physics,* 38**,** 415-434.

Pinnau, I. & Koros, W. J. 1991. Relationship between Substructure Resistance and Gas Separation Properties of Defect-Free Integrally Skinned Asymmetric Membranes. *Industrial & Engineering Chemistry Research,* 30**,** 1837-1840.

Pixton, M. R. & Paul, D. R. 2018. Relationships between Structure and Transport Properties for Polymers with Aromatic Backbones. *In:* Paul, D. R. & Yampol'skii, Y. P. (eds.) *Polymeric Gas Separation Membranes.* Florida, USA: CRC Press.

Redon, C., Brochard-Wyart, F. & Rondelez, F. 1991. Dynamics of dewetting. *Phys Rev Lett,* 66**,** 715-718.

Salih, A. A. M., Yi, C., Peng, H., Yang, B., Yin, L. & Wang, W. 2014. Interfacially polymerized polyetheramine thin film composite membranes with PDMS inter-layer for CO_2 separation. *Journal of Membrane Science,* 472**,** 110-118.

Slepička, P., Trostová, S., Slepičková Kasálková, N., Kolská, Z., Malinský, P., Macková, A., Bačáková, L. & Švorčík, V. 2012. Nanostructuring of polymethylpentene by plasma and heat treatment for improved biocompatibility. *Polymer Degradation and Stability,* 97**,** 1075-1082.

Thompson, C. V. 2012. Solid-State Dewetting of Thin Films. *Annual Review of Materials Research,* 42**,** 399-434.

Tin, P. S., Chung, T.-S., Liu, Y. & Wang, R. 2004. Separation of CO2/CH4 through carbon molecular sieve membranes derived from P84 polyimide. *Carbon,* 42**,** 3123-3131.

Visser, T., Ungerank, M., Balster, J. & Fuhrer, C. 2016. *Method for Producing Polyimide Membranes*. United States patent application 14/900,012.

Wijmans, J. G. & Hao, P. 2015. Influence of the porous support on diffusion in composite membranes. *Journal of Membrane Science,* 494**,** 78-85.

Yampolskii, Y. 2012. Polymeric Gas Separation Membranes. *Macromolecules,* 45**,** 3298-3311.

Yasuda, H. & Rosengren, K. 1970. Isobaric measurement of gas permeability of polymers. *Journal of Applied Polymer Science,* 14**,** 2839-2877.

Zhu, L., Jia, W., Kattula, M., Ponnuru, K., Furlani, E. P. & Lin, H. 2016a. Effect of porous supports on the permeance of thin film composite membranes: Part I. Track-etched polycarbonate supports. *Journal of Membrane Science,* 514**,** 684-695.

Zhu, L., Yavari, M., Jia, W., Furlani, E. P. & Lin, H. 2016b. Geometric Restriction of Gas Permeance in Ultrathin Film Composite Membranes Evaluated Using an Integrated Experimental and Modeling Approach. *Industrial & Engineering Chemistry Research,* 56**,** 351-358.

Résumé

La structuration de membranes composites est inévitable pour la prochaine étape de développement de membranes à matrices mixtes (MMM), car l'utilisation de membranes asymétriques couramment non composites signifierait que la majorité des additifs seraient gaspillées dans le support poreux. Dans cette thèse, la possibilité d'utiliser du poly(4-méthyl-1-pentène) (PMP) comme substrat et comme couche intermédiaire dans une membrane composite a été comparée au polydiméthylsiloxane (PDMS), qui est couramment utilisé comme couche intermédiaire. Il est supporté sur un support poreux en polyéthersulfone (PES), modifié avec du chlorure de lithium (LiCl) pour obtenir des architectures variables de surface de pores. La membrane composite à base de PDMS/PES a montré une perméance de 26,6 ± 2,6 GPU pour le N_2 et de 354,4 ± 27,9 GPU pour le CO_2 avec une épaisseur de revêtement minimale d'environ 1 µm. Cependant, cette valeur est inférieure à celle obtenue avec la membrane dense asymétrique à base de PMP ; 84,6 ± 6,2 GPU pour le N_2 et 607,3 ± 31,3 GPU pour le CO_2. Bien que le PDMS ait une perméabilité intrinsèque bien supérieure à celle du PMP, la membrane composite à base de PDMS/PES souffre d'un problème d'intrusion de solution et de restriction géométrique à son interface dense – poreux, ce qui réduit sa perméance à 4% de sa perméance supposée idéale, à faible épaisseur de revêtement. Il est en outre élucidé que l'uniformité de la surface du support poreux affecte également de manière significative la perméance de la membrane résultante. En comparaison, la membrane à base de PMP asymétrique avec une fine couche dense s'est avérée avantageuse en tant que support et couche intermédiaire, car elle permet d'atténuer le problème d'interface noté précédemment pour les membranes composites tout en étant très perméable, minimisant ainsi la résistance au transfert. Les gaz $N_2/CO_2/CH_4$ ont été choisis comme gaz perméants modèles pour la fabrication ultérieure de membranes composites à base de polyimide P84 (P84 PI) comme couche sélective. Cependant, la faible énergie de surface du PMP limite sa compatibilité pour former une membrane composite. Il a été montré qu'il est possible de déposer par immersion le P84 PI sur une membrane PMP à couche dense, sans qu'il y ait besoin de prétraitement. Du P84 PI a été déposé par immersion à 5 mm/s sur une membrane de PMP à fibre creuse et à peau dense. Différentes concentrations de la solution de dépôt ont été étudiées. Les membranes composites ainsi fabriquées ont été testées pour vérifier leur performance de perméation des gaz. Les résultats ont montré une sélectivité idéale aussi élevée que 42,36 ± 19,08 pour le CO_2/CH_4 et 18,55 ± 6,06 pour le CO_2/N_2. Ces valeurs ont été atteintes pour des solutions de dépôt à 14 % en masse de P84 PI. Toutefois, malgré la résistance du PMP au solvant agressif N-méthyl-2-pyrrolidone (NMP), utilisé pour la solvatation du P84 PI, l'utilisation du P84 PI à faible concentration (2 - 10 % en masse) endommage la couche dense du PMP. Ceci compromet les performances de séparation de la membrane composite. Il est supposé que le rétrécissement du P84 PI lors du séchage a déchiré la couche de PMP sous-jacente. Ainsi, il existe une concentration minimale de polymère P84 PI pour laquelle une couche sélective sans défaut peut être réalisée (qui est d'environ 14 % en masse). À cette concentration, la vitesse de revêtement par

immersion peut être contrôlée pour obtenir une couche sélective sans défaut et mince,adaptée à la fabrication de membranes composites. Ceci, bien que le démouillage de la solution de revêtement se produise encore et s'amplifie à mesure que l'épaisseur du revêtement est réduite.

Mots clés : Membranes composites, élaboration de membranes, polyimide P84, dépôt par immersion, perméation de gaz

Abstract

In this work, the possibility of using poly(4-methyl-1-pentene) (PMP) as substrate-gutter layer in composite membrane was compared with commonly used polydimethylsiloxane (PDMS) as gutter layer, supported on lithium chloride (LiCl) modified polyethersulfone (PES) porous substrate of varying surface pore architectures. High permeability, glassy nature of PMP allows it to be used as a co-substrate-gutter layer, which is expected to mitigate the complexity of solution intrusion and lateral diffusion at dense-porous interface in composite membranes. Results showed that the fabricated composite PES/PDMS was able to obtain permeance as high as 26.6 ± 2.6 GPU for N_2 and 354.4 ± 27.9 GPU for CO_2 at about 1 µm coating thickness. Nevertheless, these values are lower than asymmetric dense skin PMP membrane at 84.6 ± 6.2 GPU for N_2 and 607.3 ± 31.3 GPU for CO_2. Solution intrusion and geometric restriction at the PES/PDMS dense-porous interface reduces its permeance efficiency to as low as 4% of its supposedly ideal permeance at low coating thickness. Using modified resistances-in-series (RiS) model, a correlation was developed to predict the composite membrane's efficiency as a factor of the pre-coat substrate's permeance, coating layer's intrinsic permeance, geometric factor, and penetration factor. It was elucidated that substrate surface uniformity also significantly affects the resulting composite membrane permeance, which was found to be a constant of the substrate used regardless of the coating layer thickness. In comparison, asymmetric PMP with thin dense surface layer was noted to be advantageous as the substrate-gutter layer for the current work as it possesses a lower overall resistance as compared to the PES/PDMS layers and was not affected by geometric restriction and solution intrusion. Hence, asymmetric PMP membrane was chosen as a co-substrate-gutter layer while N_2, CO_2 and CH_4 gases were chosen as the model permeants for further composite membrane fabrication with P84 polyimide (PI), a commercial polymer notable for gas separation in industry, as selective layer. Fabrication of multi-layered composite membranes are usually limited by the suitability of the solvent for each layer's fabrication, which might damage the underlying layers. As PMP is non-soluble in N-methyl-pyrrolidone (NMP) that is used for dissolving P84 PI, it was found that PMP fiber is compatible to form a bilayer through dip coating with P84 PI, without the need for pre-treatment to overcome the low surface energy of PMP. Hence, P84 PI of various concentration was dip coated at 5 mm/s onto PMP-based dense skin hollow fiber membrane and tested for gas permeation performance. Results showed that ideal selectivity as high as 42.36 ± 19.08 for CO_2/CH_4 and 18.55 ± 6.06 for CO_2/N_2 was

achieved at 14 wt.% P84 PI coating. Nevertheless, despite of PMP's resistibility to NMP, introduction of P84 PI at low concentration (2-10 wt.%) damages the thin, dense skin layer of the PMP's membrane surface which jeopardize the composite's separation performance. It is hypothesised that P84 PI's shrinkage during drying period tore the underlying dense PMP layer, exposing the porous structure underneath. Hence, there exist a minimum P84 PI polymer concentration in which defect free P84 PI/PMP composite membranes can be made, which is at about 14 wt.%. At this concentration, dip coating speed can be manipulated to obtain a thinner selective layer suitable for composite membrane fabrication, although dewetting of the coating solution still occurred and magnified as the coating thickness is reduced, reducing the gas selectivity below the intrinsic values of P84 PI and more towards the intrinsic values noted by the PMP substrate-gutter layer.

Keywords : Composite membranes, membrane development, P84 polyimide, dip coating, gas permeation